

Linear theory of plasma waves and instabilities

From ion-electron to MHD descriptions

Jordi De Jonghe

Supervisor:
Prof. dr. Rony Keppens

Dissertation presented in partial
fulfilment of the requirements for the
degree of Doctor of Science (PhD):
Mathematics

June 2023

Linear theory of plasma waves and instabilities

From ion-electron to MHD descriptions

Jordi DE JONGHE

Examination committee:

Prof. dr. Stefan Van Aelst, chair
Prof. dr. Rony Keppens, supervisor
Prof. dr. Fabio Bacchini
Prof. dr. Christian Maes
Prof. dr. ir. Giovanni Samaey
Prof. dr. Paul Gibbon
(Focused Energy Inc.)
Prof. dr. Maria Elena Innocenti
(Ruhr Universität Bochum)

Dissertation presented in partial fulfilment of the requirements for the degree of Doctor of Science (PhD): Mathematics

June 2023

© 2023 KU Leuven – Faculty of Science
Uitgegeven in eigen beheer, Jordi De Jonghe, Celestijnenlaan 200B box 2400, B-3001 Leuven (Belgium)

Alle rechten voorbehouden. Niets uit deze uitgave mag worden vermenigvuldigd en/of openbaar gemaakt worden door middel van druk, fotokopie, microfilm, elektronisch of op welke wijze ook zonder voorafgaande schriftelijke toestemming van de uitgever.

All rights reserved. No part of the publication may be reproduced in any form by print, photoprint, microfilm, electronic or any other means without written permission from the publisher.

*In loving memory of
my mother*

Preface

Dear reader

The work you are about to read (or scan for pictures and condemn to an eternity on the shelf afterwards) is the culmination of four long years, with quite a few ups and downs. Though these years turned out fairly differently from what I had envisioned, I am glad to say in all honesty that this has been an incredible journey, made all the better by the wonderful people around me. Therefore, it should come as no surprise that this thesis would not have seen the light of day without the help and support of many others, who all deserve a word of thanks. First and foremost, I would like thank my supervisor, prof. dr. Rony Keppens, for this opportunity. At the end of the initial interview, you did not hesitate to offer me a PhD position despite my lack of experience in plasma physics. Once I actually started, it quickly became clear to me that I could not wish for a better mentor. If acquiring a PhD is the process of maturing into an independent researcher, I can truly say that you took my hand, walked me to the plasma physics playground, and encouraged me to explore it further on my own. Of course, you always watched me play from a distance and I could run back to you whenever I got stuck. And when I eventually came knocking on your door for a lengthy discussion, I always left with more questions than I had arrived with. To me this has become a hallmark of fruitful research though, since any worthwhile endeavour starts with asking the right questions. Hence, once more, a heartfelt thank you.

Secondly, this manuscript would not have reached the level it has without the thoughtful comments of the members of the examination committee: prof. dr. Fabio Bacchini, prof. dr. Christian Maes, prof. dr. ir. Giovanni Samaey, prof. dr. Paul Gibbon, and prof. dr. Maria Elena Innocenti. You have already given me a lot of food for thought and ideas on how to move forward with this research. I would also like to thank the chair of the examination committee, prof. dr. Stefan Van Aelst, for guiding the discussions following the preliminary and public defences.

Of course, science is a collaborative effort, and I would like to extend my gratitude to both Niels and Michał. Firstly, Niels, thank you for involving me in the development of the *Legolas* code and swiftly bringing me up to speed on the topic of spectroscopy. You have been very patient in answering my barrage of questions every couple of weeks, sometimes because I simply forgot what you said last time. I am proud of what we accomplished and impressed with where you are taking the code next. Secondly, Michał, I really appreciate that you offered me the opportunity to visit you to collaborate on neural networks, a topic

I knew preciously little about initially. Those three weeks at IPP were extremely educational and I tremendously enjoyed our discussions, both scientific and otherwise.

Due to the pandemic, our office time was severely limited for a while, and after the return to regular office hours, I found that the CmPA crew had changed dramatically. To proceed in chronological order, I would first like to thank the “welcome crew” (in alphabetical order): the original occupants of my office, Alexandros, Camilla, Christine, Dana, Dimitris, Evangelia, and Nicolas W., as well as Brecht, Julia, Kostas, and Michaël in the office across the hall. After my arrival more faces continued to show up, who I would like to thank for the many fun discussions during lunch and coffee breaks (ding!): Anwesha, Daniela, Daria, Dion, Elena, Hanne, Joris, Nicolas B., Tinatin, and Veronika; and to relax after-hours I could always count on Angelo, Madhurjya, and Receb to enjoy a Belgian beer together. To round out the colleagues, I am also grateful to the rest of Rony’s team for the valuable comments during the many group meetings and the fond memories of team outings: Beatrice, Fabio, Ileyk, Jack, Jean-Baptiste, Malcolm, Nitin, Samrat, Valeriia, Wenzhi, Xiaohong, Xiaozhou, and Yuhao. A final thanks to all my other wonderful colleagues as well!

Naturally, work cannot continue uninterrupted and I feel blessed that I have so many great friends to fall back on to help me unwind. Bart, Lennart, and Matthias, though I clearly love the games we play at our (almost-)weekly boardgame night, the chance to simply talk or vent is equally instrumental in finding peace of mind. Similarly, I cannot thank Arthur, Florian, Frédéric, Pieter, Robin, Roel, Simon, and Thomas enough for all the amazing get-togethers, getaways, and gossip hours disguised as long (or not-so-long) runs. I especially appreciate you all asking enthusiastically about my research time and time again knowing full well I will not be able to explain it better than last time.

Needless to say, I would not have started or finished this journey without the people closest to me. I am eternally grateful to my parents, who gave me the freedom to pursue whatever I fancied. In the end, it just so happened that I wanted to follow in your footsteps, at least in part. My brother Jiri deserves a shout-out too, for always humbling me and keeping me grounded. Lastly, I am forever indebted to all of my grandparents for their endless love and support. Penultimately, but most importantly, I am extremely fortunate to have Lieve in my life. You stood with me through thick and thin, and helped me weather the storm several times, all whilst putting up with my continually growing list of time-consuming hobbies. You are my anchor in this increasingly overwhelming reality I create for myself.

Finally, I would like to thank you, the reader, if I have not done so above already. The list of people to thank is simply endless, and I wanted to ensure that the preface is not longer than the abstract.

— Jordi De Jonghe, May 2023

Abstract

As the most common, fundamental state of matter in the universe, plasmas are observed in a variety of phenomena, ranging from small-sized fusion experiments to gas clouds on stellar and interstellar scales. As a consequence, an assortment of models exists to describe plasma behaviour on different scales. Within each model the natural oscillations and instabilities supported by a particular plasma configuration can be studied to interpret the plasma's behaviour and evolution. In this thesis, we employ three models to investigate the behaviour of both mechanical and electromagnetic waves: the two-fluid, ion-electron model, Hall-magnetohydrodynamics (HMHD), and regular magnetohydrodynamics (MHD).

Firstly, we consider waves in a homogeneous, ideal ion-electron plasma at rest to address the literature's inconsistent wave labelling schemes that rely on wave behaviour at parallel and perpendicular propagation to the magnetic field. Using a polynomial form of the dispersion relation, which describes six wave types, it is shown that at oblique propagation angles the well-known MHD frequency ordering extends to the ion-electron model, including its additional three wave types compared to MHD, which only has three wave types. In this respect, parallel and perpendicular propagation are unique because the frequency ordering is violated there, thus making these angles unfit for classifying wave types at all angles. This violation of the frequency ordering is characterised by waves crossing in the frequency-wave number diagram. These crossings are then replaced by avoided crossings at oblique angles. In addition, which wave types cross or avoid crossing depends on the specific parameters of the plasma environment. As it turns out, the parameter space contains six distinct regimes of crossing behaviour. Finally, the highly anisotropic behaviour of all wave types is highlighted by their phase and group speed diagrams.

Subsequently, this ion-electron model is applied to a couple of relevant use cases. Whistler waves, which travel in Earth's magnetosphere and are characterised by rapid variations in group speed for small changes in frequency, were recently witnessed to travel at oblique angles to the magnetic field, unlike previous surveys indicating their propagation along the magnetic field lines. With the use of the polynomial ion-electron dispersion relation, known whistler approximations at parallel propagation are meaningfully extended to oblique angles, though any damping effects are inherently absent in this description. Furthermore, considering the avoided crossings at oblique angles, their influence on the whistling behaviour is charted, exposing the split of whistling behaviour across two different wave types in select cases. In a second application, the widely-used, magneto-ionic Appleton-Hartree equation is extended to include the effect of a

non-zero, thermal electron velocity. A final application shows that in a warm plasma the emission of laser-induced Cherenkov radiation is restricted to a cone centered around the laser beam.

In the second half of the thesis, the methodology changes to a spectroscopic approach, computing all natural oscillations and instabilities of a specific configuration numerically with the *Legolas* code, in the HMHD and MHD models. Here, we present how the HMHD spectrum of a homogeneous slab captures the analytic wave solutions, and how the inclusion of electron inertia modifies the short wavelength MHD behaviour to be in line with the ion-electron model.

With the shift to numerical spectroscopy, *Legolas*'s low numerical cost is exploited to examine the resistive tearing instability parametrically. This instability is a form of spontaneous magnetic reconnection, which is a necessary process for many eruptive and disruptive events in the solar corona and Earth's magnetosphere. One of the outstanding questions relating to magnetic reconnection, however, is the fact that observed reconnection rates do not match theoretical predictions. In this regard, it is recognised that the tearing growth rate is affected by Hall physics, ambient flow, and viscosity. The significance of all three factors is scrutinised in compressible conditions, contrary to many reviews limiting themselves to the incompressible case.

In this analysis of the tearing growth rate, the popular Harris current sheet, which features a magnetic field reversal across the sheet, is adopted as the equilibrium configuration. Unlike the incompressible case, the introduction of a “guide field”, i.e. a constant magnetic field component perpendicular to the reversing component, causes the Hall current to suppress the tearing growth rate in the compressible case. This is not the only difference between the compressible and incompressible configurations, though, since the incompressible, analytic scaling laws as a function of the resistivity also require adjustment to account for compressibility. This effect is especially pronounced in the presence of ambient flow, where the flow completely eliminates the instability in certain regions of the parameter space. In this regard, the effect of viscosity is similar to that of background flow.

Finally, we offer perspectives for future research. There, we outline the extension of the ion-electron study to multifluid models, in which a numerical approach similar to the *Legolas* code may prove useful to quantify waves and instabilities. Ultimately, the linear analysis presented here should be compared to non-linear simulations, to identify when and where non-linear effects take over. At the same time, the linear results may aid in the interpretation of non-linear simulations.

Beknopte samenvatting

Als de meest voorkomende aggregatietoestand in het universum, komt plasma voor in diverse omgevingen, variërend van kleinschalige fusie-experimenten tot gaswolken op stellaire en interstellaire schaal. Als gevolg hiervan bestaat er een hele reeks modellen om plasmagedrag op verschillende schalen te beschrijven. Binnen elk model kunnen de natuurlijke oscillaties en instabiliteiten van een bepaalde plasmaconfiguratie worden bekeken om het gedrag en de evolutie van het systeem te bestuderen. In dit proefschrift gebruiken we drie modellen om het gedrag van zowel mechanische als elektromagnetische golven te onderzoeken: het twee-vloeistoffen, ion-elektron model, Hall-magnetohydrodynamica (HMHD) en reguliere magnetohydrodynamica (MHD).

Eerst beschouwen we golven in een homogeen, ideaal ion-elektronplasma in rust om de inconsistente golfsystemen in de literatuur aan te pakken, die berusten op het gedrag bij parallelle en loodrechte voortplanting op het magnetische veld. Met behulp van een polynome vorm van de dispersierelatie, die zes golven beschrijft, wordt aangetoond dat bij schuine voortplantingshoeken de bekende MHD-frequentieordening zich doortrekt in het ion-elektronmodel, inclusief de drie bijkomende golven die MHD mankeert. In dit opzicht zijn parallelle en loodrechte voortplanting uniek omdat de frequentieordening daar wordt geschonden, waardoor deze hoeken niet geschikt zijn voor golfclassificatie onder alle hoeken. Deze schending van de frequentieordening wordt gekenmerkt door het kruisen van golven in het frequentie-golfgetal diagram. Deze kruisingen worden dan vervangen door vermeden kruisingen bij schuine hoeken. Bovendien hangt het af van de parameters van de plasma-omgeving welke golven elkaar kruisen of mijden. Het blijkt dat de parameterruimte zes verschillende regimes bevat. Ten slotte wordt het anisotrope gedrag van alle golven benadrukt door hun fase- en groepssnelheidsdiagrammen.

Vervolgens wordt dit ion-elektronmodel toegepast op een aantal relevante onderwerpen. Whistler-golven, die zich voortbewegen in de magnatosfeer van de aarde en worden gekenmerkt door snelle variaties in groepssnelheid voor kleine frequentieveranderingen, werden onlangs waargenomen als schuin propagerend ten opzichte van het magnetische veld, in tegenstelling tot eerdere onderzoeken die hun voortplanting langs de magnetische veldlijnen observeerden. Met het gebruik van de polynome, ion-elektron dispersierelatie, worden bekende whistlerbenaderingen bij parallelle voortplanting betekenisvol uitgebreid naar schuine hoeken, hoewel alle dampingseffecten inherent afwezig zijn in deze beschrijving. Bovendien wordt, rekening houdend met de vermeden kruisingen bij schuine hoeken, hun invloed op het fluitgedrag in kaart gebracht, waardoor in sommige gevallen de splitsing van het fluitgedrag over twee verschillende

golven wordt vastgesteld. In een tweede toepassing wordt de veelgebruikte, magneto-ionische Appleton-Hartree-vergelijking uitgebreid met het effect van een niet-nul thermische elektronensnelheid. Een laatste toepassing laat zien dat in een warm plasma de emissie van laser-geïnduceerde Cherenkovstraling beperkt is tot een kegel rond de laserstraal.

In de tweede helft van het proefschrift verandert de methodologie naar een spectroscopische aanpak, waarbij alle natuurlijke oscillaties en instabiliteiten van een specifieke configuratie numeriek worden berekend met de *Legolas*-code, in de HMHD- en MHD-modellen. Hier laten we zien hoe het HMHD-spectrum van een homogene plak de analytische golfoplossingen bevat, en hoe de opname van elektroneninertie het MHD-gedrag met korte golflengte wijzigt om overeenstemming te bereiken met het ion-elektronmodel.

Met de verschuiving naar numerieke spectroscopie worden de laag-numerieke kost van *Legolas* uitgebuit om de resistieve “tearing” instabiliteit parametrisch te onderzoeken. Deze instabiliteit is een vorm van spontane “magnetic reconnection”, wat een noodzakelijk proces is voor vele explosieve en verstorende gebeurtenissen in de zonnecorona en de magnetosfeer. Een van de openstaande vragen rond magnetic reconnection is echter het feit dat de waargenomen reconnectionsnelheden niet overeenkomen met de theoretische voorspellingen. Hieromtrent weet men dat de tearing groeisnelheid wordt beïnvloed door Hall-effecten, omgevingsstrooming en viscositeit. De invloed van alle drie de factoren wordt onderzocht in samendrukbare omstandigheden, in tegenstelling tot veel studies die zich beperken tot het niet-samendrukbaar geval.

In deze analyse van de tearing groeisnelheid wordt de populaire Harris “current sheet”, die een magnetische veldomkering doorheen de sheet vertoont, aangenomen als de evenwichtsconfiguratie. In tegenstelling tot het niet-samendrukbaar geval zorgt de introductie van een “guide field”, d.w.z. een constante magnetische veldcomponent loodrecht op de omkerende component, ervoor dat de Hall-stroom de tearing groeisnelheid in het samendrukbaar geval bedwingt. Dit is echter niet het enige verschil tussen de samendrukbare en niet-samendrukbare configuraties, aangezien de niet-samendrukbare, analytische schalingswetten als functie van de resistiviteit ook een aanpassing vereisen omwille van de samendrukbaarheid. Dit effect is vooral uitgesproken in de aanwezigheid van omgevingsstrooming, waarbij de stroming de instabiliteit in bepaalde gebieden van de parameterruimte volledig elimineert. In dit opzicht is het effect van viscositeit vergelijkbaar met dat van achtergrondstroming.

Tot slot bieden we enkele perspectieven op toekomstig onderzoek. We schetsen de uitbreiding van de ion-elektronstudie naar multivloeistofmodellen, waarin een numerieke aanpak zoals de *Legolas*-code nuttig kan zijn om golven en instabiliteiten te kwantificeren. Uiteindelijk kunnen lineaire analyse en niet-lineaire simulaties hand in hand gaan om plasmagedrag beter te verklaren.

List of Abbreviations

AFW ascending frequency whistling. 59

AU astronomical unit. 5

CMA Clemmow–Mullaly–Allis (diagram). 44

CR Cherenkov radiation. 74

DFW descending frequency whistling. 59

ECA eigenfunction classification algorithm. 131

FEM finite element method. 86

HED high energy density (experiment). 38

HMHD Hall magnetohydrodynamics. 9

KHI Kelvin-Helmholtz instability. 99

MHD magnetohydrodynamics. 7

MRI magnetorotational instability. 96

ReLU rectified linear unit. 129

SARI super-Alfvénically rotating instability. 97

List of Symbols

A	vector potential
B	magnetic field
E	electric field
g	gravitational acceleration
J	current density
k	wave vector
κ	thermal conductivity tensor
r	position
u	single-species velocity
v	center of mass velocity
v_g	group velocity
v_{ph}	phase velocity
X	state vector in an eigenvalue problem
δ	combined skin depth
\hat{e}_B	unit vector along background magnetic field
\hat{e}_k	unit vector along wave vector
ϵ_0	vacuum permittivity
η	resistivity
η_e	electron inertia coefficient
η_H	Hall coefficient
γ	ratio of specific heats
\mathcal{L}	heat-loss function (energy losses minus energy gains)
\mathcal{L}_ρ	density derivative of the heat-loss function

\mathcal{L}_T	temperature derivative of the heat-loss function
i	imaginary unit
κ_{\parallel}	thermal conduction coefficient parallel to the magnetic field
κ_{\perp}	thermal conduction coefficient perpendicular to the magnetic field
λ	cosine of the angle θ between the wave vector \mathbf{k} and the background magnetic field
λ_{De}	electron Debye length
A	A-matrix in generalised eigenvalue problem
B	B-matrix in generalised eigenvalue problem
μ	dynamic viscosity OR ratio of masses over charges
μ_0	vacuum permeability
ν	kinematic viscosity
ω	wave frequency
Ω_e	electron cyclotron frequency
Ω_i	ion cyclotron frequency
ω_{pe}	electron plasma frequency
ω_{pi}	ion plasma frequency
ω_p	plasma frequency
Pm	magnetic Prandtl number
ρ	density
x	state vector
θ	angle between the wave vector \mathbf{k} and the background magnetic field
ε	scale factor (1 in Cartesian geometry, r in cylindrical geometry)
c	speed of light in a vacuum
c_a	dimensionless Alfvén speed
c_s	dimensionless sound speed

d_i	ion skin depth
E	dimensionless electron cyclotron frequency (normalised to the plasma frequency)
e	dimensionless electron plasma frequency (normalised to the plasma frequency) OR elementary charge
f_e	electron fraction
I	dimensionless ion cyclotron frequency (normalised to the plasma frequency)
i	dimensionless ion plasma frequency (normalised to the plasma frequency)
k_B	Boltzmann constant
m_e	electron mass
m_p	proton mass
n	number density OR refractive index
p	pressure
r_E	Earth's radius
T	temperature
t	time
v	dimensionless electron thermal speed (normalised to the light speed)
v_a	Alfvén speed
v_e	electron thermal speed
v_i	ion thermal speed
v_s	sound speed
w	dimensionless ion thermal speed (normalised to the light speed)
Z	ion charge number

Contents

Abstract	v
Beknopte samenvatting	vii
List of Abbreviations	ix
List of Symbols	xiii
Contents	xv
1 Introduction	1
1.1 Plasmas in natural and laboratory settings	2
1.1.1 Tokamaks	2
1.1.2 Earth's magnetosphere	3
1.1.3 Solar wind	5
1.1.4 Solar corona	5
1.1.5 Pulsar magnetospheres	6
1.2 Plasma models	7
1.2.1 Magnetohydrodynamics	7
1.2.2 Hall magnetohydrodynamics	9
1.2.3 Multifluid models	10
1.2.4 Kinetic plasma theory	11
1.3 Magnetic reconnection	12
1.3.1 Current sheets	13
1.3.2 Resistive tearing instability	13
1.4 Outline	15
2 Waves in the ion-electron model	17
2.1 Ion-electron dispersion relation	18
2.1.1 Derivation	18
2.1.2 SAFMOX wave labelling scheme	21
2.1.3 Cutoffs, resonances, and limit behaviour	22
2.1.4 The role of the propagation angle	26
2.2 Dispersion diagrams	28
2.2.1 Parallel propagation	29
2.2.2 Perpendicular propagation	33
2.2.3 Wave ordering at oblique angles	34
2.2.4 Critical magnetisation	37

2.3	Wave velocities	39
2.3.1	Phase speed	39
2.3.2	Group speed	40
2.4	Discussion	44
3	Applications of the ion-electron model	47
3.1	Whistler waves	48
3.1.1	Conventions and methodology	49
3.1.2	Classical whistlers	51
3.1.3	Ascending frequency whistlers	53
3.1.4	Ion cyclotron whistlers	55
3.1.5	High-frequency whistlers	56
3.1.6	Pair plasma whistlers	58
3.1.7	Whistling at oblique angles	59
3.1.8	Cross-field whistlers	68
3.2	Warm Appleton-Hartree equation	69
3.3	Laser-induced Cherenkov radiation	73
3.4	Relation to other plasma models	76
3.4.1	Kinetic theory	76
3.4.2	Low-frequency waves	78
3.4.3	Hall-magnetohydrodynamics	79
3.5	Discussion	80
4	Hall-magnetohydrodynamic spectroscopy	83
4.1	Magnetohydrodynamic spectroscopy with the <i>Legolas</i> code	85
4.2	Hall-magnetohydrodynamics	87
4.2.1	Homogeneous plasma slab	89
4.2.2	Resistive Harris sheet	93
4.3	Discussion	95
5	Interplay of flow and resistivity	99
5.1	Resistive tearing instability	100
5.1.1	Conventions	100
5.1.2	Tearing in a plasma slab	101
5.2	Viscous flow	112
5.2.1	Taylor-Couette flow	113
5.2.2	Viscoresistive Harris sheet	119
5.3	Discussion	120
6	Classification of <i>Legolas</i> data with neural networks	125
6.1	Instabilities in jets	126
6.2	Mathematical framework	127
6.2.1	Statement of the problem	128

6.2.2	Neural network construction	128
6.2.3	Class preserving maps	130
6.2.4	Handling of multiple inputs and decision making	131
6.3	Application to <i>Legolas</i> jet data	132
6.3.1	Data generation	132
6.3.2	Network architecture	133
6.3.3	Probability thresholds and performance metric	134
6.3.4	Filtering	134
6.4	Results	134
6.5	Conclusion	136
7	Conclusion & Outlook	139
A	Environment parameters	145
B	Ion-electron equations	147
B.1	Polynomial dispersion relation	147
B.2	Group speed polynomials	149
B.3	Test cases for parallel propagation	150
C	Specifics of the <i>Legolas</i> code	155
C.1	Linearised MHD equations	155
C.2	Solvers	159
C.2.1	QR-invert	160
C.2.2	inverse-iteration	160
C.3	Incompressible approximation	160
C.4	Derived quantities	161
C.5	Grid accumulation	162
Bibliography		163
Curriculum		177

It's the questions we can't answer that teach us the most. They teach us how to think. If you give a man an answer, all he gains is a little fact. But give him a question and he'll look for his own answers.

— Kvothe, in *The Wise Man's Fear*
(Patrick Rothfuss)

1

Introduction

Of the four fundamental states of matter (gas, fluid, solid, and plasma), the most prevalent state of visible matter in the universe is the plasma state, where a significant fraction of the atoms is split into their constituent ions and electrons. Hence, it is not surprising that plasmas are studied across a wide range of applications, ranging from tightly confined laboratory experiments to interstellar clouds. Whilst they are host to a variety of physical phenomena, one of the most fundamental aspects is the occurrence of waves. Since waves transport energy, potentially across large distances, without moving matter, their presence implies that local forces or events can have long-range effects. A great example is the light of the Sun. Even though the Sun is millions of kilometers removed from the Earth, the Sun's rays, which are of the electromagnetic variety, transmit energy all the way from the Sun to Earth, where the energy is most easily appreciated in the heating of the planet's surface and atmosphere. This is just one possible example to illustrate that a firm understanding of waves is crucial to explaining energy transport across large distances in numerous plasma (and other) environments.

During the last century, waves in plasmas have been studied extensively using diverse plasma models, both analytically and, in more recent years, numerically. Though fully non-linear simulations provide an unprecedented perspective on the evolution of plasma systems, we here take a step back and return to linear perturbation theory. Initially, this return to linear theory serves to motivate a change in wave classification. In this regard, the pervading plasma literature may have been too singularly focused on wave propagation parallel and perpendicular to the ambient magnetic field. Here, we revisit the literature results and extend them to oblique angles of propagation to identify why this distinction is important.

In the second half of this study we shift our attention to unstable configurations.

Despite the fact that instabilities typically feature a strongly non-linear stage, the initial evolution is regularly sufficiently linear to treat without non-linear simulations. In this regard, we revived the spectroscopic approach, which quantifies all linear waves of a given configuration, in a modern computational code, including physical effects that were not explored spectroscopically before. This computationally inexpensive approach, compared to non-linear simulations, allows for extensive parametric surveys charting the influence of specific physical factors in the linear regime, in turn leading to a better understanding of the onset of eventually non-linear evolutions.

First, however, this preliminary chapter serves to demonstrate the range of scales that plasma models have to cover and how a handful of models approaches this description. In order to do so, we start with an assortment of plasma environments, presented in Sec. 1.1. Subsequently, Sec. 1.2 introduces the most prevalent plasma models, each one supporting certain types of waves. For each model, we highlight its advantages and use cases. Penultimately, Sec. 1.3 lays out the basics and some open questions of magnetic reconnection to motivate the final component of this thesis. Finally, we conclude this chapter with a general outline.

1.1 Plasmas in natural and laboratory settings

Whilst a large fraction of this treatise concerns itself with the representation of waves across plasma descriptions, it is instructive to get a sense of the wide extremes that plasma theory has to deal with first. Of course, there are many more unique plasma environments than an introductory chapter can hope to cover, so we limit ourselves to a selection of cases from the laboratory scale to the stellar scale. All of the environments offered here will return in some capacity in later chapters as practical applications of plasma theory. Therefore, general values for each environment, along with the appropriate references, are available in App. A.

1.1.1 Tokamaks

Plasmas are often studied in laboratories in the context of thermonuclear fusion research. The aim of fusion research is to combine atomic nuclei, i.e. positively charged ions, into new nuclei and rest particles such that energy is released in the process. For this process to take place, a significant amount of particles has to be ionised to make these ion-ion interactions possible. Hence, the first step towards fusion is to create a fusion plasma. To do so, it suffices to ionise a neutral gas through heating or by introducing a strong potential difference across the gas. It is the second step that poses a bigger challenge: the plasma must be confined in a stable configuration.

Early fusion experiments struggled to construct a magnetic configuration that led to a stable plasma. In the 1960s it was realised that several confinement issues could be somewhat controlled (or eliminated) in a toroidal plasma configuration with a magnetic field winding around the plasma in a helical way. This design, which thus features both poloidal and toroidal magnetic field components, became known as a tokamak (Goedbloed et al., 2019). Even though the tokamak is a more stable configuration than earlier attempts, it is still susceptible to instabilities. A common example is the sawtooth crash, which is named for the repeated sudden drops in electron temperature, which results in a sawtooth pattern when charted as a function of time. During this event, the confinement is disrupted due to resistive instabilities (Yamada et al., 2010; Wesson, 2011). Whilst a typical tokamak is the smallest plasma configuration in this section with a toroidal radius of around 3 m, it features the highest plasma density of all the environments discussed here with a typical number density on the order of $\sim 10^{19} \text{ m}^{-3}$, and its magnetic field strength of a few Tesla ($\sim 3 \text{ T}$) is only trumped by the pulsar environment.

1.1.2 Earth's magnetosphere

Moving away from the surface of Earth, the first plasma one encounters is the ionosphere, which forms the inner layer of Earth's magnetosphere. Here, particles are ionised by the constant bombardment of Earth by the Sun's ultraviolet radiation. Though the ionosphere is actually made up of multiple layers with different particle compositions, densities, and degrees of ionisation, the particle density is generally of the order 10^{11} m^{-3} and the magnetic field is about 10^{-5} T . The ionosphere plays an important role in long-distance radio communication, allowing for the reflection of radio waves by exciting electron oscillations in the plasma (Milone and Wilson, 2014).

Surrounding the ionosphere is the plasmasphere, which stretches outward up to a few Earth radii. Here, the magnetic field strength is comparable to ionosphere conditions whilst the particle density decreases by a few orders of magnitude with a lower bound of $\sim 10^8 \text{ m}^{-3}$. Though reasonably dense, this plasma is “cold”, meaning that thermal effects have a negligible influence on its behaviour. Ground-based observations of “whistler waves”, whose group speeds depend strongly on their frequency, showed that the particle density drops sharply at the plasmasphere’s edge. This transition is now known as the plasmapause (Kivelson and Russell, 1995). Whistler waves are the subject of Sec. 3.1.

Past the plasmapause lies the outer magnetosphere, which terminates at the bow shock. Here, the incoming solar wind is deflected to form the magnetosheath, creating the outermost layer of the magnetosphere. On the inside, this region consisting mostly of solar wind particles terminates at the magnetopause. This layer of strong currents (i.e. a current sheet, see Sec. 1.3.1) separates the solar-wind plasma in the magnetosheath from the “terrestrial” plasma and Earth’s

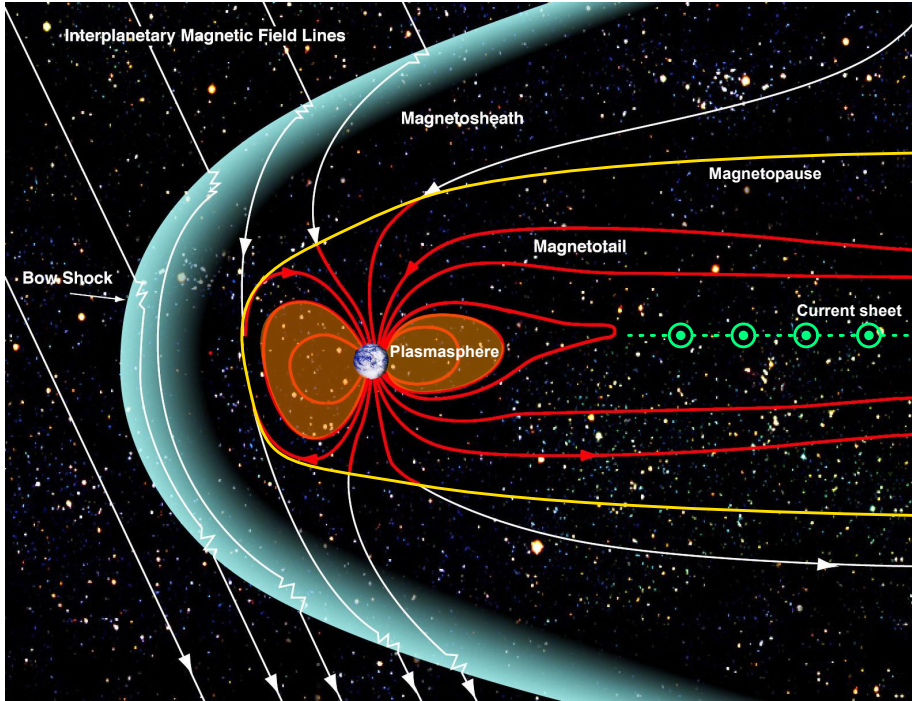


FIGURE 1.1: Overview of Earth’s magnetosphere structure. (Adapted from image by NASA/Goddard/Aaron Kaase)

magnetic field below. Hence, the magnetic field strength changes drastically across the magnetopause. A final feature of the magnetosphere is its elongated structure pointing away from the Sun, called the magnetotail. The magnetic field strength and particle density are significantly lower here, on the order of 10^{-8} T and 10^4 m $^{-3}$, respectively. Embedded in this tail-like structure is another current sheet (Kivelson and Russell, 1995), where magnetic reconnection (see Sec. 1.3) can take place (Yamada et al., 2010). A visual summary of the magnetosphere structure is presented in Fig. 1.1.

Clearly, the magnetosphere consists of a variety of plasma conditions. However, when we refer to magnetosphere parameters in this work, the general magnetosphere parameters in App. A are used rather than any particular layer or substructure.

1.1.3 Solar wind

As we continue our journey outward, we encounter the solar wind at the magnetosphere's bow shock. This stream of charged particles with a particle density of around 10^7 m^{-3} , consisting mostly of electrons, protons, and α particles, is accelerated radially outward from the Sun, after which the solar wind travels throughout the solar system with an almost-constant speed (Milone and Wilson, 2014). Though some driving mechanisms behind the wind's acceleration have been identified, a complete picture of the initial acceleration process remains an outstanding problem in solar wind physics (Viall and Borovsky, 2020).

With it the solar wind carries a weak magnetic field ($\sim 10^{-9} \text{ T}$) lying nearly in the ecliptic plane and at an angle of 45° to the Sun-Earth line at 1 astronomical unit (AU). Due to its charged nature and the field it carries, the solar wind interacts with the planetary magnetic fields. Its dynamic pressure compresses Earth's magnetic field on the dayside whilst it results in an elongated magnetotail on the nightside. As a consequence, the size of the magnetosphere changes with the activity of the solar wind, since it depends on the pressure balance between Earth's magnetic field and the incoming solar wind (Kivelson and Russell, 1995; Milone and Wilson, 2014).

Aside from its interactions with the magnetosphere, the solar wind forms an interesting addition to our selection of plasma cases, thanks to its significantly weaker magnetic field and lower particle density compared to the other plasmas in this section.

1.1.4 Solar corona

As a star, the Sun is of course a prime example of a natural fusion plasma. However, the Sun's interior and atmosphere can be divided into different layers with diverging properties, and the nuclear reactions themselves only take place in the core. Moving outward from the core we find two more layers before reaching the solar atmosphere: the radiative and convection zones. Throughout both layers, the energy from the nuclear reactions in the core is transported towards the solar surface, but the transport mechanism differs. As their names imply, radiative transport occurs in the radiative zone whilst the convection zone contains convection cells. Sitting atop the convection zone and blending with it is the inner layer of the atmosphere: the photosphere. This layer is the Sun's visible surface, and the Sun reaches its temperature minimum here. Ascending into the chromosphere, the density decreases, but the temperature slowly rises again, before experiencing a sharp increase in the transition layer with the tenuous solar corona (Kivelson and Russell, 1995; Roberts, 2019). This rapid increase in temperature away from the solar surface is not yet understood and is known as the coronal heating problem.

Not only does the solar corona feature a peculiar temperature profile, it is also host to a plethora of structures and events. Many of these structures are related in some way to solar active regions, where the magnetic field becomes extremely strong and intricate, and the corona's density and temperature increase. More often than not active regions are bipolar, with magnetic field lines running from the island of positive polarity, where the radial magnetic field component points outward, to that of negative polarity, where it points inward. When the field lines form a magnetic flux tube, i.e. parallel magnetic field lines assume a tube-like shape, plasma is trapped inside, resulting in a coronal loop. Since loops follow the magnetic field lines, their footpoints are anchored in the photosphere, essentially creating a plasma bridge between regions. The coronal loop structure allows various types of waves, either inside the loop (body modes) or on their boundaries (surface modes), which result in deformations and oscillations of or along the entire tube, and which can travel from one footpoint to the other (Priest, 2014; Roberts, 2019).

Whilst singular coronal loops form and decay gradually, the corona is also home to eruptive events, rapidly launching plasma into interplanetary space. A typical example is the eruption of a prominence. Prominences are arcades of cool, dense plasma embedded in the corona. They occur above polarity-inversion lines, i.e. boundaries between regions of positive and negative polarity, in sheared magnetic fields and occur both inside and outside of active regions. When a prominence becomes unstable, it rises and twists before it erupts, expelling part of their material whilst the remainder glides down into the chromosphere. If the prominence eruption occurs in an active region, it is accompanied by another eruptive event: a solar flare. Evidence suggests that during a flare event magnetic energy, built up through shearing and twisting of the field lines, is converted into kinetic energy by a process called magnetic reconnection (see Sec. 1.3) to eject high-energy particles. In the wake of these events, coronal loops are again formed across the polarity-inversion lines (Kivelson and Russell, 1995; Mackay and Yeates, 2012; Parenti, 2014; Priest, 2014).

1.1.5 Pulsar magnetospheres

Finally, outside of our solar system we find a more exotic plasma in pulsar magnetospheres. As a subtype of neutron stars, pulsars are one of the final outcomes at the end of a star's lifecycle. They feature extremely strong magnetic fields (typically $\sim 10^6$ T) and rotate with a regular period. Similarly to Earth's magnetosphere, several characteristic regions can be identified in pulsar magnetospheres. However, here we limit ourselves to the pulsar wind. Analogously to the solar wind, pulsars emit steady streams of particles, but they differ in their constituent particles. Contrary to the other plasmas in this section, the pulsar wind is made up of the leptonic electron-positron pair (Beskin et al., 2006; Pétri, 2016). Consequently, such plasmas are also called

pair plasmas. This combination of strong magnetic fields and mass parity across the particle species leads to a unique plasma environment.

Additionally, pulsar magnetospheres provide a captivating environment to study beam instabilities, which come about due to highly relativistic lepton beams penetrating the ambient wind (Lyutikov, 1999). These instabilities are beyond the scope of this manuscript though.

1.2 Plasma models

When we are dealing with many charged particles at once, solving the equations of motion for single particles subjected to electric and magnetic fields becomes prohibitively expensive computation-wise. There are two main complications that plasma models have to address. The first one is that the motion of the plasma particles generates electromagnetic fields, governed by Maxwell's equations, and these induced fields in turn influence the particles' subsequent movement (Boyd and Sanderson, 2003). The second matter concerns particle interactions. How these interactions are tackled, depends on the frequency of particle collisions and the scale one wishes to describe. For a microscopic description kinetic plasma theory provides a statistical description in terms of particle distribution functions. On the other hand, fluid models lend themselves to a macroscopic perspective (Goedbloed et al., 2019).

Together, frequency of collisions and scale inform the choice of plasma model. Therefore, the plasma models can be ordered in a hierarchy, visualised in Fig. 1.2. At one end of the hierarchy we find the magnetohydrodynamics model, a single-fluid model that is widely-used to study wave phenomena in macroscopic plasma structures. At the other end kinetic theory describes interactions on the particle level. In this section we briefly discuss a handful of models that will be employed or touched upon in the following chapters, starting with the macroscopic view and subsequently zooming in.

1.2.1 Magnetohydrodynamics

The large-scale magnetohydrodynamics (MHD) model can be understood as the combination of fluid mechanics and electromagnetism. Rather than treating the motion of the plasma particles, it employs a continuum approach to model the plasma as a single, conductive fluid of ions, neglecting electron mass and inertia (but assuming quasi-charge neutrality). In this description, the general conservation laws of mass, momentum, and energy govern the time evolution of three macroscopic variables: density, bulk velocity, and pressure (or temperature, related through a closure relation like the ideal gas law). Combining the Maxwell-Faraday equation with Ohm's law finally results in an equation for the time evolution of the magnetic field, which has a contribution in the momentum

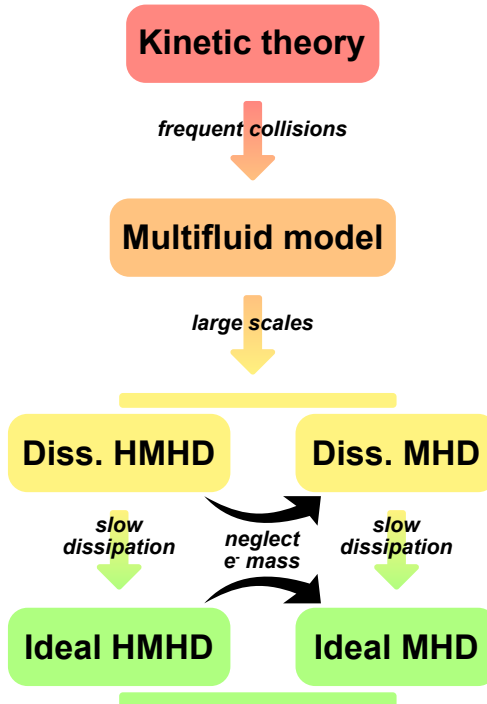


FIGURE 1.2: Hierarchy of plasma models.

equation. In this description the displacement current is neglected (Roberts, 2019). However, in the relativistic ideal MHD description, it is again retained (Goedbloed et al., 2019), and we will make contact with relativistic expressions for wave speeds when handling ion-electron dispersion relations.

Since the displacement current in Ampère's law is ignored, the Newtonian MHD model does not feature electromagnetic waves and only offers a description of mechanical waves. Early studies of MHD focused on incompressible plasmas, which led to the discovery of Alfvén waves by Swedish physicist Hannes Alfvén in 1942 (Alfvén, 1942), for which he received the Nobel prize in 1970. At the origin of these dispersionless waves lies the tension of the magnetic field lines, which acts as the restoring force. The Alfvén waves propagate along the field

lines and perturb them transversely. Once we consider compressibility again, another class of waves appears: magnetoacoustic or magnetosonic waves. This class features two types, the slow and fast magnetoacoustic waves, and as their names suggest, they are distinguished by their difference in speed. Contrary to the Alfvén waves, both thermal and magnetic pressure play a role in their propagation (Goedbloed et al., 2019). In fact, for propagation parallel to the magnetic field one of the magnetoacoustic waves reduces to a purely acoustic wave, uninfluenced by the magnetic field and fully driven by the gas pressure (Boyd and Sanderson, 2003). In any case for any direction of propagation the wave frequencies are ordered as

$$\omega_{\text{slow}} \leq \omega_{\text{Alfvén}} \leq \omega_{\text{fast}}. \quad (1.1)$$

This property will play an important role in the investigation of the ion-electron model in Ch. 2.

Finally, the most important property of the MHD model is arguably its scale independence. Any choice of reference length, magnetic field, and time allows us to write the MHD equations in a dimensionless form. Consequently, whether the plasma in question is astronomically large or contained in a laboratory is inconsequential for the application of MHD theory. However, the dimensionless equations now stress the importance of the ratio of thermal pressure to magnetic pressure,

$$\beta = \frac{p}{p_{\text{magnetic}}} = \frac{2\mu_0 p}{B^2}, \quad (1.2)$$

referred to as the plasma- β (or just β value). As is common, p , B , and μ_0 denote the pressure, magnetic field strength, and vacuum permeability, respectively. For many plasmas of interest the magnetic pressure dominates, such that β is much smaller than 1 (Goedbloed et al., 2019). For each plasma discussed in Sec. 1.1, their typical β -value is specified in App. A.

1.2.2 Hall magnetohydrodynamics

Similarly to MHD, Hall magnetohydrodynamics (HMHD) treats the plasma as a single fluid, but unlike MHD it does not neglect the electron mass and pressure. Whilst the mass, momentum, and energy equations are the same as in MHD, the Hall terms enter the system through the generalised Ohm's law,

$$\mathbf{E} = -\mathbf{v} \times \mathbf{B} + \eta \mathbf{J} + \underbrace{\frac{1}{ne} \mathbf{J} \times \mathbf{B}}_{\text{Hall}} - \underbrace{\frac{\nabla p_e}{ne}}_{e^- \text{ pressure}} + \underbrace{\frac{m_e}{ne^2} \frac{\partial \mathbf{J}}{\partial t}}_{e^- \text{ inertia}}, \quad (1.3)$$

where \mathbf{E} and \mathbf{B} are the electric and magnetic field, \mathbf{v} the velocity, $\mathbf{J} = (\nabla \times \mathbf{B})/\mu_0$ the current, μ_0 the vacuum permeability, η the resistivity, n the number

density, p_e the electron pressure, e the fundamental charge, m_e the electron mass, and t time. This is then combined with the Maxwell-Faraday equation to derive the Hall-modified time evolution of the magnetic field (Gurnett and Bhattacharjee, 2005). The new terms appearing in the induction equation are due to the Hall current, the electron pressure gradient, the electron inertia, and the electron viscosity (Biskamp, 2000).

Whilst both MHD and HMHD describe the plasma as a single fluid, the inclusion of the Hall current decouples the motion of ions and electrons at the ion inertial length (= light speed over ion plasma frequency, see Ch. 2) scale. By introducing this additional length scale, the inclusion of the Hall current results in the breaking of MHD's scale independence. The Hall current is also responsible for the presence of whistler waves in the model (Biskamp, 2000; Huba, 2003).

Since the role of the electron inertia and viscosity is only important when the electron flux is large, their effect is only non-negligible in the short wavelength limit (Biskamp, 2000). Therefore, they are oftentimes ignored. However, as we will see in Ch. 4, the electron inertia bridges the gap with multifluid models by approximately recovering the electron cyclotron resonance in the short wavelength limit.

HMHD has recently seen a resurgence in popularity due to the role it could play in the process of magnetic reconnection. We will revisit the interaction between the Hall current and reconnection in Sec. 1.3, and in more detail in Ch. 4.

1.2.3 Multifluid models

If we still opt for a continuum approach, but acknowledge that the plasma consists of various particle species with their own set of macroscopic variables (density, bulk velocity, and pressure), we enter the domain of the multifluid formalism. Here, each species that is included in the description gets its own set of equations for the conservation laws of mass, momentum, and energy. For an ideal plasma the species-specific conservation laws are then coupled through the addition of the full set of Maxwell's equations, where all the species' densities appear in Gauss's law, and their individual velocities in the current term of Ampère's law (Thorne and Blandford, 2017). In the non-ideal case the momentum conservation laws are additionally coupled through collisional terms featuring the involved species' velocities (Goedbloed et al., 2019).

As we will do in Ch. 2, the multifluid model is often limited to two particle species, and in this case referred to as a two-fluid model. Three common choices stand out: (1) pair plasmas, consisting of electrons and positrons; (2) ion-electron plasmas, where the ion species is often H^+ , i.e. a proton; and (3) ion-neutral mixtures, describing partially ionised plasmas, containing both charged ions and neutral particles. Irrespective of this choice, for a homogeneous background at rest the amount of waves in the two-fluid model can be derived by counting

the degrees of freedom in the equations. Each particle species contributes five degrees of freedom – density, pressure, and three velocity components – whereas Maxwell’s equations contribute four – two free components of both the electric and magnetic field – since the remaining field components are restricted by Gauss’s laws fixing their divergences. Hence, there are 14 different wave types in the two-fluid model, with five more waves for each additional particle species. Assuming static conditions, however, two of these 14 waves are non-moving in the rest frame, i.e. their frequency vanishes. They only perturb the particle densities (Goedbloed et al., 2019). Restricting ourselves to the moving waves, the remaining twelve waves in an ion-electron plasma are the main topic of Ch. 2.

In the absence of background flow, these waves occur in forward-backward propagating pairs. For an ion-electron plasma, these pairs can then be divided into two groups: the ion and electron oscillations. The three waves caused by ion oscillation reduce to the MHD Alfvén and magnetoacoustic waves in the long wavelength limit whilst the electron oscillations feature an electrostatic wave pair and two electromagnetic wave pairs (Goedbloed et al., 2019; Thorne and Blandford, 2017). Although the behaviour of the ion oscillations is often satisfactorily described by MHD or HMHD for a given application, a multifluid model including electrons offers a macroscopic treatment of light waves in plasmas.

1.2.4 Kinetic plasma theory

Unlike the single- and multifluid models in the previous sections, kinetic plasma theory (or simply kinetic theory) foregoes the continuum approach in favor of a statistical, microscopic description. This statistical description relies on distribution functions defined in phase space, i.e. the six-dimensional space with three position components \mathbf{r} and three velocity components \mathbf{v} , which represents a particle’s dynamical state. For each particle species, the distribution function defines the average number density of these particles in a phase space volume element. The integration of a distribution function over the entirety of the phase space then gives the total number of particles (Gurnett and Bhattacharjee, 2005). In addition, using the distribution as the weighting function, position-dependent macroscopic variables, such as number density or average velocity, can be derived from expectation values of particle dynamical quantities, where the integration is performed over the velocity in phase space (Bittencourt, 2004). Subsequently, the average macroscopic quantities of mass, charge, and current density can be obtained by combining the expectation values of number density and velocity of the different particle species (Gurnett and Bhattacharjee, 2005). Whilst the particle distribution functions are functions of position and velocity, i.e. the coordinates in phase space, they also feature a time dependence. Their evolution, then, is governed by the Boltzmann equation. In the absence of

particle collisions, this equation is known as the Vlasov equation and follows from the observation that a particle's phase space coordinates (\mathbf{r}, \mathbf{v}) evolve in an infinitesimal time interval dt as

$$\begin{cases} \mathbf{r}'(t + dt) = \mathbf{r}(t) + \mathbf{v} dt, \\ \mathbf{v}'(t + dt) = \mathbf{v}(t) + \frac{\mathbf{F}}{m_\alpha} dt, \end{cases} \quad (1.4)$$

where m_α is the particle's mass and \mathbf{F} the external force acting on the particle. This means that if a volume element around (\mathbf{r}, \mathbf{v}) evolves in a time interval dt to a volume element around $(\mathbf{r}', \mathbf{v}')$, that the particles in the original volume element at time t are in the new volume element around $(\mathbf{r}', \mathbf{v}')$ at time $t + dt$. However, if collisions are taken into account, the Boltzmann equation has to be modified since particles can leave and enter a volume element through their interactions. Different approaches and approximations exist for the collision term (Bittencourt, 2004). Once there is a prescription for the evolution of distribution functions, the macroscopic quantities can be determined in any position at any time by calculating expectation values.

Due to its microscopic approach kinetic theory is able to describe effects that are inherently absent in fluid descriptions. The classic textbook example is Landau damping, which arises when the assumption of plane wave solutions is substituted in the collisionless Boltzmann equation. Despite the lack of collisions and thus dissipation, kinetic theory predicts damping of plasma oscillations (Bittencourt, 2004; Gurnett and Bhattacharjee, 2005; Goedbloed et al., 2019). Even though in this sense kinetic theory provides the most complete plasma description, fluid models regularly suffice for certain applications, and are favored for their less computationally-intensive formulation of plasma dynamics.

1.3 Magnetic reconnection

In the ideal MHD description of a plasma, Ohm's law Eq. (1.3) reduces to $\mathbf{E} = -\mathbf{v} \times \mathbf{B}$, thus constraining the magnetic field to move with the plasma. This is called the "frozen-in" condition or Alfvén's theorem. Consequently, this implies that the magnetic topology cannot change. In a reconnection event, however, two field lines moving with the plasma approach each other closely and locally violate the frozen-in condition by breaking and reconnecting in a new way (Biskamp, 1993), as illustrated in Fig. 1.3. One glance at the generalised Ohm's law (1.3) immediately reveals that this behaviour can be established by deviating from ideal MHD with the inclusion of different terms. Here, we are mainly concerned with two types of reconnection that can be incorporated by expanding upon ideal MHD: resistive and Hall reconnection. The former relies on collisions, represented by the inclusion of the resistive term $\eta \mathbf{J}$ in

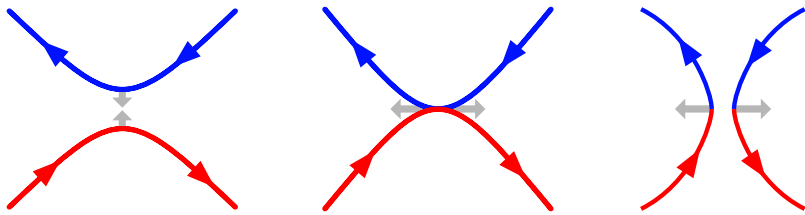


FIGURE 1.3: Illustration of a simple reconnection event.

Ohm's law, whereas the latter is an example of collisionless reconnection. In this collisionless case the reconnection directly follows from the plasma's two-fluid nature, encapsulated in the addition of the Hall term in Ohm's law (Treumann and Baumjohann, 2013).

Though magnetic reconnection is an intrinsically local process, it can alter the global magnetic topology of the system, e.g. by untying a twisted structure. During this reconnection process, magnetic energy is converted to thermal and kinetic energy, which may lead to destabilisations and eruptions such as solar flares or tokamak sawtooth crashes (Yamada et al., 2010).

Despite the variety in reconnection models, one common issue remains: reconnection rates in observations are higher than the models can account for (Yamada et al., 2010). Although this discrepancy is likely not attributable to a single factor, Ch. 4 explores the combination of resistive and Hall reconnection whereas Ch. 5 addresses the effects of flow and viscosity on resistive reconnection in the MHD model.

1.3.1 Current sheets

Whilst there are multiple models for magnetic reconnection, we here focus on one: the current sheet model. This model assumes that the electric current is initially confined to a thin layer of plasma, which is called the current sheet. Through Ampère's law such plane-confined currents are associated with a (quasi-)discontinuous reversal of the magnetic field direction across this layer. Such structures commonly occur in Earth's magnetosphere and the solar corona (Kivelson and Russell, 1995; Biskamp, 2000; Goedbloed et al., 2019).

An example of a current sheet is the Harris sheet, which is an essentially one-dimensional equilibrium solution of the kinetic equations. In this solution, a smooth reversal of the magnetic field direction is realised by a hyperbolic tangent profile, as shown in Fig. 1.4. As a result, the current sheet thickness is

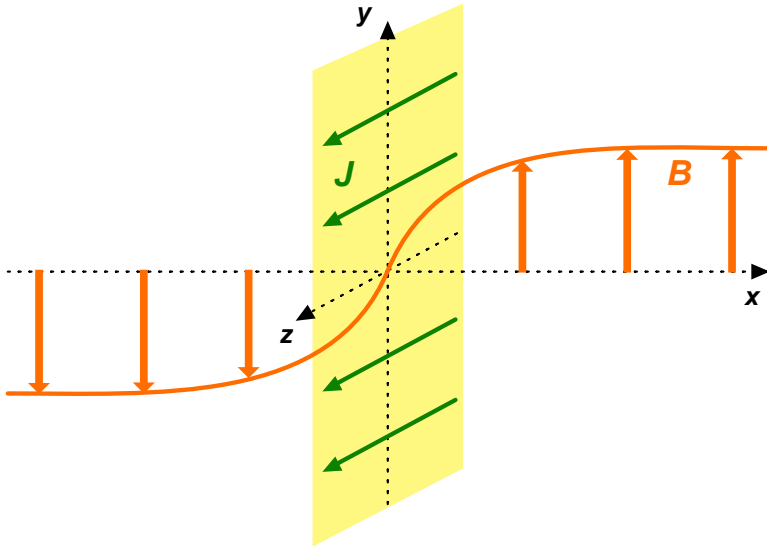


FIGURE 1.4: Depiction of the Harris current sheet structure. \mathbf{B} marks the magnetic field, \mathbf{J} the current.

a free parameter of the equilibrium appearing in the magnetic field description (Yamada et al., 2010). Although the Harris sheet is an equilibrium solution from kinetic theory, it also lends itself to analysis in the MHD and HMHD models, where it is unstable to resistive instabilities due to its magnetic shear.

1.3.2 Resistive tearing instability

Of all the instabilities that can play a role in magnetic reconnection, the most well-known is perhaps the resistive tearing instability, or simply tearing mode, which was first derived by Furth et al. (1963). This instability, which arises in the presence of magnetic shear, is an example of spontaneous reconnection and only requires resistive MHD theory to be adequately described (Biskamp, 2000). The fact that the mode occurs in the MHD model implies that the tearing instability should be viewed as a macroscopic mode with a small-scale resistive effect (Goedbloed et al., 2019).

When resistive tearing occurs along a current sheet, it leads to the formation of magnetic islands. These islands, also called plasmoids and represented in Fig. 1.5, are isolated structures, often asymmetric with a drop-like shape,

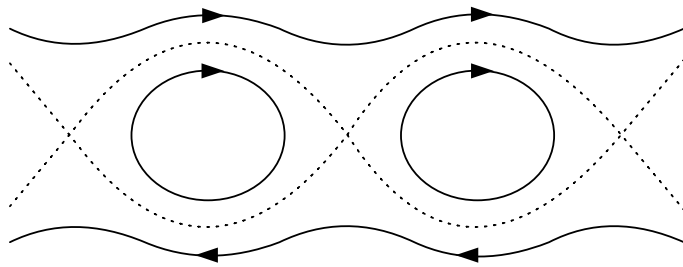


FIGURE 1.5: Creation of magnetic islands by resistive tearing.

featuring closed magnetic field lines. Multiple plasmoids are frequently observed to form simultaneously, creating plasmoid chains. Furthermore, the asymmetry of a plasmoid establishes a new current sheet in its tail, again resulting in the formation of smaller plasmoids. Hence, the self-repeating nature of this process expedites reconnection events (Biskamp, 2000).

In light of this, the growth rate of the tearing instability is of particular interest to expand our understanding of fast reconnection events. In Chs. 4 and 5 we therefore investigate how the tearing mode is affected in the presence of Hall and flow effects.

1.4 Outline

In this treatise on plasma dynamics we focus on two related, yet distinct phenomena: waves and instabilities. The first part focuses on waves in the ideal ion-electron two-fluid model (Chs. 2 and 3) whilst the second half mostly relates to the resistive tearing instability in MHD and HMHD theory.

Starting with a general, warm ion-electron description in Ch. 2, we concentrate on the unique status of propagation exactly parallel or perpendicular to the ambient magnetic field. The fixation on these two remarkable angles of propagation in the literature has led to unintuitive naming conventions, which we rectify by adopting an unambiguous labelling scheme across all angles of propagation, introduced by Keppens and Goedbloed (2019a,b); Keppens et al. (2019). Subsequently, we investigate wave properties at oblique propagation, both analytically and numerically. In this examination we pay special attention to the emerging avoided crossings in the frequency-wave number diagrams, where two types of waves propagate with nearly-identical frequency and wave vector. At these critical points in the frequency-wave number space, the wave coupling is at its strongest and the avoided crossings are expected to facilitate mode conversion (Stix, 1992).

In the consecutive chapter (Ch. 3) the ion-electron model is applied to a selection of topical plasma configurations. The first application concerns whistler waves in Earth's magnetosphere, where we inspect how the avoided crossings affect whistling behaviour across all wave types. Secondly, we show how the warm Appleton-Hartree relation, which is heavily used in magneto-ionic theory, is derived from the ion-electron dispersion relation. In this high-frequency approximation, we explore the influence of the thermal velocities on Faraday rotation. In a third section we question how a warm ion-electron plasma is excited by a laser beam and how the thermal velocity affects the resulting Cherenkov radiation. Finally, to round out this chapter we review how the ion-electron model relates to other plasma models.

When it comes to instabilities, theoretical plasma physics has two strong methods at its disposal: analytic calculations and numerical simulations. Due to the complexity of the various plasma models, analytic calculations are frequently limited to linearised approximations and simple configurations, such as those presented in Chs. 2 and 3. Whilst numerical simulations do not suffer from these limitations, they are restricted by the resources needed to execute them with satisfactory accuracy and have to be navigated carefully to avoid numerical errors. However, in recent years a revival of the spectroscopic approach has been actualised in the *Legolas* code (Claes et al., 2020). Rather than simulating the evolution of a complicated system, *Legolas* quantifies all linear eigenoscillations and instabilities of a chosen MHD equilibrium, thus offering a preview of the dynamics with minimal resources compared to simulations. This numerical tool is introduced in Ch. 4, where it is expanded from MHD to HMHD and verified against literature results.

As we will observe in Ch. 4, the Hall current significantly affects the growth rate of the resistive tearing instability. However, the Hall current is likely not the only physical effect influencing the tearing growth rate. Therefore, Ch. 5 focuses on the interplay between background flow and resistivity, and asks the question when the flow exerts a stabilising and destabilising influence on the tearing mode. Taking this a step further, the addition of viscosity in the *Legolas* code moves the study further along towards a realistic analysis of resistive tearing.

Finally, we take a sharp turn in Ch. 6 and focus on a more practical consideration. Due to the nature of the *Legolas* code, it computes a multitude of eigenoscillations, which can make it hard to identify specific modes of interest in the output. Therefore, we look for an automated way to detect physical characteristics, and to classify modes accordingly.

Precept Forty-Five: ‘One Thing Is Not Another’. This one should be obvious, but I’ve had others try to argue that one thing, which is clearly what it is and not something else, is actually some other thing, which it isn’t. Stay on your guard!

— Zote the Mighty, in *Hollow Knight*
(Team Cherry)

2

Waves in the ion-electron model

The majority of this chapter was published in De Jonghe and Keppens (2020). J. De Jonghe performed the calculations and visualisations, and wrote the manuscript. R. Keppens contributed to the revision of the paper.

Similarly to many textbooks, we start our exploration of plasma waves in an infinite, homogeneous, ideal ion-electron plasma at rest. The advantage of this description with both positively and negatively charged particles is that the model contains both mechanical and electromagnetic waves, contrary to e.g. the more widely applied Newtonian MHD model, which only accommodates mechanical waves. Unlike textbooks, however, where they usually only discuss these waves at parallel and perpendicular propagation with respect to the background magnetic field and sometimes in terms of the refraction index, we here consider the approach pioneered by Denisse and Delcroix (1961); Goedbloed et al. (2019).

Firstly, the dispersion relation is derived from the linearised ion-electron equations in terms of the frequency and wave number. As we will see, this dispersion relation is a bivariate polynomial in the frequency and wave number, where the coefficients are determined by the plasma’s environmental properties: pressure, magnetisation, and the particle species. Subsequently, a modern wave labelling scheme (Keppens and Goedbloed, 2019a,b; Keppens et al., 2019) is introduced, which does not rely on the properties of waves at parallel and perpendicular propagation, unlike the prevailing naming conventions. After establishing these conventions, the dispersion relation is thoroughly probed

across all propagation angles, with a focus on mode crossings — pairs of frequency and wave number which are allowed for multiple wave types — and avoided crossings, leading to a handful of distinct parameter regimes. As solutions of interest, the (avoided) crossings can be determined numerically, and analytic approximations are provided. Finally, the phase and group velocities are explored and visualised. Here as well, exact analytic expressions and limit case approximations are determined.

2.1 Ion-electron dispersion relation

Following the presentation of the ion-electron model in Goedbloed et al. (2019), which is based on the description of Denisse and Delcroix (1961), the wave types of this model are governed by a polynomial dispersion relation of sixth order in the wave frequency squared (ω^2), thus describing six pairs of forward-backward propagating wave pairs. Here, a brief outline of the derivation of the dispersion relation is presented (for a more thorough derivation, see Goedbloed et al., 2019, p. 86–92). Afterwards, the modern labelling scheme from (Keppens and Goedbloed, 2019a) is introduced. Finally, Sec. 2.1.3 shows how well-known limit behaviour is recovered from the dispersion relation and Sec. 2.1.4 highlights the importance of the propagation angle. All expressions in this chapter and the next were obtained or checked with Python’s SymPy package for symbolic computations.

2.1.1 Derivation

For each particle species s in the ideal ion-electron model, i.e. $s = e$ for electrons and $s = i$ for ions, we adopt a continuity equation

$$\left(\frac{\partial}{\partial t} + \mathbf{u}_s \cdot \nabla \right) n_s + n_s \nabla \cdot \mathbf{u}_s = 0, \quad (2.1)$$

a momentum equation

$$n_s m_s \left(\frac{\partial}{\partial t} + \mathbf{u}_s \cdot \nabla \right) \mathbf{u}_s + \nabla p_s - q_s n_s (\mathbf{E} + \mathbf{u}_s \times \mathbf{B}) = 0, \quad (2.2)$$

and an energy equation¹

$$\left(\frac{\partial}{\partial t} + \mathbf{u}_s \cdot \nabla \right) p_s + \gamma p_s \nabla \cdot \mathbf{u}_s = 0, \quad (2.3)$$

¹Here, a single adiabatic index γ is used for both ions and electrons. However, one could differentiate between ions and electrons by replacing γ with a species-specific index γ_s . Alternatively, one could even replace Eq. (2.3) with a different closure relation for one or both species, like the polytropic process equation.

where \mathbf{u}_s , n_s , m_s , and p_s denote a species's bulk velocity, particle density, mass, and pressure, respectively. \mathbf{E} and \mathbf{B} represent the electric and magnetic field, and t the time. Finally, q_s represents a species's charge and equals $q_e = -e$ for electrons and $q_i = Ze$ for ions, with e the fundamental charge and Z the ion charge number. These equations are then complemented by Maxwell's equations (in SI units)

$$\nabla \times \mathbf{E} = -\frac{\partial \mathbf{B}}{\partial t}, \quad (2.4)$$

$$\nabla \times \mathbf{B} = \mu_0 \sum_s q_s n_s \mathbf{u}_s + \frac{1}{c^2} \frac{\partial \mathbf{E}}{\partial t}, \quad (2.5)$$

$$\nabla \cdot \mathbf{E} = \frac{1}{\epsilon_0} \sum_s q_s n_s, \quad (2.6)$$

$$\nabla \cdot \mathbf{B} = 0, \quad (2.7)$$

where μ_0 and ϵ_0 are the vacuum permeability and permittivity, respectively, and $c = (\epsilon_0 \mu_0)^{-1/2}$ is the light speed.

After linearising these equations, we consider a charge-neutral ($n_e = Zn_i$), homogeneous background at rest subject to a uniform magnetic field \mathbf{B} . Subsequently, we insert small amplitude oscillations (indicated below with a tilde) and assume plane wave solutions ($\sim \exp[i(\mathbf{k} \cdot \mathbf{r} - \omega t)]$). Due to the plane wave assumption, all differential operators can be replaced by $\nabla \rightarrow i\mathbf{k}$, $\partial/\partial t \rightarrow -i\omega$, resulting in a set of algebraic equations. With a smart choice of reference frame

$$\hat{\mathbf{e}}_1 = \hat{\mathbf{e}}_2 \times \hat{\mathbf{e}}_3, \quad \hat{\mathbf{e}}_2 = \frac{\mathbf{B} \times \mathbf{k}}{|\mathbf{B} \times \mathbf{k}|}, \quad \hat{\mathbf{e}}_3 = \frac{\mathbf{k}}{|\mathbf{k}|} \quad (2.8)$$

the electric \tilde{E}_3 and magnetic \tilde{B}_3 components are eliminated. For non-marginal waves ($\omega \neq 0$), the remaining components of the magnetic field perturbation $\tilde{\mathbf{B}}$ can then be written in terms of the electric field perturbation $\tilde{\mathbf{E}}$ through Maxwell-Faraday's law, whilst the density and pressure perturbations of each species can be expressed in terms of the $\hat{\mathbf{e}}_3$ -component of that species's velocity perturbation through the continuity and energy equation, respectively. Additionally, for these ideal equations, the $\hat{\mathbf{e}}_2$ -component of each species's velocity perturbation is eliminated by writing it as an expression in $\tilde{\mathbf{E}}$ and the other two components of the velocity perturbation of that species. After these reductions, we are left with a system of six equations

$$\mathbf{A}(\omega, k) \cdot (\tilde{E}_1, \tilde{E}_2, \tilde{u}_{e1}, \tilde{u}_{e3}, \tilde{u}_{i1}, \tilde{u}_{i3})^\top = 0. \quad (2.9)$$

The dispersion relation, which connects the wave frequency ω and the wave number $k = |\mathbf{k}|$, is ultimately obtained as the determinant of \mathbf{A} .

The resulting dispersion relation of the warm, ion-electron plasma is a polynomial of sixth order in ω^2 and of fourth order in k^2 . Furthermore, the combined order of ω^2 and k^2 is at least three and at most six. The dispersion relation can thus be written as (Goedbloed et al., 2019)

$$\sum_{\substack{0 \leq m \leq 6 \\ 0 \leq n \leq 4 \\ 3 \leq m+n \leq 6}} \alpha_{mn} \omega^{2m} k^{2n} = 0. \quad (2.10)$$

The coefficient notation α_{mn} will be used to discuss particular terms in the remainder of this chapter and the next, and follows the conventions of Goedbloed et al. (2019).

The coefficients in this polynomial are determined by various physical quantities of the plasma. These quantities are defined separately for each species, namely the species's plasma frequency $\omega_{ps} = \sqrt{q_s^2 n_s / \epsilon_0 m_s}$, cyclotron frequency $\Omega_s = |q_s|B/m_s$, and sound speed $v_s = \sqrt{\gamma p_s / n_s m_s}$ (not to be confused with the bulk velocity \mathbf{v}_s !). Here, B denotes the strength of the background uniform magnetic field and γ the adiabatic index. The plasma frequency is then given by $\omega_p = \sqrt{\omega_{pe}^2 + \omega_{pi}^2}$. To write the dispersion relation in terms of dimensionless quantities, frequencies are normalised to the plasma frequency and speeds to the light speed. Adopting the notation of Goedbloed et al. (2019), we define the dimensionless quantities

$$\begin{aligned} e &\equiv \omega_{pe}/\omega_p, & E &\equiv \Omega_e/\omega_p, & v &\equiv v_e/c, \\ i &\equiv \omega_{pi}/\omega_p, & I &\equiv \Omega_i/\omega_p, & w &\equiv v_i/c. \end{aligned} \quad (2.11)$$

Introducing the ratio of masses over charges $\mu = Zm_e/m_i$, these quantities satisfy the relations

$$e^2 = \frac{1}{1 + \mu}, \quad i^2 = \frac{\mu}{1 + \mu}, \quad I = \mu E. \quad (2.12)$$

The final parameter appearing in the coefficients α_{mn} is defined as $\lambda = \cos \theta$, where θ is the angle between the wave vector \mathbf{k} and the magnetic field \mathbf{B} . This results in a set of five dimensionless parameters E , μ , v , w , and λ to govern all wave behaviour.

The entire dispersion relation can now be written in terms of dimensionless quantities by normalising the frequency and wave number as

$$\bar{\omega} = \omega/\omega_p, \quad \bar{k} = ck/\omega_p, \quad (2.13)$$

where $c/\omega_p \equiv \delta$ is the combined skin depth. The coefficients for this dimensionless dispersion relation can be found in App. B.1. Note that the

expression $i^2v^2 + e^2w^2$ here has been related to the normalised, combined ion-electron sound speed²,

$$c_s^2 \equiv \frac{v_s^2}{c^2} = i^2v^2 + e^2w^2. \quad (2.14)$$

To lighten the notation, all bars are hereafter omitted but implied unless specified otherwise.

2.1.2 SAFMOX wave labelling scheme

The SAFMOX labelling scheme was first introduced by Keppens and Goedbloed (2019a) for a cold ($T = 0$, and thus $v = w = 0$) electron-positron plasma (also called a pair plasma), which only features five different wave types, which they named A, F, M, O, and X. Later, the S label was added for a warm pair plasma case (Keppens et al., 2019). These six labels were inspired by textbook naming conventions and will thus be assigned in such a way that they reduce to these textbook waves.

The labels S, A, and F are short for the well-established MHD Alfvén (A), and slow (S) and fast (F) magnetohydrodynamic waves and should reduce to these waves in the long wavelength (small k) limit. Hence, at any angle these modes are labelled by their *long wavelength behaviour* such that the MHD ordering $\omega_S \leq \omega_A \leq \omega_F$ is satisfied for sufficiently small wave numbers. Further, the M label stands for modified electrostatic mode and is identified by the *short wavelength behaviour* behaviour $\omega^2 \simeq k^2 \max\{v^2, w^2\}$. If $v \geq w$, it corresponds to the textbook Langmuir wave at parallel propagation³, which is given by the dispersion relation

$$\omega^2 = \omega_{pe}^2 + \gamma_e C_e^2 k^2 \quad (\text{no bars implied}), \quad (2.15)$$

where ω_{pe} and γ_e are the electron plasma frequency and adiabatic index, respectively, and $C_e^2 = p_e/n_e m_e$. Here, the second term comes from the electron pressure (Gurnett and Bhattacharjee, 2005). Note that we temporarily distinguish an electron-specific adiabatic index (γ_e). In our conventions, Eq. (2.15) implies short wavelength behaviour (large k) of $\omega^2 \simeq k^2 v^2$. Finally, the O and X labels are borrowed from the literature which speaks of ordinary (O) and extraordinary (X) electromagnetic modes. The short wavelength behaviour of either mode is electromagnetic, meaning $\omega = k$, but they are distinguished from each other by their long wavelength behaviour where they have a different

²Note that the subscript s refers to “sound” here, and no longer to “species”.

³Although the Langmuir wave inspired the M label, we do not define the M mode as reducing to this textbook wave at parallel propagation because this would lead to ambiguous labelling if $v < w$. We will soon assume that $v > w$, so this is not important for the remainder of this chapter.

cutoff value $\omega^2(k^2 \rightarrow 0) = \text{constant} > 0$. The X mode has the highest cutoff value of all wave types whereas the O mode has the lower cutoff of these two modes.

With these conventions, we have established our wave labelling scheme. To label the different wave types and study their behaviour it is necessary to examine their long and short wavelength limits as well as how these regimes connect. This connectivity of course raises the question if the long wavelength behaviours used to identify the S, A, and F modes can connect to the short wavelength behaviour that identifies the M, O, and X modes, thus resulting in ambiguous labelling (and worse, leaving some modes without a label!). As we will see, the answer turns out to be no, such that this labelling scheme is unambiguous. To show this, we will first focus on the limit behaviour of the dispersion relation. Afterwards, we will study the connection between long and short wavelength regimes.

As a final note, we adopt a colour convention for all ion-electron figures, where each mode is always represented in its own colour: S—green, A—red, F—blue, M—purple, O—cyan, and X—black.

2.1.3 Cutoffs, resonances, and limit behaviour

Now let us look at the limit behaviour of the dispersion relation. To demonstrate the methodology and establish a basis of comparison, we first consider an unmagnetised, warm ion-electron plasma. Next, we discuss how the limit behaviour changes when a magnetic field is applied to the plasma.

Unmagnetised plasma

For an unmagnetised plasma ($B = 0$), the parameters E and I are zero, which naturally eliminates all terms that depend on the propagation angle, i.e. terms featuring λ . Note, however, that $\mu = I/E$ remains a finite nonzero constant. The remaining three parameters describing all wave types are thus the electron and ion sound speeds v and w , and the ratio of masses over charges μ . The factorised dispersion relation becomes

$$\begin{aligned} & \omega^4 (\omega^2 - k^2 - 1)^2 \\ & \times \{\omega^4 - \omega^2[1 + k^2(v^2 + w^2)] + k^2[c_s^2 + k^2v^2w^2]\} = 0. \end{aligned} \tag{2.16}$$

Note how assuming $c_s \simeq w$ (i.e. $m_e \ll m_i$) and immobile ions ($w = 0$) reduces this expression to

$$\omega^6(\omega^2 - \omega_p^2 - c^2k^2)^2(\omega^2 - \omega_p^2 - v_e^2k^2) = 0 \quad (\text{no bars implied}) \tag{2.17}$$

after reintroducing dimensions, recovering the Langmuir $\omega^2 = \omega_p^2 + v_e^2k^2$ and two electromagnetic $\omega^2 = \omega_p^2 + c^2k^2$ waves.

Introducing the term *branch* to indicate an irreducible polynomial in ω^2 , Eq. (2.16) contains two degenerate first order branches and one quadratic branch. As could be anticipated from MHD, two trivial solutions $\omega^2 = 0$ describe the S (slow) and A (Alfvén) modes, which do not propagate in the absence of a magnetic field.

To assign wave labels to each of the branches we consider the small and large wave number limits of the dispersion relation (2.16). In the small wave number limit the quadratic branch reduces to $\omega^2(\omega^2 - 1) = 0$ whereas the other two modes reduce to $\omega^2 = 1$. Hence, we can already conclude that the quadratic branch describes the F mode thanks to the ω^2 factor. Furthermore, the quadratic branch will also describe either the M, O, or X mode. To ascertain which one it is, we consider the local, high-frequency limit ($\omega^2 \rightarrow \infty, k^2 \rightarrow \infty, \omega^2/k^2$ finite) of the quadratic branch. In this limit the dispersion relation can be written as

$$(\omega^2 - k^2 v^2)(\omega^2 - k^2 w^2) = 0. \quad (2.18)$$

Independent of the relation between v and w , this branch contains the short wavelength behaviour $\omega^2 \simeq k^2 \max\{v^2, w^2\}$, which we defined to be the M mode. Thus, we conclude that the quadratic branch describes the F and M modes. (We will later verify that the $\omega^2 \simeq k^2 \min\{v^2, w^2\}$ short wavelength behaviour connects to the long wavelength behaviour of the F mode.)

The global, low-frequency limit ($\omega^2 \rightarrow 0, k^2 \rightarrow 0, \omega^2/k^2$ finite) retrieves the long wavelength behaviour of the acoustic F mode, $\omega^2 = k^2 c_s^2$, which is how Eq. (2.14) was obtained. Note that $\min\{v, w\} < c_s < \max\{v, w\}$. From now on we will assume that $v > w$ such that the ordering becomes $w < c_s < v$. This assumption of having an electron thermal velocity above the ion thermal velocity is fairly representative of expected behaviour since ions are more immobile. A plasma where $w > v$ can be analysed as well from our general dispersion relation, but is outside the scope of the treatment here. In the limit case $v = w$, and thus $c_s = v = w$, the quadratic branch factorises further into

$$(\omega^2 - k^2 c_s^2)(\omega^2 - 1 - k^2 c_s^2) = 0 \quad (2.19)$$

and both modes have the same short wavelength (large k) behaviour.

Magnetised plasma

Now turning to the magnetised plasma, we derive the cutoff, resonance, local high-frequency, and global low-frequency limits. All but the latter were already offered in Goedbloed et al. (2019) whereas the global, low-frequency limit was only given in approximate form. They are invaluable to our discussion though, so they are reproduced and discussed here. The cutoffs reveal some previously unexplored behaviour and we show how the global, low-frequency limit reduces to MHD.

Cutoffs. Starting with the cutoff limit the dispersion relation gives

$$\omega^2(k^2 \rightarrow 0) = \begin{cases} 1, \\ 1 + \frac{1}{2}(E^2 + I^2) \pm \frac{1}{2}|E - I|\sqrt{(E + I)^2 + 4} \\ \quad \equiv \omega_{u,l}^2, \end{cases} \quad (2.20)$$

where ω_u signifies the plus (upper) sign and ω_l the minus (lower) sign. First of all, note that the triple $\omega^2 = 1$ degeneracy in the cutoff limit of the unmagnetised case has been lifted by applying a magnetic field. Secondly, a pair plasma satisfies $E = I$ and substituting this in the equation recovers the result (5.1) from Keppens et al. (2019). Thirdly, note that ω_u is always larger than 1 and ω_l . Therefore, it will always correspond to the X mode. Additionally, using $I = \mu E$ it can be shown that $\omega_l < 1$ if and only if

$$E < \frac{1 - \mu}{\mu} \quad \equiv E_{cr}. \quad (2.21)$$

This was already briefly pointed out in Keppens and Goedbloed (2019b), but will be discussed here in more detail later. We will refer to this value E_{cr} as the critical electron cyclotron frequency or critical magnetisation. Alternatively, this critical value can be expressed in terms of the electron and ion plasma frequencies, $E_{cr} = (\omega_{pe}^2 - \omega_{pi}^2)/\omega_{pi}^2$, or we can define a critical (normalised) Alfvén speed⁴, $c_{a,cr} = (1 - \mu)/\sqrt{1 - \mu + \mu^2}$. This result is the main reason why the M mode is defined by its short wavelength behaviour rather than by the ordering at $k^2 = 0$. This definition of the M mode (and consequently the O mode) results in a consistent labelling across this critical value.

As it turns out, this quantity E_{cr} will also appear multiple times in the discussion to follow. It is also worth pointing out that for a pair plasma ($\mu = 1$) the critical electron cyclotron frequency is zero such that any magnetised pair plasma satisfies $\omega_l > 1$. This is confirmed by the result (5.1) in Keppens et al. (2019) stating $\omega_{u,l}^2 = 1 + E^2$.

Since $\omega_l = 1$ for $E = 0$ and $\omega_l < 1$ for $0 < E < E_{cr}$ there must also be a value of E for which ω_l is minimal. This minimising value of E can be computed to be

$$E_m = \frac{1}{\sqrt{\mu}} \frac{1 - \mu}{1 + \mu}. \quad (2.22)$$

In agreement with our previous remark on the result obtained in Keppens et al. (2019), the minimising value of E is zero for a pair plasma ($\mu = 1$).

⁴To avoid any possible confusion with the A mode, we use a lowercase ‘a’ subscript to denote the Alfvén speed.

Resonances. Two resonances are present,

$$\omega^2(k^2 \rightarrow \infty) = \begin{cases} \lambda^2 E^2, \\ \lambda^2 I^2. \end{cases} \quad (2.23)$$

Due to the λ dependence there is a clear difference between parallel and perpendicular propagation. In the case of parallel ($\lambda = 1$) and oblique propagation ($0 < \lambda < 1$) two modes will display a resonance, the ion and electron cyclotron resonances. For perpendicular propagation ($\lambda = 0$) both resonances are absent, which is related to the fact that the S and A modes do not propagate perpendicular to the magnetic field.

Local, high-frequency limit. Considering there are two resonances, the other four modes are expected to behave linearly for $k^2 \rightarrow \infty$. Taking the local, high-frequency limit ($\omega^2 \rightarrow \infty, k^2 \rightarrow \infty, \omega^2/k^2$ finite) confirms this expectation and gives

$$\frac{\omega^2}{k^2} \rightarrow \begin{cases} 1 & (\text{twice}), \\ v^2, \\ w^2. \end{cases} \quad (2.24)$$

Two modes show electromagnetic behaviour and the remaining two behave acoustically with the ion and electron sound speeds respectively. Further note that in the case of a pair plasma the result (5.3) from Keppens et al. (2019) is obtained by using equal sound speeds, $v = w$.

Global, low-frequency limit. Finally, examining the global, low-frequency (MHD) limit ($\omega^2, k^2 \rightarrow 0, \omega^2/k^2$ finite) produces

$$\frac{\omega^2}{k^2} \rightarrow \begin{cases} \frac{\lambda^2 EI}{1 + EI}, \\ v_{\text{sl,f}}^2 \equiv \frac{1}{2(1 + EI)} \left\{ EI + c_s^2 + \lambda^2 EI c_s^2 \pm \left[\lambda^4 E^2 I^2 c_s^4 + 2\lambda^2 EI c_s^2 (c_s^2 - EI - 2) + (EI + c_s^2)^2 \right]^{1/2} \right\} \end{cases} \quad (2.25)$$

The global, low-frequency limit can be reduced to MHD so the three modes described by this behaviour are related to the MHD slow, Alfvén, and fast waves. The first result describes the Alfvén wave with the relativistic expression for the normalised squared Alfvén speed, $c_a^2 \equiv v_a^2/c^2 = EI/(1 + EI)$.

The second expression corresponds to the fast (+) and slow (−) waves. Reorganising the expression and comparing to Eq. (22.130) in Goedbloed et al. (2019) shows that we recover the relativistic phase speed for the fast and slow MHD waves. Furthermore, it can also be compared to the cold ion-electron plasma case and the warm pair plasma case like before. Setting the sound speed c_s to zero reduces the fast speed v_f to the Alfvén speed in agreement with Eq. (16) in Keppens and Goedbloed (2019b). The slow speed v_{sl} vanishes for a cold setting. For a warm pair plasma this expression reduces to Eq. (4.7) in Keppens et al. (2019) by substituting $c_s^2 = v^2$ and $I = E$.

Moreover, the expression of $v_{sl,f}^2$ simplifies significantly in the cases of parallel and perpendicular propagation. For perpendicular propagation ($\lambda = 0$) the expression reduces to $v_{\perp,f}^2 = (EI + c_s^2)/(1 + EI)$ and $v_{\perp,sl}^2 = 0$. As expected, only the fast wave propagates with a behaviour of $\omega^2 = k^2 v_{\perp,f}^2$.

For parallel propagation it is a bit more nuanced. The square root in Eq. (2.25) simplifies to $|c_s^2(1 + EI) - EI|$. Therefore, at parallel propagation we get $v_{\parallel,f}^2 = \max\{c_a^2, c_s^2\}$ and $v_{\parallel,sl}^2 = \min\{c_a^2, c_s^2\}$ in accordance with MHD. The low-frequency limit expressions are ordered as $v_{sl} \leq \lambda c_a \leq v_f$ and this corresponds to the ordering of the slow (S), Alfvén (A), and fast (F) frequencies $\omega_S \leq \omega_A \leq \omega_F$.

2.1.4 The role of the propagation angle

Now that the relevant limits have been identified, it can be studied how they appear in the different branches of oblique, parallel, and perpendicular propagation. The interest lies in how the modes connect the long wavelength limits to the short wavelength limits. Of particular interest is whether modes cross or not. In this context, a *mode crossing* is a frequency-wave number pair (ω, k) that is a solution for multiple modes. Stringer (1963) argued that if two modes at parallel propagation can exist with identical frequency and wave number, it is natural to interpret this frequency-wave number pair as a crossing of these modes in the frequency-wave number diagram, hence the name.

A first step towards finding such mode crossings consists of checking when the dispersion relation factorises into lower order branches. That is because modes described by one branch do not cross.⁵ Interestingly, the dispersion relation does not factorise at all angles like it does in the case of a warm pair plasma (Keppens et al., 2019). However, the dispersion relation does factorise in the edge cases of parallel and perpendicular propagation with respect to the magnetic field ($\lambda = 1$ and $\lambda = 0$, respectively). In fact, this special status of parallel and perpendicular propagation was already noted by Stringer (1963) for low-frequency waves. Consequently, when moving from parallel to oblique angles, we look for evidence of crossings changing into avoided crossings, where two modes have minimal frequency differences for the same wave number.

⁵This is not a mathematical property, but an observation for this specific problem.

Oblique propagation

As already mentioned above, the dispersion relation does not factorise at all angles. In fact, it only factorises at exactly parallel or perpendicular propagation. For all oblique angles, there is only one branch to describe all six wave types. As a consequence, none of the modes cross and the frequency ordering

$$\omega_S \leq \omega_A \leq \omega_F \leq \omega_M \leq \omega_O \leq \omega_X,$$

is established at oblique angles. This frequency ordering generalises the MHD frequency ordering to the ion-electron model.

Parallel propagation

In the case of parallel propagation the parameter $\lambda = 1$ is fixed such that there are four remaining parameters (E , I , v , and w). The dispersion relation splits into a quadratic branch,

$$0 = \omega^4 - \omega^2[1 + k^2(v^2 + w^2)] + k^2(c_s^2 + k^2v^2w^2), \quad (2.26)$$

and a quartic branch,

$$\begin{aligned} & \omega^8 - \omega^6 [2 + E^2 + I^2 + 2k^2] \\ & + \omega^4 \left[(1 + EI)^2 + 2k^2 (1 + E^2 + I^2) + k^4 \right] \\ & - \omega^2 k^2 [2EI(1 + EI) + k^2(E^2 + I^2)] + k^4 E^2 I^2 = 0. \end{aligned} \quad (2.27)$$

First of all, note that the quadratic branch is the same expression as the one found in Eq. (2.16) of the unmagnetised case. However, labelling the waves described by this branch is a little less straightforward this time. As shown in Sec. 2.1.3, this quadratic branch has one mode that behaves like $\omega^2 = k^2v^2$ in the short wavelength limit. This is undisputedly the M mode (recall that we work under the assumption that $v > w$). The label of the second mode on the other hand depends on the relation between the sound speed c_s and the Alfvén speed c_a . The long wavelength limit of this mode goes like $\omega^2 = k^2c_s^2$ (see Sec. 2.1.3) which corresponds to the S mode if $c_s < c_a$ or to the F mode if $c_s > c_a$. Naturally, this implies that the quartic branch describes the A, O, and X modes as well as the remaining mode of the S or F variety.

Secondly, looking at the expressions of both branches, it is immediately clear that only the quadratic branch features the sound speeds v and w (and the linear combination c_s thereof) whereas only the quartic branch is influenced by the magnetic field (E , I). Thus, reducing these expressions to the cold case by imposing $v = w = c_s = 0$ does not alter the quartic branch, but does reduce

the quadratic branch to $\omega^2(\omega^2 - 1)$. In doing so, we effectively recover the cold plasma result of Keppens and Goedbloed (2019b) after decomposing the quartic branch into two fourth order factors in ω rather than ω^2 . This is their Eq. (19),

$$\begin{aligned} & [\omega^4 + \omega^3|E - I| - \omega^2(k^2 + EI + 1) - \omega k^2|E - I| + k^2EI] \\ & \times [\omega^4 - \omega^3|E - I| - \omega^2(k^2 + EI + 1) + \omega k^2|E - I| + k^2EI] = 0. \end{aligned} \quad (2.28)$$

Since applying the transformation $\omega \rightarrow -\omega$ to either factor results in the other one, this expression mixes forward and backward propagating wave pairs. It was already argued in Keppens and Goedbloed (2019b) that this factorisation does not offer any advantage over (2.27). Nevertheless, this factorisation is omnipresent in the literature. We will return to this factorisation in the next chapter (Sec. 3.4.1).

Perpendicular propagation

Similarly to parallel propagation, substituting $\lambda = 0$ to describe perpendicular propagation makes the dispersion relation factorise. The perpendicular dispersion relation then becomes

$$\begin{aligned} & \omega^4 (\omega^2 - k^2 - 1) \left\{ \omega^6 - \omega^4 [2 + E^2 + I^2 + k^2(1 + v^2 + w^2)] \right. \\ & + \omega^2 [(1 + EI)^2 + k^2(1 + E^2 + I^2 + E^2w^2 + I^2v^2 + v^2 + w^2 + c_s^2) \\ & \left. + k^4(v^2w^2 + v^2 + w^2)] \right. \\ & \left. - k^2 [(1 + EI)(EI + c_s^2) + k^2(E^2w^2 + I^2v^2 + v^2w^2 + c_s^2) + k^4v^2w^2] \right\} = 0. \end{aligned} \quad (2.29)$$

From MHD it is known that the S (slow) and A (Alfvén) modes do not propagate perpendicular to the magnetic field. Hence, we see that these two modes factor out as ω^4 . The non-zero modes are described by a linear branch and a cubic branch in ω^2 . Note that the cubic branch contains both magnetic characteristics (E, I) and acoustic characteristics (v, w) unlike the branches at parallel propagation.

The linear branch is clearly an electromagnetic wave with a cutoff of 1. Since the highest cutoff ($\omega_u > 1$) always corresponds to the X mode, this must be the O mode. This is also in accordance with the definition of the ordinary mode in the literature as the mode that does not depend on the magnetic field (Gurnett and Bhattacharjee, 2005). The remaining three modes, F, M, and X, are thus described by the cubic branch.

2.2 Dispersion diagrams

Once a choice is made for the parameters E , μ , v , and w , the six branches $\omega(k)$ can be computed numerically at any angle ($\lambda^2 \in [0, 1]$). From MHD it is known that at long wavelengths (small k) the slow, Alfvén, and fast frequencies are always ordered as $\omega_S \leq \omega_A \leq \omega_F$. Additionally, the frequencies of the M, O, and X modes lie above these with their cutoffs at 1 and $\omega_{u,l}$. It was shown that for pair plasmas and cold ion-electron plasmas a complete ordering of modes $\omega_S \leq \omega_A \leq \omega_F \leq \omega_M \leq \omega_O \leq \omega_X$ is satisfied at all angles except for parallel and perpendicular propagation (Keppens and Goedbloed, 2019a,b; Keppens et al., 2019). At these extreme angles, the ordering is violated due to the introduction of crossings inbetween the long and short wavelength limits. In this section the crossings are discussed and visualised for parallel and perpendicular propagation for the warm ion-electron case. Afterwards, it is shown that at intermediate angles no crossings occur such that in the warm ion-electron case the modes are ordered as well.

For all dispersion diagrams, the $\omega(k)$ curves were calculated by defining an array of k values and for each value using the `roots` function in Python's NumPy package to solve for ω^2 .

2.2.1 Parallel propagation

As discussed in Sec. 2.1.4, at parallel propagation the dispersion relation splits into two factors, a quadratic and a quartic branch. It was already mentioned that the quadratic branch is the same as in the unmagnetised case whilst the quartic branch appears in the cold case as well. This means that the four modes described by the quartic branch are not influenced by the thermal speeds. Hence, the cold and warm dispersion diagrams will look similar.

In the cold case, the remaining mode is a constant mode (Keppens and Goedbloed, 2019b), which is no longer constant in the warm case due to the non-zero electron sound speed. Consequently, its high-frequency behaviour is altered dramatically. This is the textbook Langmuir wave, given by Eq. (2.15) (Gurnett and Bhattacharjee, 2005), or M mode. Additionally, the S (slow) mode appears. To visualise these differences, Fig. 2.1 offers a side-by-side view of the cold (appearing in Keppens and Goedbloed, 2019b, Fig. 4) and warm parallel dispersion diagrams.

A brief glance at Fig. 2.1(b) suffices to notice several modes crossing. In fact, the case shown there is only one possible regime in which crossings appear ($E < 1$, $c_s < c_a$). Which modes cross is determined by the strength of the magnetic field, the sound speed, and the ratio of masses over charges. Eight regimes can be identified. They are characterised by the value of $E = eB/m_e\omega_p$ ($E < 1$, $1 < E < E_{cr}$, $E_{cr} < 1/\mu$, or $E > 1/\mu$) and whether $c_s < c_a$ or $c_s > c_a$. However, if E exceeds E_{cr} for a realistic value $\mu \lesssim 1/1836$, the relation $c_s > c_a$

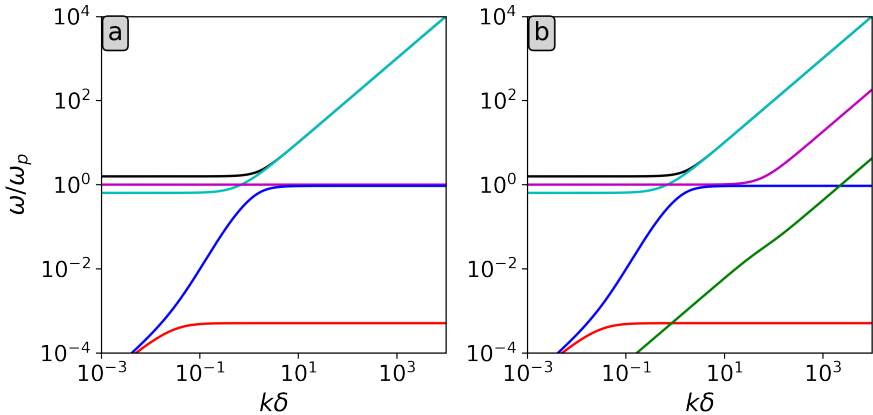


FIGURE 2.1: Parallel dispersion diagram using coronal loop parameters (Goedbloed et al., 2019) ($E \simeq 0.935$, $\mu \simeq 1/1836$) for (a) a cold ion-electron plasma, and (b) a warm ion-electron plasma ($v \simeq 0.018$, $w \simeq 0.0004$). Note that the A (red), F (blue), O (cyan), and X (black) modes are identical in the cold and warm case. The M (purple) mode's short wavelength (large k) behaviour is altered and the S (green) mode only appears in the warm case.

TABLE 2.1: Overview of crossings at parallel propagation in different regimes as determined using both analytic and numerical methods. Each crossing is indicated by the two letters corresponding to the crossing modes.

	$c_s < c_a$	$c_s > c_a$
$E < 1$	MO, SA, SF	MO, AF (2×)
$1 < E < E_{\text{cr}}$	MO, SA, SF, FM (2×)	MO, AF (2×), AM (2×)
$E_{\text{cr}} < E < 1/\mu$	SA, SF, FM (2×)	unphysical
$E > 1/\mu$	SA, SF, FM (2×), AM (2×)	unphysical

is no longer physically feasible because the relativistic sound speed is bounded by $c_s^2 < \gamma - 1$ ($\gamma = 5/3$, or $\gamma = 4/3$ in a relativistic regime) (Goedbloed et al., 2019). Hence, we limit ourselves to the remaining six cases here. A summary of all crossings in all regimes is given in Table 2.1.

To discuss analytic expressions of these crossings, a closer look at the quadratic branch is required. Due to its quadratic nature, the expressions for ω^2 as a function of k^2 can be written explicitly, namely

$$\omega^2 = \frac{1}{2} + \frac{1}{2}k^2(v^2 + w^2) \pm \frac{1}{2}\sqrt{k^4(v^2 - w^2)^2 + 2k^2(v^2 + w^2 - 2c_s^2) + 1}. \quad (2.30)$$

In Eq. (2.30), the solution with the positive sign is the M mode as can be seen by taking the short wavelength limit, $\omega^2 = k^2 v^2$. This leaves the negative sign to describe the S or F mode because the long wavelength limit is $\omega^2 = k^2 c_s^2$ (see Sec. 2.1.3). From Eq. (2.30) it is also immediately clear that these two modes can never cross and could only coincide if the square root became zero. Observing that the expression underneath the square root is a quadratic polynomial in k^2 , we can compute the discriminant $\Delta = (c_s^2 - v^2)(c_s^2 - w^2)$. Since $\min\{v^2, w^2\} \leq c_s^2 \leq \max\{v^2, w^2\}$, this is always negative and thus there are no real crossings of the modes in the quadratic branch. The quartic branch was discussed in Keppens and Goedbloed (2019b) and no crossings appear within this branch either.

The remaining question is when and where the quadratic branch crosses the quartic branch. In Table 2.1 we already summarised when the modes cross. Unfortunately, a first attempt to solve the quadratic and quartic branch as a system in the variables ω^2 and k^2 did not yield simple, closed-form, analytic results. However, with the use of a Taylor expansion in Eq. (2.30) it is possible to retrieve approximate analytic solutions for the locations of the crossings. In Fig. 2.2 three regimes are shown as a reference for the analytic approximations that follow. All analytic approximations are marked in this figure with a black dot.

First off, consider the crossing of the M and O modes. These modes cross at parallel propagation if $E < E_{cr}$ and can be seen in Figs. 2.2(a,b) in purple (M) and cyan (O). Analytically, this is clear from observing that the short wavelength limit of the M mode $\omega^2 = k^2 v^2$ is smaller than the corresponding limit of the O mode $\omega^2 = k^2$ whilst the cutoff of the M mode $\omega^2 = 1$ is larger than the cutoff of the O mode $\omega^2 = \omega_1^2$ if $E < E_{cr}$. Assuming the crossing occurs at relatively small k as suggested by Fig. 2.2, $\omega_M^2 = 1$ to zeroth order. Unfortunately, retaining any term of first or higher order in k^2 makes the substitution in the quartic branch a lot more involved. The equation would become fourth order in k^2 which is analytically solvable, but becomes extremely lengthy. To keep it simple, substituting $\omega^2 = 1$ in the quartic branch and solving for k^2 gives for the parallel crossing of the M and O mode

$$k_{MO,\parallel}^2 \simeq \frac{EI - (E - I)}{EI - 1 - (E - I)}. \quad (2.31)$$

Since $\omega^2 = 1$ is an exact solution in the cold ion-electron case, this expression also appears there as an exact crossing (Keppens and Goedbloed, 2019b). Comparing this approximation of the crossing $(\omega, k) = (1, k_{MO,\parallel})$ to numerical results shows that this approximation is usually quite good.

For the lower solution $(-)$ of Eq. (2.30), using a first order Taylor approximation of the square root and discarding the second order term in k^2 , the mode's behaviour becomes $\omega^2 = k^2 c_s^2$. Substituting this simple expression into the

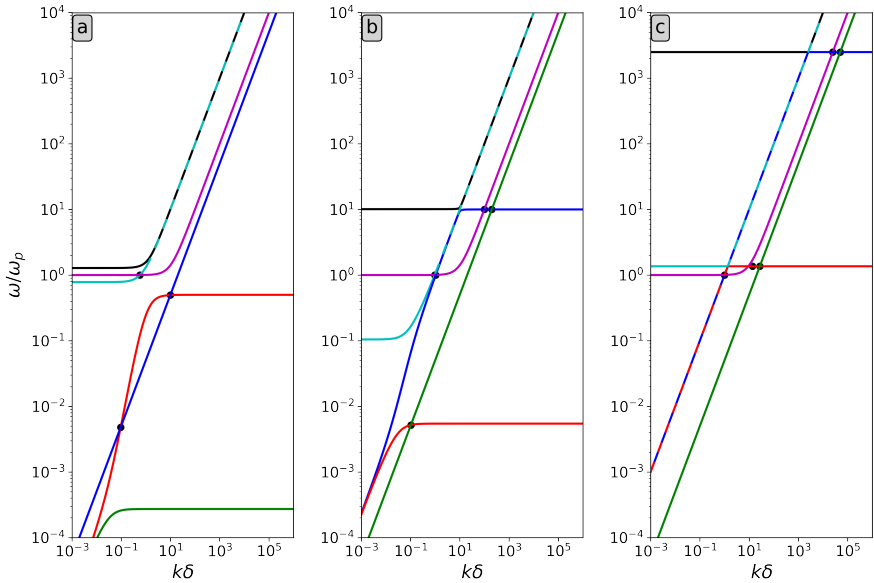


FIGURE 2.2: Dispersion diagram of a proton-electron plasma at parallel propagation with increasing magnetic field strength from left to right: (a) $E = 0.5$, (b) $E = 10$, and (c) $E = 2500$. All three cases satisfy $\mu \simeq 1/1836$, $v = 0.1$ and $w = 0.05$. For increasing magnetic field strength new crossings appear of the M mode with the F and A modes. Above E_{cr} , in (c), the M and O modes no longer cross. analytic approximations of the crossings are marked by a black dot. Dashed lines are used when modes are too close to discern otherwise.

quartic branch and solving for k^2 yields

$$k^2 \simeq [2c_s^2(1 - c_s^2)]^{-1} \left\{ (E^2 + I^2)(1 - c_s^2) - 2c_s^2 \right. \\ \left. \pm |E - I| \sqrt{(1 - c_s^2) [(E + I)^2(1 - c_s^2) - 4c_s^2]} \right\}. \quad (2.32)$$

This expression can give either 0, 1, or 2 real, positive solutions. The solutions agree fairly well with numerical solutions. To discuss which crossings this expression describes, we have to differentiate between the two regimes $c_s < c_a$ and $c_s > c_a$.

The first regime, $c_s < c_a$, is shown in Figs. 2.2(b,c). Here, the lower mode of the quadratic branch is the S mode which crosses both the A and F mode once. In this case the smaller solution of Eq. (2.32) gives the SA crossing whereas the larger solution gives the SF crossing. In the other regime, $c_s > c_a$, the lower quadratic branch solution is the F mode, which starts above both the S and A

mode. This case is shown in Fig. 2.2(a). Since $\omega_S < \omega_A < \omega_F$ holds in both the long and short wavelength limits and there are at most two crossings, it follows that the F mode never crosses the S mode, but it can cross the A mode twice with each solution of Eq. (2.32) describing an AF crossing.

It should be pointed out that the upper solution in Eq. (2.32) can become rather large. In this case using a small k approximation is questionable at best. However, note that the short wavelength limit of this mode is $\omega^2 = k^2 w^2$ and is linear like the long wavelength limit, but with a different coefficient. This means that if the crossing appears at high k we can simply replace c_s with w in Eq. (2.32).

Finally, two more crossings appear for values of E larger than $E > 1$ and another two for E larger than $E > 1/\mu$ (with $c_s < c_a$). When E becomes larger than 1, the largest resonance $\omega^2 = E^2$ exceeds the M mode cutoff $\omega^2 = 1$. Then the M mode will cross the mode approaching this resonance twice. If $c_s < c_a$, this means the M and F modes cross. If $c_s > c_a$ on the other hand, the M and A modes cross instead. As an aside, note that in the latter case this means that the A mode crosses four times with other modes, in the order F, M, M and F for k ranging from 0 to $+\infty$. Additionally, the F and M modes never cross if $c_s > c_a$.

The way we can approximate these crossings is by replacing the frequency in the quartic branch with the long and short wavelength limits of the M mode, i.e. $\omega_M^2 \simeq 1$ for the first crossing and $\omega_M^2 \simeq k^2 v^2$ for the second crossing. For the first crossing this gives

$$k^2 \simeq \frac{EI + (E - I)}{EI - 1 + (E - I)}. \quad (2.33)$$

Once again, this is an exact solution in the cold ion-electron case (Keppens and Goedbloed, 2019b). In our test cases this yields an acceptable approximation. The approximation for the second crossing is given by replacing c_s with v in Eq. (2.32). However, for values of E relatively close to (but larger than) $E = 1$ ($1 < E \lesssim 10$ in our test cases where $\mu = 1/1836$), the second crossing falls into the transitional regime between the long and short wavelength limits of the M mode which results in a rather suboptimal approximation. For large values of E ($E \gtrsim 10$) the approximation is exceptionally good though.

If $E > 1/\mu$, the lower resonance $\omega^2 = I^2 = \mu^2 E^2$ also becomes greater than the M mode cutoff $\omega_M^2 = 1$. Since $c_s < c_a$, the A mode crosses the M mode twice. As can be seen in Fig. 2.2(c), for strong magnetic fields the F and A mode almost coincide such that the same approximation (2.33) can be used for both the AM and FM crossing. For the second crossing, the short wavelength limit $\omega_M^2 = k^2 v^2$ can be used to find the lower solution Eq. (2.32) with c_s replaced by v . Once again, this is not a great approximation because the M mode might not be entirely in the short wavelength regime.

All approximations offered in this section were tested against numerical results of the crossings using test cases for each regime. These test cases are differentiated by their parameters and can be found in App. B.3. For each case the numerical crossings and their analytic approximations are listed.

2.2.2 Perpendicular propagation

As shown before, the perpendicular case splits into two branches. The linear branch $\omega^2 = 1 + k^2$ is the O mode and the remaining cubic branch describes the F, M, and X modes.

For the perpendicular case the issue of crossings is less involved than in the parallel case mainly because there are less propagating modes. There are no crossings or avoided crossings within the cubic branch, so the only remaining question is if the linear branch crosses any of the modes in the cubic branch. Substituting $\omega^2 = 1 + k^2$ into the cubic branch and solving for k^2 , the solution can be written as

$$k_{\text{MO},\perp}^2 = \frac{\mu^2(1+\mu)(E^2 - E_{\text{cr}}^2)}{(1-w^2) + \mu(1-v^2)}. \quad (2.34)$$

The subscript MO indicates that this is the wave number of the crossing of the M and O modes. Now it should be noted that the denominator is always positive whilst the numerator goes from a negative to a positive value for increasing E at $E = E_{\text{cr}}$. Therefore, a real crossing between the M and O modes appears if $E > E_{\text{cr}}$ at the indicated wave number value. The corresponding frequency is simply $\omega_{\text{MO},\perp}^2 = 1 + k_{\text{MO},\perp}^2$. For $E = E_{\text{cr}}$ the “crossing” is the cutoff point ($\omega^2 = 1, k^2 = 0$). The perpendicular dispersion diagram is shown in Fig. 2.3.

As a final check we can compare to the cold pair plasma case. In Keppens and Goedbloed (2019a) they reported an MO crossing at perpendicular propagation at $(\omega, k) = (\sqrt{1+E^2}, E)$. As noted before, for a cold pair plasma the ratio of masses over charges is $\mu = 1$ and the critical electron cyclotron frequency is $E_{\text{cr}} = 0$ as well as the sound speeds $v = 0$ and $w = 0$. These simplifications reduce Eq. (2.34) to $k = E$ such that we recover the cold pair plasma result.

2.2.3 Wave ordering at oblique angles

For cold and warm pair plasmas (Keppens and Goedbloed, 2019a; Keppens et al., 2019) as well as cold ion-electron plasmas (Keppens and Goedbloed, 2019b) crossings are replaced by avoided crossings as soon as there is any deviation from parallel or perpendicular propagation. Consequently, this means that the connectivity between long and short wavelength limits is angle dependent. As it turns out, similar changes occur in a warm ion-electron plasma. At oblique angles, modes almost surely do not cross, and the ordering

$$\omega_S \leq \omega_A \leq \omega_F \leq \omega_M \leq \omega_O \leq \omega_X$$

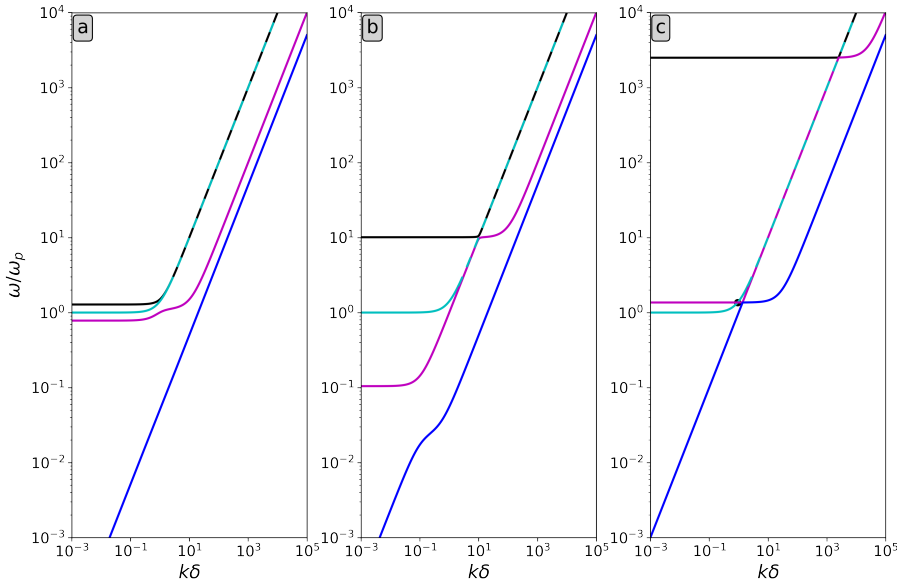


FIGURE 2.3: Dispersion diagram of a proton-electron plasma at perpendicular propagation with increasing magnetic field strength from left to right: (a) $E = 0.5$, (b) $E = 10$, and (c) $E = 2500$. All three cases satisfy $\mu \simeq 1/1836$, $v = 0.1$ and $w = 0.05$. Above E_{cr} , in (c), a new crossing appears between the M and O modes. The analytic expression of the crossing is marked by a black dot. Dashed lines are used when modes are too close to discern.

is obeyed at all wavelengths. The fact that this ordering of the eigenfrequencies persists through all oblique orientations makes this a more robust basis for categorising all waves in ion-electron plasmas. It also forms a natural extension of the five waves found in the cold limit and remains true for all realistic values of μ (up to the pair plasma limit where $\mu = 1$). We therefore argue that it should replace previous labelling schemes, which actually mixed wave labels due to insisting to connect parallel to perpendicular wave properties, and/or confused forward and backward wave pairs resulting from artificial factorisations such as Eq. (2.28).

As soon as we move away from exactly parallel propagation, *all* crossings that were present at parallel propagation seem to turn into avoided crossings. The avoided crossings are shown in Fig. 2.4 for a small angle. This change from crossing to avoided crossing with the smallest deviation from parallel propagation gives the parallel case a special status. This is actually worrisome for classical textbook treatments where purely parallel (or purely perpendicular)

orientations serve to identify and categorise mode properties. The location of these avoided crossings for small angles can be pinpointed by computing the crossings at parallel propagation numerically or they can be approximated using the crossing expressions in Sec. 2.2.1.

However, for the AF crossing the location of the avoided crossing away from parallel propagation does not match the numerical crossing at parallel propagation. In fact, from numerical results it seems that the location of this crossing is extremely angle sensitive. When varying the angle θ (and thus λ), the point of closest approach between the two modes, i.e. the avoided crossing, varies rapidly as well. Even for small angles close to parallel propagation the distance between the crossing at parallel propagation and the avoided crossing is significantly larger than the closest distance between the two modes in the avoided crossing.⁶ As can be seen in Fig. 2.4(c), for an angle $\theta = 0.01$ the numerical crossing at parallel propagation is already well outside of the avoided crossing's frame. Note the scale on the axes though, since the A and F modes approach each other closely.

For the perpendicular MO crossing in the $E > E_{\text{cr}}$ regime, the situation is a little different. As soon as the angle deviates from $\pi/2$, the S and A mode are reintroduced. Due to their appearance the MO crossing does not simply become an avoided crossing, but several modes approach each other closely without crossing. The result looks a lot like the parallel case in Fig. 2.2(c) with all crossings replaced by avoided crossings. All six modes are present and the avoided crossings related to crossings at parallel propagation persist through all angles up to near-perpendicular propagation. Recolouring the branches appropriately reveals that the avoided crossings are SA, FM twice and AF three times. Since these avoided crossings actually originated from crossings at parallel propagation, comparing them to Table 2.1 reveals that the (parallel) SF crossing and both AM crossings became AF avoided crossings. This is simply due to the fact that modes no longer cross. Thus, the labelling of avoided crossings at higher wave numbers can be affected by avoided crossings at smaller wave numbers. As an example, consider the parallel SF crossing, visible in Fig. 2.2(b) and its corresponding nearly-parallel case in Figs. 2.4(a,c). The S mode approaches the F mode because it already crossed the A mode at a smaller wave number. However, when that SA crossing becomes an avoided crossing, it is now the A mode (instead of the S mode) that approaches the F mode, so the SF crossing becomes an AF avoided crossing. Consequently, due to the S, A, F, M, O, X frequency ordering at oblique angles, avoided crossing labels are always made up of two consecutive modes in this order, e.g. SA, AF, and FM avoided crossings, whilst this is not necessarily the case for the true crossings at parallel propagation, e.g. SF and AM crossings, where the S and A mode

⁶To test this we could only go up to $\theta = 0.001$ because smaller values were no longer numerically well-resolved.

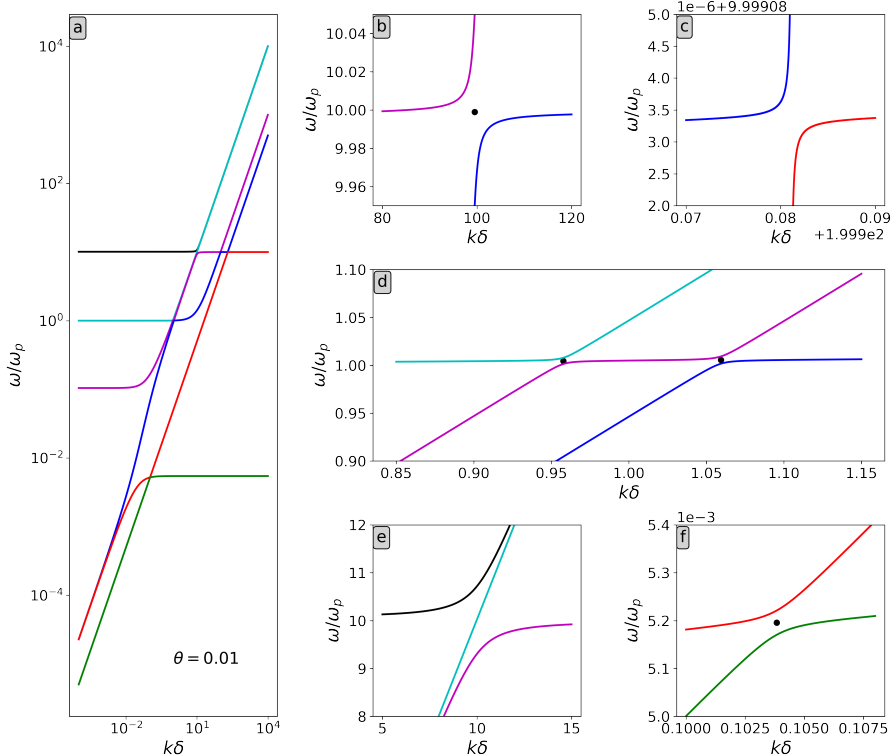


FIGURE 2.4: (a) A proton-electron dispersion diagram for nearly-parallel propagation ($\theta = 0.01$) using the parameters of Fig. 2.2(b). The close-ups show the (b) FM region, (c) AF region, (d) FMO region, (e) MOX region, and (f) SA region. All crossings are replaced by avoided crossings. The numerical crossings at parallel propagation are indicated by black dots. For the AF crossing, close-up in (c), the numerical result at parallel propagation lies outside of the frame, $(\omega, k) = (9.99974909, 199.83187597)$. The MOX region, close-up in (e), has no crossing at parallel propagation.

already crossed the A and F modes respectively at smaller wave numbers.

2.2.4 Critical magnetisation

Clearly, the critical electron cyclotron frequency E_{cr} plays an important role in the behaviour of the different wave types. When E crosses the threshold imposed by the critical value, crossings between the M and O modes appear or disappear at parallel and perpendicular propagation. Consequently, at parallel and perpendicular propagation the ordering of the M and O modes switches at

$k^2 = 0$ across the critical value. On the other hand, for oblique propagation the ordering is fixed and their cutoff expression are interchanged. This distinction based on the strength of the magnetic field was absent in the case of a warm pair plasma (Keppens et al., 2019) because there the critical value is $E_{\text{cr}} = 0$. Since the critical value only depends on μ , the function can be shown in a 2D plot as is done in Fig. 2.5(a).

Whilst it is clear that it is zero for a pair plasma, it rapidly increases for smaller values of μ . Therefore, a pair plasma is always in the upper regime, but there are two possible regimes for any ion-electron plasma ($\mu \ll 1$). However, as Fig. 2.5(b) shows, the upper regime is rather extraordinary for an ion-electron plasma due to the necessity of immensely strong magnetic fields. In this figure the critical magnetic field strength B_{cr} corresponding to E_{cr} is plotted for a proton-electron plasma ($\mu \simeq 1/1836$) and a carbon-electron plasma as a function of the number density. A couple of physical cases have been added to the figure, both for the lower and the upper regime. Noting the logarithmic scale of the figure, it is clear that for many regular cases the magnetic field is several orders of magnitude below the critical value (Goedbloed et al., 2019). The strongest artificially generated magnetic fields are employed in high-energy density (HED) experiments and a typical HED carbon-electron plasma experiment based on the parameters from Fiksel et al. (2014); Fox et al. (2017); Hare et al. (2017) is also shown for reference, although it is still well below the critical value. However, for more extreme cases such as pulsars and magnetars, the magnetic field exceeds the critical value for their proton-electron wind. Estimates of the magnetic field B_w in Pétri (2019) were used alongside Goldreich-Julian density estimates (Goldreich and Julian, 1969) for the pulsar (J1734-3333) and magnetar (Swift J1834) cases in Fig. 2.5(b). A summary of all parameters is given in App. A. Considering that the strongest artificial magnetic field had a strength of 1200 T (Nakamura et al., 2018), applying such a field to a low-density plasma may create a suitable environment to study this upper regime experimentally.

2.3 Wave velocities

Naturally, each wave has two speeds associated with it, namely the phase and group speed. Since the dispersion relation is a sixth order polynomial in ω^2 , it is not possible in general to write down an analytic expression for these speeds for a given mode as a function of the wave number k . In the case of parallel or perpendicular propagation, the sixth order dispersion relation reduces to factors of at most fourth order, which are analytically solvable for functions $\omega(k)$. However, the resulting phase and group speed expressions are too involved to show. Moreover, if the pair (ω, k) is determined numerically, these values can be used to compute the phase and group speed at any angle. Hence, with the use of numerical methods it is more convenient to show the results in phase

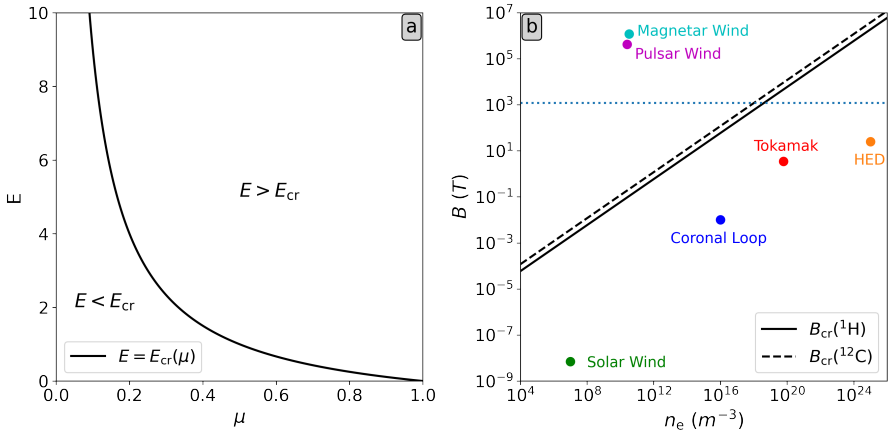


FIGURE 2.5: (a) The critical value E_{cr} as a function of the ratio of masses over charges μ . For a pair plasma ($\mu = 1$) the critical value goes to zero whilst for an ion-electron plasma ($\mu \ll 1$) it becomes very large. (b) The magnetic field strength for which the critical value E_{cr} would be attained for a proton-electron plasma (solid line) and a carbon-electron plasma (dashed line) as functions of the (electron) density. A selection of physical environments are represented by a dot (see App. A). The dashed blue line indicates the record artificial magnetic field strength, $B = 1200$ T (Nakamura et al., 2018).

and group speed diagrams which will collect the information of plane wave propagation speeds (phase diagram) or energy flow (group diagram) for all angles at once at a given wave number k (hence given wavelength). As the dispersion relations showed earlier that all 6 waves are dispersive, i.e. all $\omega(k)$ branches deviate from a mere proportionality $\omega(k) \propto k$, and this essentially at all angles, the phase and group speeds that collect anisotropic wave propagation characteristics will differ for varying wavelengths. Thereby, the long and short wavelength limits can be computed analytically.

2.3.1 Phase speed

The (dimensionless) phase speed defined as $v_{\text{ph}} = \omega/k$ can only be written as an explicit function of k for each mode in the case of parallel or perpendicular propagation by solving the quadratic and quartic branch for functions $\omega(k)$. However, these expressions do not offer any insight and have been omitted here. In the long and short wavelength limit though, the expressions reduce significantly and can be found for all orientations between the wave vector and the magnetic field. Hence, these limit cases have been summarised in Table

TABLE 2.2: Phase speeds of all modes in the short and long wavelength limit (large and small k respectively) assuming $E < E_{\text{cr}}$. All labels refer to oblique angles ($0 < \lambda < 1$).

Long wavelengths ($k \rightarrow 0$)	Short wavelengths ($k \rightarrow \infty$)
$\left(\frac{\omega}{k}\right)_X \hat{e}_k = \frac{\omega_u}{k} \hat{e}_k$	$\left(\frac{\omega}{k}\right)_X \hat{e}_k = \hat{e}_k$
$\left(\frac{\omega}{k}\right)_O \hat{e}_k = \frac{1}{k} \hat{e}_k$	$\left(\frac{\omega}{k}\right)_O \hat{e}_k = \hat{e}_k$
$\left(\frac{\omega}{k}\right)_M \hat{e}_k = \frac{\omega_l}{k} \hat{e}_k$	$\left(\frac{\omega}{k}\right)_M \hat{e}_k = v \hat{e}_k$
$\left(\frac{\omega}{k}\right)_F \hat{e}_k = v_f \hat{e}_k$	$\left(\frac{\omega}{k}\right)_F \hat{e}_k = w \hat{e}_k$
$\left(\frac{\omega}{k}\right)_A \hat{e}_k = \lambda c_a \hat{e}_k$	$\left(\frac{\omega}{k}\right)_A \hat{e}_k = \frac{\lambda E}{k} \hat{e}_k$
$\left(\frac{\omega}{k}\right)_S \hat{e}_k = v_{sl} \hat{e}_k$	$\left(\frac{\omega}{k}\right)_S \hat{e}_k = \frac{\lambda I}{k} \hat{e}_k$

2.2. Here, the unit vector \hat{e}_k is defined as $\hat{e}_k = \mathbf{k}/k$. These expressions are in accord with the cutoff, resonance, MHD, and short wavelength limits discussed in Sec. 2.1.3.

For all intermediate wave numbers it is also possible to create complete phase speed diagrams. These diagrams show the phase speed in a polar plot, where the angle corresponds to the angle between the magnetic field and the wave vector. Fig. 2.6 is an example of such a diagram. In these diagrams the background magnetic field points to the right. The evolution of these diagrams whilst varying k offers an interesting look at the structure of the various modes.

2.3.2 Group speed

Much like the warm pair plasma case discussed in Keppens et al. (2019) it is possible to write down a general expression for the group speeds of all the waves as a function of the pair (ω, k) . Since the dispersion relation does not factorise in general, the group speed expression must be achieved with the use of differentiation with respect to \mathbf{k} on the sixth degree polynomial dispersion relation. Doing so, the group speed can be written as

$$\frac{\partial \omega}{\partial \mathbf{k}} = -(v_{\text{ph}} P_\omega)^{-1} \left[P_k \hat{e}_k + \frac{\lambda P_\lambda}{k^2} (\hat{e}_B - \lambda \hat{e}_k) \right]. \quad (2.35)$$

In this formula \hat{e}_k and \hat{e}_B are unit vectors defined as $\hat{e}_k = \mathbf{k}/k$ and $\hat{e}_B = \mathbf{B}/B$, v_{ph} indicates the phase speed as before, and P_ω , P_k , and P_λ are polynomials

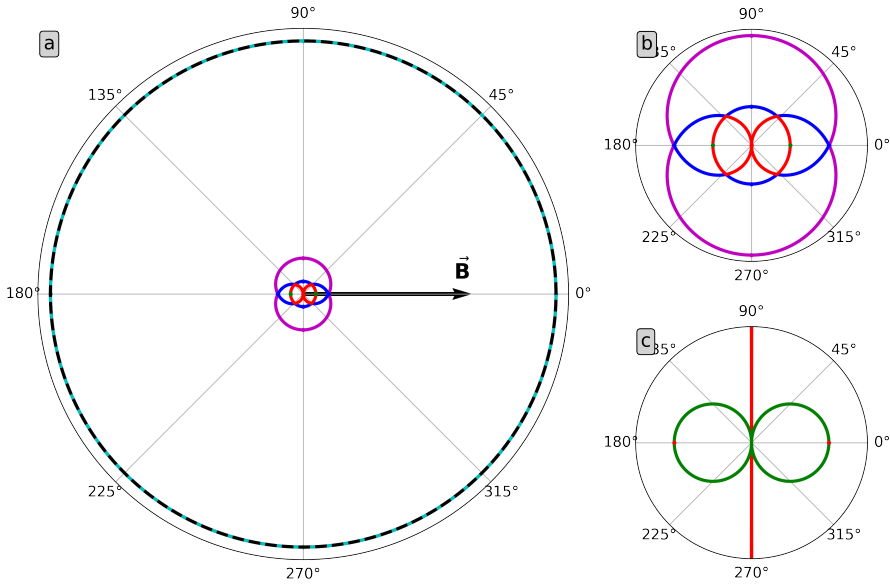


FIGURE 2.6: (a) Phase speed diagram for $k = 100$ of a proton-electron plasma with $E = 10$, $\mu = 1/1836$, $v = 0.1$, and $w = 0.05$. The dashed black line indicates the light circle. (b-c) Successively zoomed views of the central region of (a).

defined as

$$P_\omega = \sum_{\substack{1 \leq m \\ 0 \leq n \\ 3 \leq m+n \leq 6}} m \alpha_{mn} \omega^{2(m-1)} k^{2n}, \quad (2.36)$$

$$P_k = \sum_{\substack{0 \leq m \\ 1 \leq n \\ 3 \leq m+n \leq 6}} n \alpha_{mn} \omega^{2m} k^{2(n-1)}, \quad (2.37)$$

$$\text{and } P_\lambda = \sum_{\substack{0 \leq m,n \\ 3 \leq m+n \leq 6}} \frac{\partial \alpha_{mn}}{\partial \lambda^2} \omega^{2m} k^{2n}. \quad (2.38)$$

A detailed explanation of these polynomials has been moved to App. B.2. The relation $\partial \lambda^2 / \partial \mathbf{k} = 2\lambda(\hat{\mathbf{e}}_B - \lambda \hat{\mathbf{e}}_k)/k$ was invoked to reach expression (2.35). (Note that $\partial \lambda^2 / \partial \mathbf{k} = 0$ at perpendicular ($\lambda = 0$) and parallel ($\lambda = 1$) propagation using $\hat{\mathbf{e}}_B = \lambda \hat{\mathbf{e}}_k$ for parallel propagation.) Of course, to obtain the group speed of any specific wave the pair (ω, k) solving the dispersion

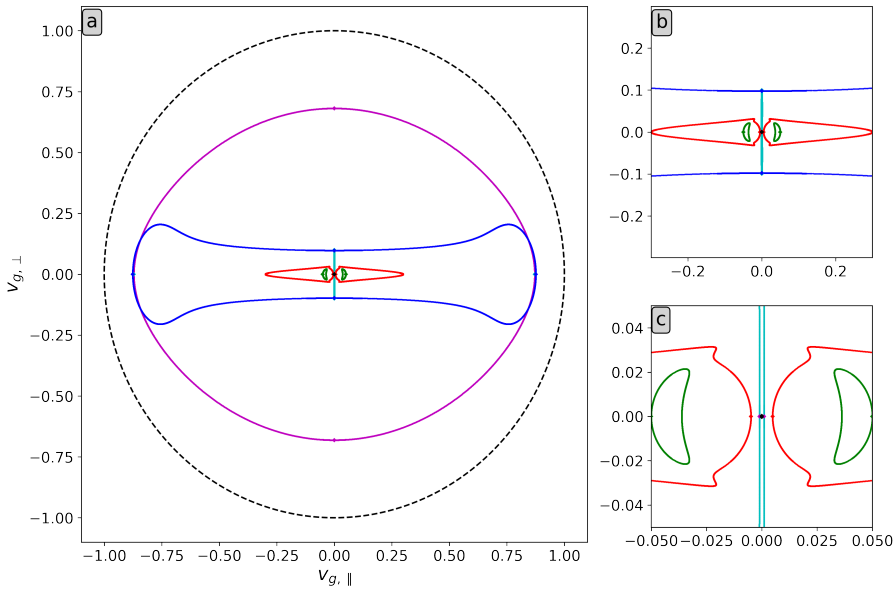


FIGURE 2.7: (a) Group speed diagram for $k = 0.1$ of a proton-electron plasma with $E = 10$, $\mu = 1/1836$, $v = 0.1$, and $w = 0.05$. The dashed black line indicates the light circle. (b-c) Successively zoomed views of the central region of (a).

relation should be substituted into Eq. (2.35). Analytically, this is only possible for parallel or perpendicular propagation, but group speeds can be computed numerically at any angle. In doing so, it is possible to draw group speed diagrams with $\hat{\mathbf{e}}_B$ pointing along the horizontal axis in the positive direction as is done in Fig. 2.7.

The occurrence of an (avoided) crossing is especially pronounced in animations of the group speed diagram when varying the wave number. Across an avoided crossing, the group speed curves of the modes in question are observed to reconnect. For coronal loop parameters, snapshots of the situation for k smaller and larger than the MO avoided crossing value $k \simeq 0.695$ are shown in Fig. 2.8. For long and short wavelengths explicit limit expressions can be obtained from eqs. (2.35) to (2.38) and the phase speed limits in Table 2.2. The results are summarised in Tables 2.3 and 2.4 (at the end of this chapter). The latter was moved to an appendix due to the size of the expressions. A similar summary was presented for a warm pair plasma in Keppens et al. (2019). Substituting $\mu = 1$ and $w = v$ into our expressions we expect to recover the warm pair results. This is indeed the case except for the M and X mode. For these modes, the long wavelength group speed expressions in Table 2.4 become identical because

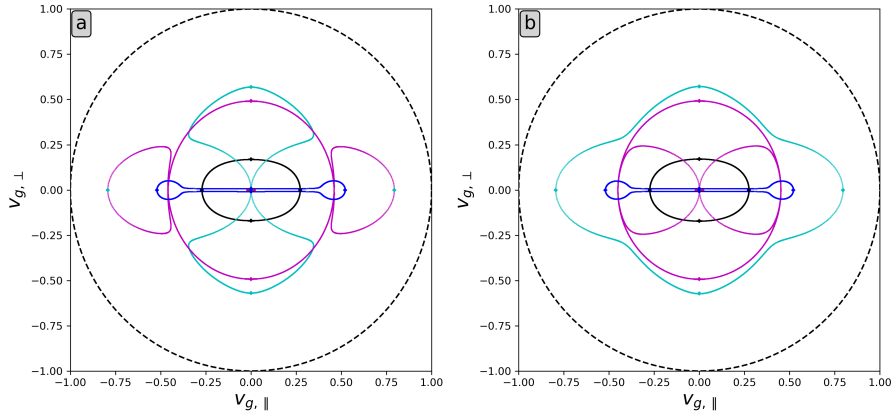


FIGURE 2.8: For coronal loop parameters, the group speed diagram is given for (a) $k = 0.692$ and (b) $k = 0.698$, showing the situation for k smaller and larger than the MO avoided crossing value $k \simeq 0.695$.

both ω_u^2 and ω_l^2 reduce to $1 + E^2$. Their long wavelength group speeds were not the same in the warm pair case, however (Keppens et al., 2019). Performing the warm pair substitutions this gives

$$\frac{\partial \omega}{\partial \mathbf{k}} = \frac{k}{(1 + E^2)^{3/2}} \left[\frac{(1 - v^2 - v^2 E^2) + (-v^2 E^2)}{2} \lambda \hat{\mathbf{e}}_B + \frac{(v^2 + v^2 E^2) + (1 + v^2 E^2)}{2} \hat{\mathbf{e}}_k \right] \quad (2.39)$$

which is the arithmetic average of the expressions in Keppens et al. (2019). That this ‘discrepancy’ exists between the warm pair plasma discussion in Keppens et al. (2019) and our current, general discussion for warm ion-electron plasmas may have to do with a lifted degeneracy as $w = v$ must be adopted. We note that the warm pair plasma dispersion relation turned out to always factorise in two branches (XFS versus OMA), whilst this exact factorisation is no longer possible in our current general treatment.

2.4 Discussion

Earlier discussions of plasma waves using an ion-electron treatment (Keppens and Goedbloed, 2019a,b; Keppens et al., 2019) were extended to the warm ion-electron plasma case. The previously introduced SAFMOX labelling scheme

TABLE 2.3: Group speeds of all modes in the short wavelength limit (large k) assuming $E < E_{\text{cr}}$. All labels refer to oblique angles ($0 < \lambda < 1$).

Short wavelengths ($k \rightarrow \infty$)	
$\left(\frac{\partial\omega}{\partial\mathbf{k}}\right)_X = \hat{\mathbf{e}}_k$	$\left(\frac{\partial\omega}{\partial\mathbf{k}}\right)_F = w \hat{\mathbf{e}}_k$
$\left(\frac{\partial\omega}{\partial\mathbf{k}}\right)_O = \hat{\mathbf{e}}_k$	$\left(\frac{\partial\omega}{\partial\mathbf{k}}\right)_A = \frac{E}{k}(\hat{\mathbf{e}}_B - \lambda \hat{\mathbf{e}}_k)$
$\left(\frac{\partial\omega}{\partial\mathbf{k}}\right)_M = v \hat{\mathbf{e}}_k$	$\left(\frac{\partial\omega}{\partial\mathbf{k}}\right)_S = \frac{I}{k}(\hat{\mathbf{e}}_B - \lambda \hat{\mathbf{e}}_k)$

was shown to be unambiguous for warm ion-electron plasmas and preserves the wave mode frequency ordering at all oblique angles. Additionally, parallel and perpendicular propagation were confirmed as exceptional cases where the modes can cross. Hence, we argue against any wave type classification relying on parallel and perpendicular propagation like those present in many textbooks in favor of the SAFMOX classification. As an example, reconsider Fig. 2.4(a). In a classification based on parallel propagation, the part of the blue curve around $k = 10$ could be referred to as the Langmuir wave because $n \simeq 1/v$ here despite not connecting to the same behaviour at even shorter wavelengths. In the SAFMOX labelling scheme, it is unambiguously the F mode, since for a fixed value of k it is the third frequency in ascending order.

The mode crossings appearing at parallel and perpendicular propagation could all be identified, with up to 6 different possibilities in the number of crossings, depending on the plasma parameters. Approximate analytical expressions were given for all of them. Numerically, all crossings can be computed and frequency-wave number diagrams can be drawn for all angles. Complementary, the evolution of phase and group speed diagrams when varying the wave number further reveals the intricate structure and the unavoidable fact that all 6 wave modes, from MHD to Langmuir and electromagnetic wave modes, can be highly anisotropic in their phase and group speed behaviour.

The generality of our classification scheme is a major advantage over any earlier treatments that assume non-relativistic conditions, or adopt one or more species in the cold regime. All our results can be translated to diagrams focusing rather on the behaviour of the refractive index with wave and plasma parameters, or to equivalent descriptions that analyse all possible solutions at fixed frequency, such as done for obtaining the Clemmow–Mullaly–Allis (CMA) diagrams (Gurnett and Bhattacharjee, 2005) of the cold plasma regime. Those latter diagrams actually render the wave interpretations even more ambiguous,

since they confuse slow/fast and other wave modes, as explained in Keppens and Goedbloed (2019b). We argue that the unambiguous SAFMOX scheme is in that sense superior. The high frequency O and X waves that give well-known Faraday rotation effects (Keppens and Goedbloed, 2019b) are now known for all orientations and plasma parameters.

Whilst the ion-electron treatment here is complete, in the sense that it describes both mechanical and electromagnetic wave phenomena, it lacks the typical velocity phase space resonant aspects of kinetic theory, like Landau damping (Gurnett and Bhattacharjee, 2005). A more detailed comparison to kinetic theory is left for the next chapter. However, it is possible to include resistive damping through the addition of effective collision frequencies, either between particle species or within each species. This is left for a follow-up study.

TABLE 2.4: Group speeds of all modes in the long wavelength limit (small k) assuming $E < E_{\text{cr}}$. All labels refer to oblique angles ($0 < \lambda < 1$).

Long wavelengths ($k \rightarrow 0$)	
$\left(\frac{\partial \omega}{\partial k}\right)_x$	$\begin{aligned} &= \omega_u^{-1} \left\{ 6\omega_u^6 - 5\omega_u^4(E^2 + I^2 + 3) + 4\omega_u^2 [E^2 I^2 + (E + I)^2 + 3] - 3(1 + EI)^2 \right\}^{-1} \\ &\quad \times \left\{ \left(\omega_u^6(v^2 + w^2 + 2) - \omega_u^4[E^2 w^2 + I^2 v^2 + 2(E^2 + I^2) + 2(v^2 + w^2) + c_s^2 + 4] \right. \right. \\ &\quad \left. \left. + \omega_u^2[E^2 w^2 + I^2 v^2 + E^2 + I^2 + EI(3 + 2EI + c_s^2) + v^2 + w^2 + 2c_s^2 + 2] - (1 + EI)(EI + c_s^2) \right) \hat{e}_k \right. \\ &\quad \left. - \lambda \left(\omega_u^4(E^2 v^2 + I^2 w^2) - \omega_u^2[E^2 + I^2 + EI((v^2 + w^2)(3 + EI) - 3c_s^2 - 1)] + EI(1 + EI)(1 + c_s^2) \right) \hat{e}_B \right\} \end{aligned}$
$\left(\frac{\partial \omega}{\partial k}\right)_o$	$= k \hat{e}_k - \lambda k \frac{EI [1 + 3c_s^2 + (1 + EI)(1 + c_s^2) - (3 + EI)(v^2 + w^2)] + E^2 v^2 + I^2 w^2 - (E^2 + I^2)}{E^2 I^2 - (E - I)^2} \hat{e}_B$
$\left(\frac{\partial \omega}{\partial k}\right)_m$	$\begin{aligned} &= \omega_l^{-1} \left\{ 6\omega_l^6 - 5\omega_l^4(E^2 + I^2 + 3) + 4\omega_l^2 [E^2 I^2 + (E + I)^2 + 3] - 3(1 + EI)^2 \right\}^{-1} \\ &\quad \times \left\{ \left(\omega_l^6(v^2 + w^2 + 2) - \omega_l^4[E^2 w^2 + I^2 v^2 + 2(E^2 + I^2) + 2(v^2 + w^2) + c_s^2 + 4] \right. \right. \\ &\quad \left. \left. + \omega_l^2[E^2 w^2 + I^2 v^2 + E^2 + I^2 + EI(3 + 2EI + c_s^2) + v^2 + w^2 + 2c_s^2 + 2] - (1 + EI)(EI + c_s^2) \right) \hat{e}_k \right. \\ &\quad \left. - \lambda \left(\omega_l^4(E^2 v^2 + I^2 w^2) - \omega_l^2[E^2 + I^2 + EI((v^2 + w^2)(3 + EI) - 3c_s^2 - 1)] + EI(1 + EI)(1 + c_s^2) \right) \hat{e}_B \right\} \end{aligned}$
$\left(\frac{\partial \omega}{\partial k}\right)_f$	$= \frac{[v_f^2(EI + c_s^2) - \lambda^2 EI c_s^2] \hat{e}_k + \lambda EI c_s^2(v_f^2 - 1) \hat{e}_B}{v_f [2v_f^2(1 + EI) - EI - c_s^2 - \lambda^2 EI c_s^2]}$
$\left(\frac{\partial \omega}{\partial k}\right)_a$	$= c_a \hat{e}_B$
$\left(\frac{\partial \omega}{\partial k}\right)_s$	$= \frac{[v_{sl}^2(EI + c_s^2) - \lambda^2 EI c_s^2] \hat{e}_k + \lambda EI c_s^2(v_{sl}^2 - 1) \hat{e}_B}{v_{sl} [2v_{sl}^2(1 + EI) - EI - c_s^2 - \lambda^2 EI c_s^2]}$

*The same logical notion
Concealed secret emotion*

— Leprous, *Rewind*

3

Applications of the ion-electron model

This chapter contains results from three different publications. The contents of Secs. 3.1 and 3.2 were published in De Jonghe and Keppens (2021a), those of Sec. 3.3 in De Jonghe and Keppens (2021b), and those of Sec. 3.4 in De Jonghe and Keppens (2020). For all three publications J. De Jonghe performed all calculations, computations, and visualisations, and wrote the first draft of the manuscript. R. Keppens contributed to the discussions in and revisions of the manuscripts.

To illustrate the versatility of the polynomial ion-electron description, this chapter employs the dispersion relation to explore a handful of phenomena. The first of these phenomena is that of “whistler waves”. So-called whistlers are waves of different frequencies that are often observed to travel along magnetic field lines with varying (group) speeds. The polynomial nature of the ion-electron dispersion relation makes the investigation of group speed variations relatively straightforward, and in Sec. 3.1 we attempt to create a full whistler catalogue by exploring the ion-electron group speed expressions in Earth’s magnetosphere. In this regard, the appearance of avoided mode crossings at oblique propagation angles raises many questions about the nature of whistlers at oblique angles. Whilst the classical whistlers that appear in the magnetosphere have relatively low frequencies, magneto-ionic theory takes an interest in the ionosphere’s high-frequency waves. In Sec. 3.2 we show how the Appleton-Hartree relation, which describes high-frequency waves in a cold plasma and is heavily used in

magneto-ionic theory, can be extended to warm plasmas as a limit case of the ion-electron dispersion relation.

Penultimately, the ion-electron model is applied to a laboratory setting, where a warm plasma at rest is subjected to a laser pulse. In this case the laser excites waves in the plasma medium, ultimately resulting in the emission of Cherenkov radiation.

Finally, as a central model in the plasma model hierarchy, it is also of interest to investigate how the ion-electron model relates to the models above and below it in the hierarchy. In Sec. 3.4 we compare some mode properties to those recovered in kinetic theory, which is higher up in the hierarchy, and show how to reduce the ion-electron dispersion relation to the low-frequency dispersion relation of Stringer (1963); Bellan (2012); Zhao et al. (2014) and the HMHD dispersion relation of Hameiri et al. (2005).

3.1 Whistler waves

The detection of whistler waves was first recorded in 1918 by radio operators who observed audio signals with a rapidly changing pitch (Barkhausen, 1919). Presently, they are covered in various plasma physics textbooks like Stix (1992), Baumjohann and Treumann (1997), Treumann and Baumjohann (1997), Bittencourt (2004), Gurnett and Bhattacharjee (2005), Bellan (2006), and Thorne and Blandford (2017). In the literature these so-called whistlers are described as modes whose group speed varies drastically for small changes in frequency in the interval between the ion and electron cyclotron frequencies. This dispersive nature is observed by the aforementioned change in pitch due to waves with higher frequencies arriving first. For Earth's magnetosphere, the frequency range of this behaviour overlaps with the audible frequencies, such that the signal can be converted to a whistling sound. After their initial discovery, it was shown by Storey (1953) that the detected signals were created by lightning in the southern hemisphere and that the waves travelled along the magnetic field to the northern hemisphere. Hence, the discussion of these waves in the literature is often limited to propagation parallel to the magnetic field. However, as shown by the analysis of the ion-electron dispersion relation in the previous chapter, parallel propagation is uniquely special for mode behaviour in a two-fluid plasma, since it shows different connectivity between small and large wave number behaviour of the 6 pairs of supported modes (S, A, F, M, O, and X). The appearance of avoided crossings suggests that whistler behaviour at oblique angles, observed by Cattell et al. (2008), differs from parallel propagation.

Later on, a whistler with frequencies below the ion cyclotron frequency was discovered by Earth orbiting spacecraft (Gurnett et al., 1965). These modes are called ion cyclotron whistlers and they occur for frequencies approaching the ion cyclotron frequency asymptotically from below for growing wave number.

Contrary to the classical whistlers, this results in dispersive behaviour where lower frequency waves arrive first (Gurnett and Bhattacharjee, 2005). In the present discussion we consider a plasma with only a single ion species. Hence, in this section there will be only one ion cyclotron frequency and one corresponding whistler. To allow for multiple ion cyclotron whistlers, the general two-fluid derivation explained in Ch. 2 and Goedbloed et al. (2019) has to be extended to a similar three- or multifluid description with one fluid for each ion species present in the plasma.

In the recent literature, whistlers have been discussed using various approaches such as electron magnetohydrodynamics (Damiano et al., 2009), electron fluid models (Zhao, 2017), two-fluid models (Huang and Lyu, 2019) and kinetic descriptions (Gary and Smith, 2009). Although they are often discussed as travelling parallel to the magnetic field, oblique whistler waves were also detected (Cattell et al., 2008) and prompted further studies (Yoon et al., 2014; Artemyev et al., 2016; Ma et al., 2017). Furthermore, whilst they were originally discovered in Earth's magnetosphere, spacecraft observations showed that whistler waves also occur in solar wind (Narita et al., 2016) and the atmospheres of Venus (Pérez-Invernón et al., 2017) and Jupiter (Imai et al., 2018). In solar wind, observations of whistler-like waves have been attributed to the whistler heat flux instability. This instability is part of a group of kinetic instabilities that regulate the electron heat flux, which plays an important role in the energy balance during the wind's acceleration (Gary et al., 1999; Gary and Li, 2000; López et al., 2019; Berčič et al., 2021).

This section will focus on whistling behaviour in Earth's magnetosphere at parallel, oblique, and perpendicular propagation, and how it is affected by the occurrence of avoided crossings compared to parallel propagation (De Jonghe and Keppens, 2020). This includes the regular whistlers and ion cyclotron whistlers, but also any rapid variations in group speed with small changes in frequency of other wave types, even when it occurs outside of the audible frequency range. Finally, we also comment on the absence of whistlers in pair plasmas, which is a statement pervading the literature on pair plasma behaviour (Stewart and Laing, 1992; Iwamoto, 1993; Gary and Smith, 2009).

Note, however, that various studies have pointed out that whistlers are usually subjected to damping effects, both collisional and collisionless (Crabtree et al., 2012). This can lead to an upper limit on the refractive index (Ma et al., 2017) or spectrum gaps (Hsieh and Omura, 2018). At the same time, damping effects may not be significant for some modes until after several magnetospheric reflections (Bell et al., 2002). The two-fluid model of an ideal, warm ion-electron plasma in Ch. 2 does not capture any damping effects. Though Landau damping is intrinsically absent in any two-fluid description, collisional damping can be included. However, this significantly complicates the model. Despite the lack of damping effects in our two-fluid model, it can describe the propagation of

whistler waves in an ideal setting. However, here the focus is on the whistling behaviour itself rather than the wave propagation. Also the conversion of whistler waves into “lower hybrid waves” at density striations (Bamber et al., 1994; Rosenberg and Gekelman, 1998; Shao et al., 2012) is beyond the scope of our discussion.

3.1.1 Conventions and methodology

Since any whistling behaviour is governed by the variation in group speed with frequency (or wave number), we focus on the ion-electron group speed expression, introduced in Sec. 2.3.2. Consequently, writing the group speed as a function of a single variable, either the frequency or the wave number, is of primary interest. However, due to the high polynomial degree of the dispersion relation, this is not analytically feasible. Therefore, approximations are used to obtain single-variable group speed expressions. Whilst similar approximations can be found in the literature, they are limited to parallel propagation and/or neglect ion contributions. Here, these approximations are extended to include ion effects and describe propagation at any angle. The approximations are complemented by numerical evaluations of the mode group speeds to create a complete picture of two-fluid whistling behaviour. Since the study here is mainly limited to Earth’s magnetosphere, it should be noted that results may differ for other environments based on the 6 regimes identified in Sec. 2.2. Depending on the prevailing plasma parameters (temperatures, field strengths, densities), the location and number of (avoided) crossings between the 6 wave pair branches differs, which is of direct consequence to whistler behaviour.

Although the term whistler usually refers to the low-frequency S, A, and F modes, because their frequencies lie in the audible range, similar behaviour can also be found in the high-frequency M, O, and X modes near their respective cutoffs. However, for Earth’s magnetosphere these cutoffs lie well above the audible frequencies, which approximately span 20 Hz to 20 kHz for the human ear, so it is not directly “translated” by a receiver into a whistling sound. Nevertheless, we will also consider these high-frequency modes and refer to their rapid variations in group speed as high-frequency whistling.

Conventions

When representing the group speed v_g of waves travelling at oblique angles, solid lines represent $v_g \cdot \hat{e}_k$ whilst dashed lines represent $v_g \cdot \hat{e}_B$. When evaluating dispersion relations, group speed expressions, and their approximations, we use the parameters for Earth’s magnetosphere, which can be found in App. A. In our current, dimensionless formalism they become $E \simeq 0.935$, $\mu \simeq 1/1836$, $v \simeq 1.7 \times 10^{-3}$, and $w \simeq 3.9 \times 10^{-5}$ with a plasma frequency of $\omega_p \simeq 5.64$ MHz. Whilst our value of E is significantly larger than the $E \simeq 0.1$ used in the

two-fluid study by Huang and Lyu (2019), both values describe the same regime from those identified in Sec. 2.2 and should thus be comparable.

Whistler terminology

In the literature the term whistler has been used for different waves showing a rapid variation in group speed within a small frequency interval. Naturally, the group speed can either increase or decrease when the frequency is increased. Both behaviours have been observed, although they occur in different frequency and/or wave number ranges. The first type, which we will refer to as classical whistlers, are the modes with an increasing group speed for increasing frequency such that high-frequency waves of this type travel faster. These are the waves that were first observed during the First World War as descending tones (Barkhausen, 1919; Bittencourt, 2004; Gurnett and Bhattacharjee, 2005; Bellan, 2006). A second type, which we call ascending frequency whistlers (Bittencourt, 2004), features the opposite behaviour. At parallel propagation, the first and second type actually correspond to the same mode in a different wave number range. Finally, a third type, dubbed ion cyclotron whistlers (Gurnett and Bhattacharjee, 2005), also describes decreasing group speed for increasing frequency near the ion cyclotron frequency, as the name suggests.

Resonance cone

Whilst the literature usually opts for a refractive index formulation for whistlers, we employ a formulation in terms of frequency and wave number. In particular, the resonance cone is often used to discuss oblique propagation. This cone follows from the observation that for any frequency ω below the electron cyclotron frequency Ω_e , there is an angle θ_{res} such that $\omega = \Omega_e \cos \theta_{\text{res}}$. Since $\Omega_e \cos \theta$ is a resonance and thus an asymptotic upper bound on the frequency of one of the wave types at a propagation angle θ , the resonance cone angle is the maximal propagation angle for a given frequency of that wave type. Hence, this angle defines a cone centered around the magnetic field line in which a wave of this type and frequency is allowed to travel (Gurnett and Bhattacharjee, 2005). However, as we will show, the appearance of avoided crossings allows the wave type in which the traditional whistler occurs to exist at any frequency at oblique angles, contrary to parallel propagation where it is bounded by Ω_e . Hence, we forego the use of the resonance cone and work with a fixed propagation angle.

3.1.2 Classical whistlers

The classical whistlers are usually described as the whistling waves with frequencies between the ion and electron cyclotron frequency (I and E). Which mode that is at parallel propagation, depends on whether $c_s < c_a$ or $c_s > c_a$.

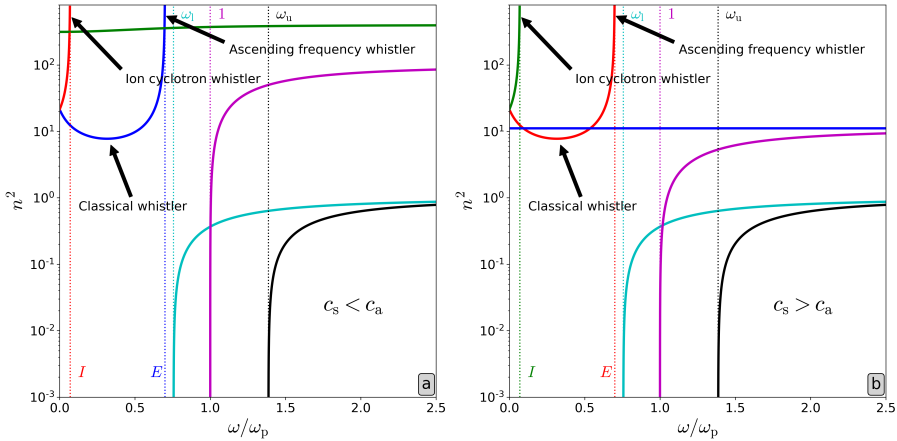


FIGURE 3.1: Refractive index $n = ck/\omega$ squared as a function of the frequency at parallel propagation for the values $E = 0.7$ and $\mu = 0.1$ (values chosen for demonstrational purposes). In case (a), $v = 0.1$, $w = 0.05$, and the classical whistler mode is the (blue) F mode. In case (b), $v = w = 0.3$ and the classical whistler mode is the (red) A mode.

In Sec. 2.2 we pointed out how up to six different parameter regimes in (E, I, v, w) can be distinguished where in each regime an a priori known amount of crossings between $\omega(k)$ branches can be identified as well as the locations of these crossings. In Fig. 3.1, we choose parameters representative of the two $E < 1$ regimes, as is the case for the magnetosphere, but similar figures can be produced for other regimes. Here, the squared index of refraction $n = ck/\omega$ is shown as a function of the frequency. In these diagrams, the mode with the classical whistler behaviour is characterised by a finite minimum index of refraction n at a non-zero frequency. If $c_s < c_a$, as is the case for the magnetosphere, the classical whistler is related to the F mode (Fig. 3.1(a), in blue). However, if $c_s > c_a$, it would be the A mode (Fig. 3.1(b), in red).

With the use of a large index of refraction approximation ($n \gg 1$) and neglecting ion contributions, the literature offers the approximate group speed expression (Gurnett and Bhattacharjee, 2005)

$$\frac{\partial\omega}{\partial k} = 2c \frac{\omega^{1/2} (\Omega_e - \omega)^{3/2}}{\Omega_e \omega_{pe}} \hat{e}_B, \quad \text{or equivalently,} \quad \frac{\partial\bar{\omega}}{\partial \bar{k}} = 2 \frac{\bar{\omega}^{1/2} (E - \bar{\omega})^{3/2}}{E} \hat{e}_B, \quad (3.1)$$

where the normalisation in the dimensionless form assumes $\omega_p \simeq \omega_{pe}$. This result can be obtained from the general dispersion relation, which at exactly parallel orientation splits in a quadratic and quartic factor in $\bar{\omega}^2$ (see Sec. 2.1.4), with

the quartic branch given by Eq. (2.27). As shown previously, this expression can be factorised further to give Eq. (2.28), which mixes forward-backward propagating wave pairs. Even though Eq. (2.27) should be preferred, if we take the second factor in Eq. (2.28), only keep up to second order in $\bar{\omega}$, and ignore the ion contributions, i.e. $I = 0$ and $\omega_p \simeq \omega_{pe}$, we get the simplified dispersion relation

$$\bar{k}^2(E - \bar{\omega}) - \bar{\omega} = 0. \quad (3.2)$$

From this expression, the literature group speed (3.1) is easily derived without further approximations.

Clearly, keeping ion contributions in (2.28) results in a dispersion relation that is quadratic in $\bar{\omega}$, which is more difficult to treat. However, to expand upon the literature approximation we can start from Eq. (2.27) and keep the $\mathcal{O}(\bar{\omega}^4)$ and $\mathcal{O}(I)$ terms to get

$$\bar{\omega}^2 = \frac{\bar{k}^2(2EI + \bar{k}^2E^2)}{1 + 2EI + 2\bar{k}^2(1 + E^2) + \bar{k}^4}. \quad (3.3)$$

From this relation, the phase and group speed expressions with the first order ion correction can be obtained,

$$\mathbf{v}_{ph} = \left[\frac{2EI + \bar{k}^2E^2}{1 + 2EI + 2\bar{k}^2(1 + E^2) + \bar{k}^4} \right]^{1/2} \hat{\mathbf{e}}_B \quad (3.4)$$

and

$$\frac{\partial \bar{\omega}}{\partial \bar{k}} = \frac{2\bar{k}}{\bar{\omega}} \frac{(EI + \bar{k}^2E^2)(1 + 2EI) + \bar{k}^4[E^2(1 + E^2) - EI]}{[1 + 2EI + 2\bar{k}^2(1 + E^2) + \bar{k}^4]^2} \hat{\mathbf{e}}_B, \quad (3.5)$$

where we made use of $\hat{\mathbf{e}}_B = \hat{\mathbf{e}}_k$ for parallel propagation. Using Eq. (3.3) to substitute $\bar{\omega}$ or \bar{k} in Eq. (3.5) yields a group speed expression in one variable. How this $\mathcal{O}(I)$ approximation compares to the usual literature approximation is shown in Fig. 3.2 along with a numerical evaluation of the full dispersion relation and an indication of observed whistler frequencies. In the classical whistler region, where the group speed is increasing with frequency $\bar{\omega}$, it follows the numerical result more closely.

3.1.3 Ascending frequency whistlers

The term ascending frequency whistler refers to the whistling behaviour that occurs near, but below, the electron cyclotron resonance $\bar{\omega} = E$ at parallel propagation (Bittencourt, 2004). The mode that approaches this resonance once again depends on the parameter regime. Looking at Fig. 3.1 again, the ascending frequency whistler is the mode asymptotically approaching $\bar{\omega} = E$ from the left. At parallel propagation, this is the F mode if $c_s < c_a$ and the

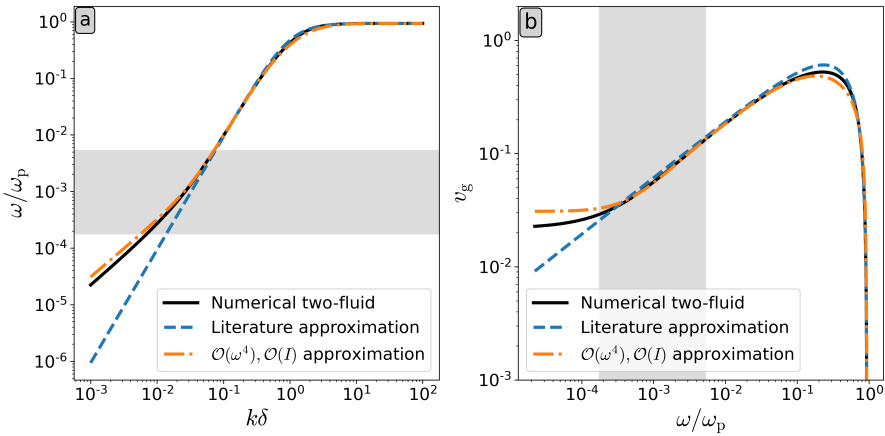


FIGURE 3.2: Comparison of the literature whistler approximation and our improved approximations from Eqs. (3.3) and (3.5) to numerical evaluations of the full ion-electron dispersion relation for Earth’s magnetosphere parameters at parallel propagation. The grey areas indicate the observed frequency range shown in Gurnett and Bhattacharjee (2005). (a) Whistler mode dispersion diagram showing frequency variation with wave number. (b) Whistler mode group speed showing group speed magnitude versus frequency.

A mode if $c_s > c_a$. Note that both the classical whistler and the ascending frequency whistler are hence described by the same mode at parallel propagation, regardless of the regime. At oblique angles, the situation will be more nuanced due to the avoided crossing near the electron cyclotron frequency.

As can be seen in Fig. 3.2, the approximation Eq. (3.1) is usually used for both classical and ascending frequency whistlers. Sometimes, for ascending frequency whistlers this is approximated further by using $\omega \simeq \Omega_e$ in the non-vanishing factor (Thorne and Blandford, 2017),

$$\frac{\partial \omega}{\partial \mathbf{k}} = \frac{2\Omega_e c}{\omega_{pe}} \left(1 - \frac{\omega}{\Omega_e}\right)^{3/2} \hat{\mathbf{e}}_B. \quad (3.6)$$

However, since $\bar{\omega}$ is close to E , the small frequency approximation used to obtain this result may no longer be the best approach. Alternatively, observe that the resonance behaviour $\bar{\omega} \rightarrow E$ occurs in the short wavelength (large k) limit. Hence, we will instead consider a large wave number approximation.

In order to expand the literature approximation to include ion effects, we only keep terms of order $\mathcal{O}(\bar{k}^2)$ or higher in Eq. (2.27), discard the rest, and assume

that $I < \bar{\omega} < E$. This leads to a phase speed of

$$\mathbf{v}_{\text{ph}} = \left[\frac{(E^2 - \bar{\omega}^2)(\bar{\omega}^2 - I^2)}{-2[\bar{\omega}^4 - \bar{\omega}^2(1 + E^2 + I^2) + EI(1 + EI)]} \right]^{1/2} \hat{\mathbf{e}}_{\mathbf{B}} \quad (3.7)$$

and a group speed

$$\begin{aligned} \frac{\partial \bar{\omega}}{\partial \bar{k}} = & \frac{E^{3/2}}{2} \left\{ -2 [\bar{\omega}^4 - \bar{\omega}^2(1 + E^2 + I^2) + EI(1 + EI)] \right\}^{1/2} \\ & \times \left\{ \bar{\omega}^8 - 2\bar{\omega}^6(E^2 + I^2) + \bar{\omega}^4 [(E^2 + I^2)(1 + E^2 + I^2) - EI(1 - 2EI)] \right. \\ & \left. - 2\bar{\omega}^2 E^2 I^2 (1 + E^2 + I^2) + E^3 I^3 (1 + EI) \right\}^{-1} \\ & \times (\bar{\omega}^2 - I^2)^{3/2} (\bar{\omega} + E)^{3/2} \left(1 - \frac{\bar{\omega}}{E} \right)^{3/2} \hat{\mathbf{e}}_{\mathbf{B}}, \end{aligned} \quad (3.8)$$

where we once again used that $\hat{\mathbf{e}}_{\mathbf{B}} = \hat{\mathbf{e}}_{\mathbf{k}}$ for parallel propagation. These expressions are real if $0 < I < E$, which is guaranteed for an ion-electron plasma since $I = \mu E$ and $0 < \mu < 1$. Although we started from a different approximation, note that the group speed expression (3.8) reduces to Eq. (3.6) if all ion terms are set to zero ($I = 0$, $\omega_p = \omega_{pe}$) and the approximation $\bar{\omega} = E$ is used in all factors except for the last one, which would vanish. However, if the ion terms are kept, using $\bar{\omega} = E$ gives an ion correction in both the phase speed,

$$\mathbf{v}_{\text{ph}} = \sqrt{E(E + I)} \left(1 - \frac{\bar{\omega}}{E} \right)^{1/2} \hat{\mathbf{e}}_{\mathbf{B}}, \quad (3.9)$$

and the group speed,

$$\frac{\partial \bar{\omega}}{\partial \bar{k}} = 2\sqrt{E(E + I)} \left(1 - \frac{\bar{\omega}}{E} \right)^{3/2} \hat{\mathbf{e}}_{\mathbf{B}}. \quad (3.10)$$

Note that the factor c is implicit since we are working with dimensionless quantities. However, for a proton-electron plasma under magnetosphere conditions the correction introduced by the inclusion of ion contributions is negligible compared to the textbook approximation (3.6).

Looking at expression (3.10), the ascending frequency whistling behaviour can be seen in the last factor $(1 - \bar{\omega}/E)^{3/2}$. As the frequency comes closer to the resonance, this factor becomes smaller. Since $\omega \xrightarrow{<} E$, the higher frequencies have a lower group speed. An observer listening for these signals will notice that the lower frequencies arrive first, resulting in an apparent increase in pitch.

3.1.4 Ion cyclotron whistlers

Just like the ascending frequency whistler, the ion cyclotron whistler occurs in the resonance regime, but here the frequency approaches the ion cyclotron frequency asymptotically for increasing wave number, $\bar{\omega} \rightarrow I$, at parallel propagation. Once again, which mode describes these whistlers depends on whether $c_s < c_a$ or vice versa. If $c_s < c_a$, they are related to the A mode (see Fig. 3.1(a)–red) whereas they occur in the S mode (see Fig. 3.1(b)–green) if $c_s > c_a$.

At parallel propagation, the ion cyclotron resonance is contained within the quartic branch from Eq. (2.27) and corresponds to the lowest frequency solution. Hence, to obtain approximate phase and group speed expressions, we start from Eq. (2.27) and keep only $\mathcal{O}(\bar{\omega}^2)$ terms. This gives

$$0 = \bar{\omega}^2 [2EI(1 + EI) + k^2(E^2 + I^2)] - k^2E^2I^2. \quad (3.11)$$

From this expression, the approximate phase and group speed expressions, as functions of the frequency, are

$$\mathbf{v}_{\text{ph}} = \left[\frac{E^2I^2 - \bar{\omega}^2(E^2 + I^2)}{2EI(1 + EI)} \right]^{1/2} \hat{\mathbf{e}}_B \quad (3.12)$$

and

$$\frac{\partial \bar{\omega}}{\partial \bar{k}} = \frac{[E^2I^2 - \bar{\omega}^2(E^2 + I^2)]^{3/2}}{E^2I^2 [2EI(1 + EI)]^{1/2}} \hat{\mathbf{e}}_B. \quad (3.13)$$

The exact numerical solution obtained from Eq. (2.27) and the approximation (3.13) are shown in Fig. 3.3. The whistling behaviour is captured fairly well.

3.1.5 High-frequency whistlers

Although the high-frequency M, O, and X modes only propagate at frequencies well above the audio frequency range, the group speed of all three modes increases quickly for increasing frequency near their respective cutoffs, as can be seen for parallel propagation in Figs. 3.4(b-d). This is indicative of a whistler that descends in frequency. Since these cutoff frequencies define the lower bounds for these modes, observations focused on the frequency bands slightly above each cutoff should be able to observe this behaviour. Theoretically, for Earth's magnetosphere, these cutoffs are approximately $\omega_M = 5.64$ MHz, $\omega_O = 3.59$ MHz and $\omega_X = 8.87$ MHz.

Comparing Fig. 3.4(d) to 3.4(e,f), it should be noted that the group speed range of the M mode whistling is significantly smaller than that of both the F and A mode whistling. Additionally, the O and X mode group speeds cover the full velocity range from 0 to 1 (see Figs. 3.4(b,c)), which is in full accord with their light wave behaviour. Hence, observations of the different whistling behaviours

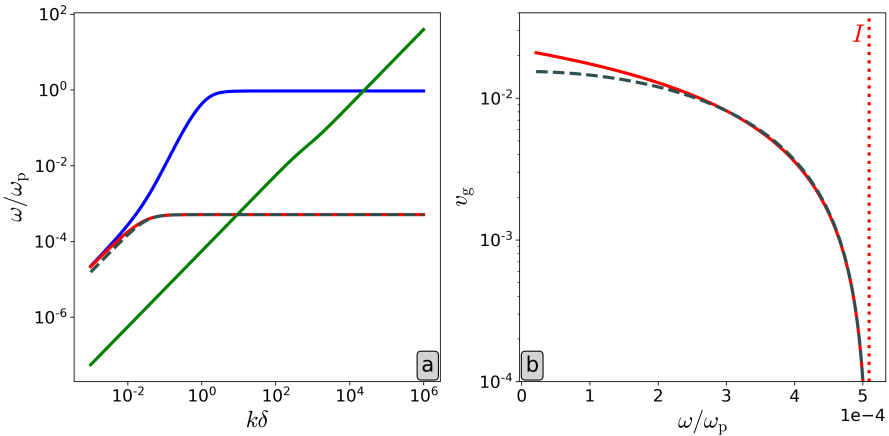


FIGURE 3.3: (a) Dispersion diagram of the S, A, and F modes for Earth’s magnetosphere parameters at parallel propagation. In this situation, the ion cyclotron whistler is associated with the (red) A mode. The dashed grey line is the ion cyclotron whistler approximation (3.11). (b) The group speed of the ion cyclotron whistler (A mode, red) and its approximation (3.13) (dashed grey).

along the magnetic field would happen on different timescales, assuming the travelling distance is fixed. To demonstrate this, consider a magnetic dipole to model Earth’s magnetic field and a field line at an angle of 15° to the dipole axis at a distance of 1 Earth radius ($1 r_E$) away from the dipole. Then the length of the field line from the northern to the southern surface is approximately $l \simeq 39 r_E$. Under the crude assumption that the plasma parameters were to stay the same along the entire trajectory such that the travel time is simply $t(\bar{\omega}) = l/cv_g(\bar{\omega})$, the classical whistler (F mode, from $\bar{\omega} = I$ up to the frequency with maximal group speed) would be observed in an interval of ~ 20 s, the ascending frequency whistler (F mode, from the frequency with maximal group speed up to $\bar{\omega} = 0.99 I$) in ~ 7 min, the ion cyclotron whistler (A mode, from $\bar{\omega} = 10^{-5}$ up to $\bar{\omega} = 0.95 I$) in ~ 30 min, the M mode whistling in the frequency interval $[1.01, 10] \omega_p$ in ~ 50 min, the O mode whistling (from 1.01 times the cutoff frequency up to the frequency where $v_g = 0.99$) in ~ 4 s, and the X mode whistling (from 1.01 times the cutoff frequency up to the frequency where $v_g = 0.99$) in ~ 0.1 s. Therefore, different whistling behaviours occur on different timescales. These theoretical frequency ranges and timescales also indicate where to look for high-frequency whistling in observations.

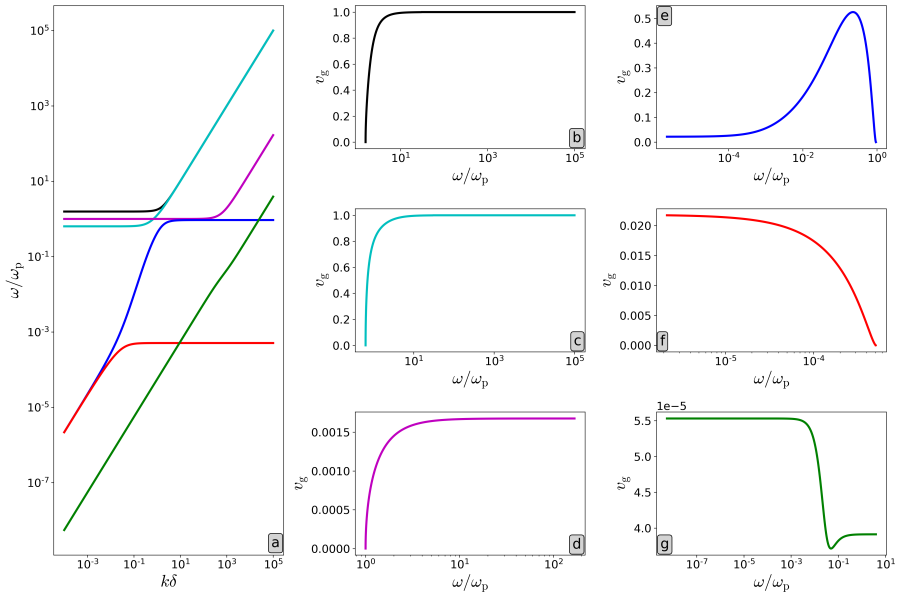


FIGURE 3.4: (a) Dispersion diagram of magnetosphere conditions at parallel propagation ($E < 1$, $c_s < c_a$). (b-g) Mode group speeds along the magnetic field for the (b) X mode, (c) O mode, (d) M mode, (e) F mode, (f) A mode, and (g) S mode, for varying frequency ranges based on cutoffs and/or resonances.

3.1.6 Pair plasma whistlers

As a small excursion to the cases discussed thus far, where we always used Earth's magnetosphere conditions and looked at purely parallel propagation, we here briefly consider the case of a pulsar magnetosphere. There, the strong electromagnetic fields create a pair plasma satisfying $E = I$, which is a rather different magnetospheric environment than encountered on Earth. Although the treatment below is mostly parameter independent, we consider a typical pulsar with a period of $P = 0.5$ s and a magnetic field strength of $B = 10^8$ T (Lyutikov, 1999). Additionally, we use a sound speed of $v^2 = 0.3$ (i.e. a relativistically hot plasma that reached its maximal sound speed limit) and a Goldreich-Julian density estimate (Goldreich and Julian, 1969), resulting in a cyclotron frequency of $E \simeq 5.89 \times 10^8$ with a plasma frequency of $\omega_p \simeq 29.8$ GHz.

As pointed out by Stewart and Laing (1992), there are no classical whistlers in equal-mass plasmas. To consider such a pair plasma in our formalism at parallel propagation, it suffices to substitute I by E in our dispersion relation

(2.27). In this case, the dispersion relation reduces to

$$0 = [\bar{\omega}^4 - \bar{\omega}^2(1 + E^2 + \bar{k}^2) + E^2\bar{k}^2]^2. \quad (3.14)$$

It was noted by Keppens et al. (2019) that the warm pair dispersion relation factorises into two third order branches in $\bar{\omega}^2$, named the XFS and OMA branches. Substituting $\lambda = 1$ in these branches reveals that one factor in Eq. (3.14) comes from the XFS branch and the other from the OMA branch. Due to this degeneracy, the phase and group speeds also simplify significantly,

$$\mathbf{v}_{\text{ph}} = \left(\frac{E^2 - \bar{\omega}^2}{1 + E^2 - \bar{\omega}^2} \right)^{1/2} \hat{\mathbf{e}}_{\mathbf{B}} \quad (3.15)$$

$$\simeq E \left(1 - \frac{\bar{\omega}^2}{E^2} \right)^{1/2} \hat{\mathbf{e}}_{\mathbf{B}} \quad \text{for } \bar{\omega} \rightarrow E \quad (3.16)$$

and

$$\mathbf{v}_{\text{g}} = \frac{\bar{k}(E^2 - \bar{\omega}^2)}{\bar{\omega}(1 + E^2 + \bar{k}^2 - 2\bar{\omega}^2)} \hat{\mathbf{e}}_{\mathbf{B}} \quad (3.17)$$

$$= \frac{(1 + E^2 - \bar{\omega}^2)^{1/2}(E^2 - \bar{\omega}^2)^{3/2}}{E^2 + (E^2 - \bar{\omega}^2)^2} \hat{\mathbf{e}}_{\mathbf{B}} \quad (3.18)$$

$$\simeq E \left(1 - \frac{\bar{\omega}^2}{E^2} \right)^{3/2} \hat{\mathbf{e}}_{\mathbf{B}} \quad \text{for } \bar{\omega} \rightarrow E. \quad (3.19)$$

Eq. (3.18) is a decreasing function on the frequency interval $(0, E)$, where any classical whistler mode would be. Hence, we indeed conclude that there is no classical whistler behaviour at parallel propagation. However, near the electron cyclotron frequency E the group speed decreases rapidly for increasing frequency, as is immediately clear from the approximation (3.19). Therefore, a pair plasma does have an ascending frequency whistler. In fact, due to the degeneracy in Eq. (3.14), a pair plasma has two coinciding, indistinguishable modes with ascending frequency whistling behaviour, one associated to each of the species. Note that this mode degeneracy is lifted at oblique angles. These are the A and F modes if $c_s < c_a$, as is the case in a typical pulsar magnetosphere. If a pair plasma would occur in an environment such that $c_s > c_a$, these would be the S and A modes instead.

3.1.7 Whistling at oblique angles

Returning to the general case, and specifying parameters to the Earth's magnetosphere again, we now discuss how whistling behaviour is certainly

not limited to purely parallel propagation alone. Whilst whistlers are often only considered as propagating (quasi-)parallel to the magnetic field, the polynomial two-fluid formalism allows us to extend the discussion to all angles. As explained in Keppens and Goedbloed (2019a,b); Keppens et al. (2019) and the previous chapter, it is impossible to make an unambiguous wave labelling scheme starting from purely parallel and purely perpendicular orientations, since those behave differently from all intermediate oblique orientations, where the wave frequencies are ordered. Due to the appearance of avoided crossings at oblique angles, which were discussed at length in Sec. 2.2.3, the complete picture of whistling behaviour is more complicated. First of all, whereas in the case of parallel propagation the group speed is always along the direction of the magnetic field, as seen in expressions (3.5), (3.8), (3.13), and (3.18), the group speed of any wave S, A, F, M, O, or X for oblique propagation now has contributions along the directions of both the magnetic field and the wave vector. Secondly, at an avoided crossing, new whistling behaviour may appear in the two involved modes. Since the number of avoided crossings depends on the regime (see Sec. 2.2.1), the whistling behaviour at oblique angles also depends on this regime. In this section we focus on the parameter regime that is representative of the Earth’s magnetosphere, $E < 1$ and $c_s < c_a$, using the magnetosphere parameters from Goedbloed et al. (2019).

In Fig. 3.5, the dispersion curve and the group speed of each mode are shown for Earth’s magnetosphere parameters at a propagation angle $\theta = \pi/6$. Strong increases correspond to descending frequency whistling behaviour (abbreviated DFW), like the classical whistlers, and strong decreases to ascending frequency whistling behaviour (abbreviated AFW), like the ascending frequency and ion cyclotron whistlers.

In Fig. 3.5(e), the F mode, which featured both the classical whistler and the ascending frequency whistler at parallel propagation, shows similar whistling behaviour, where a classical whistler for small frequencies is followed by an ascending frequency whistler. Near the electron cyclotron resonance however, the avoided crossing occurs and the group speed “jumps” to a constant in the short wavelength limit where $\bar{\omega}^2 \simeq \bar{k}^2 w^2$ for the F mode, as can be seen in the inset. In (f), one can see that the A mode, which featured the ion cyclotron whistler at parallel propagation, still has this ascending frequency whistling behaviour near the ion cyclotron resonance, after which it vanishes at the electron cyclotron frequency, which is shown in the inset. Finally, in (g), one can see that the S mode now features ion cyclotron whistling behaviour at the ion cyclotron frequency due to the SA avoided crossing.

Classical whistlers

From Fig. 3.5(e), it is clear that the F mode also describes classical whistler behaviour at oblique propagation angles in the frequency interval between the

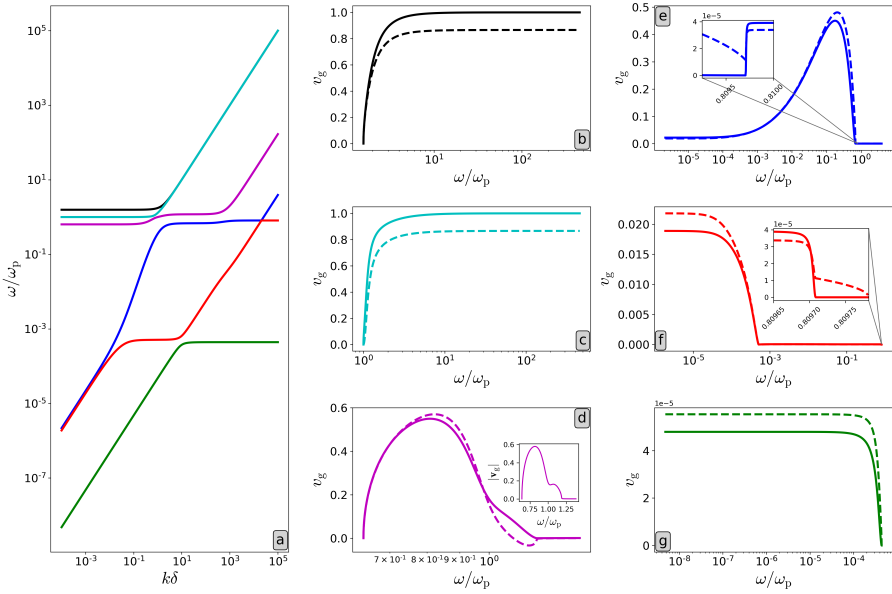


FIGURE 3.5: (a) Dispersion diagram of Earth's magnetosphere conditions at an angle $\theta = \pi/6$ ($E < 1$, $c_s < c_a$). (b-g) Mode group speed components along the wave vector $v_g \cdot \hat{e}_k$ (solid) and the magnetic field $v_g \cdot \hat{e}_B$ (dashed) for the (b) X mode, (c) O mode, (d) M mode, (e) F mode, (f) A mode, and (g) S mode, for varying frequency ranges based on cutoffs and/or resonances. The inset of (d) shows the magnitude of the M mode's group speed $|v_g|$, showing two peaks. The insets of (e) and (f) show the group speed behaviour near the AF avoided crossing.

two resonance frequencies λI and λE , at least in the regime $E < 1$, $c_s < c_a$. Like the parallel case, we can use a similar approximation in the general, sixth order dispersion relation to describe this whistling behaviour and expand textbook approximations to oblique angles. However, now we have to keep up to $\mathcal{O}(\bar{\omega}^6)$ in the dispersion relation to include the F mode. Once again, the ion contributions are limited to first order $\mathcal{O}(I)$. Additionally, at oblique angles the thermal speeds v and w also enter the equation. However, we will discard these thermal contributions for Earth's magnetosphere conditions, as v is of similar order of magnitude as I (and $v > w$) and the electron and ion sound speeds only appear squared. In fact, discarding these terms removes the S mode and thus tremendously simplifies the expression. It reduces the approximation to a first order equation in $\bar{\omega}^2$,

$$\bar{\omega}^2 = \frac{\bar{k}^2 [EI(1 + \lambda^2) + \bar{k}^2 (EI + \lambda^2 E(E - I))]}{1 + 2EI + \bar{k}^2 [2(1 + 2EI) + (1 + \lambda^2)E(E - I)] + \bar{k}^4(1 + E^2)}. \quad (3.20)$$

Whilst this approximation is reasonably good in the whistler region, it should be noted that it does not capture the avoided crossing behaviour at all. Nevertheless, starting from this expression, the phase and group speed expressions can be derived once again,

$$\mathbf{v}_{\text{ph}} = \left[\frac{EI(1 + \lambda^2) + \bar{k}^2(EI + \lambda^2 E(E - I))}{1 + 2EI + \bar{k}^2[2(1 + 2EI) + (1 + \lambda^2)E(E - I)] + \bar{k}^4(1 + E^2)} \right]^{1/2} \hat{\mathbf{e}}_k \quad (3.21)$$

and

$$\frac{\partial \bar{\omega}}{\partial \bar{k}} = -\frac{\bar{k}}{\bar{\omega} P_\omega} \left[\left(P_k - \frac{\lambda^2 P_\lambda}{\bar{k}^2} \right) \hat{\mathbf{e}}_k + \frac{\lambda P_\lambda}{\bar{k}^2} \hat{\mathbf{e}}_B \right] \quad (3.22)$$

where

$$P_\omega = 1 + 2EI + \bar{k}^2 [2(1 + 2EI) + (1 + \lambda^2)E(E - I)] + \bar{k}^4(1 + E^2), \quad (3.23)$$

$$\begin{aligned} P_k &= 2\bar{k}^2 [\bar{\omega}^2(1 + E^2) - E(I + \lambda^2(E - I))] \\ &\quad + \bar{\omega}^2 [2(1 + 2EI) + (1 + \lambda^2)E(E - I)] - (1 + \lambda^2)EI, \end{aligned} \quad (3.24)$$

$$P_\lambda = \bar{k}^2 E [\bar{\omega}^2(E - I) - I - \bar{k}^2(E - I)]. \quad (3.25)$$

Using Eq. (3.20) we can once again obtain a single-variable group speed expression. These expressions are already quite involved for such a simple approximation. Keeping any correction from thermal contributions complicates it even more. As it turns out, the first order ion correction is not as significant as in the parallel case discussed in Sec. 3.1.2. Therefore, the above expression can be reduced further by substituting $I = 0$. However, it seems that the ion correction becomes more important the further we deviate from parallel propagation.

In Fig. 3.6, the evaluation of the approximation given by Eqs. (3.20) and (3.22) to (3.25) is shown for different angles alongside a numerical evaluation of the full dispersion relation group speed. As can be seen from the figure, the approximation is quite good in the classical whistler region, but underestimates the height of the peak.

Ascending frequency whistlers

At parallel propagation, the ascending frequency whistler occurs in the F mode when the frequency approaches the electron cyclotron resonance E asymptotically. For the magnetosphere regime ($E < 1$, $c_s < c_a$), the S mode crosses the F mode at a frequency close to E . At oblique angles, this means that the S, A, and F modes are affected, and that there is an avoided crossing in the frequency interval where we expect the ascending frequency whistler to be. Fig.

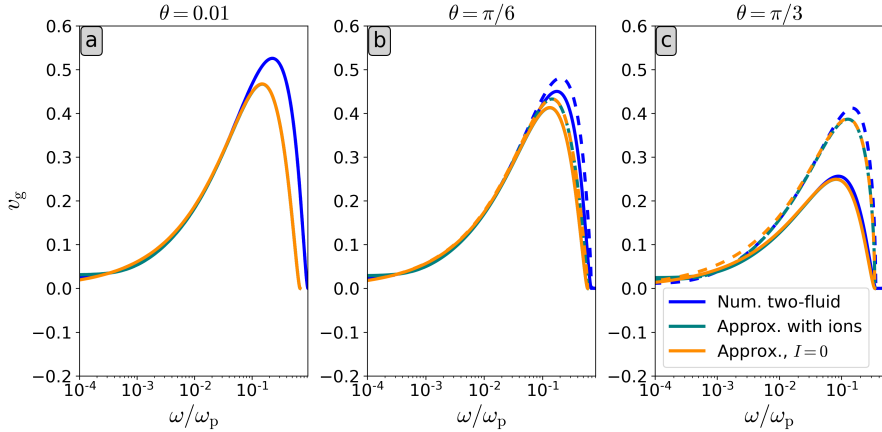


FIGURE 3.6: Comparison of the oblique whistler group speed approximation (3.22) to (3.25) and (3.20) and the exact two-fluid solution under magnetosphere conditions for different propagation angles: (a) $\theta = 0.01$, (b) $\theta = \pi/6$, and (c) $\theta = \pi/3$ ($v_g \cdot \hat{e}_k$ —solid, $v_g \cdot \hat{e}_B$ —dashed).

3.7(a) shows a closer look at the AFW region where the avoided crossing between the A and F modes occurs. Now note that the F mode has two plateau-like regions. This is due to the fact that at oblique angles the resonances of the cold and warm plasma differ. The highest plateau occurs near $\bar{\omega} = \lambda E$, where we expect the avoided crossing to be, and the associated whistling behaviour. This is a warm plasma resonance. An approximate value for the lowest plateau on the other hand can be found by calculating the resonance limit for a cold plasma, and neglecting ion contributions, to get (Keppens and Goedbloed, 2019b)

$$\bar{\omega}^2 \simeq \frac{1}{2} \left(1 + E^2 - \sqrt{(1 + E^2)^2 - 4\lambda^2 E^2} \right). \quad (3.26)$$

This frequency lies between zero (for $\lambda = 0$) and the parallel resonance limit $\bar{\omega}^2 = E^2$ (for $\lambda = 1$). Near perpendicular propagation the ion contributions should not be neglected though, and we find a lower bound of

$$\bar{\omega}_{\text{LH}}^2 = \frac{1}{2} \left(1 + E^2 + I^2 - \sqrt{(1 + E^2 + I^2)^2 - 4EI(1 + EI)} \right), \quad (3.27)$$

which is commonly referred to as the lower hybrid frequency $\bar{\omega}_{\text{LH}}$ (Keppens and Goedbloed, 2019b) and is $\omega_{\text{LH}} = 90$ kHz for the typical reference Earth's magnetosphere parameters. Looking at Fig. 3.7(b), the lowest plateau marks the end of the large scale AFW behaviour. Hence, this strong AFW behaviour occurs near the cold plasma resonance that falls from the electron cyclotron frequency

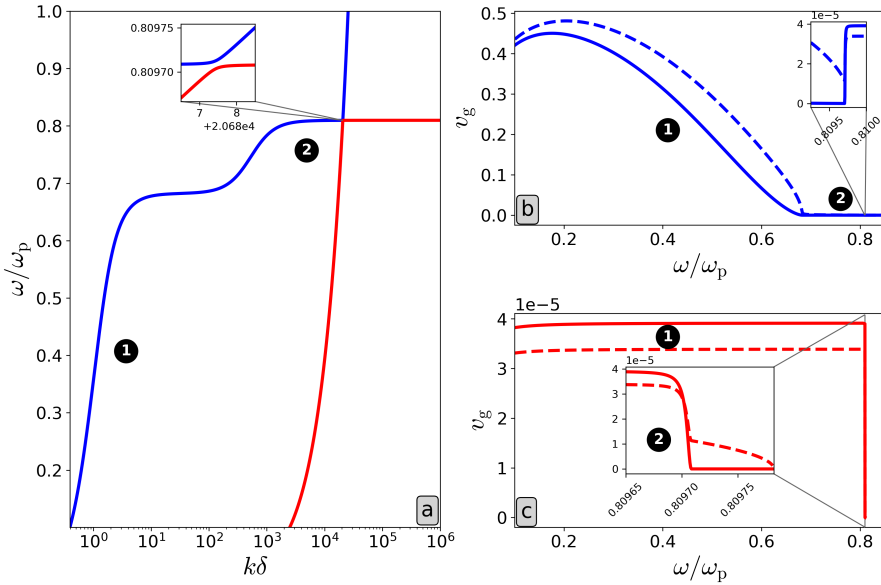


FIGURE 3.7: (a) Dispersion diagram of the A and F modes in the ascending frequency whistler region for Earth's magnetosphere conditions at $\theta = \pi/6$. This is a zoom of Fig. 3.5(a). The inset shows the avoided crossing. (b) F mode group speed. (c) A mode group speed. ($v_g \cdot \hat{e}_k$ —solid, $v_g \cdot \hat{e}_B$ —dashed)

at parallel propagation to the lower hybrid frequency (3.27) at perpendicular propagation, and is approximately given by Eq. (3.26), except near $\lambda = 0$. This behaviour is described adequately by the cold plasma limit.

Above the cold plasma resonance given approximately by Eq. (3.26), the insets of Figs. 3.7(b,c) show that near the electron cyclotron frequency (the F mode's highest plateau) there is also AFW behaviour in the F mode, albeit on a much smaller scale, and the A mode, due to the avoided crossing. In the F mode, the avoided crossing causes small scale DFW behaviour immediately after this small scale AFW behaviour.

If one would like to analytically approximate the small scale whistling behaviour near the resonance (region 2 in Fig. 3.7), a short wavelength approximation similar to the one used in the parallel case (see Sec. 3.1.3) can be obtained for oblique angles by keeping only terms of order $\mathcal{O}(\bar{k}^8)$ and $\mathcal{O}(\bar{k}^6)$ in the general ion-electron dispersion relation Eq. (2.10). Assuming $\lambda I < \bar{\omega} < \lambda E$ and applying the approximation $\bar{\omega} = \lambda E$ in all but the vanishing factor, an extension of the previous phase and group speed expressions to oblique angles

is obtained, including ion and thermal contributions,

$$\mathbf{v}_{\text{ph}} = \lambda v \sqrt{\frac{2E(E+I)}{2v^2 + E(E+I)(1-\lambda^2)}} \left(1 - \frac{\bar{\omega}}{\lambda E}\right)^{1/2} \hat{\mathbf{e}}_k \quad (3.28)$$

and

$$\begin{aligned} \frac{\partial \bar{\omega}}{\partial k} &= v \sqrt{\frac{2E(E+I)}{2v^2 + E(E+I)(1-\lambda^2)}} \\ &\times \left(1 - \frac{\bar{\omega}}{\lambda E}\right)^{1/2} \left\{ 2\lambda \left(1 - \frac{\bar{\omega}}{\lambda E}\right) \hat{\mathbf{e}}_k + (\hat{\mathbf{e}}_B - \lambda \hat{\mathbf{e}}_k) \right\}. \end{aligned} \quad (3.29)$$

These expressions reduce to Eqs. (3.9) and (3.10) at parallel propagation where $\lambda = \pm 1$ and $\hat{\mathbf{e}}_B = \lambda \hat{\mathbf{e}}_k$. Interesting to note is that the oblique behaviour is influenced by the electron sound speed v whilst the ion sound speed w drops out of the expression.

In Fig. 3.8, the group speed approximation (3.29) is shown alongside the exact solutions of the general dispersion relation for the A and F mode. The approximation is unaware of the avoided crossing and thus approximates the F mode up until the avoided crossing, whereafter it approximates the A mode closer to the resonance. This can be seen most clearly in the inset of panel (c). The approximation is reasonably good near the resonance, but becomes progressively worse for smaller values of $\bar{\omega}$, where the wave number is also smaller and the large wave number approximation breaks down.

Ion cyclotron whistlers

The ion cyclotron resonance is given at any angle by $\bar{\omega} = \lambda I$. Since the ion cyclotron whistler occurs at frequencies near I at parallel propagation, we look for similar behaviour near λI at oblique angles. Once again, at parallel propagation two modes cross near $\bar{\omega} = I$ in the magnetosphere regime ($E < 1$, $c_s < c_a$), namely the S and A modes. Just like the previous case, an avoided crossing appears at a small deviation from parallel propagation. This avoided crossing can still be seen at a larger propagation angle in Fig. 3.9(a), although the modes no longer approach each other extremely closely.

When moving further away from parallel propagation, it becomes clear that there are two frequencies of interest, $\bar{\omega} = I$ and $\bar{\omega} = \lambda I$. This is illustrated in Fig. 3.9 for an angle $\theta = \pi/6$. Here, you can see in (a) that the S mode approaches $\bar{\omega} = \lambda I$ asymptotically and the A mode has a plateau near $\bar{\omega} = I$. The exact value of the plateau is given by the lowest resonance of the cold plasma, which is very close to the ion cyclotron frequency at all angles except near perpendicular propagation, where the A mode vanishes. The S mode's

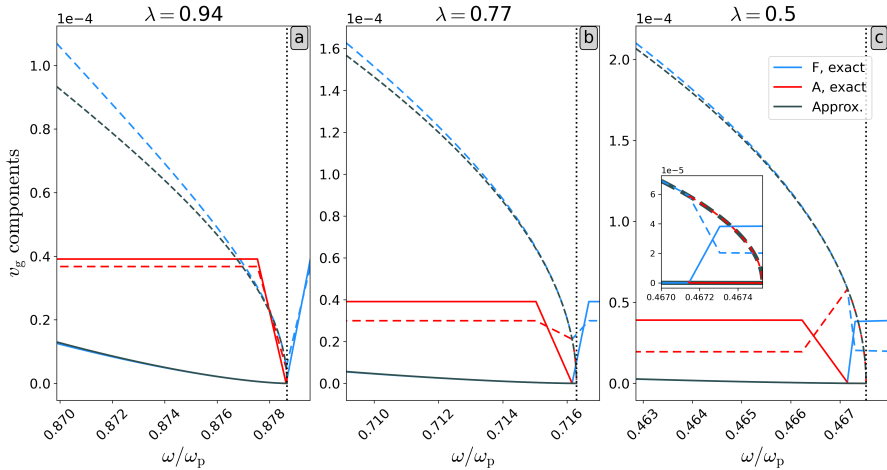


FIGURE 3.8: The A and F mode group speeds for Earth’s magnetosphere conditions are shown in red and blue, respectively, and the AFW approximation in black for (a) $\lambda = 0.94$, (b) $\lambda = 0.77$, and (c) $\lambda = 0.5$, in the interval $(0.99 \lambda E, 1.001 \lambda E)$. ($v_g \cdot \hat{e}_k$ —solid, $v_g \cdot \hat{e}_B$ —dashed) The approximation is unaware of the avoided crossing and follows the F mode before and the A mode after the avoided crossing. A close-up of this behaviour is shown in the inset of (c). The resonance λE is indicated by the vertical dotted black line.

group speed is visualised near the resonance in (c), where it varies relatively rapidly. There is indeed AFW behaviour, although the group speed is quite small. Hence, the avoided crossing leads to the occurrence of the oblique ion cyclotron whistler in the S mode near $\bar{\omega} = \lambda I$. The group speed of the A mode near the plateau is shown in the inset of (b). It appears to have both AFW and minor DFW behaviour near this cold plasma resonance.

High-frequency whistlers

For Earth’s magnetosphere, Fig. 3.5(b) shows that the X mode’s oblique behaviour is largely unaltered from parallel propagation, in Fig. 3.4(b). The M and O modes, which cross in the O mode’s whistling region at parallel propagation, switch their cutoffs such that $\omega_M < \omega_O$ at all wave numbers. Since the cutoffs are where the whistling behaviour occurs, this behaviour is heavily influenced. This is especially pronounced in the oblique M mode, which can be seen by comparing Figs. 3.4(c,d) and Figs. 3.5(c,d). In the parallel case, both the M and O mode only feature DFW behaviour whereas at oblique angles the M mode shows strong DFW and AFW behaviour. Both behaviours occur in

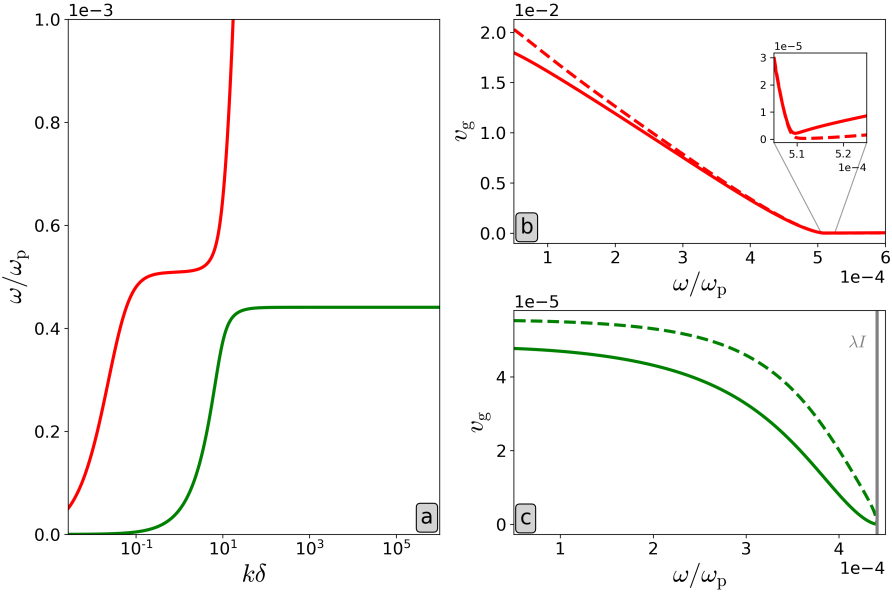


FIGURE 3.9: (a) Dispersion diagram of the S and A modes in the ion cyclotron whistler region for Earth's magnetosphere conditions at $\theta = \pi/6$. This is a zoom of Fig. 3.5(a). (b) A mode group speed. (c) S mode group speed. ($v_g \cdot \hat{e}_k$ —solid, $v_g \cdot \hat{e}_B$ —dashed) Note that the vertical axis in all panels has a multiplicative scale factor indicated at their top left corner.

the frequency range between the lower cutoff frequency

$$\omega_l = \left[1 + \frac{1}{2}(E^2 + I^2) - \frac{1}{2}|E - I|\sqrt{(E + I)^2 + 4} \right]^{1/2} \omega_p \quad (3.30)$$

and the highest cold plasma resonance given approximately by (Keppens and Goedbloed, 2019b)

$$\bar{\omega}^2 \simeq \frac{1}{2} \left(1 + E^2 + \sqrt{(1 + E^2)^2 - 4\lambda^2 E^2} \right), \quad (3.31)$$

ignoring ion contributions. This value rises from the plasma frequency at parallel propagation ($\lambda = 1$) to the upper hybrid frequency $\bar{\omega}_{\text{UH}}$, given by (Keppens and Goedbloed, 2019b)

$$\bar{\omega}_{\text{UH}}^2 = \frac{1}{2} \left(1 + E^2 + I^2 + \sqrt{(1 + E^2 + I^2)^2 - 4EI(1 + EI)} \right), \quad (3.32)$$

at perpendicular propagation ($\lambda = 0$). As shown in Fig. 3.5(d), the magnitude of the group speed actually has two peaks, which are separated by the plasma

frequency ($\omega_p = 5.64$ MHz, $\omega_l = 3.59$ MHz, $\omega_{UH} = 7.72$ MHz for the typical reference Earth's magnetosphere parameters). The O mode's whistling behaviour is situated directly above its cutoff at the plasma frequency and is limited to DFW behaviour.

Pair plasma whistlers

Returning to a pulsar magnetosphere environment for a moment, it was shown that even though a pair plasma does not feature classical whistlers, it does have AFW behaviour in the A and F modes at parallel propagation. At oblique angles, the frequency ordering in a pair plasma (Keppens et al., 2019) ensures that it are now the S and A modes that both approach the cyclotron resonance λE . Figs. 3.10(f,g) shows that both the S and A mode display AFW behaviour near the resonance. Additionally, the A mode also features AFW behaviour near the plasma frequency ($\bar{\omega} = 1$), followed by smaller scale DFW behaviour. The same behaviour, AFW followed by DFW, is also present in the F and M modes, which nearly coincide for short wavelengths, near the cyclotron frequency ($\bar{\omega} = E$). Furthermore, the O and X modes also feature DFW behaviour near their cutoff frequencies. Note that since the plasma frequency is well above the audible frequency range ($\omega_p \simeq 29.8$ GHz), none of these behaviours actually occurs in the audible range. Hence, whilst a pair plasma does not feature classical whistlers at parallel propagation, there is still a lot of interesting whistling behaviour occurring across all modes.

3.1.8 Cross-field whistlers

In the limit of perpendicular propagation, the S and A modes no longer propagate, in exact correspondence with the known MHD property of slow and Alfvén waves, resulting in a different factorisation of the dispersion relation (see Sec. 2.1.4). Additionally, there are no resonances at perpendicular propagation, where AFW behaviour occurred at parallel and oblique angles. However, computing the group speed of the F mode numerically, which is then perpendicular to the magnetic field, shows that small scale AFW behaviour occurs at the previously introduced lower hybrid frequency, Eq. (3.27). The group speed behaviour of all four perpendicularly propagating modes is shown for Earth's magnetosphere conditions in Fig. 3.11. In particular, the F mode's steep decrease in group speed, shown in (e), is caused by the presence of a plateau in the F mode dispersion curve at the lower hybrid frequency, shown in (a). Note that the group speed difference is of the same scale as the parallel ion cyclotron whistler in Fig. 3.3. However, this AFW whistling occurs near the lower hybrid frequency at 90 kHz, which is outside of the audible frequency range. The high-frequency M, O, and X modes again show DFW behaviour near their cutoffs, similar to their oblique behaviour. For the M mode, this

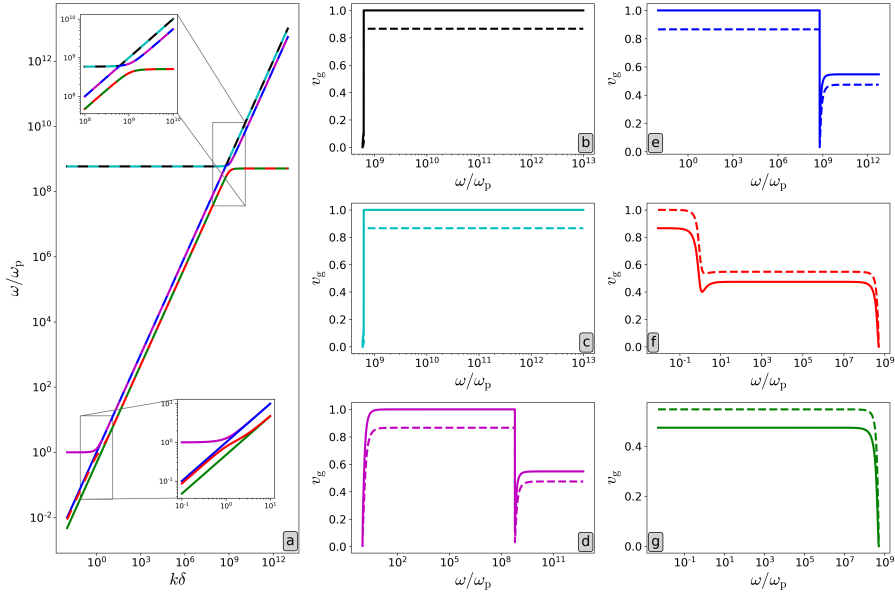


FIGURE 3.10: (a) Dispersion diagram of a pair plasma under pulsar magnetosphere conditions at an angle $\theta = \pi/6$ ($E \simeq 5.89 \times 10^8$). Note that due to the extreme conditions inherent in the pulsar magnetosphere, modes that virtually overlap are shown as lines that show both associated colours, even in some of the zoomed inset views. (b-g) Mode group speed components along the wave vector $v_g \cdot \hat{e}_k$ (solid) and the magnetic field $v_g \cdot \hat{e}_B$ (dashed) for the (b) X mode, (c) O mode, (d) M mode, (e) F mode, (f) A mode, and (g) S mode, for varying frequency ranges based on cutoffs and/or resonances.

DFW behaviour is followed by equally strong AFW behaviour as the frequency approaches the upper hybrid frequency $\bar{\omega}_{\text{UH}}$. Unlike in the oblique case, the whistling behaviour of the M mode does not show any changes at the plasma frequency.

3.2 Warm Appleton-Hartree equation

In most whistler applications discussed so far, the pairs involved from the six mode dispersion relation are the S, A, and F low-frequency ones. As a different application of the general, sixth order dispersion relation, we can also study high-frequency waves. The Appleton-Hartree equation (Appleton, 1932) is often used in magneto-ionic theory to describe high-frequency waves in a cold ion-electron plasma neglecting ion motion. This relation is valid for frequencies

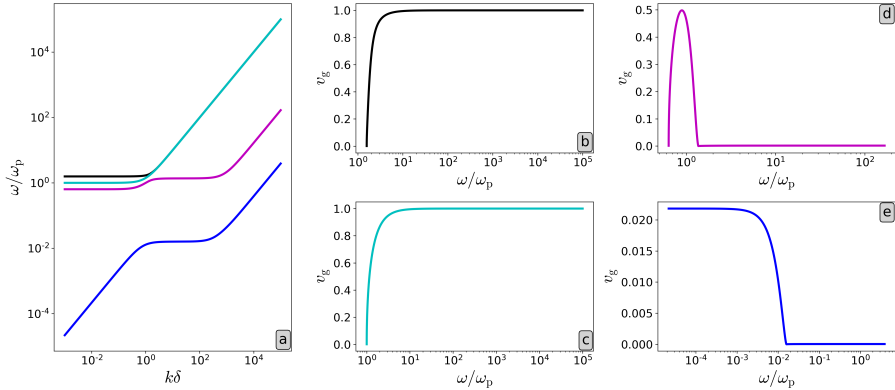


FIGURE 3.11: (a) Dispersion diagram of the F, M, O, and X modes for Earth’s magnetosphere at perpendicular propagation. (b-e) Mode group speeds along the wave vector, perpendicular to the magnetic field, for the (b) X mode, (c) O mode, (d) M mode, and (e) F mode, for varying frequency ranges based on cutoffs.

above the electron plasma frequency ω_{pe} at any angle θ between the wave vector and the background magnetic field. It was pointed out by Keppens and Goedbloed (2019b) that the collisionless relation can be obtained from the polynomial description of the cold ion-electron plasma waves by taking the (unphysical) $\mu = 0$ limit (recall: μ is the ratio of masses over charges, i.e. a physical property of the plasma). This limit results in infinitely heavy ions and thus forces them to be immobile.

Relatively recently, Bawa’aneh et al. (2013) extended the Appleton-Hartree relation, which is presented in the majority of plasma physics textbooks, to describe the high-frequency waves of a warm ion-electron plasma. To obtain the warm Appleton-Hartree equation in a manner consistent with the SAFMOX labelling scheme, it suffices to consider the $\mu = 0$ limit of the general ion-electron dispersion relation in $\bar{\omega}$ and \bar{k} . For the cold ion-electron case, where only 5 mode pairs exist, this was already done in Keppens and Goedbloed (2019b), where the equation was shown to retain 4 out of the 5 mode pairs. The $\mu = 0$ limit implies that $I = 0$ and $c_s^2 = w^2$. With these substitutions the fully general dispersion relation factors out a trivial mode $\bar{\omega}^2 = 0$ just like the cold case and it separates the ion and electron sound speeds v and w resulting in the

dispersion relation

$$\begin{aligned}
& \bar{\omega}^2(\bar{\omega}^2 - \bar{k}^2 w^2) \\
& \times \left\{ \bar{\omega}^8 - \bar{\omega}^6 [3 + E^2 + \bar{k}^2(2 + v^2)] \right. \\
& + \bar{\omega}^4 [3 + E^2 + \bar{k}^2 (4 + 2v^2 + 2E^2 + \lambda^2 E^2 v^2) + \bar{k}^4(1 + 2v^2)] \\
& - \bar{\omega}^2 [1 + \bar{k}^2 (2 + v^2 + (1 + \lambda^2)E^2) + \bar{k}^4 (1 + 2v^2 + E^2 + 2\lambda^2 E^2 v^2) + \bar{k}^6 v^2] \\
& \left. + \bar{k}^4 \lambda^2 E^2 (1 + \bar{k}^2 v^2) \right\} = 0. \tag{3.33}
\end{aligned}$$

It can be argued that the factor $\bar{\omega}^2 - \bar{k}^2 w^2$ should be disregarded or replaced by $\bar{\omega}^2$ because the $\mu = 0$ limit implies that the ions are infinitely heavy and therefore immobile. Hence, their thermal speed w should also be $w = 0$. Mathematically, it is interesting that it factors out anyway. This leaves the polynomial of fourth degree in $\bar{\omega}^2$ as a generalisation of the Appleton-Hartree dispersion relation to the warm case. Expression (24) in Bawa'aneh et al. (2013), ignoring collision terms, can be reordered to retrieve Eq. (3.33).

It is easily checked that substituting $v = 0$, i.e. setting the electron thermal speed to zero, in this polynomial retrieves Eq. (40) from Keppens and Goedbloed (2019b), which they showed to be equivalent to the Appleton-Hartree relation, usually written as a function of the refractive index $n = ck/\omega = \bar{k}/\bar{\omega}$. This usual way of expressing this relation is only for historical reasons preferred and is possible because the polynomial is of second degree in \bar{k}^2 in the cold case. However, including a non-zero thermal velocity v adds two terms of third degree in \bar{k}^2 . Writing n^2 as an explicit function of the other variables is thus more involved. Additionally, as pointed out in Keppens and Goedbloed (2019b), this hopelessly confuses the unique and unambiguous SAFMOX wave labelling and identification.

Nevertheless, adopting the usual Appleton-Hartree variables X and Y defined as $X = 1/\bar{\omega}^2$ and $Y = E/\bar{\omega}$, and introducing a new variable $V = v/\bar{\omega}$ related to the thermal velocity, the warm equivalent of the Appleton-Hartree relation

can be expressed as a third degree polynomial in n^2

$$\begin{aligned}
 & -X(1-X) [(1-X)^2 - Y^2] \\
 & + n^2 [2X(1-V^2) + V^2(1-Y^2 \cos^2 \theta) + 2X^2(X-2) \\
 & \quad - 2XY^2 + X^2V^2 + (1+\cos^2 \theta)X^2Y^2] \\
 & - n^4 [X + 2V^2(1-X) - X^2(1-Y^2 \cos^2 \theta) - Y^2(X + 2V^2 \cos^2 \theta)] \\
 & + n^6 V^2(1-Y^2 \cos^2 \theta) = 0.
 \end{aligned} \tag{3.34}$$

The formula for roots of a cubic polynomial can then be used to write the squared refractive index n^2 as a function of X , Y , V , and θ . However, the expression does not simplify significantly. Thus, it is omitted here in favor of the polynomial expression. It is to be noted that roots of arbitrary degree polynomials are routinely computed numerically anyway.

Similar to how the full dispersion relation factorised for parallel and perpendicular propagation, the generalised Appleton-Hartree relation (3.34) factorises if we substitute $\theta = 0$ or $\theta = \pi/2$. For parallel propagation ($\theta = 0$), the expression becomes

$$\begin{aligned}
 & [n^2V^2 - X(1-X)][n^2(1-Y) - (1-X-Y)] \\
 & \times [n^2(1+Y) - (1-X+Y)] = 0.
 \end{aligned} \tag{3.35}$$

Comparing this to the parallel factorisation in De Jonghe and Keppens (2020), the last two factors come from the quartic branch whilst the first factor comes from the quadratic branch. The discarded factor $\bar{\omega}^2 - \bar{k}^2 w^2$ also came from the quadratic branch. Note that the substitution $\omega \rightarrow -\omega$ transforms the variables as $X \rightarrow X$, $Y \rightarrow -Y$ and $V \rightarrow -V$. Therefore, the last two factors in this relation mix forward-backward wave types as was also pointed out in Keppens and Goedbloed (2019b) and in the previous chapter. This intrinsic mixing of forward-backward wave types seems to be a recurring habit in all the plasma physics literature, and it is “justified” by the fact that at these special parallel or perpendicular orientations, some wave modes become then classifiable as left or right hand polarised wave types. It is to be noted that the forward-backward pairing, which we advocate as preferential, carries over to moving reference frames, and has been crucial in rigorously analysing MHD waves in stationary configurations with spatially varying equilibrium conditions (Goedbloed et al., 2019).

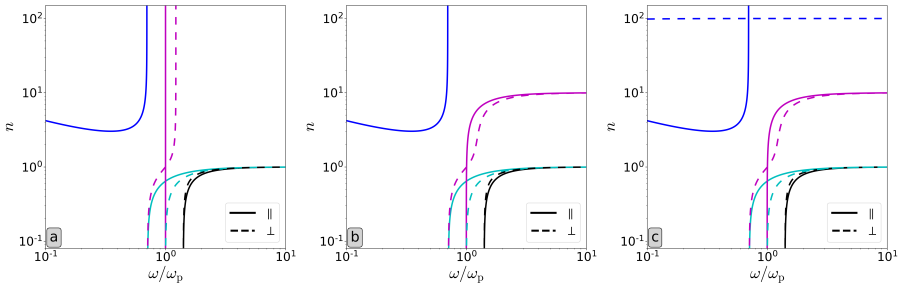


FIGURE 3.12: (a) The (cold) Appleton-Hartree relation in an $n(\bar{\omega})$ -diagram. (b) The extended warm Appleton-Hartree equation (3.34) with $v = 0.1$. (c) The corresponding modes from the full dispersion diagram for an ion-electron plasma ($\mu \approx 1/1836$) with $v = 0.1$ and $w = 0.01$. All cases use $E = 0.7$ and are shown in the limits of parallel (solid) and perpendicular (dashed) propagation.

Analogously, for perpendicular propagation ($\theta = \pi/2$) the factorisation is

$$(n^2 - 1 + X) \left\{ n^4 V^2 - n^2 [V^2(1 - X) + X(1 - X - Y^2)] + X [(1 - X)^2 - Y^2] \right\} = 0. \quad (3.36)$$

Once again, this result corresponds to the perpendicular factorisation Eq. (2.29). The linear branch matches without simplification whilst the cubic branch reduces to the quadratic expression in n^2 here and the factor $\bar{\omega}^2 - \bar{k}^2 w^2$ in the $\mu = 0$ limit.

Finally, a closer look at how the warm version improves upon the cold Appleton-Hartree equation is visualised in Fig. 3.12. Here, (a) shows the cold Appleton-Hartree relation, (b) shows the warm extension, and (c) shows an evaluation of the F, M, O, and X modes in the full dispersion relation for reference. For the two electromagnetic O and X modes, and the F mode, there does not seem to be a noticeable improvement from cold to warm. In fact, the short wavelength (large \bar{k}) limit of the F mode is not captured correctly for oblique and perpendicular propagation. It should be $n^2 \approx 1/w^2$, but w only appears in a different factor in Eq. (3.33). However, the M mode (purple), related to the Langmuir wave, now exhibits a more correct high-frequency behaviour. Comparing Figs. 3.12(b) and 3.12(c), the three high-frequency modes follow the correct behaviour now, whereas the F mode's behaviour is only correct at parallel propagation.

Whilst Fig. 3.12 only shows the parallel and perpendicular case, it was pointed out in the previous chapter that all crossings between modes become avoided crossings at oblique angles. This applies to the parallel MO crossing in Fig. 3.12

and also to any crossing appearing for higher values of E . If the MO crossing in (a) is replaced by an avoided crossing, the curves represent how the oblique M and O modes behave at near-parallel propagation before reconnecting and thus crossing at exactly parallel propagation. This recovers Fig. 4.37 in Gurnett and Bhattacharjee (2005).

To conclude this section, we discuss the well-known Faraday rotation (Bittencourt, 2004; Gurnett and Bhattacharjee, 2005; Thorne and Blandford, 2017; Keppens and Goedbloed, 2019b) in the cold and warm Appleton-Hartree equations. This effect occurs when we take a superposition of the electromagnetic O and X modes, with a frequency above the upper cutoff frequency ω_u , which is

$$\omega_u^2 = 1 + \frac{E^2}{2} + \frac{E}{2}\sqrt{E^2 + 4} \quad (3.37)$$

in both the cold and the warm Appleton-Hartree relation. Since the O and X modes have a different wave number for a given frequency, and thus a different phase speed, the resulting electric field of this wave will rotate as the wave propagates. This is usually discussed at parallel propagation, where the dispersion relation factorises as Eq. (3.35). In this equation, the last two factors correspond to the electromagnetic X and O modes, respectively.

The angular rotation rate ψ can be quantified using the index of refraction for both modes, denoted n_O and n_X , because ψ is proportional to Δn , $\psi \sim n_O - n_X$. At parallel propagation, it gives identical results for the cold (Keppens and Goedbloed, 2019b) and warm Appleton-Hartree relations, and is approximately

$$n_O - n_X \simeq \frac{E}{\bar{\omega}^3}. \quad (3.38)$$

Numerically, it can be evaluated at any angle and any frequency. Doing so for the warm Appleton-Hartree expression, the result is shown in Fig. 3.13(a). It looks almost identical to the general cold ion-electron case reported in Keppens and Goedbloed (2019b). The difference of this numerical evaluation of the warm and the cold Appleton-Hartree relation is shown in Fig. 3.13(b). As pointed out earlier, there is no difference at parallel propagation. The largest deviation between the cold and warm Appleton-Hartree expression occurs near perpendicular propagation. Even there, the difference is negligible though. Therefore, we conclude that the warm Appleton-Hartree relation derived above does not offer any significant advantage over its cold equivalent with respect to Faraday rotation.

3.3 Laser-induced Cherenkov radiation

Cherenkov radiation is a phenomenon that can occur whenever a charged particle travels through a medium with a refractive index n larger than 1.

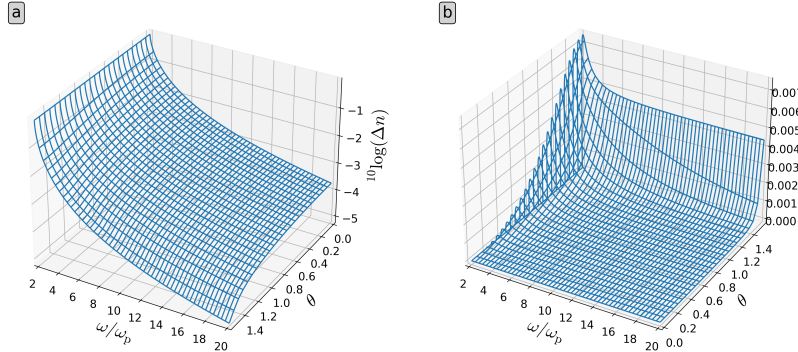


FIGURE 3.13: (a) The Faraday rotation angle ψ present in the warm Appleton-Hartree equation is quantified using $\psi \sim \Delta n = n_O - n_X$. (b) The influence of the warm extension to the Appleton-Hartree relation on the Faraday rotation angle ψ is quantified as the difference of the logarithms of the rotation angles, $\log(n_O - n_X)_{\text{warm}} - \log(n_O - n_X)_{\text{cold}}$. For both panels parameter values were set to $E = 1.5$ and $v = 0.1$. Note that the θ -axis is differently oriented for panels (a) and (b).

However, it can also occur for photon bunches propagating in a plasma, as verified experimentally by (Yugami et al., 2002). As an application of the two-fluid description of a warm, ion-electron plasma, in this section we consider a laser pulse exciting a plasma wave in a warm, homogeneous ion-electron plasma at rest, as described by (Yoshii et al., 1997; Muggli et al., 1999). The laser beam propagates perpendicular to the background magnetic field \mathbf{B} , say $\mathbf{B} = B \hat{\mathbf{e}}_3$ and $\mathbf{k}_{\text{laser}} = k_{\text{laser}} \hat{\mathbf{e}}_1$, as shown in Fig. 3.14(a). In the SAFMOX labelling scheme, the laser beam interacts with the M mode. As we will show, the laser-pulsed Cherenkov emission in a warm plasma is restricted to a cone around the laser pulse, contrary to the cold plasma case, where radiation can theoretically be emitted at any forward angle.

In this setup, the phase speed of the laser pulse, which is approximately the light speed c , can exceed the M mode's phase speed. When this occurs, the laser and the M mode will couple through the emission of Cherenkov radiation (CR). For a first consideration, we limit ourselves to emission perpendicular to the magnetic field (i.e. in the xy -plane). In this case, only 4 modes (F, M, O, and X) are left from the full sextet since slow and Alfvén branches do not propagate perpendicular to \mathbf{B} . This case is illustrated in Fig. 3.14(b), where the dashed orange $\omega = ck$ line exceeds the purple M mode line for larger values of k . The angle θ_{CR} in the xy -plane with respect to the laser beam at which

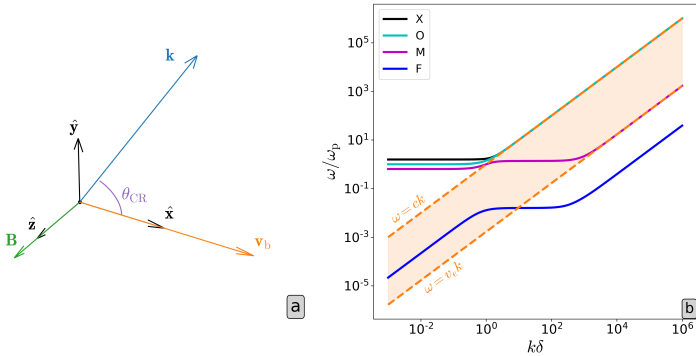


FIGURE 3.14: (a) The laser beam propagates with velocity \mathbf{v}_b perpendicular to the magnetic field \mathbf{B} . The Cherenkov radiation with propagation vector \mathbf{k} is emitted at an angle θ_{CR} with respect to the laser beam. (b) Ion-electron dispersion diagram of perpendicular propagation for typical magnetosphere parameters ($\mu = 1/1836$, $E = 0.935$, $v = 1.68 \times 10^{-3}$, $w = 3.92 \times 10^{-5}$, from (Goedbloed et al., 2019)). The orange area visualises all angles at which the laser can couple to the M mode through the relation $\omega = (v_b \cos \theta_{\text{CR}})k$.

this radiation is emitted, depends on the refractive index $n_M(\omega) = ck_M(\omega)/\omega$ as

$$\cos \theta_{\text{CR}} = \frac{1}{\beta_{\text{ph}} n_M(\omega)}, \quad (3.39)$$

where $\beta_{\text{ph}} = v_{\text{ph}}/c \simeq 1$ is the normalised phase speed of the laser beam (Buts et al., 2006). As can be seen in Eq. (3.39), the emission angle depends on the frequency, and thus different frequencies are emitted at different angles.

In a cold plasma the M mode's frequency at perpendicular propagation is confined to the interval between the lower cutoff frequency

$$\omega_l = \left[1 + \frac{1}{2}(E^2 + I^2) - \frac{1}{2}|E - I|\sqrt{(E + I)^2 + 4} \right]^{1/2} \omega_p, \quad (3.40)$$

and the upper hybrid frequency

$$\omega_{\text{UH}} = \left[\frac{1}{2} \left(1 + E^2 + I^2 + \sqrt{(1 + E^2 + I^2)^2 - 4EI(1 + EI)} \right) \right]^{1/2} \omega_p, \quad (3.41)$$

for all wave numbers. Since the wave number can take any positive value, the refractive index $n_M = ck/\omega_M(k)$ can then also take any positive value and thus radiation can be emitted at all angles ($0 \leq \theta_{\text{CR}} \leq \pi/2$), with the angle

depending on the emitted frequency (Yoshii et al., 1997; Muggli et al., 1999). Although in a warm plasma the M mode is still bounded from below by the lower cutoff frequency, neither the wave number nor the M mode frequency are bounded from above because the frequency ω_M is always larger than $v_e k$, with the M mode behaving as $\bar{\omega} \simeq v \bar{k}$ in the short wavelength limit ($k \rightarrow \infty$), i.e. like an electron ‘sound’ wave. This is shown in Fig. 3.14(b) by the lower bound of the orange area. Hence, the refractive index has an asymptotic upper bound of $n_M = 1/v$. Consequently, radiation can no longer be emitted at all angles because the angle is bounded by $\cos \theta_{CR} \simeq 1/n_M = \bar{\omega}_M/\bar{k} \geq v\bar{k}/\bar{k} = v$ (assuming $\beta_{ph} \simeq 1$). Concurrently, the emitted frequency would go to infinity as the emission angle approaches $\theta_{CR} = \arccos v$. Hence, the emission is limited to a 2D cone around the laser beam with angle $\arccos v$ in the \mathbf{B} -perpendicular plane. For Earth’s magnetosphere values, the emission cone is nearly all-encompassing with an angle of 89.9° whilst for a typical tokamak with electron thermal speed $v_e = 5.5 \times 10^7$ m/s (Goedbloed et al., 2019), the angle narrows slightly to 79.4° . Even for a relativistically hot plasma that reached its maximal sound speed limit ($v^2 \simeq 0.3$), the cone angle is still as large as 56.8° . In general, the lowest frequency (defined by $n_M = 1$) is emitted parallel to the laser beam whereas all higher frequencies ($n_M > 1$) are emitted at an oblique angle between zero and $\arccos v$.

Of course, the case to which we limited ourselves, propagation perpendicular to the magnetic field, differs significantly from oblique propagation due to the presence of avoided crossings at such angles. However, the M mode also behaves as $\omega \simeq v_e k$ in the oblique short wavelength limit, such that θ_{CR} is still limited by the electron thermal velocity v_e . Hence, Cherenkov radiation is limited to a 3D cone around the laser beam with angle $\arccos v$. It should be noted, however, that most radiation is expected to be emitted at or near the plasma frequency because the group speed is largest there, and consequently propagates (nearly) parallel to the laser beam, since $\theta_{CR}(\omega_p) = 0$.

3.4 Relation to other plasma models

The study of waves in two-fluid descriptions of ion-electron plasmas is discussed in many textbooks (e.g. Stix, 1992; Boyd and Sanderson, 2003; Gurnett and Bhattacharjee, 2005; Thorne and Blandford, 2017), but is nowhere found to be as complete in its wave categorisations as our current, general ion-electron discussion. In (up to recent) literature (Stringer, 1963; Hameiri et al., 2005; Ishida et al., 2005; Damiano et al., 2009; Bellan, 2012; Zhao, 2015, 2017), approximate results are obtained or presented for special limits, like dispersion relations focusing only on high- versus low-frequency modes. With this general two-fluid framework, parallels can be drawn to some of these results in the literature and how they are retrieved or altered using our polynomial ion-electron

approach. To this end, all bars on the frequency and wave number are made explicit again for ease of comparison to published results.

3.4.1 Kinetic theory

In all textbooks on plasma physics and the literature, the two-fluid formalism is often used as a stepping stone for the much more involved treatment offered by kinetic theory (Gurnett and Bhattacharjee, 2005; Thorne and Blandford, 2017). Although it is well-known that some intricacies are inevitably lost in a fluid treatment, e.g. Landau damping, a comparison between analytic results from either approach can be meaningful to understand the possibilities and limits of the ion-electron description. Using Gurnett and Bhattacharjee (2005) as guidance, a couple of results are compared here.

Hot unmagnetised plasma

The ion-electron analysis of waves in a hot unmagnetised plasma was presented in Sec. 2.1.3. All modes split with the exception of the F and M modes. Assuming $c_s \simeq w$ and taking the immobile ion approximation where $w = 0$, the quadratic branch describing these modes, given generally by

$$\bar{\omega}^4 - \bar{\omega}^2 [1 + \bar{k}^2(v^2 + w^2)] + \bar{k}^2(c_s^2 + \bar{k}^2v^2w^2) = 0, \quad (3.42)$$

splits into a trivial mode (F mode) and $\omega^2 = \omega_p^2 + v_e^2k^2$, the M mode or Langmuir wave. Whilst already present in a two-fluid model, kinetic theory contains information that is lacking in the ion-electron description. In kinetic theory, the Langmuir dispersion relation using a Maxwellian distribution for the thermal velocity gives (Gurnett and Bhattacharjee, 2005)

$$\omega^2 = \omega_p^2 + 3 \left(\frac{p_e}{n_e m_e} \right) k^2. \quad (3.43)$$

From our definition of v_e , i.e. $v_e^2 = \gamma_e p_e / n_e m_e$, this implies that $\gamma_e = 3$. This means that the electrons influenced by the Langmuir wave move with only one degree of freedom, which is not apparent from the ion-electron description. That this information only arises naturally in kinetic theory, and not in the ion-electron model, has been pointed out before in Gurnett and Bhattacharjee (2005) using a less complete two-fluid approach.

Secondly, the kinetic literature regularly derives the phase speed of ion acoustic waves, which must relate to our F mode. Here, we show how to obtain this expression from the ion-electron model for any ion species. Under the assumption that $w^2 \ll \bar{\omega}^2/\bar{k}^2 \ll v^2$, the quadratic branch (3.42) divided by \bar{k}^4 reduces to

$$\frac{\bar{\omega}^2}{\bar{k}^2} = \frac{c_s^2}{1 + \bar{k}^2v^2} \quad (3.44)$$

after discarding the terms $\bar{\omega}^4/\bar{k}^4$, $-w^2\bar{\omega}^2/\bar{k}^2$, and v^2w^2 . If it is assumed that $ZT_e \gg T_i$ and $\mu \ll 1$, this result can be reformulated as

$$\frac{\omega^2}{k^2} = \frac{\mu v_e^2}{1 + k^2 v_e^2 / \omega_{pe}^2} = \frac{\mu v_e^2}{1 + k^2 \lambda_{De}^2} \quad (3.45)$$

where λ_{De} signifies the electron Debye length. This agrees with the result (8.4.24) of Gurnett and Bhattacharjee (2005) where they use Maxwellian distributions for ions and electrons and consider the case $n_e = n_i$, which implies $Z = 1$ through charge neutrality. In that sense this result is more general, since it holds for any value of Z .

Magnetised plasma

At parallel propagation more known results from kinetic theory can be recovered in the ion-electron formalism. Consider once more the parallel quartic branch, which can be factored as was done in Eq. (2.28) (although we repeat here that this manner of writing the results mixes forward and backward wave pairs and is to be disfavored). These two factors can be reordered as

$$1 - \frac{c^2 k^2}{\omega^2} - \frac{\omega_{pe}^2}{\omega(\omega + E)} - \frac{\omega_{pi}^2}{\omega(\omega - I)} = 0 \quad (3.46)$$

$$\text{and } 1 - \frac{c^2 k^2}{\omega^2} - \frac{\omega_{pe}^2}{\omega(\omega - E)} - \frac{\omega_{pi}^2}{\omega(\omega + I)} = 0, \quad (3.47)$$

which is how they appear in the kinetic theory literature (Gurnett and Bhattacharjee, 2005).¹ The first factor then describes the left-hand polarised waves whilst the second one describes the right-hand polarised waves.

The polarisation properties of the various waves, as well as their electromagnetic versus electrostatic wave character, are invariably related to either purely parallel or purely perpendicular properties. In Keppens et al. (2019), it was already discussed that the SAFMOX labelling scheme necessarily abandons such terminology, since the waves simply show varying characteristics at small, intermediate, and large wavelengths. This relates to a discussion of the eigenfunctions, in addition to the eigenfrequencies, which is left to future research.

3.4.2 Low-frequency waves

In 1963, a dispersion relation for the low-frequency modes (S, A, and F) was derived in Stringer (1963) using an HMHD model, which was later recovered in

¹Note that in the literature the cyclotron frequencies are sometimes defined including the charge sign such that the electron cyclotron frequency is $-\Omega_e$ rather than the Ω_e used here.

TABLE 3.1: Terms contributing to dispersion relation (3.48) are highlighted in red.

	1	\bar{k}^2	\bar{k}^4	\bar{k}^6	\bar{k}^8
$\bar{\omega}^{12}$	α_{60}				
$\bar{\omega}^{10}$	α_{50}	α_{51}			
$\bar{\omega}^8$	α_{40}	α_{41}	α_{42}		
$\bar{\omega}^6$	α_{30}	α_{31}	α_{32}	α_{33}	
$\bar{\omega}^4$		α_{21}	α_{22}	α_{23}	α_{24}
$\bar{\omega}^2$			α_{12}	α_{13}	α_{14}
1				α_{03}	α_{04}

Bellan (2012). More recently, an ideal ion-electron model was used by Zhao et al. (2014) to correct this HMHD equation. As a description of the low-frequency S, A, and F waves, this equation should be obtainable from our general dispersion relation (2.10) as an extension of the global, low-frequency MHD limit. In order to verify this, Eq. (A17) in Zhao et al. (2014) can be rewritten with our conventions and notation as

$$\begin{aligned}
0 = & (1 + \mu)^3 \times \left\{ \bar{\omega}^6 (1 + \bar{k})^2 \right. \\
& - \bar{\omega}^4 \bar{k}^2 [\bar{k}^4 c_s^2 + \bar{k}^2 (EI + 2c_s^2 + \lambda^2(E^2 + I^2 - EI)) + (1 + \lambda^2)EI + c_s^2] \\
& \left. + \bar{\omega}^2 \bar{k}^4 \lambda^2 [\bar{k}^2 c_s^2 (E^2 + I^2) + EI(EI + 2c_s^2)] - \lambda^4 \bar{k}^6 E^2 I^2 c_s^2 \right\},
\end{aligned} \tag{3.48}$$

using $Z = 1$ and the non-relativistic Alfvén speed expression $v_a^2/c^2 \simeq EI$. From this equation the contributing terms in our much more general dispersion relation can be identified by counting powers of $\bar{\omega}^2$ and \bar{k}^2 . The contributing terms are shown schematically in Table 3.1. Comparing α_{03} to its equivalent in Eq. (3.48) reaffirms that a non-relativistic expression should be used for the Alfvén speed in Zhao et al. (2014). It is to be noted that this is already an important drawback of the reduced dispersion relation (3.48), as our original equation was shown to be fully compatible with the relativistic expressions of the slow, Alfvén, and fast speeds.

To go from the coefficients α_{mn} to the corresponding coefficients in Eq. (3.48), which we will call $\tilde{\alpha}_{mn}$, some further approximations are necessary (and an overall change of sign). First of all, note that $v_a^2/c^2 \simeq EI$ implies that E and $I = \mu E$ are both $\mathcal{O}(c^{-1})$. Furthermore, c_s , v , and w are also $\mathcal{O}(c^{-1})$. To go from α_{mn} to $\tilde{\alpha}_{mn}$ can now be summarised as keeping only the terms of order $\mathcal{O}(c^{2(m-3)})$. This eliminates all α_{mn} with $m \geq 4$ as well as α_{33} , α_{24} , α_{14} , and α_{04} . For the remaining α_{mn} , the highest order terms in c are $\mathcal{O}(c^{2(m-3)})$. Effectively, this reduction gives the MHD limit extended with correction terms coming from the higher diagonals in Table 3.1. Performing this reduction, we

indeed recover Eq. (3.48) rather than the expressions in Stringer (1963) and Bellan (2012). As pointed out in Zhao et al. (2014), this is due to the absence of some $\mathcal{O}(\mu)$ terms in Stringer (1963) and Bellan (2012).

Whilst this is a meaningful reduction for non-relativistic regimes, there seems to be no obvious reason not to use the general dispersion relation for all 6 wave pairs in all regimes (unmagnetised to superstrongly magnetised, cold to warm), although an interest in the purely non-relativistic, low-frequency MHD waves for all wavelengths could use Eq. (3.48).

3.4.3 Hall-magnetohydrodynamics

The dispersion relation of (non-relativistic) HMHD reported on by Hameiri et al. (2005) can also be recovered from the ion-electron dispersion relation. Rewriting their expression somewhat and using our conventions it becomes

$$\begin{aligned} \left(\frac{\omega}{k}\right)^6 - \left(\frac{\omega}{k}\right)^4 [(1 + \lambda^2)EIc^2 + v_s^2 + \lambda_H \lambda^2 EIc^2] \\ + \lambda^2 EIc^2 \left(\frac{\omega}{k}\right)^2 [EIc^2 + 2v_s^2 + \lambda_H v_s^2] - \lambda^4 E^2 I^2 c^4 v_s^2 = 0. \end{aligned} \quad (3.49)$$

Here, the Hall parameter λ_H is proportional to \bar{k}^2 as $\lambda_H = \bar{k}^2/\mu$. Since $\lambda_H \sim k^2$, the prefactors of the Hall terms should be contained in α_{22} and α_{13} . Indeed, multiplying the general dispersion relation (2.10) by c^6/\bar{k}^6 and taking the non-relativistic limit $c \rightarrow \infty$ and the $\mu = 0$ limit results without any further approximation in the non-relativistic Hall dispersion relation (3.49).

3.5 Discussion

Since whistler waves were originally observed as travelling parallel to the magnetic field, most plasma physics textbooks focus on approximating this behaviour at parallel propagation, discarding ion terms. However, more recent observations proved the existence of whistler waves at oblique angles (Cattell et al., 2008; Yoon et al., 2014; Artemyev et al., 2016; Ma et al., 2017). Using the ion-electron formalism, we showed that the parallel textbook approximations can be meaningfully extended to oblique angles. In the SAFMOX labelling scheme, the “classical” descending frequency whistler occurs in the F mode for Earth’s magnetosphere conditions, both at parallel and oblique propagation. The ascending frequency and ion cyclotron whistlers, occurring in the F and A modes respectively at parallel propagation under Earth’s magnetosphere conditions, are affected by the introduction of avoided crossings at oblique angles. The location of these avoided crossings in whistling regions effectively splits whistling behaviour across two modes at oblique angles. At perpendicular

propagation, it turned out that the remaining F mode also features small scale ascending frequency whistling behaviour. Furthermore, the high-frequency M, O, and X modes also show whistler-like behaviour at all angles, albeit near their cutoffs, which lie outside of the audible frequency range.

Due to the avoided crossings, the whistling behaviour across all modes depends strongly on the parameters. Whilst the analysis in this chapter is representative of Earth's magnetosphere, it will already be different for other objects in our solar system, like Jupiter's magnetosphere. Modelling Jupiter as a magnetic dipole with a dipole moment of $1.584 \times 10^{20} \text{ T m}^3$ (Milone and Wilson, 2014), neglecting its offset for simplicity, and using the ingress peak electron density from Hinson et al. (1997) results in an electron cyclotron frequency of $E \simeq 5$ for a proton-electron plasma, which describes a different regime than Earth's magnetosphere ($E < 1$). Entirely different setups such as pair plasmas in pulsar magnetospheres are very distinct as well. In such a pair plasma there are no classical descending frequency whistlers at parallel propagation, but these plasmas do have modes with ascending frequency whistling behaviour at parallel propagation. At oblique angles, they even show a wide variety of whistling behaviour across all modes.

Additionally, the damping-free Appleton-Hartree equation was extended to incorporate the effect of a non-zero thermal electron velocity. Although this extension does not improve much upon the approximations of the F, O, and X modes, it does introduce an improved description of the M mode, related to the textbook Langmuir wave, capturing its unique high-frequency $\bar{\omega}^2 \simeq \bar{k}^2 v^2$ behaviour. The polynomial form is more involved than for the cold case and consequently, explicit expressions of the refractive index, although possible, are not very insightful.

Whilst the employed ion-electron treatment is complete, all intricacies of damping effects (Bell et al., 2002; Ma et al., 2017; Hsieh and Omura, 2018) are inherently absent, although collisional damping, which may be strong for whistler waves (Crabtree et al., 2012), could be included in the future. Hence, the ion-electron approach could be applied to include collisional damping in the whistler description or the warm Appleton-Hartree equation, as is done in Bawa'aneh et al. (2013), but studying the effects of Landau or cyclotron damping on whistler waves requires a different framework.

In a third application, it was shown that for a warm ion-electron plasma the angle at which laser-induced Cherenkov radiation is emitted (with respect to the laser beam) is limited to a cone by the electron thermal velocity (and thus temperature) of the plasma, for a laser beam propagating perpendicular to the applied magnetic field. This is not the case in a cold plasma description, where Cherenkov radiation can be emitted at all forward angles. Despite this difference, it should be noted that most radiation is emitted at or near the plasma frequency because the group speed is largest there, and consequently

propagates (nearly) parallel to the laser beam, since $\theta_{\text{CR}}(\omega_p) = 0$.

Finally, this complete ion-electron treatment was applied to recover a couple of results from the literature. Even though any ideal ion-electron methodology is unable to derive any damping effects, a selection of results from kinetic theory could also be retrieved. Additionally, in the future one could also include collisional damping to compare the ion-electron and the kinetic dispersion relations in more detail.

We're no strangers to failure. What makes this the City of Progress is that we keep trying until we get it right.

— Jayce Talis, in *Arcane* S1 E8
(Fortiche & Riot Games)

4

Hall-magnetohydrodynamic spectroscopy

The contents of this chapter were published in De Jonghe et al. (2022). J. De Jonghe performed the calculations, implementation, validation of the results, and wrote the manuscript. N. Claes and R. Keppens contributed to the discussions in and revision of the manuscript.

One rung down in the plasma model hierarchy from the ion-electron model is the Hall-magnetohydrodynamics model. As a single-fluid model, it focuses on the movement of the ions. Contrary to regular magnetohydrodynamics though, HMHD does not neglect the electron mass (and inertia, if desired).

In this chapter we explore a spectroscopic approach to HMHD. Here, the term *spectroscopy* refers to the quantification of all possible waves in a particular plasma configuration. To achieve this goal for the MHD model, we developed the spectroscopic code *Legolas* (Claes et al., 2020, see <https://legolas.science>). This code allows for computation of all linear eigenmodes and their eigenfunctions, for one-dimensionally (1D) stratified plasmas in a wide range of settings. Such non-homogeneous three-dimensional plasma states with 1D variation are very common, e.g. in plane-parallel, gravitationally stratified atmospheres, or in cylindrical setups for Taylor-Couette experiments, or in magnetic flux tubes or loops in the solar atmosphere. Spectroscopy is useful to determine the complete stability properties of a given force-balanced equilibrium state, and quantifies how this (in)stability is influenced by specific equilibrium ingredients, such as the magnetic pitch, or the presence of non-trivial background flows. In the original release (Claes et al., 2020, summarised in Sec. 4.1), the

linearised set of compressible MHD equations included the (possibly combined) effects of flow, external gravity, resistivity, anisotropic thermal conduction, and radiative cooling. The code was tested and validated against a wide variety of theoretically known plasma stability results, e.g. those from modern plasma physics textbooks focusing on MHD spectroscopy (Goedbloed et al., 2019).

Ideal MHD stability aspects have been studied extensively in the plasma physics literature, in various applications. For fusion devices such as tokamaks, a solid understanding of instabilities is required to create MHD-stable operation conditions, whilst in solar physics both stable wave modes and instabilities are of interest to understand the observed periodicities, or the evolution of initially stable coronal loops towards destructive events such as coronal mass ejections (CMEs). The non-adiabatic effects already included in Claes et al. (2020) allow for investigating radiatively driven processes such as solar coronal rain or prominence formation. Non-ideal effects like resistivity are known to introduce new paths to instability: the well-known resistive tearing instability (Furth et al., 1963) has been the subject of many studies and received renewed interest due to the role it plays in triggering magnetic reconnection events. However, physical effects that were previously omitted in *Legolas*, in particular viscosity and the Hall current, may influence growth rates or modify stability properties in a significant way.

For resistive tearing and the resulting reconnection in particular, non-linear simulations have shown that the rates at which magnetic field lines reconnect (and convert magnetic energy into kinetic or thermal energy in the process) can become much higher than resistivity can account for on its own (see e.g. the review by Yamada et al., 2010). Both viscosity and Hall effects are candidates for modifying the growth rate of the resistive tearing instability. In fact, it has been known for quite some time that viscosity can act as a stabilising mechanism (Coppi et al., 1966; Loureiro et al., 2013; Tenerani et al., 2015) whilst the Hall current may introduce destabilising effects, resulting in faster reconnection rates (Terashawa, 1983; Pucci et al., 2017). Similarly, exploration of the relationship between resistivity and viscosity on tearing by Dahlburg et al. (1983) revealed more intricacies of the growth rate as a function of the resistivity and viscosity. More recent work has focused on evaluating the influence of the Hall effect on the tearing instability in current sheets (Shi et al., 2020). In Sec. 4.2 we document the extension of *Legolas* with the Hall terms, and benchmark our MHD spectroscopy tool on these and some other published results. At the same time, we show how we can easily extend published findings with full spectral knowledge, or with quantifications of how incompressible and compressible regimes differ. The viscosity module is presented in the next chapter.

4.1 Magnetohydrodynamic spectroscopy with the *Legolas* code

The goal of the *Legolas* code is quite straightforward. It aims to quantify all waves resulting from the perturbation of a one-dimensional (1D), mechanical¹ equilibrium in Cartesian or cylindrical geometries. Thereto we consider the equilibrium quantities density ρ , velocity \mathbf{v} , temperature T , and magnetic field \mathbf{B} of the form

$$\begin{aligned} \rho_0 &= \rho_0(u_1), & \mathbf{v}_0 &= v_{02}(u_1) \hat{\mathbf{e}}_2 + v_{03}(u_1) \hat{\mathbf{e}}_3, \\ T_0 &= T_0(u_1), & \mathbf{B}_0 &= B_{02}(u_1) \hat{\mathbf{e}}_2 + B_{03}(u_1) \hat{\mathbf{e}}_3, \end{aligned} \quad (4.1)$$

where in Cartesian coordinates u_1 is the x -coordinate, and $\hat{\mathbf{e}}_2$ and $\hat{\mathbf{e}}_3$ are the unit vectors in the then invariant y - and z -direction, respectively. In cylindrical coordinates, u_1 is the radial coordinate, $\hat{\mathbf{e}}_2$ is then a unit vector in the angular direction, and $\hat{\mathbf{e}}_3$ is aligned along the cylinder axis. The dependence of the background equilibrium state on the u_1 -coordinate is considered on a bounded domain (e.g. a slab of a plane-parallel atmosphere of a given vertical extent, or a flux tube of given radius), whilst the other coordinates are unrestricted (but the u_2 -coordinate is periodic in the cylindrical case). Here, the 0 subscript indicates equilibrium quantities.

Next, the full set of compressible MHD equations, which consists of a continuity, momentum, energy, and induction equation, is perturbed around this equilibrium. The MHD equations, including non-ideal effects, are

$$\frac{\partial \rho}{\partial t} = -\nabla \cdot (\rho \mathbf{v}), \quad (4.2)$$

$$\rho \frac{\partial \mathbf{v}}{\partial t} = -\nabla p - \rho \mathbf{v} \cdot \nabla \mathbf{v} + \mathbf{J} \times \mathbf{B} + \rho \mathbf{g}, \quad (4.3)$$

$$\begin{aligned} \rho \frac{\partial T}{\partial t} &= -\rho \mathbf{v} \cdot \nabla T - (\gamma - 1)p \nabla \cdot \mathbf{v} - (\gamma - 1)\rho \mathcal{L} \\ &\quad + (\gamma - 1)\nabla \cdot (\boldsymbol{\kappa} \cdot \nabla T) + (\gamma - 1)\eta \mathbf{J}^2, \end{aligned} \quad (4.4)$$

$$\frac{\partial \mathbf{B}}{\partial t} = \nabla \times (\mathbf{v} \times \mathbf{B}) - \nabla \times (\eta \mathbf{J}), \quad (4.5)$$

with $p = \rho T$ pressure and $\mathbf{J} = \nabla \times \mathbf{B}$ the current density. We adopt a suitable dimensionalisation, so dimensional factors like the gas constant or the permeability of vacuum no longer appear. The adiabatic index is denoted by γ , and taken equal to 5/3 usually. Additionally, \mathbf{g} is the (external) gravitational

¹If thermal conduction is included, the equilibrium is also checked for thermal balance.

acceleration, \mathcal{L} the heat loss function, defined as energy losses (optically thin radiation) minus energy gains (e.g. heating), κ the thermal conduction tensor, and η the resistivity. Later on, we will add the HMHD terms in Sec. 4.2 and viscosity in Sec. 5.2.

This introduces the perturbations $(\rho_1, \mathbf{v}_1, T_1, \mathbf{B}_1)$, which in principle are fully three-dimensionally structured, time-dependent functions. However, rather than working with \mathbf{B}_1 we adopt a vector potential \mathbf{A}_1 to describe the perturbed magnetic field as $\mathbf{B}_1 = \nabla \times \mathbf{A}_1$. Subsequently, after linearising the resulting equations, a 3D Fourier analysis is applied to all perturbed quantities $(\rho_1, \mathbf{v}_1, T_1, \mathbf{A}_1)$ as

$$f_1(\mathbf{r}, t) = \hat{f}_1(u_1) \exp[i(k_2 u_2 + k_3 u_3 - \omega t)], \quad (4.6)$$

introducing the wave vector $\mathbf{k} = k_2 \hat{\mathbf{e}}_2 + k_3 \hat{\mathbf{e}}_3$ and the frequency ω (note that in the cylindrical case, k_2 is an integer usually denoted by m , enforcing annular periodicity). In essence, this reduces the problem to a generalised eigenvalue problem²

$$\mathbf{Ax} = \omega \mathbf{Bx} \quad (4.7)$$

for matrices \mathbf{A} and \mathbf{B} , and the state vector $\mathbf{x} = (\rho_1, \mathbf{v}_1, T_1, \mathbf{A}_1)^\top$. Subsequently, it is transformed using a finite element method (FEM), where the domain is discretised using a specified number of grid points N and linear combinations of basis functions are used to approximate all perturbed quantities $\hat{f}_1(u_1)$ in every subinterval. Note that this discretisation and the subsequent construction of the matrices \mathbf{A} and \mathbf{B} means that the number of output eigenmodes is directly related to the number of grid points N (for more information, see Claes et al., 2020). The resulting eigenproblem is passed to a user-specified solver from the *LAPACK* (Anderson et al., 1999) or *ARPACK* library (Lehoucq et al., 1998). Whilst *Legolas* supports a variety of solvers, all runs in this thesis were performed with the *QR-invert* option, detailed in App. C.2, unless specified otherwise. The linearised equations of the eigenvalue problem itself are given in App. C.1 (including the Hall and viscous terms, introduced in Secs. 4.2 and 5.2, respectively). The *Legolas* code then returns couples of eigenvalues ω and state vectors $\mathbf{x} = (\rho_1, \mathbf{v}_1, T_1, \mathbf{A}_1)^\top$, each of which describes a fundamental linear wave of the system. Any system may have both discrete and continuous solutions, such that all of these eigenmodes in the spectrum either belong to a continuum, or correspond to a discrete solution or overtone thereof (see e.g. Goedbloed et al., 2019).

For the boundaries in the u_1 -direction we consider perfectly conducting walls, i.e.

$$\mathbf{B} \cdot \hat{\mathbf{e}}_1 = 0, \quad \mathbf{v} \cdot \hat{\mathbf{e}}_1 = 0 \quad (4.8)$$

²Note that ω and \mathbf{x} are an eigenvalue-eigenvector pair of $\mathbf{B}^{-1} \mathbf{A}$. Hence, this generalised eigenvalue problem can be solved by solving $(\mathbf{B}^{-1} \mathbf{A})\mathbf{x} = \omega \mathbf{x}$.

at the edges ($\hat{\mathbf{e}}_1$ is the normal to the wall). The choice of equilibrium above guarantees that the equilibrium fields automatically satisfy these boundary conditions. For the perturbed quantities, these boundary conditions become

$$v_1 = 0, \quad k_3 A_2 - k_2 A_3 = 0, \quad (4.9)$$

where v_1 is the first component of the velocity perturbation $\mathbf{v}_1 = (v_1, v_2, v_3)^\top$, and A_2 and A_3 denote components of the vector potential $\mathbf{A}_1 = (A_1, A_2, A_3)^\top$. However, instead of this second equation the more stringent condition $A_2 = A_3 = 0$ is imposed if both k_2 and k_3 are non-zero. If either wave vector component vanishes, only the corresponding \mathbf{A}_1 -component is set to zero, i.e. if $k_2 = 0$ ($k_3 = 0$), the constraint reduces to $k_3 A_2 = 0$ ($k_2 A_3 = 0$) and only A_2 (A_3) is set to zero.

4.2 Hall-magnetohydrodynamics

To go from MHD to HMHD, the induction equation (4.5), following from the Maxwell-Faraday equation

$$\frac{\partial \mathbf{B}}{\partial t} = -\nabla \times \mathbf{E}, \quad (4.10)$$

has to be extended to include the effects of the Hall current and the electron pressure. Additionally, electron inertia can be added as well. To do so, we express the electric field \mathbf{E} , using the (dimensionless) generalised Ohm's law, as

$$\mathbf{E} = -\mathbf{v} \times \mathbf{B} + \eta_{\text{H}} \mathbf{J} + \frac{\eta_{\text{H}}}{\rho} (\mathbf{J} \times \mathbf{B} - \nabla p_e) + \frac{\eta_e}{\rho} \frac{\partial \mathbf{J}}{\partial t}. \quad (4.11)$$

Here, p_e denotes the electron pressure and is related to p through the electron fraction f_e as $p_e = f_e p$, with $f_e = n_e/(n_e + n_p) = 1/2$ for a charge-neutral electron-proton plasma with electron and proton number densities n_e and n_p . Furthermore, η_{H} and η_e are the normalised Hall and electron inertia coefficients,

$$\eta_{\text{H}} = \frac{m_i}{e} \frac{V_R}{L_R B_R}, \quad \eta_e = \frac{m_e m_i}{e^2} \left(\frac{V_R}{L_R B_R} \right)^2, \quad (4.12)$$

respectively. Here, e denotes the elementary charge, and V_R , L_R , and B_R are the reference velocity, length, and magnetic field strength. Consequently, the electron inertia coefficient η_e is several orders of magnitude smaller than the Hall coefficient η_{H} . Therefore, the effect of electron inertia is often negligible. Hence, most results in the literature do not include it. Whilst this effect is implemented in *Legolas*, the reference tests that follow all set $\eta_e = 0$, except for one limit case. It should also be pointed out that any equilibrium of the

form (4.1) that satisfies the ideal MHD equilibrium conditions, also satisfies the HMHD equilibrium conditions (neglecting electron inertia) because the Hall term that is added to the right hand side of the induction equation (4.5), given by

$$\nabla \times \mathbf{E}_{\text{Hall},0} = \nabla \times \left[\frac{\eta_{\text{H}}}{\rho_0} (\mathbf{J}_0 \times \mathbf{B}_0 - \nabla p_{e0}) \right], \quad (4.13)$$

reduces to zero. For the first term this follows because \mathbf{B}_0 and \mathbf{J}_0 both lie in the $\hat{\mathbf{e}}_2\hat{\mathbf{e}}_3$ -plane, such that their vector product is proportional to $\hat{\mathbf{e}}_1$, and since they only depend on u_1 , this implies that $\nabla \times f(u_1) \hat{\mathbf{e}}_1 = 0$. For the second term we have

$$\nabla \times \left(\frac{\nabla p_{e0}}{\rho_0} \right) = \nabla \times \left[\nabla \left(\frac{p_{e0}}{\rho_0} \right) + \frac{p_e \nabla \rho_0}{\rho_0^2} \right] = \nabla \times \left(\frac{p_e \rho'_0}{\rho_0^2} \hat{\mathbf{e}}_1 \right). \quad (4.14)$$

Now the first term vanishes because it is the curl of a gradient, which is always zero, and the second term too because it is again of the form $\nabla \times f(u_1) \hat{\mathbf{e}}_1$. Note that whilst there are many similarities between the resistive and Hall terms, here they differ since the resistive term does not disappear in the induction equation (4.5) for an equilibrium of the form (4.1). As pointed out in Claes et al. (2020), the resistive term is neglected in the equilibrium equations by assuming that the timescales on which magnetic fields decay is much larger than the timescales of resistive modes.

The Hall and electron pressure terms in the induction equation are not implemented directly in *Legolas* as written in Eq. (4.11). Instead, $\mathbf{J} \times \mathbf{B}$ is substituted into this expression using the momentum equation (4.3) as done in e.g. Ahedo and Ramos (2009) because it is observed to be more numerically stable. The result is

$$\begin{aligned} \mathbf{E} = & -\mathbf{v} \times \mathbf{B} + \eta \mathbf{J} + \frac{\eta_e}{\rho} \frac{\partial \mathbf{J}}{\partial t} \\ & + \eta_{\text{H}} \left\{ \frac{\partial \mathbf{v}}{\partial t} + \mathbf{v} \cdot \nabla \mathbf{v} - \frac{\mu}{\rho} \left[\nabla^2 \mathbf{v} + \frac{1}{3} \nabla (\nabla \cdot \mathbf{v}) \right] - \mathbf{g} + \frac{\nabla p_i}{\rho} \right\}. \end{aligned} \quad (4.15)$$

This equation now features the ion pressure p_i instead, which is related to the total pressure as $p_i = (1 - f_e)p$. Note that this expression for the electric field now has two time derivatives in the right hand side, which will then enter the induction equation. Exploiting \mathbf{A}_1 instead of \mathbf{B}_1 , the linearised induction equation becomes $\partial \mathbf{A}_1 / \partial t = -\mathbf{E}_1$. Hence, we linearise Eq. (4.15), allowing for

a temperature-dependent Spitzer resistivity $\eta(T)$, which gives

$$\begin{aligned} \mathbf{E}_1 = & -\mathbf{v}_1 \times \mathbf{B}_0 - \mathbf{v}_0 \times (\nabla \times \mathbf{A}_1) + \eta_0 \nabla \times (\nabla \times \mathbf{A}_1) + \frac{d\eta}{dT} T_1 \nabla \times \mathbf{B}_0 \\ & + \eta_H \left\{ \frac{\partial \mathbf{v}_1}{\partial t} + \mathbf{v}_1 \cdot \nabla \mathbf{v}_0 + \mathbf{v}_0 \cdot \nabla \mathbf{v}_1 - \frac{\mu}{\rho_0} \left[\nabla^2 \mathbf{v}_1 + \frac{1}{3} \nabla (\nabla \cdot \mathbf{v}_1) \right] \right. \\ & \left. + \mu \frac{\rho_1}{\rho_0^2} \left[\nabla^2 \mathbf{v}_0 + \frac{1}{3} \nabla (\nabla \cdot \mathbf{v}_0) \right] + \frac{\nabla p_{i1}}{\rho_0} - \frac{\rho_1 \nabla p_{i0}}{\rho_0^2} \right\} \\ & + \frac{\eta_e}{\rho_0} \frac{\partial}{\partial t} [\nabla \times (\nabla \times \mathbf{A}_1)] - \eta_e \frac{\rho_1}{\rho_0^2} \frac{\partial}{\partial t} (\nabla \times \mathbf{B}_0). \end{aligned} \quad (4.16)$$

This expression can be simplified by observing that the term $\nabla p_{i1}/\rho_0$ can be written as

$$\frac{\nabla p_{i1}}{\rho_0} = \nabla \left(\frac{p_{i1}}{\rho_0} \right) + \frac{\nabla \rho_0}{\rho_0^2} p_{i1}. \quad (4.17)$$

Hence, this term is a pure gradient if ρ_0 is uniform. Since the electric field is only defined up to a gradient, we can redefine it as $\tilde{\mathbf{E}}_1 = \mathbf{E}_1 - \eta_H \nabla (p_{i1}/\rho_0)$ (with \mathbf{E}_1 expression (4.16)) such that after substituting Eq. (4.17) p_{i1} only appears in $\tilde{\mathbf{E}}_1$ in the term $\eta_H p_{i1} \nabla \rho_0 / \rho_0^2$, and thus only if ρ_0 is not uniform. The resulting induction equation $\partial \mathbf{A}_1 / \partial t = -\tilde{\mathbf{E}}_1$ is implemented in the *Legolas* code. Note that in the generalised eigenvalue problem (4.7) resulting from the Fourier analysis (4.6) the time derivatives in the Hall and electron inertia terms enter in the \mathbf{B} -matrix and break its former symmetry.

In the remainder of this chapter, we present a series of stringent test cases to validate our HMHD linear solver.

4.2.1 Homogeneous plasma slab

For the first test case we return to the dispersion relation of Hameiri et al. (2005) in Sec. 3.4.3, which in our current notation becomes

$$\begin{aligned} \left(\frac{\omega}{kv_{a0}} \right)^6 - \left(\frac{\omega}{kv_{a0}} \right)^4 \left[1 + \frac{\gamma T_0}{v_{a0}^2} + \cos^2 \theta \left(1 + \frac{(k\eta_H)^2}{\rho_0} \right) \right] \\ + \left(\frac{\omega}{kv_{a0}} \right)^2 \cos^2 \theta \left[1 + \frac{\gamma T_0}{v_{a0}^2} \left(2 + \frac{(k\eta_H)^2}{\rho_0} \right) \right] - \frac{\gamma T_0}{v_{a0}^2} \cos^4 \theta = 0. \end{aligned} \quad (4.18)$$

Here, $v_{a0} = |\mathbf{B}_0|/\sqrt{\mu_0 \rho_0}$ is the equilibrium Alfvén speed. This dispersion relation holds for an ideal, infinite, homogeneous plasma at rest. However, since we cannot consider an infinite plasma with *Legolas*, we consider a

homogeneous Cartesian plasma slab confined between two perfectly conducting walls (perpendicular to the x -axis). The equilibrium is given by

$$\rho_0 = 1, \quad T_0 = 1, \quad \mathbf{B}_0 = \hat{\mathbf{e}}_3, \quad (4.19)$$

and our normalisation is chosen such that $\eta_H = 1$. We want to quantify the HMHD eigenmodes of this slab, which we then compare to the analytical result of waves for an infinite homogeneous plasma, Eq. (4.18).

The inclusion of the Hall term introduces a length scale into the previously scale-independent MHD equations through the ion skin depth $d_i = \eta_H / \sqrt{\rho_0}$. This makes the HMHD waves dispersive, which is demonstrated in the dispersion relation by the appearance of the wave number in the Hall terms. To simulate an infinite medium, we need to ensure that the ratio of the equilibrium ion skin depth to the system size is sufficiently small. Hence, for the choice of $d_{i0} = 1$, we solve in the interval $x \in [0, 10^3]$. The exact choice of interval size is largely arbitrary, but it should be kept in mind that when we increase the interval size, we may also be forced to increase the resolution to ensure that *Legolas* picks up the Hall modes. This is due to the fact that the grid resolution can be directly linked to the dimensions of the \mathbf{A} and \mathbf{B} matrices in the eigenvalue problem Eq. (4.7), and thus also to the number of eigenvalues returned (Claes et al., 2020). Since the medium in *Legolas* is bounded in the x -direction, each solution of the dispersion relation (4.18) should approximate the first mode in a sequence in the spectrum, which can be verified by the number of nodes in the mode's corresponding eigenfunctions. For given angles θ fixing the wave vector $\mathbf{k} = \pi (\sin \theta \hat{\mathbf{e}}_2 + \cos \theta \hat{\mathbf{e}}_3)$, the first mode of each sequence is shown in Fig. 4.1(a) alongside the theoretical curves and a comparison to the ideal MHD dispersion relation. A full spectrum version is also shown in Fig. 4.1(b). Here, each vertical line represents a full (real) spectrum for a certain angle θ . As can be seen in Eq. (4.18), in the case of perpendicular propagation the dispersion relation is not influenced by the Hall parameter ($\cos \theta = 0$). There, the highest mode reduces to the regular fast MHD mode and the lower two modes (slow and Alfvén) vanish, also visible in Figs. 4.1(a,b). A single spectrum is shown for an angle $\theta \approx 0.564$ in Fig. 4.1(c) alongside the analytical infinite-medium solutions, each one corresponding to the start of a sequence, indicated by vertical lines. The sequences themselves, whose modes are much more tightly packed than in the ideal MHD sequences, are shown in the insets of Fig. 4.1(c). The smallest sequence displays anti-Sturmian behaviour, similar to the ideal MHD slow modes, whilst the two larger sequences behave in a Sturmian way, like the ideal MHD Alfvén and fast modes.

Furthermore, the (real) ρ_1 eigenfunctions of the first three modes in the smallest sequence of the $\theta \approx 1.007$ spectrum are given in Fig. 4.1(d). Contrary to the slow, Alfvén, and fast modes in ideal MHD, the density perturbation vanishes at the edges here. This behaviour is easily derived from the equations in App. C.1 for

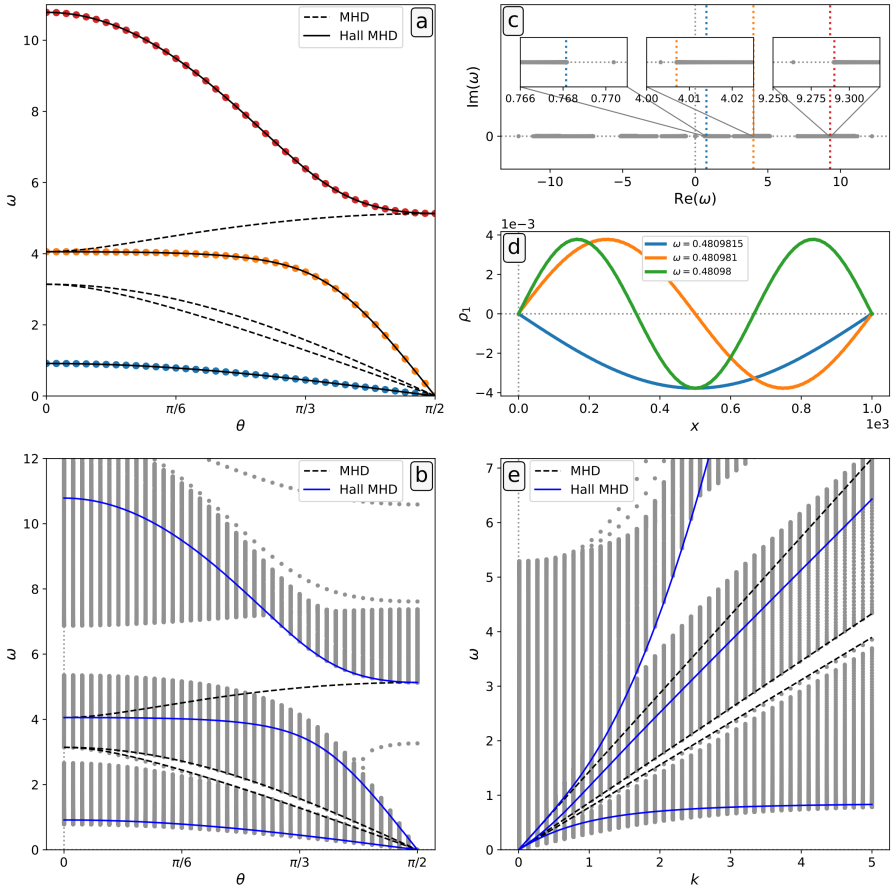


FIGURE 4.1: (a) Comparison of the first mode of each sequence (dots) to the theoretical Hall prediction by Hameiri et al. (2005) (solid lines) and ideal MHD (dashed lines) as a function of the angle θ between $\mathbf{k} = \pi(\sin \theta \hat{\mathbf{e}}_2 + \cos \theta \hat{\mathbf{e}}_3)$ and $\mathbf{B}_0 = \hat{\mathbf{e}}_3$ with $\rho_0 = 1$, $T_0 = 1$, $\eta_H = 1$, and $x \in [0, 10^3]$. (b) Comparison of the full spectrum to MHD and HMHD solutions for the setup from (a). (The isolated branches are unresolved modes.) (c) Spectrum for an angle $\theta \approx 0.564$ with the three (positive) solutions of the dispersion relation (4.18) as vertical (dotted) lines. (d) ρ_1 eigenfunctions of the first three modes of the smallest solution sequence for $\theta \approx 1.007$. (e) Comparison of the full spectrum to ideal and HMHD predictions for varying wave number for $\mathbf{k} = k(\hat{\mathbf{e}}_2/2 + \sqrt{3}\hat{\mathbf{e}}_3/2)$, $\mathbf{B}_0 = \hat{\mathbf{e}}_3$, $\rho_0 = 1$, $T_0 = 1$, $\eta_H = 1$, and $x \in [0, 10^3]$.

the adiabatic homogeneous setup considered here. Neglecting equilibrium flow, resistivity, and viscosity, and applying the perfectly conducting wall boundary

conditions $\tilde{v}_1 = \tilde{a}_2 = \tilde{a}_3 = 0$ (with the tildes indicating the transformed variables C.2) reduces the second and third components of the induction equation (C.10) and (C.11) to $\tilde{v}_2 = 0$ and $\tilde{v}_3 = 0$, respectively, for non-zero frequency. Since these equations vanish altogether for an adiabatic homogeneous setup in ideal MHD, these emerging no slip boundary conditions are naturally imposed by the Hall current. Using these newfound conditions alongside the others in the continuity equation (C.4), the third component of the momentum equation (C.7), and the energy equation (C.8) reduces these equations to $\omega\tilde{\rho}_1 = -\rho_0\tilde{v}'_1$, $k_3(\tilde{\rho}_1T_0 + \rho_0\tilde{T}_1) = 0$, and $\omega\tilde{T}_1 = -(\gamma - 1)T_0\tilde{v}'_1$, respectively, where we also used that $B_{02} = 0$ in our reference frame.³ Combining all three implies that $\tilde{\rho}_1 = \tilde{T}_1 = \tilde{v}'_1 = 0$ at the wall boundaries. Since this derivation made no assumptions about the waves, this behaviour is present for all modes in the adiabatic homogeneous Hall spectrum. Note however that it only holds for oblique angles between \mathbf{k} and \mathbf{B}_0 . If \mathbf{k} is parallel to \mathbf{B}_0 and along the y - or z -axis in a reference frame of choice, either $\tilde{a}_2 = 0$ or $\tilde{a}_3 = 0$ does not hold and therefore the other equations do not reduce in the way described above. Therefore, for parallel propagation the density perturbation is non-zero at the boundaries, just like in the ideal MHD case.

Finally, Fig. 4.1(e) shows the dispersion of all three sequences by comparing the full spectrum for different wave numbers to the theoretical ideal MHD and HMHD predictions (the dispersive nature of the middle sequence is more subtle). This dispersive behaviour identifies the largest sequence as the whistler wave, discussed in the ion-electron description in Sec. 3.1. The smallest sequence is sometimes called the ion cyclotron wave because its frequency approaches $\Omega_i \cos \theta$ asymptotically for increasing wave number.⁴ Note that the final (intermediate) mode in this panel, which is related to the MHD Alfvén wave and ion-electron A mode, fails to capture the electron cyclotron resonance $\omega \rightarrow \Omega_e \cos \theta$ in the short wavelength (large wave number) limit, which is present in the ion-electron description (see Sec. 2.1.3), because $\eta_e (\propto m_e)$ was set to zero (Hameiri et al., 2005). It has been verified that the sequences indeed start at the theoretical HMHD results (up to an error of 10^{-5} at 501 grid points and a ratio of 10^{-3} of η_H to slab thickness), even though it is somewhat unclear in this image due to the large frequency range and the proximity of various sequences.

To conclude this section, we note that a typical two-fluid effect is recovered if the electron inertia term is included ($\eta_e \neq 0$). In this case, the HMHD behaviour of the intermediate mode approximates the ion-electron behaviour near the electron cyclotron resonance for large wave numbers. This is shown in Fig. 4.2.

³For a different reference frame a linear combination of Eqs. (C.6) and (C.7) gives similar results for any constant \mathbf{B}_0 .

⁴In *Legolas*, the ions are protons.

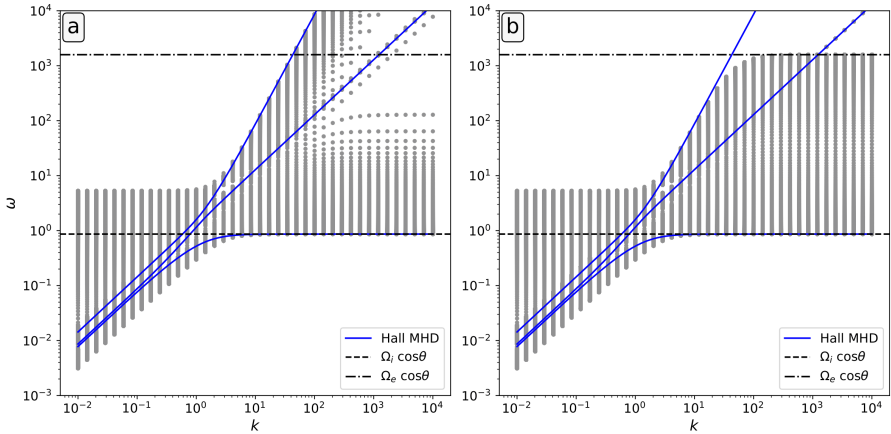


FIGURE 4.2: Comparison to the theoretical HMHD curves from Hameiri et al. (2005, where $\eta_e = 0$) and two-fluid resonances ($\Omega_e \cos \theta$, $\Omega_i \cos \theta$) of the frequency ω as a function of wave number k in HMHD (a) without electron inertia ($\eta_e = 0$) and (b) with electron inertia ($\eta_e \neq 0$). The setup is identical to the one used in Fig. 4.1(e).

4.2.2 Resistive Harris sheet

In Shi et al. (2020), the authors investigate the influence of the Hall current in HMHD on the resistive tearing mode of a Harris current sheet. The equilibrium profile takes the form

$$\rho_0 = \tilde{\rho}_0, \quad T_0 = \frac{B_0^2}{2\tilde{\rho}_0} \operatorname{sech}^2\left(\frac{x}{a}\right), \quad \mathbf{B}_0 = B_0 \tanh\left(\frac{x}{a}\right) \hat{e}_2 + B_g \hat{e}_3 \quad (4.20)$$

with $\tilde{\rho}_0 = B_0 = a = 1$ and B_g a variable guide field parameter. The included physical effects are a constant resistivity $\eta = 10^{-4}$ and a Hall current with coefficient $\eta_H = 1$. As explained earlier, in the vector potential formulation in *Legolas* we include the Hall term and the electron pressure term, but in this test we ignore the electron inertia effect (i.e. $\eta_e = 0$). Furthermore, Shi et al. (2020) assume incompressibility, so we also use an incompressible approximation in *Legolas* (see App. C.3).

Shi et al. (2020) solve for the tearing mode on the interval $x \in [-15, 15]$ and assume exponential decay of the perturbed quantities outside of that interval since the profile (4.20) is approximately constant there for the chosen parameters. In *Legolas*, the default boundary settings are conducting wall boundary conditions at a finite distance, which may modify the linear MHD spectrum due to e.g. wall stabilisation effects. However, for $a = 1$ the interval $[-15, 15]$ seems large enough such that the stabilising influence of the conducting walls is negligible. Our results are shown for two different values of k_2 in Fig.

4.3, recovering Fig. 4 in Shi et al. (2020). In this figure, we show the growth rate $\text{Im}(\omega)$ and frequency $\text{Re}(\omega)$ in top and bottom panels, respectively. Each marker represents the tearing mode in a *Legolas* run at 501 grid points, where a Laplace distributed grid was used to focus the grid points around the region of strongest change in equilibrium magnetic field at $x = 0$. Note that the non-zero $\text{Re}(\omega)$ values are due to the inclusion of the Hall terms, which results in spectrum asymmetry with respect to the imaginary axis here, similar to equilibrium flow. For any guide field value B_g , the growth rate is influenced by the wave vector, with the maximum growth rate depending on both wave vector components, k_2 and k_3 . Whilst the real part of the frequency $\text{Re}(\omega)$ has an extremum as a function of k_3 in the presence of a guide field ($B_g \neq 0$), $|\text{Re}(\omega)|$ increases linearly with increasing k_3 in the absence of a guide field ($B_g = 0$), until the tearing mode is fully damped.

Besides quantifying the tearing mode complex eigenfrequencies, Shi et al. (2020) also reported on the tearing mode eigenfunctions. Up to a complex factor, the eigenfunctions obtained by *Legolas*, shown in Fig. 4.4 (501 grid points), match the results in the first two rows of Fig. 7 in Shi et al. (2020). For the cases in columns a and b of Fig. 4.4, where $B_g = 0$, the B_1 and v_1 eigenfunctions are symmetric and antisymmetric, respectively, with respect to the location of the Harris sheet ($x = 0$) whereas the (anti)symmetry is broken with the introduction of a non-zero guide field B_g (column c).

Shi et al. (2020) only quantify incompressible linear eigenmodes, which they justify by stating that the resistive tearing mode has a negligible contribution due to compressibility, based on the reasoning followed by Furth et al. (1963). We can here easily verify that assumption, using the full compressible functionality of *Legolas*. Unlike previously believed, it appears that the inclusion of Hall terms in the treatment of the tearing mode causes differences in incompressible versus compressible plasma settings. The influence of compressibility is shown in Figs. 4.5(a,b) at 501 grid points, where the compressible growth rate and frequency, respectively, are shown for $k_2 = 0.155$, to be compared to the incompressible case in Figs. 4.3(a,b). Although Furth et al. (1963) showed that compressibility has a negligible effect on the resistive tearing mode, which our tests with *Legolas* also confirm, their treatment did not take the Hall current into account. When the Hall terms are taken into account, the effect of compressibility on the resistive tearing mode growth rate is no longer negligible. In particular, stronger guide fields result in stronger damping of the growth rate, as evidenced by Fig. 4.5. Additionally, new unstable modes appear in the spectrum and become more unstable than the tearing mode for sufficiently large k_3 . These are Hall instabilities, occurring in a Cartesian slab when the magnetic field is sufficiently curved, i.e. if $\partial^2 \mathbf{B}_0 / \partial x^2$ is non-zero (Rheinhardt and Geppert, 2002). The ranges where the largest Hall instability overtakes the tearing instability as the most unstable mode are indicated in Fig. 4.5(a) with lines on the horizontal axis.

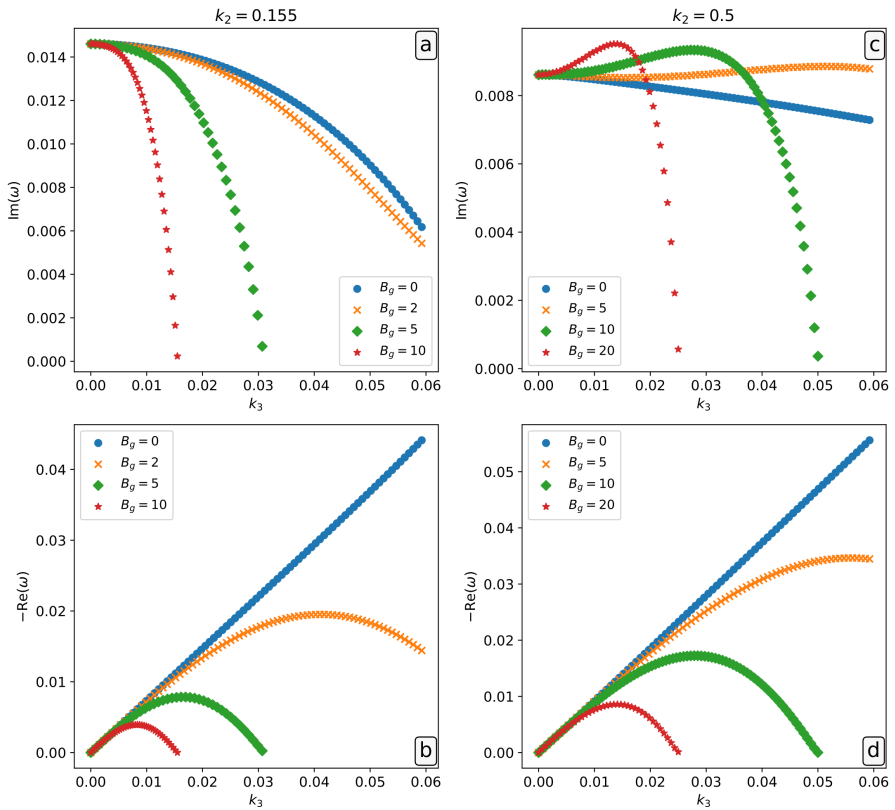


FIGURE 4.3: The real (b, d) and imaginary (a, c) parts of the tearing mode in a Harris current sheet, Eq. (4.20), as a function of k_3 , with $\tilde{\rho} = 1$, $a = 1$, $B_0 = 1$, $\eta = 10^{-4}$, and $\eta_H = 1$ for different guide field strengths B_g . (a) and (b) correspond to a wave vector $\mathbf{k} = 0.155 \hat{\mathbf{e}}_2$, and (c) and (d) to $\mathbf{k} = 0.5 \hat{\mathbf{e}}_2$.

The part of a spectrum containing the tearing mode and the other unstable modes is shown in Fig. 4.5(c).

4.3 Discussion

In this chapter we introduced the MHD spectroscopy code *Legolas* (Claes et al., 2020), which we will also employ extensively in the next chapter, and presented the extension to HMHD. Subsequently, the Hall module was verified using test cases taken from the literature. To validate the implementation of the Hall module, two cases were considered. The simplest case considered an ideal,

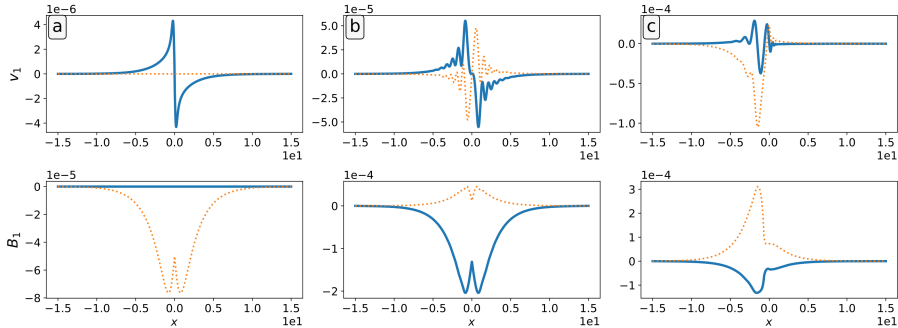


FIGURE 4.4: The incompressible tearing mode's v_1 and B_1 eigenfunctions for $\eta = 10^{-4}$, $\eta_H = 1$, and $k_2 = 0.5$, with different values of k_3 and B_g : column (a) $k_3 = 0$, $B_g = 0$; column (b) $k_3 = 0.06$, $B_g = 0$; and column (c) $k_3 = 0.06$, $B_g = 5$. Real parts are shown as solid blue lines, imaginary parts as dotted orange lines.

homogeneous, Cartesian plasma slab with a Hall current. For a small ratio of ion inertial length to plate separation this case is comparable to the infinite, homogeneous medium, described by the dispersion relation of Hameiri et al. (2005), which was derived from the ion-electron formalism in Sec. 3.4.3. The solutions of the infinite medium corresponded to the first modes in several sequences of modes, as evidenced by the eigenfunctions, which is expected when going from an infinite medium to a semi-infinite medium that is bounded in one direction. Whilst the smallest sequence behaves anti-Sturmian, the larger two display Sturmian behaviour. All three wave sequences become dispersive in Hall-MHD, and the smallest and largest sequences are known as ion cyclotron and whistler modes respectively. The middle sequence fails to capture the electron cyclotron resonance because the electron mass was set to zero. If the electron inertia term is included as well, the electron cyclotron resonance is recovered.

The more advanced test case introduced the Harris current sheet and its resistive tearing mode, whose growth rate is modified by the Hall current as described by Shi et al. (2020). The reproduction of these results required an incompressible approximation (see Sec. C.3), but a good match between both the tearing mode and the eigenfunctions was achieved. However, contrary to the assumption of Shi et al. (2020) that compressibility has a negligible effect on the resistive tearing mode, which was shown for the purely resistive MHD case by Furth et al. (1963), a guide field introduces a non-negligible damping effect when both compressibility and the Hall current are considered.

Besides its effect on the resistive tearing mode, the inclusion of the Hall current also opens up various other research avenues, such as the investigation of its effect on the magnetorotational instability (MRI) (Lesur, 2021), which destabilises

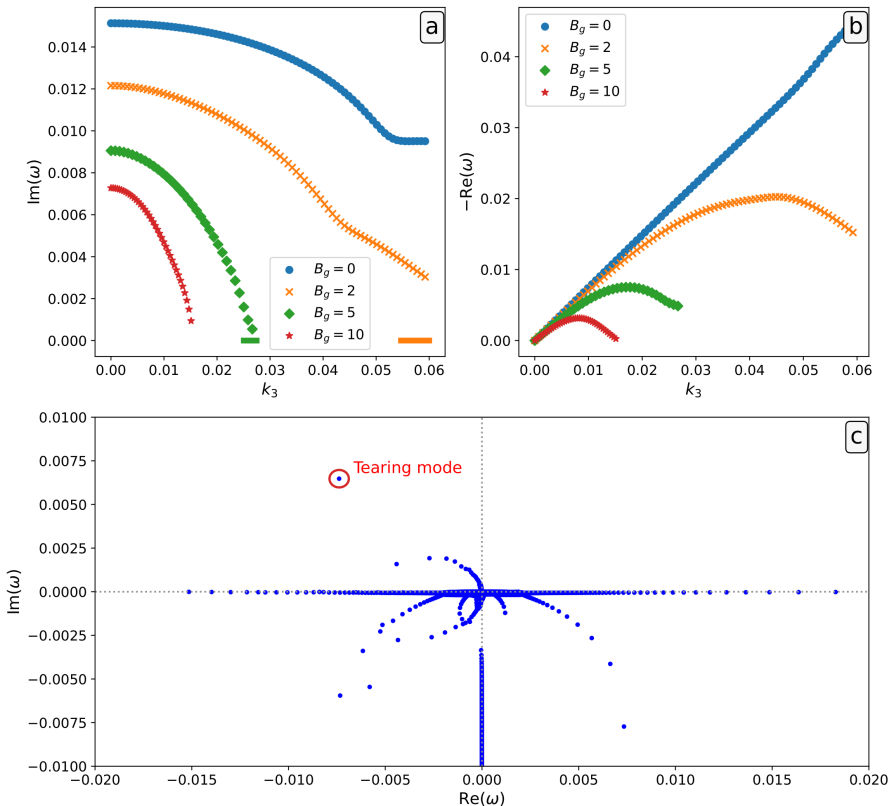


FIGURE 4.5: The real (a) and imaginary (b) parts of the compressible tearing mode in a Harris current sheet, Eq. (4.20), as a function of k_3 , with $k_2 = 0.155$, $\tilde{\rho} = 1$, $a = 1$, $B_0 = 1$, $\eta = 10^{-4}$, and $\eta_H = 1$ for different guide field strengths B_g , to be compared to the incompressible case in Figs. 4.3(a,b). The horizontal lines in (a) indicate the ranges where the tearing mode is not the most unstable mode in the spectrum. (c) Spectrum from the $B_g = 5$ series with $k_3 \approx 0.015346$. The tearing mode is circled in red.

accretion disks surrounding massive objects by converting rotational kinetic energy into magnetic energy (Kulsrud, 2005), or to explore instabilities requiring a Hall current, such as the Hall-shear instability (Kunz, 2008). In the context of the MRI, a similar future extension of the *Legolas* code can implement ambipolar diffusion as a proxy for charge-neutral decoupling effects. This would also introduce the ambipolar-diffusion-shear instability (Kunz, 2008). Note though that recent work (Goedbloed and Keppens, 2022) challenges the role of the MRI in the context of accretion disks by pointing to non-axisymmetric,

super-Alfvénically rotating instabilities (SARIs) that trace out entire regions in the complex eigenfrequency plane.

The code isn't important. It's where the code takes you that is important.

— g00ru, in *Android: Netrunner*
(Fantasy Flight Games)

5

Interplay of flow and resistivity

Parts of Secs. 5.2 and 5.3 were published in De Jonghe et al. (2022). J. De Jonghe performed the calculations, implementation, and validation of the viscosity module in *Legolas*. Additionally, J. De Jonghe wrote the first draft, which was revised by N. Claes and R. Keppens.

In most applications both flow and resistivity play an important role in the stability of the plasma configuration, since both effects can introduce their own instabilities into the system. In the presence of flow shear, the flow may develop a Kelvin-Helmholtz instability (KHI) whilst magnetic shear induces the resistive tearing instability in plasmas with finite conductivity. However, though it is known that their effects influence each other (Hofmann, 1975), their interaction has not been fully mapped out. Although we will not develop a full understanding of the interplay between flow and resistivity in this chapter, we explore the influence of background flow and viscosity on a resistive configuration, with a particular emphasis on the resistive tearing instability.

In Sec. 5.1, we study the influence of background flow on the resistive tearing instability in two distinct configurations: a magnetic field with an x -dependent direction and a Harris current sheet. In Sec. 5.2, we introduce viscosity into the *Legolas* code and validate its implementation. Subsequently, we explore the viscoresistive spectrum.

5.1 Resistive tearing instability

Ever since the discovery of the resistive tearing mode, first by Furth et al. (1963) in a plasma slab and later by Coppi et al. (1966) in a plasma cylinder, it has been the subject of many studies, with recently renewed interest sparked by its role in magnetic reconnection events. Though fast reconnection is regularly observed and reproduced in simulations, many questions remain regarding the circumstances of its onset. In particular, with various paths towards reconnection, the question becomes how the growth rates of the different mechanisms (e.g. the resistive tearing instability or Hall reconnection) depend on the parameter regime, such as the background flow (Li and Ma, 2010, 2012), despite stabilising influences such as the resistive diffusion of the magnetic field (Dobrott et al., 1977). In addition, there is the question of how they interact, like the modification of resistive tearing by the Hall current (Shi et al., 2020). In this endeavour, the influence of equilibrium flow on the resistive tearing mode has already been studied extensively using both analytical methods (Hofmann, 1975; Paris and Sy, 1983; Pollard and Taylor, 1979; Chen and Morrison, 1990) and numerical simulations (Li and Ma, 2010; Zhang et al., 2011; Li and Ma, 2012; Wu and Ma, 2014).

To take the analytical results one step further, we employ *Legolas* to explore plasma stability parametrically for a selection of configurations and show that equilibrium flow can enhance the growth rate of the resistive tearing mode in some regimes. The effect of equilibrium flow has been studied analytically by Chen and Morrison (1990) and we connect our results to their power laws. In the remainder of this chapter, we assume a constant resistivity $\eta = 10^{-4}$, unless specified otherwise.

5.1.1 Conventions

The literature (most notably Furth et al., 1963; Chen and Morrison, 1990) differentiate between constant- ψ and nonconstant- ψ tearing modes, where ψ denotes the normalised B_x -perturbation and the classification refers to its behaviour across the magnetic nullplane at $x = x_0$, where

$$F(x) = \frac{\mathbf{k}}{|\mathbf{k}|} \cdot \mathbf{B}_0(x) \quad (5.1)$$

vanishes, $F(x_0) = 0$. Similarly, for the equilibrium flow we define the angle-modulated Alfvén Mach number (following Chen and Morrison, 1990)

$$G(x) = \frac{\mathbf{k} \cdot \mathbf{v}_0(x)}{|\mathbf{k}|c_a}. \quad (5.2)$$

Like usual, \mathbf{k} denotes the wave vector, and \mathbf{B}_0 and \mathbf{v}_0 are the dimensionless equilibrium magnetic field and velocity, respectively. Here, c_a indicates the

dimensionless Alfvén speed $c_a = |\mathbf{B}_0|/\sqrt{\rho_0}$ for the dimensionless equilibrium density ρ_0 . Following Chen and Morrison (1990), the expression

$$R_0 = \left| \frac{G'(x_0)}{F'(x_0)} \right|, \quad (5.3)$$

where the prime denotes the derivative with respect to x , acts as a diagnostic parameter to quantify the relative strength of the flow shear compared to the magnetic shear. We will refer to R_0 as the shear ratio.

Relative growth rate. Throughout this chapter, we compare the tearing growth rate under the influence of equilibrium flow to the equivalent configuration without flow. In these cases, we oftentimes opt to use the relative growth rate γ , which we define as

$$\gamma = \frac{\text{Im}(\omega_{\text{flow}}) - \text{Im}(\omega_{\text{no flow}})}{\text{Im}(\omega_{\text{no flow}})}. \quad (5.4)$$

Hence, γ ranges from -1 , which means the tearing instability is completely stabilised, to $+\infty$. If $\gamma = 0$, the growth rate is unaltered.

Colour bars. Whenever the relative growth rate is shown in a colour-coded way, two colour bars are used. The first colour bar, which appears on the bottom of the figure, indicates the region where the growth rate is unaltered or damped. The other colour bar, to the right of the figure, designates a further destabilisation of the tearing instability.

5.1.2 Tearing in a plasma slab

In this section we consider a semi-infinite plasma confined in the x -direction between two perfectly conducting plates, described in Cartesian coordinates. All equilibrium profiles are only allowed to vary in the x -direction and we examine the resistive tearing mode for two separate configurations. In the first configuration, the magnetic field varies its direction continuously throughout the plasma slab with a constant size and is complemented by a linear velocity profile. Due to the lack of an inflection point in the velocity profile, Rayleigh's inflection point theorem ensures that the background flow is not susceptible to the KHI (Goedbloed et al., 2019). For the second case we return to the previously introduced Harris current sheet (see Sec. 4.2.2), where we complement the hyperbolic tangent profile for the magnetic field with a flow profile of identical form. This velocity profile does feature an inflection point, and consequently supports the KHI in certain parameter regimes.

Direction-varying magnetic field

For the first case, consider a direction-varying magnetic field complemented by a linear flow profile, as defined by Goedbloed et al. (2019, Sec. 14.3.3),

$$\begin{aligned}\rho_0(x) &= \rho_c, & \mathbf{B}_0(x) &= \sin(\alpha x) \hat{\mathbf{e}}_2 + \cos(\alpha x) \hat{\mathbf{e}}_3, \\ T_0(x) &= \frac{\beta_0 \mathbf{B}_0^2}{2\rho_c}, & \mathbf{v}_0(x) &= v_c x \hat{\mathbf{e}}_2,\end{aligned}\tag{5.5}$$

where ρ_c , v_c , and α are constants. As the notation suggests, β_0 is the equilibrium plasma- β . Note that $|\mathbf{B}_0| = 1$ such that the dimensionless Alfvén speed c_a equals $c_a = 1/\sqrt{\rho_c}$. For this equilibrium we choose \mathbf{k} proportional to $\hat{\mathbf{e}}_2$ (and thus parallel to \mathbf{v}_0), such that there is a magnetic nullplane at $x_0 = 0$, and solve in an interval symmetric around the nullplane, $x \in [-0.5, 0.5]$.

Shear ratio and multiple tearing modes. In this particular case, the shear ratio becomes

$$R_0 = \left| \frac{G'(0)}{F'(0)} \right| = \frac{v_c \sqrt{\rho_c}}{\alpha}.\tag{5.6}$$

Whilst there are three parameters in this expression, our parametric study below will only focus on the variation of the equilibrium density ρ_c and flow coefficient v_c , and we demonstrate the role of α here.

Since the parameter α regulates which directions the magnetic field adopts in a fixed interval, it also determines how many magnetic nullplanes the system has for a given wave vector. Consequently, the number of tearing modes depends on α . Additionally, if the equilibrium velocity is described by an odd function, like the linear profile in Eq. (5.5), the spectrum is symmetric with respect to the imaginary axis. This is illustrated in Figs. 5.1(a-d), where we varied the parameter α for parameters $\rho_c = 1$, $\beta_0 = 0.15$, $v_c = 0.15$, and $\mathbf{k} = 1.5 \hat{\mathbf{e}}_2$ at 251 grid points. In (a), the magnetic shear is insufficient to induce a tearing instability. Increasing α without introducing an additional nullplane results in one non-propagating tearing mode (i.e. purely imaginary), visualised in (b). In the presence of three nullplanes, (c) shows a pair of forward-backward propagating tearing instabilities and one non-propagating one. Finally, (d) contains only two pairs of forward-backward propagating tearing pairs, despite the presence of 5 nullplanes in the domain. If the flow is removed, all tearing modes become non-propagating.

For the case in panel (d), the real parts of the B_{1x} -perturbations of the unstable modes are shown in Figs. 5.1(e,f). All magnetic nullplanes are marked with a dash-dotted line. At the darker lines we observe a dip in the eigenfunction, indicative of tearing at this nullplane. Interestingly, the central nullplane has two tearing modes associated with it (f) whereas the outer nullplanes have none.

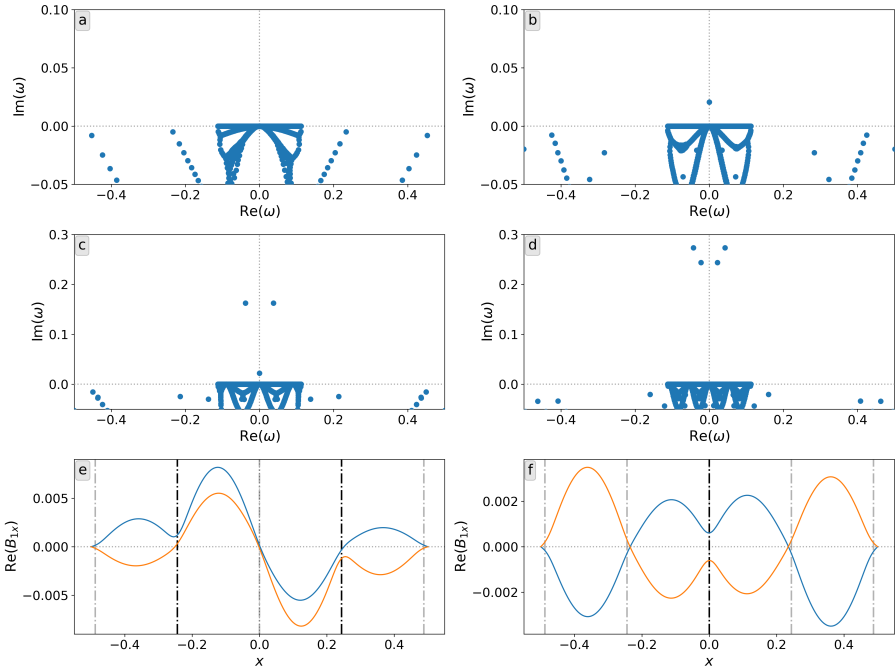


FIGURE 5.1: (a-d) Parts of the spectra of a plasma slab with direction-varying magnetic field, Eqs. (5.5), for $\rho_c = 1$, $\beta_0 = 0.15$, $v_c = 0.15$, and $\mathbf{k} = 1.5 \hat{\mathbf{e}}_2$. The angular parameter α in the magnetic field profile determines the number of magnetic nullplanes and unstable modes, and takes a different value in each panel: (a) $\alpha = \pi/2$, (b) $\alpha = 4.73884$, (c) $\alpha = 5\pi/2$, and (d) $\alpha = 4.1\pi$. (e-f) $\text{Re}(B_{1x})$ -eigenfunctions of the tearing modes in panel (d) for the (e) most and (f) least unstable pair. Magnetic nullplanes are indicated by dash-dotted lines, with darker lines marking where tearing occurs in that panel.

Therefore, one magnetic nullplane does not necessarily support exactly one tearing instability. It should be noted though that the outer nullplanes lie close to the edges of the domain, such that their associated tearing modes may be eliminated by the perfectly conducting boundary conditions. Further note that $\text{Im}(B_{1x})$ is also non-zero for all unstable modes in (d). Since the eigenfunction is only determined up to an arbitrary complex factor, this choice of factor may modify the strength of the tearing behaviour.

From now on the value of α is set to $\alpha = 4.73884$ (i.e. the value used in Fig. 5.1(b) and Goedbloed et al., 2019), such that the magnetic field makes between one-half and a full rotation in the considered domain, resulting in a single nullplane and a single tearing mode.

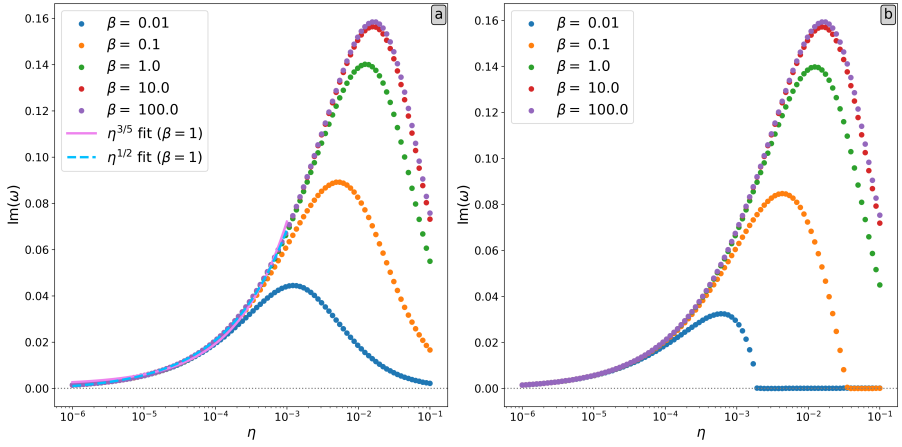


FIGURE 5.2: Resistive tearing growth rate of a direction-varying magnetic field, Eqs. (5.5), for $\rho_c = 1$ and $\mathbf{k} = 1.5 \hat{\mathbf{e}}_2$, as a function of η for various plasma- β (a) without flow and (b) for $v_c = 0.15$.

Resistivity variation. In the seminal work by Furth et al. (1963) the authors derive power laws for the scaling of the incompressible tearing growth rate as a function of the resistivity η , for small values of η . Here, we introduce compressibility and consider a wide range of resistivity values. From their derivations they conclude that the p -value in the scaling law $\text{Im}(\omega) \sim \eta^p$ depends on whether or not B_{1x} , the x -component (i.e. the direction of the equilibrium variation) of the magnetic field perturbation, is approximately constant across the magnetic nullplane. For this equilibrium we are dealing with a so-called constant- ψ mode and thus expect a scaling of $\text{Im}(\omega) \sim \eta^{3/5}$ since $R_0 \simeq 0.03 \ll 1$ (Chen and Morrison, 1990). However, Fig. 5.2(a), containing the variation of the growth rate with η for $\rho_0 = 1$ and $\mathbf{k} = 1.5 \hat{\mathbf{e}}_2$ at 301 grid points, shows that the compressible tearing growth rate does not change monotonically with η , but in fact decreases again for higher resistivities, with the resistivity of maximal growth rate depending on the plasma- β , whereas the analytic power laws were derived without any assumptions about the plasma- β . In addition, it seems that $\text{Im}(\omega) \sim \eta^{1/2}$, which Chen and Morrison (1990) indicate as the $R_0 \lesssim 1$ scaling, provides a better fit in the small- η limit despite the low R_0 value, as seen in Fig. 5.2(a). Adding velocity to this variation in resistivity steepens the growth rate dropoff for lower β -values, as evidenced by Fig. 5.2(b), going as far as eliminating the instability entirely.

Density variation. Varying the density, the difference between the flowless configuration ($v_c = 0$) and the configuration with $v_c = 0.15$ is shown in Fig.

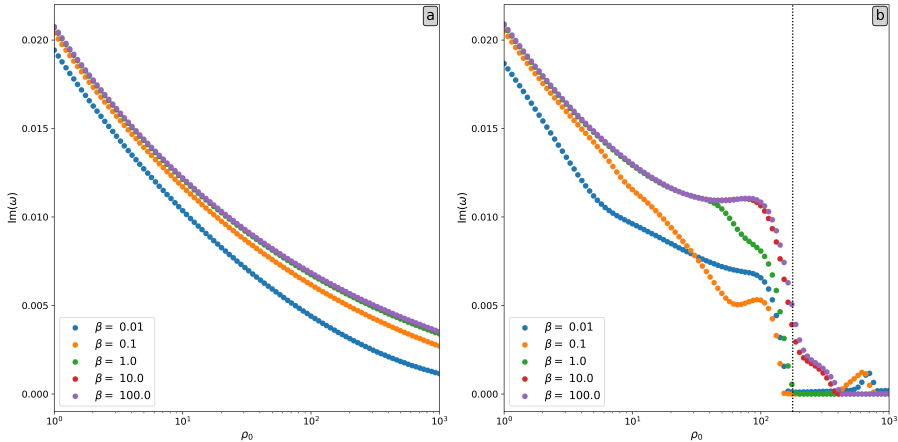


FIGURE 5.3: Resistive tearing growth rate of a direction-varying magnetic field, Eqs. (5.5), for $\eta = 10^{-4}$, as a function of ρ_0 for various plasma- β (a) without flow and (b) for $v_c = 0.15$. The dotted vertical line indicates where the maximal equilibrium speed equals the Alfvén speed.

5.3, for $\mathbf{k} = 1.5 \hat{\mathbf{e}}_2$ at 301 grid points. In the left panel, a steady decline in tearing growth rate is observed for increasing density in the absence of flow. The addition of the linear flow profile introduces a density threshold where the tearing instability is significantly damped. This transition corresponds to the point where the maximal equilibrium speed exceeds the Alfvén speed (recall that $c_a = 1/\sqrt{\rho_c}$ here), which is indicated in the right panel by a dotted black line. Henceforth, we thus only consider sub-Alfvénic speeds.

Velocity variation. Despite the simple velocity profile, the (v_c, β) -parameter space reveals surprising complexity. After assuming a constant density $\rho_0 = 1$, the present parametric survey varied v_c and β for wave vector $\mathbf{k} = 1.5 \hat{\mathbf{e}}_2$, where the v_c parameter was limited to the interval $[0, 2]$, such that the equilibrium velocity remains sub-Alfvénic ($\leq c_a$) on the entire domain, and β -values of 10^{-2} to 10^2 were studied. The results are shown in Fig. 5.4, where all runs in panel (a) were performed at 301 grid points, whereas 201 grid points were used in panel (b).

As pointed out by Hofmann (1975), the introduction of flow in a system that is unstable to the resistive tearing mode can either stabilise or further destabilise the plasma. This is also immediately clear from Fig. 5.4(b), where blue indicates a stabilised system and yellow a strong increase in tearing growth rate. Whilst the plasma is mostly destabilised further by the presence of flow for large β , as clearly evidenced by Fig. 5.4(a), the destabilising effect does not scale

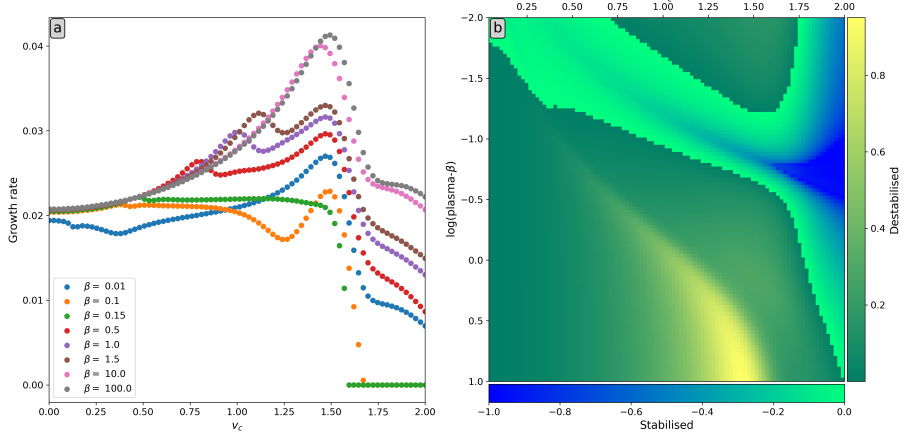


FIGURE 5.4: Resistive tearing mode growth rate of a direction-varying magnetic field, Eqs. (5.5), for $\rho_c = 1$. (a) Absolute growth rate as a function of v_c for various plasma- β values. (b) Relative growth rate for varying v_c and β with respect to the flowless growth rate.

monotonically with the velocity coefficient. Rather, the maximal destabilisation appears at some intermediate value between small speeds and the Alfvén speed. For small to intermediate β ($\lesssim 1$), on the other hand, both stabilising and destabilising influences are observed in significant fractions of the velocity space, with the strongest stabilising effect occurring at the Alfvén speed. Additionally, more than one stabilising-destabilising transition is observed along the speed axis for small β ($\ll 1$).

Harris current sheet

The effect of shear flow on the resistive tearing mode was probed by Li and Ma (2010) using non-linear incompressible MHD simulations by computing the reconnection rate for a selection of test cases. In their simulation setup they consider a Harris current sheet

$$\mathbf{B}_0(x) = B_0 \tanh\left(\frac{x}{a_B}\right) \hat{\mathbf{e}}_2, \quad (5.7)$$

which they supplement with a similar velocity profile

$$\mathbf{v}_0(x) = v_0 \tanh\left(\frac{x}{a_v}\right) \hat{\mathbf{e}}_2 \quad (5.8)$$

and a uniform density $\rho_0 = 1$. This 1D equilibrium is amenable to implementation in *Legolas* and thus an excellent candidate for a linear parametric

study. The temperature profile for *Legolas* is simply obtained by demanding that the total equilibrium pressure (the sum of plasma pressure and magnetic pressure) is constant¹, i.e.

$$\frac{\partial}{\partial x} \left(\rho_0(x) T_0(x) + \frac{1}{2} \mathbf{B}_0^2(x) \right) = 0. \quad (5.9)$$

The interval $x \in [-15 a_B, 15 a_B]$ is chosen such that the effect of the perfectly conducting boundaries on the tearing instability is negligible (according to Ofman et al., 1993, the effect of the conducting walls is negligible if they occur at a position $|x_w| \gtrsim 10 a_B$). Due to the sharp transitions in the equilibrium profiles near the origin and approximately constant behaviour away from the center, the problem is solved using a non-uniform grid concentrated near the origin, as described in App. C.5, unless indicated otherwise.

Now assuming $\mathbf{k} = k \hat{\mathbf{e}}_2$, the diagnostic parameter reduces to

$$R_0 = \frac{a_B v_0}{a_v B_0}. \quad (5.10)$$

When the flow shear exceeds the magnetic shear, i.e. $R_0 > 1$, the tearing instability is fully stabilised (Chen and Morrison, 1990).

Linear stage of tearing reconnection. From the Fourier coefficients computed by *Legolas* and the equilibrium profiles we can construct the structure of the magnetic field after linear perturbation. For a flowless case with $k = 0.12$, $\rho_0 = 0$, $B_0 = 1$, and $a_B = 1$, the tearing mode's magnetic field perturbation is shown in Figs. 5.5(a,b), where the imaginary part of B_{1x} and the real part of B_{1y} vanish. The parameters for grid accumulation (see App. C.5) for this run were $p_1 = 0.2$, $p_2 = 0$, $p_3 = 0.01$, and $p_4 = 5$, resulting in 329 grid points. Panels (c) and (d) show the field lines of the total magnetic field (equilibrium plus the real part of the linear perturbation), where the perturbation was scaled to a similar order of magnitude as the equilibrium to highlight its effect. Since the eigenfunctions are only determined up to complex factor, panel (c) shows the result for a factor of 1 whilst panel (d) illustrates a phase shift of angle $\theta = 7\pi/9$. Hence, (c) has no B_{1y} -contribution whilst (d) features contributions from both perturbed field components.

Taking a closer look at Fig. 5.5(c) reveals that the linear perturbation does not immediately form a single large plasmoid (or magnetic island) between two pinching points as presented in Fig. 1.5 of the introductory chapter. Instead, the field lines are bent. Further away from the current sheet, the field lines bend away from the sheet, creating a bump between two pinches. Close to the current sheet, however, the field lines bend towards the sheet, locally thinning

¹Sometimes, the temperature is chosen as the constant quantity and subsequently, the density profile is determined by Eq. (5.9), such as in e.g. Goedbloed et al. (2019), Sec. 14.4.1.

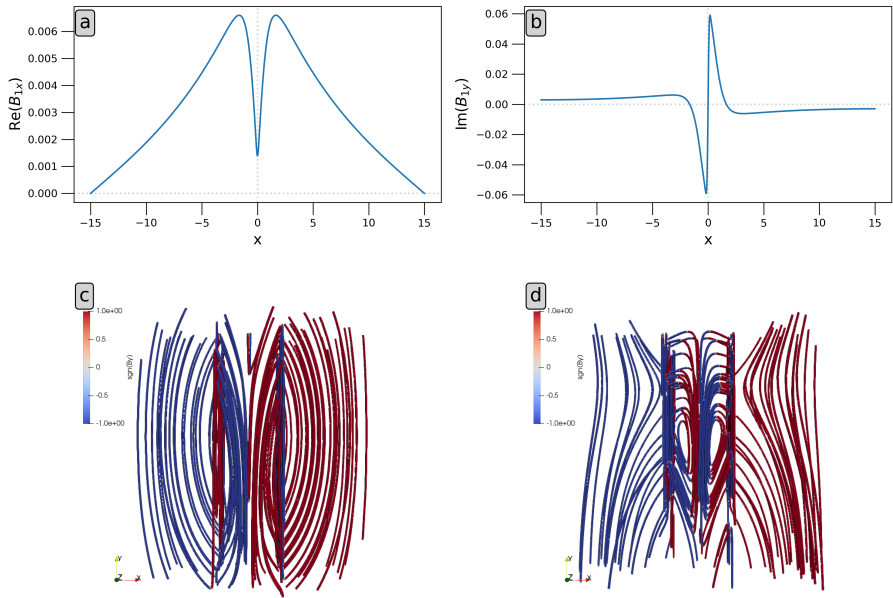


FIGURE 5.5: (a) The tearing mode’s B_{1x} -eigenfunction, with vanishing imaginary part. (b) The tearing mode’s B_{1y} -eigenfunction, with vanishing real part. (c, d) Field lines of the total magnetic field (equilibrium plus linear perturbation) for a central, vertical Harris sheet, with the colour indicating whether the field points up- or downwards for (c) only a B_{1x} -contribution, and (d) (more or less) equal contributions from B_{1x} and B_{1y} .

the sheet. If this triggers another reconnection process at the current sheet’s location, the system could evolve to form one substantial plasmoid, as illustrated schematically in Fig. 5.6.

If the magnetic field perturbation is shifted with a constant phase though, as shown in Fig. 5.5(d), two clearly defined plasmoids appear at the location of the pinch. Once more, these plasmoids could merge through subsequent reconnection events. This is demonstrated in Fig. 5.7. In this case, a plasmoid would be formed at the pinched position, which would be in accordance with simulations of the plasmoid instability (e.g. Shimizu et al., 2017; Hosseinpour et al., 2018). This instability is in essence a tearing instability in a non-steady state, which would imply that plasmoids are formed by consecutive tearing instabilities.

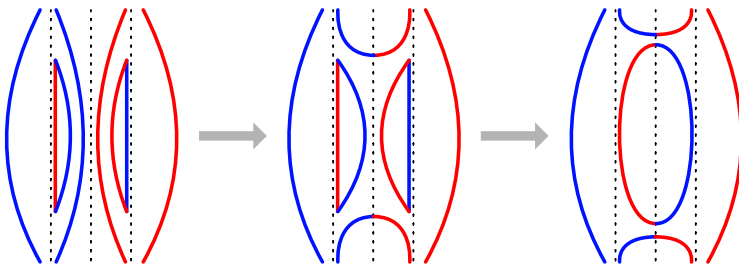


FIGURE 5.6: Schematic representation of how additional reconnection events could create a plasmoid starting from the perturbed state in Fig. 5.5(c). Red curves are oriented upwards, blue curves downwards.

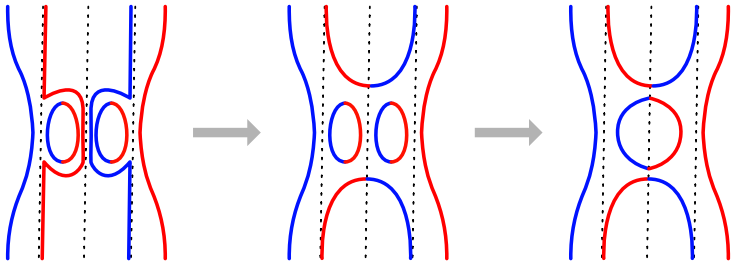


FIGURE 5.7: Schematic representation of how additional reconnection events could create a plasmoid starting from the perturbed state in Fig. 5.5(d). Red curves are oriented upwards, blue curves downwards.

Resistivity variation. Moving on to the parameter study, we first vary the resistivity η to compare to the literature's scaling laws. In Fig. 5.8(a), the flowless case is compared to the case with flow profile Eq. (5.8) for a selection of R_0 -values, which should scale differently according to the analytic power laws of Chen and Morrison (1990). For these runs the physical parameters are $\mathbf{k} = 0.5 \hat{\mathbf{e}}_2$, $\rho_0 = 1$, $B_0 = 1$, $a_B = 1$, and $v_0 = 0.5$. In addition, the grid parameters were set to $p_1 = 0.75$, $p_2 = 0$, $p_3 = 0.001$, and $p_4 = 2.5$ (285 grid points). The value of R_0 was obtained by setting $a_v = a_B v_0 / B_0 R_0$. In the absence of flow the curve seems to start deviating from the analytic scaling laws for $\eta > 10^{-2}$, although it is not as pronounced as in the case of the

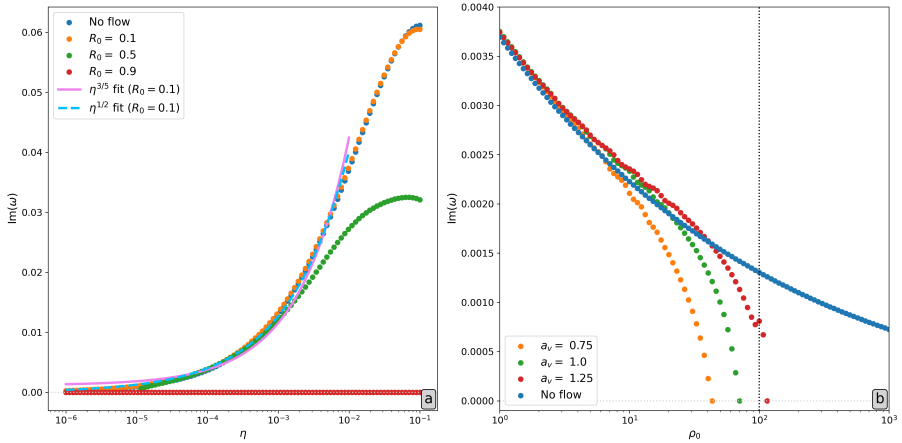


FIGURE 5.8: Resistive tearing growth rate of a Harris sheet, Eq. (5.7), as a function of (a) the resistivity η ; (b) the density ρ_0 ; for parameters $\mathbf{k} = 0.5\hat{\mathbf{e}}_2$, $\rho_0 = 1$, $B_0 = 1$, $a_B = 1$, and (a) $v_0 = 0.5$; (b) $v_0 = 0.1$, if flow was included. In (b), the density where the maximal velocity of the equilibrium configuration coincides with the Alfvén speed is indicated with a dotted line.

direction-varying magnetic field, where the growth rate also decreased again in the same interval of η . As expected for small values of R_0 , the influence of a flow with $R_0 = 0.1$ on the tearing growth rate is almost negligible compared to the flowless case. Similarly to the previous case, the $\eta^{1/2}$ -fit seems better than the $\eta^{3/5}$ -fit despite the fact that $R_0 \ll 1$. For a value of $R_0 = 0.5$, the scaling with η is not really influenced for weak resistivities, but the stronger the resistivity, the stronger the damping of the growth rate. In this regime of higher resistivity, the growth rate scaling also clearly deviates from the literature's simple power laws. Finally, the tearing mode is fully damped across all resistivities for $R_0 = 0.9$, which is well before R_0 reaches the literature's critical value of 1.

Density variation. Similarly to the previous slab configuration, the inclusion of a non-zero flow modifies the tearing growth rate variation as a function of density ρ_0 . Again, the growth rate decreases gradually with increasing density in the absence of flow whilst flow inserts a critical density above which the tearing mode is fully damped, as illustrated in Fig. 5.8(b). In this figure, we use the same parameters as in the previous paragraph, except now the density varies, $\eta = 10^{-4}$, and $v_0 = 0.1$.

From this figure it is clear that the critical density above which the tearing mode is damped in the presence of flow depends on the transition width a_v of the velocity profile. Moreover, it does not seem to coincide with the velocity

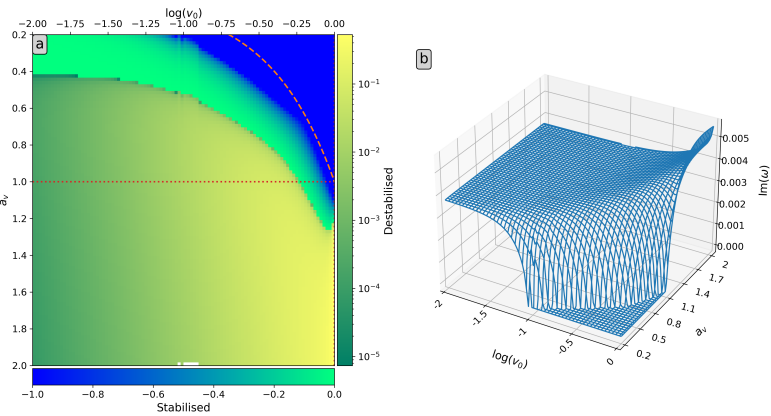


FIGURE 5.9: (a) Relative tearing growth rate γ with respect to the static case for combinations of the maximal speed v_0 and flow transition width a_v . The red dotted line indicates the magnetic field transition width a_B and the orange dashed line represents $R_0 = 1$. (b) Absolute tearing growth rate as a function of v_0 and a_v .

reaching the Alfvén speed, unlike for the previous configuration. Therefore, the Alfvén speed does not necessarily act as a transition value in the equilibrium speed with respect to tearing suppression.

Velocity variation. Since the velocity profile contains two parameters (the maximal speed v_0 and width a_v), we vary both parameters simultaneously to identify the regions of stabilisation and destabilisation. Here, the maximal speed v_0 is kept sub-Alfvénic ($v_0 < 1$) because the KHI dominates in the super-Alfvénic regime (Hofmann, 1975). The result is shown in Fig. 5.9 for fixed parameters $\mathbf{k} = 0.5 \hat{\mathbf{e}}_2$, $\rho_0 = 1$, $B_0 = 1$, $a_B = 1$, and $\eta = 10^{-4}$ and was obtained with an inverse iteration method (see App. C.2) on an equally-spaced grid with 6001 grid points. Since this method requires an initial guess, the first guess was obtained from a run with the QR-invert solver for $v_0 = 10^{-2}$ and $a_v = 1$, which was used to compute the growth rate for all values of a_v and $v_0 = 10^{-2}$ through inverse iteration. This array of growth rates was subsequently used as the initial guesses for the next value of v_0 , and so on. Visually speaking, each value (except those in the left column) in Fig. 5.9 was computed through inverse iteration by providing the value to its immediate left as the initial guess. Note that whilst the tearing mode is fully damped in the top right corner of panel (a), the system is still unstable because the KHI appears here before v_0 reaches the Alfvén speed. This was again checked with the QR-invert solver in this region of the parameter space.

In this figure, a few things stand out. First of all, the $R_0 = 1$ (orange dashed) line lies well inside the completely stabilised region and not near its boundary. Hence, whilst the tearing instability is not present if $R_0 = 1$, there is a relatively large region in the vicinity of this line where the tearing instability is already fully damped. This confirms our previous finding from the η variation. Secondly, contrary to the non-linear observation by Li and Ma (2010) that there exists a single critical a_v value ~ 0.35 where the transition from stabilising to destabilising occurs, we here observe that this critical a_v depends on the maximal speed v_0 . Furthermore, their critical value lies in our stabilised region of the parameter regime across all velocities. Note though that their simulations include a non-zero viscosity, which may affect this result. Ultimately, as indicated by Fig. 5.9(b), the flow's influence is largely negligible if it is significantly below the Alfvén speed, but for near-Alfvénic speeds the flow can both act as a stabilising or destabilising force.

5.2 Viscous flow

In MHD, viscosity appears as a force term \mathbf{F}_{visc} in the right hand side of the momentum equation (4.3). In its most general form, \mathbf{F}_{visc} can be written as $\mathbf{F}_{\text{visc}} = -\nabla \cdot \boldsymbol{\pi}$, where $\boldsymbol{\pi}$ denotes the viscous stress tensor (Braginskii, 1965). However, as shown by Erdélyi and Goossens (1995), where the authors used the full viscous stress tensor, only the shear viscosity contributes to resonant absorption, and the compressive and perpendicular components have negligible effects. Hence, for a constant dynamic viscosity μ the viscous force is in good approximation equal to (see e.g. Goedbloed et al., 2019)

$$\mathbf{F}_{\text{visc}} = \mu \left[\nabla^2 \mathbf{v} + \frac{1}{3} \nabla (\nabla \cdot \mathbf{v}) \right]. \quad (5.11)$$

The linearisation of this expression is implemented in *Legolas*. Sometimes it is assumed that the kinematic viscosity $\nu = \mu/\rho$ is constant rather than the dynamic viscosity. This introduces additional terms in the linearisation, which are not currently available in *Legolas*. Note though that in a Cartesian geometry with constant ρ_0 and \mathbf{v}_0 the additional terms introduced by assuming a constant kinematic viscosity, rather than a constant dynamic viscosity, vanish.

In addition to a contribution in the momentum equation, viscosity also introduces a viscous heating term $(\gamma-1)H_{\text{visc}}$ in the right hand side of the energy equation (4.4). In full, the source term H_{visc} is given by $H_{\text{visc}} = -(\boldsymbol{\pi} \cdot \nabla) \cdot \mathbf{v}$. However, this is again approximated as (see e.g. Goedbloed et al., 2019)

$$H_{\text{visc}} \approx \mu |\nabla \mathbf{v}|^2. \quad (5.12)$$

The linearisation of this approximation in *Legolas* assumes the Frobenius norm, resulting in the linearised term

$$H_{\text{visc},1} = 2\mu \sum_{i=1}^3 \sum_{j=1}^3 (\nabla \mathbf{v}_0)_{ij} (\nabla \mathbf{v}_1)_{ij}. \quad (5.13)$$

Note that this contribution vanishes if the equilibrium flow is constant or zero, as is the case for the setup of Sec. 5.2.1 whilst it introduces two non-zero terms for the configuration in Sec. 5.2.1. However, since both cases employ the incompressible approximation, which replaces the energy equation, this term is not represented in either test case. Note further that the background equilibrium flow \mathbf{v}_0 is always adopted as a stationary, Eulerian flow, much like one normally computes eigenspectra for an ideal MHD equilibrium with time-independent \mathbf{B}_0 , even in the presence of a finite resistivity. The viscous terms are thus omitted in the equilibrium equations.

The inclusion of viscosity also imposes additional no slip boundary conditions at a rigid wall. In essence, this implies that the total plasma velocity at the boundary equals the wall's velocity. Implementation-wise, we impose that the velocity perturbation \mathbf{v}_1 at the boundary is exactly zero,

$$v_1 = v_2 = v_3 = 0. \quad (5.14)$$

As a consequence of the no slip boundary condition, a non-zero equilibrium velocity at a boundary then simulates a boundary moving at that constant speed. We use this to study a viscous, hydrodynamic Taylor-Couette flow below, which serves as a test case for cylindrical geometry by comparing to results of Gebhardt and Grossmann (1993). Additionally, the new viscosity module is tested in an MHD setup using the results from Dahlburg et al. (1983), where the authors study the tearing mode in a viscoresistive plasma slab (i.e. in Cartesian geometry).

5.2.1 Taylor-Couette flow

When considering a viscous fluid confined between two concentric cylinders that both rotate with constant angular velocity, the flow established under no slip boundary conditions is called Taylor-Couette flow. A hydrodynamic equilibrium of this form, studied spectroscopically under incompressible conditions in Gebhardt and Grossmann (1993), is given by a uniform density ρ_0 , and temperature and velocity profiles

$$T_0(r) = \frac{1}{2} \left(A^2 r^2 + 4AB \log(r) - \frac{B^2}{r^2} \right) + C, \quad \mathbf{v}_0(r) = \left(Ar + \frac{B}{r} \right) \hat{\mathbf{e}}_2, \quad (5.15)$$

where C is an arbitrary constant to guarantee that T_0 is positive everywhere and

$$A = \frac{\beta - \left(\frac{R_1}{R_2}\right)^2 \alpha}{1 - \left(\frac{R_1}{R_2}\right)^2}, \quad B = -\frac{R_1^2(\beta - \alpha)}{1 - \left(\frac{R_1}{R_2}\right)^2}, \quad (5.16)$$

with α (β) the angular speed of the inner (outer) cylinder at radius R_1 (R_2). Since this is a hydrodynamic test case, there is no equilibrium magnetic field \mathbf{B}_0 .

Using the incompressible approximation in *Legolas*, four representative eigenspectra from Fig. 3 in Gebhardt and Grossmann (1993) are recovered in Figs. 5.10(a-d) at 251 grid points. These spectra feature two different types of modes, as described in Gebhardt and Grossmann (1993), namely translational modes with $v_1 = 0 = v_2$ (with only a non-trivial $v_3(u_1) = v_z(r)$ variation) and “azimuthal” modes with non-zero v_1 and v_2 eigenfunctions and $v_3 = 0$. Admittedly, we recover the azimuthal modes but they do have a non-vanishing v_3 eigenfunction in the test cases with *Legolas*’s incompressible approximation. However, we find that the spectra in Figs. 5.10(a,d) are almost identical in the compressible case (the spectrum is more heavily influenced by compressibility for smaller radius-to-thickness ratios), and the v_3 eigenfunction indeed vanishes in the compressible setup. Hence, the incompressible approximation results in slightly spurious v_3 eigenfunctions for this case. This is presumably due to the fact that, whilst $\nabla \cdot \mathbf{v}$ is indeed numerically zero, the v_3 component is not constrained by this expression because it only contributes to $(\nabla \cdot \mathbf{v})(r) = (rv_1)'/r + ik_2 v_2/r + ik_3 v_3$ in a term proportional to k_3 , which is zero. The v_3 eigenfunction is shown for a translational mode in Fig. 5.10(e), and the v_2 and v_3 eigenfunctions of an azimuthal mode are shown in Figs. 5.10(f,g), respectively. The corresponding modes are marked in Fig. 5.10(d). These eigenmodes in *Legolas* (ω_L) are consistent with those reported by Gebhardt and Grossmann (1993) (ω_G), namely $\omega_L = 1583.50 - 1053.70i$ and $\omega_L = 2406.82 - 579.55i$ compared to $\omega_G = 1583.56 - 1053.83i$ and $\omega_G = 2406.81 - 579.54i$. The *Legolas* eigenfunctions match their eigenfunctions up to a complex factor (this represents the freedom to choose a reference amplitude and phase in a linear eigenvalue problem) when comparing to their Figs. 6b and 8b.

Taking the analysis of Taylor-Couette flow one step further using the fully compressible functionality of the code, we take a look at the entropy perturbation in the compressible spectrum, motivated by the observation that the azimuthal modes have a non-zero entropy perturbation, whilst the translational modes have no entropy variation. In particular, we compare the entropy perturbation with and without the inclusion of viscous heating in the energy equation. Here, we use the configuration of Fig. 5.10(a) again, with parameters $k_2 = 1$, $k_3 = 0$, $R_1 = 7/3$, $R_2 = 10/3$, $\beta = 3 \times 10^3$, $\rho_0 = 1$, and $\mu = 1$, but without incompressible approximation, i.e. $\gamma = 5/3$, at 251 grid points. The compressible

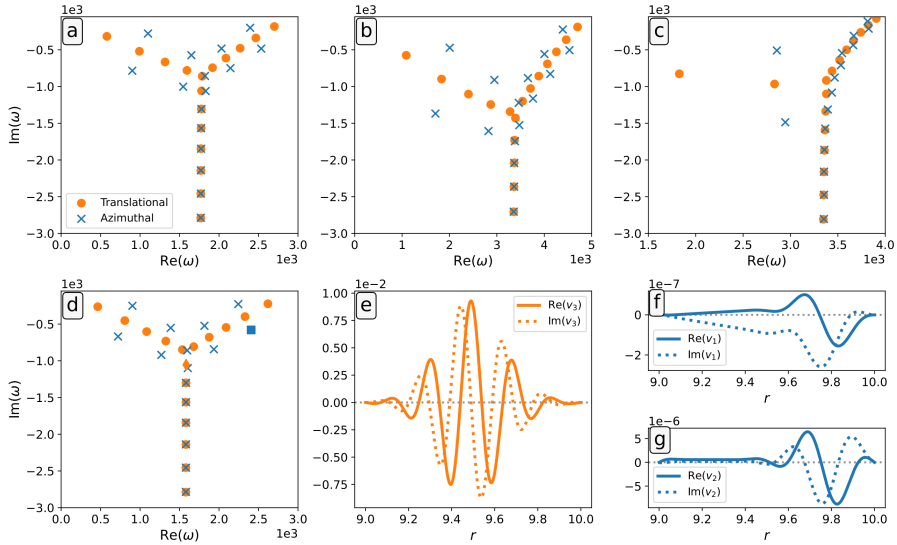


FIGURE 5.10: Parts of the incompressible ($\gamma \rightarrow \infty$) Taylor-Couette spectrum with an inner cylinder at rest ($\alpha = 0$) for $k_3 = 0$, $\rho_0 = 1$, $\mu = 1$, and different parameter choices: (a) $k_2 = 1$, $R_1 = 7/3$, $R_2 = 10/3$, $\beta = 3 \times 10^3$, (b) $k_2 = 2$, $R_1 = 1$, $R_2 = 2$, $\beta = 2.5 \times 10^3$, (c) $k_2 = 2$, $R_1 = 0.25$, $R_2 = 1.25$, $\beta = 2 \times 10^3$, and (d) $k_2 = 3$, $R_1 = 9$, $R_2 = 10$, $\beta = 10^3$. The modes represented by a dot (or \blacklozenge in (d)) are translational modes with v_1 and v_2 numerically zero whilst the crosses (and \blacksquare in (d)) represent azimuthal modes with non-zero v_1 or v_2 components. (e) The v_3 eigenfunction of the translational (d)-eigenvalue $\omega = 1583.50 - 1053.70i$ (\blacklozenge). (f) and (g) show the v_1 and v_2 eigenfunction, respectively, of the azimuthal (d)-eigenvalue $\omega = 2406.82 - 579.55i$ (\blacksquare). Solid lines represent real parts, dotted lines imaginary parts.

spectrum (without viscous heating) is shown in Fig. 5.11(a). It is extremely similar to the corresponding incompressible spectrum in Fig. 5.10(a) and is hardly influenced by viscous heating. The entropy perturbations of an azimuthal mode ($\omega = 2529.12 - 485.63i$ without viscous heating; $\omega = 2529.66 - 485.80i$ with viscous heating; marked by \blacksquare in Fig. 5.11(a)) are shown in Figs. 5.11(b,c) for the compressible case without and with viscous heating, respectively. The viscous heating introduces a limited but noticeable change in the entropy perturbation S .

Viscoresistive plasma slab

As a magnetohydrodynamic test case, consider the incompressible, viscoresistive stability analysis of a plane-parallel plasma slab from Dahlburg et al. (1983),

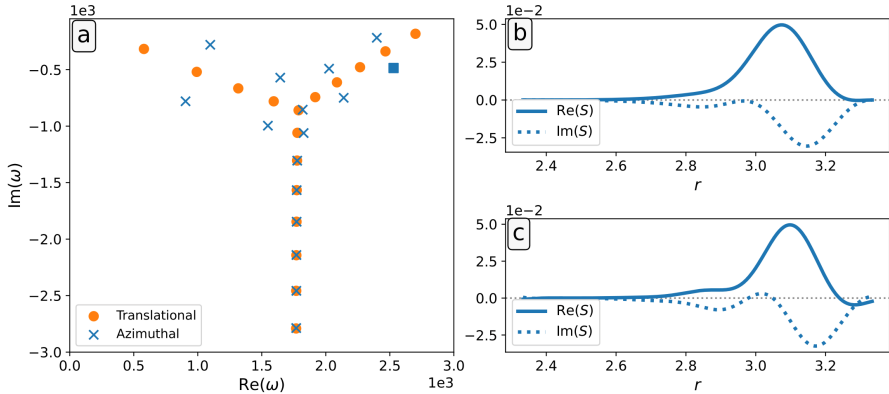


FIGURE 5.11: (a) Part of the compressible Taylor-Couette spectrum, Eqs. (5.15), with parameters $k_2 = 1$, $k_3 = 0$, $R_1 = 7/3$, $R_2 = 10/3$, $\beta = 3 \times 10^3$, $\rho_0 = 1$, and $\mu = 1$. Dots represent translational modes, crosses (and ■) are azimuthal modes. (b) Entropy perturbation S of the azimuthal mode $\omega = 2529.12 - 485.63i$ (■) without the inclusion of viscous heating. (c) Entropy perturbation S of the azimuthal mode $\omega = 2529.66 - 485.80i$ (■) with the influence of viscous heating. Solid lines represent real parts, dotted lines imaginary parts.

with equilibrium magnetic field profile

$$\mathbf{B}_0 = \left(\arctan \alpha x - \frac{\alpha x}{1 + \alpha^2} \right) \hat{\mathbf{e}}_2 \quad (5.17)$$

with parameter α , uniform density ρ_0 , and T_0 positive and satisfying the constant total pressure condition $\partial(\rho_0 T_0 + \frac{1}{2} \mathbf{B}_0^2)/\partial x = 0$. Note that the field is not force-free, and induces a current

$$\mathbf{J}_0 = \alpha \left(\frac{1}{1 + \alpha^2 x^2} - \frac{1}{1 + \alpha^2} \right) \hat{\mathbf{e}}_3, \quad (5.18)$$

which vanishes at $x = \pm 1$, where we introduce perfectly conducting walls with a no slip boundary condition. The simultaneous inclusion of resistivity and viscosity in the linear stability analysis leads to different tearing mode regimes, based on the resistivity η and dynamic viscosity μ coefficients. The formulation in Dahlburg et al. (1983) actually uses the kinematic viscosity $\nu = \mu/\rho$, but since they assume a uniform density and no equilibrium flow, our constant μ formulation is equivalent. The relation between the resistivity η and the kinematic viscosity ν is often expressed in terms of the magnetic Prandtl number $\text{Pm} = \nu/\eta = \mu/\rho_0 \eta$. In the remainder of this section, Pm will vary between 10^{-4} and 10^4 . Note that $\rho_0 = 1$ in all examples in this section, such that the Prandtl number reduces to $\text{Pm} = \mu/\eta$.

In Dahlburg et al. (1983), the authors give numerical values for the purely unstable tearing eigenmode and show the v_{1x} and B_{1x} eigenfunctions of the tearing mode for a few different values of η and μ as well as the evolution of the tearing mode growth rate as a function of η , μ , and the parallel wave number k_2 . Here, we reproduce these results using *Legolas*.

First, we recover the eigenvalues and eigenfunctions for three cases: (a) $\eta = \mu = 10^{-3}$, (b) $\eta = 0.1$, $\mu = 10^{-5}$, and (c) $\eta = 10^{-5}$, $\mu = 0.1$, all with $\rho_0 = 1$, $\alpha = 10$, and $\mathbf{k} = \hat{\mathbf{e}}_2$. Due to *Legolas*'s incompressible approximation, the tearing modes from *Legolas* (ω_L) deviate slightly from those reported in Dahlburg et al. (1983) (ω_D), namely (a) $\omega_L = 0.1965 i$ compared to $\omega_D = 0.19687 i$, (b) $\omega_L = 0.4393 i$ compared to $\omega_D = 0.4397 i$, and (c) $\omega_L = 0.002531 i$ compared to $\omega_D = 0.002537 i$. The v_{1x} and B_{1x} eigenfunctions, defined up to a complex factor and rescaled here for comparison to Figs. 2C, D, and E in Dahlburg et al. (1983), are shown in Figs. 5.12(a-c). The arbitrary complex factor is chosen for each case such that all shown eigenfunctions are real.

Next, we reproduce the evolution of the tearing mode growth rate (d) as a function of η^{-1} for fixed values of μ , (e) as a function of μ^{-1} for fixed values of η , and (f) as a function of k_2 for fixed values of η and μ . In Figs. 5.12(d-f) the tearing growth rate is shown for each configuration of parameters, obtaining the positive growth rates shown in Dahlburg et al. (1983) in their Figs. 6A, 7, and 9, respectively. Once again, they agree very well. Note that each marker represents a single *Legolas* run at 201 grid points.

Unlike Dahlburg et al. (1983), *Legolas* does not only compute the tearing mode, but the entire spectrum. Hence, we can also compare the purely resistive, purely viscous, and truly viscoresistive spectra for the same equilibrium profile, Eq. (5.17). This is shown in Fig. 5.13 for runs at 251 grid points. In this figure, the left column displays the incompressible limit and the right column shows the fully compressible spectra. All spectra are supplemented with the analytical, ideal MHD slow and Alfvén continua, which correspond to singular solutions of the ordinary differential equation obtained through a reformulation of the ideal MHD equations in terms of the x -component of the Lagrangian displacement field. It can be shown for homogeneous backgrounds (see e.g. Goedbloed et al., 2019) that in the presence of resistivity the Alfvén and slow modes trace out semi-circles in the stable part of the spectrum with infinitely degenerate (collapsed) continua. For inhomogeneous resistive spectra the ideal continuum ranges will relocate to collections of discrete modes in the stable half-plane, still resembling the semi-circular curves, as seen in Figs. 5.13(a,d), which will have links to extremal or edge values of the ideal continua. Figs. 5.13(b,e) now show that viscosity exerts a similar influence as resistivity. Finally, Figs. 5.13(c,f) represent modified variants of the semi-circle-like curves in the other panels, due to the combined effects of viscosity and resistivity. Since the ideal slow and Alfvén continua partially overlap and are symmetric with respect

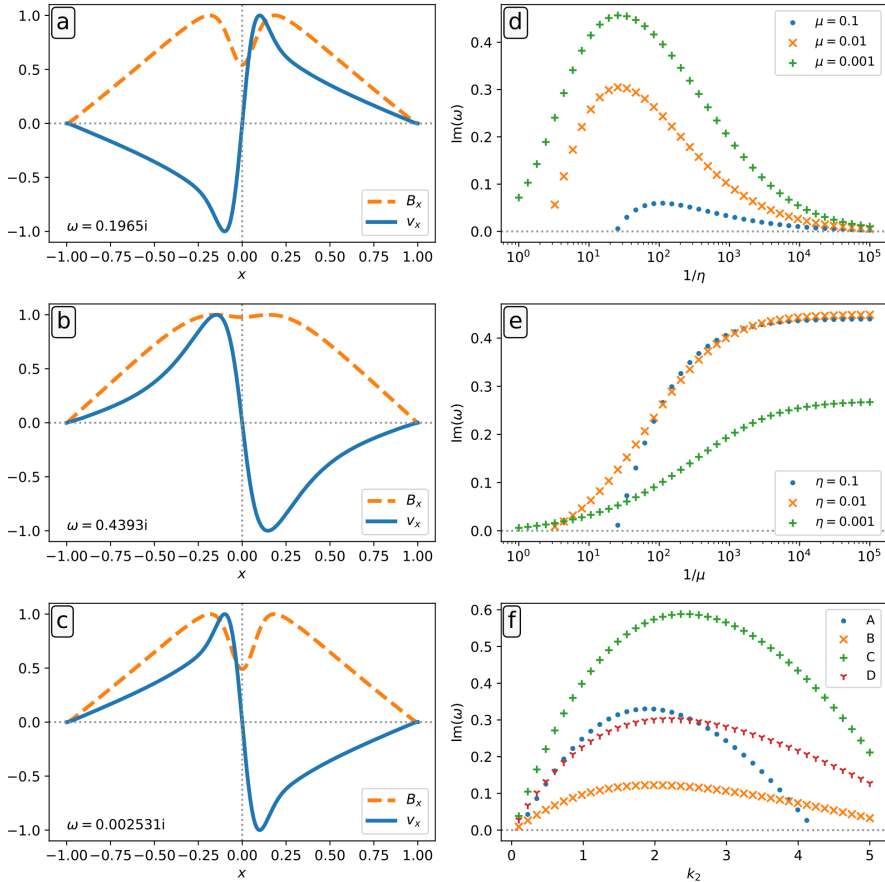


FIGURE 5.12: The v_{1x} and B_{1x} eigenfunctions are shown for the equilibrium Eqs. (5.17) with $\rho_0 = 1$, $\alpha = 10$, $\mathbf{k} = \hat{\mathbf{e}}_2$, and (a) $\eta = \mu = 10^{-3}$, (b) $\eta = 0.1$, $\mu = 10^{-5}$, and (c) $\eta = 10^{-5}$, $\mu = 0.1$. (d) Growth rate as a function of η^{-1} for given values of μ . (e) Growth rate as a function of μ^{-1} for given values of η . (f) Growth rate as a function of $\mathbf{k} = k_2 \hat{\mathbf{e}}_2$ for A) $\eta = 10^{-2}$ and $\mu = 10^{-2}$; B) $\eta = 10^{-3}$ and $\mu = 10^{-2}$; C) $\eta = 10^{-2}$ and $\mu = 10^{-3}$; D) $\eta = 2 \times 10^{-3}$ and $\mu = 2 \times 10^{-3}$.

to the imaginary axis, the slow continuum is only drawn in the left halfplane (red dashed line) and the Alfvén continuum in the right halfplane (cyan solid line). In the left column, the slow continua are eliminated by the incompressible assumption.

The first row of Fig. 5.13 (panels a and d) shows the resistive slab with $\eta = 10^{-3}$. This case is well known and discussed in e.g. Goedbloed et al. (2019). In panel

(a), the Alfvén modes form a semicircle and the slow (magnetoacoustic) modes are eliminated by the incompressible approximation. In the compressible case of panel (d), the slow modes reappear as the inner semicircle. Finally, both the compressible and incompressible spectra feature a resistive tearing mode, as the only purely unstable eigenmode of this system for the chosen parameters.

The second row of Fig. 5.13 (panels b and e) on the other hand shows the viscous case with $\mu = 10^{-3}$. The result looks surprisingly similar to the resistive case, with both the slow and Alfvén modes taking on the same semicircular shape of similar magnitude (note that the axes are scaled identically in panels a, b, d, and e). Whilst there are many minute differences with the resistive case in the first row, the key difference is the absence of a tearing mode in the viscous spectra.

Ultimately, the third row (panels c and f) shows the viscoresistive spectrum with $\eta = \mu = 10^{-3}$. Although resistivity and viscosity exert a similar influence on the slow and Alfvén modes when they are the only physical effect in consideration, the combination of both effects reveals new behaviour in both the (c) incompressible and (f) compressible case. Whilst the slow and Alfvén branches still originate in the same point on the real axis, the semicircular structures are replaced by stretched-out curves along the imaginary axis. The resistive tearing mode is still present, but damped by the viscosity. Therefore, the changes are most pronounced on the stable and damped parts of the spectrum, whose physical relevance must also consider the fact that the ideal MHD equilibrium itself will evolve on a specific diffusive timescale when viscoresistive effects are active.

5.2.2 Viscoresistive Harris sheet

To conclude this chapter on the interaction between flow and resistivity, we return to the Harris sheet to look at the influence of viscosity on the resistive tearing mode, both in the absence and presence of the shear flow, given by Eq. (5.8). Similarly to the previous section, we focus on the resistivity η , the viscosity μ , and the wave number k_2 , where we fix two of them and vary the remaining parameter on the x -axis in Fig. 5.13. The other physical parameters are $\rho_0 = 1$, $B_0 = 1$, and $a_B = 1$. When flow is included, the parameters are $v_0 = 0.1$ and $a_v = 0.8$. Again, a non-uniform grid was used (see App. C.5) on the interval $x \in [-15, 15]$ with parameters $p_1 = 0.75$, $p_2 = 0$, $p_3 = 0.001$, and $p_4 = 2.5$, resulting in 285 grid points.

As expected, the results are very similar to those in Figs. 5.12(d-f). The left column (a-c) of Fig. 5.14, which represents the static case, again shows that viscosity consistently damps the tearing growth rate when compared to the inviscid resistivity scaling in Fig. 5.8(a). The scaling with η in Fig. 5.14(a) for various values of μ is reminiscent of the behaviour observed in Fig. 5.2, for the

direction-varying magnetic field, where the introduction of flow introduced a β -dependent critical resistivity above which the tearing mode vanishes.

Additionally, Fig. 5.14(b) highlights that a stronger resistivity implies a larger growth rate, but also a greater damping, relative to the growth rate size. For extremely high viscosities ($\mu \gtrsim 1$), the instability vanishes. Though it is now apparent that resistivity and viscosity are equally important in determining a system's tearing growth rate accurately for a given wave number, Fig. 5.14(c) accentuates that the growth rate of the most unstable wave number depends on the specific combination of η and μ . In this respect, it is not only their ratio, i.e. the magnetic Prandtl number, that is important, which can be seen by comparing case B with $Pm = 10$ to case C with $Pm = 0.1$, but also the absolute magnitudes, as revealed by comparing cases A and D, which both have a Prandtl number of $Pm = 1$. Furthermore, note that near the wave number of maximal growth the growth rates are ordered from top to bottom by resistivity first and viscosity second. However, since the curves cross, this ordering is not absolute across all wave numbers.

Though the Harris magnetic field profile is comparable to the magnetic field of Dahlburg et al. (1983), we now also added a flow profile in the right column of Fig. 5.14. Comparing both columns immediately reveals that the influence of viscosity is not strongly tied to the presence of a background flow, since both columns are almost identical. However, this is only for one choice of flow parameters, and a more extensive study could be carried out where the velocity parameters and viscosity are varied simultaneously.

5.3 Discussion

As an example of spontaneous reconnection, we systematically investigated the modification of the tearing growth rate subject to equilibrium flow. For two distinctly different slab configurations, a direction-varying magnetic field and a Harris sheet, we focused on the growth rate scaling with resistivity, density, and velocity parameters.

In both cases the growth rate scaling with resistivity seemed to follow a different analytic scaling law than the one predicted based on R_0 (Chen and Morrison, 1990) in the weakly-resistive regime. This discrepancy in scaling may be due to compressibility, which was omitted in the derivation of the analytic scaling laws. Performing the analytic derivation for the compressible equations in *Legolas* could shed more light on this, but is left for future work. Furthermore, the scaling deviated from a simple power law for stronger resistivities, especially in the presence of flow. In the absence of flow, the growth rate was found to decrease gradually with increasing density in the absence of flow. When a flow was introduced however, both configurations featured a critical density above which the tearing mode is damped. Whilst this transition seems to occur near

the density where the (maximal) imposed speed equals the Alfvén speed, the second case made clear that the exact cutoff depends on the parameters of the velocity profile. Unsurprisingly then, it was shown that the maximal equilibrium speed is not the only parameter to determine the flow's influence on the tearing growth rate, but it interacts with other parameters, such as the plasma- β and flow shear width.

In addition, the tearing mode's linear perturbation of the magnetic field was superimposed on the equilibrium field for the Harris sheet to trace the field lines of the total magnetic field, revealing the perturbed topology. As it turns out, the linear perturbation is insufficient to explain the appearance of large magnetic islands in simulations, though there appears to be a way to evolve towards singular plasmoids through additional reconnection events. To test this hypothesis, the linearly perturbed magnetic topology could be entered into a non-linear code, e.g. *MPI-AMRVAC* (Keppens et al., 2023, see <https://amrvac.org>), and allowed to evolve in time, to see whether it evolves towards a single plasmoid.

To validate the implementation of the viscosity module, we first accurately reproduced the spectrum and eigenfunctions of an incompressible, hydrodynamic Taylor-Couette flow in a cylindrical setup, taken from Gebhardt and Grossmann (1993), with the newly implemented incompressible approximation. As a second test case, we considered the Cartesian, magnetohydrodynamic equilibrium with finite resistivity from Dahlburg et al. (1983), where we reproduced their results concerning the interplay of viscous and resistive effects on the growth rate of the resistive tearing instability.

As an extension of their results, we showed that the full resistive and viscous spectrum are extremely similar, with the prominent distinction that the viscous spectrum does not have an unstable tearing mode. The combination of viscous and resistive effects was mostly seen in the stable part of the spectrum, and its role in non-linear evolutions warrants further exploration. However, since both viscosity test cases used the incompressible approximation, which eliminates the energy equation, the viscous heating term did not play a role. For one selected Taylor-Couette case it was shown that the viscous heating did not significantly alter the spectrum, but had a limited influence on the entropy perturbation. In a final application, viscosity was added to the Harris current sheet, but the effect was mostly identical to viscosity's effect on the configuration of Dahlburg et al. (1983).

The flexible *Legolas* implementation allows for future linear stability studies with or without viscous heating. Such viscoresistive stability studies of magnetised Taylor-Couette setups can be very important for aiding the interpretation of dynamo experiments (Willis and Barenghi, 2002; Rüdiger et al., 2007), and especially to determine when the MRI is sufficiently suppressed by viscoresistive effects (Eckhardt and Herron, 2018) to create stable configurations.

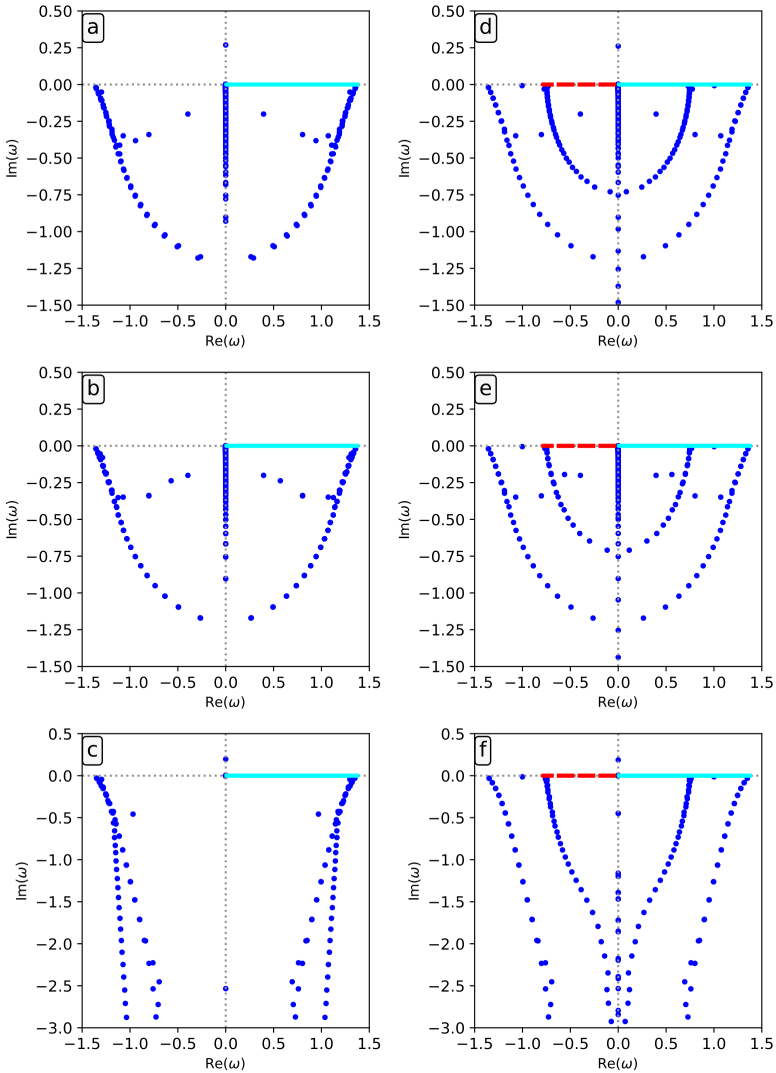


FIGURE 5.13: Comparison of spectra for equilibrium Eqs. (5.17) for resistive (a, d), viscous (b, e), and viscoresistive (c, f) cases. The left column (a, b, and c) represents the incompressible approximation, the right column (d, e, and f) the compressible equations. All runs use parameters $\mathbf{k} = \hat{\mathbf{e}}_2$, $\rho_0 = 1$, and $\alpha = 10$. In case of resistivity (viscosity), the parameter is $\eta = 10^{-3}$ ($\mu = 10^{-3}$). The cyan solid and red dashed lines represent the ideal MHD Alfvén and slow continua, respectively. Both continua are symmetric with respect to the imaginary axis, but only shown in one halfplane to avoid overlap.

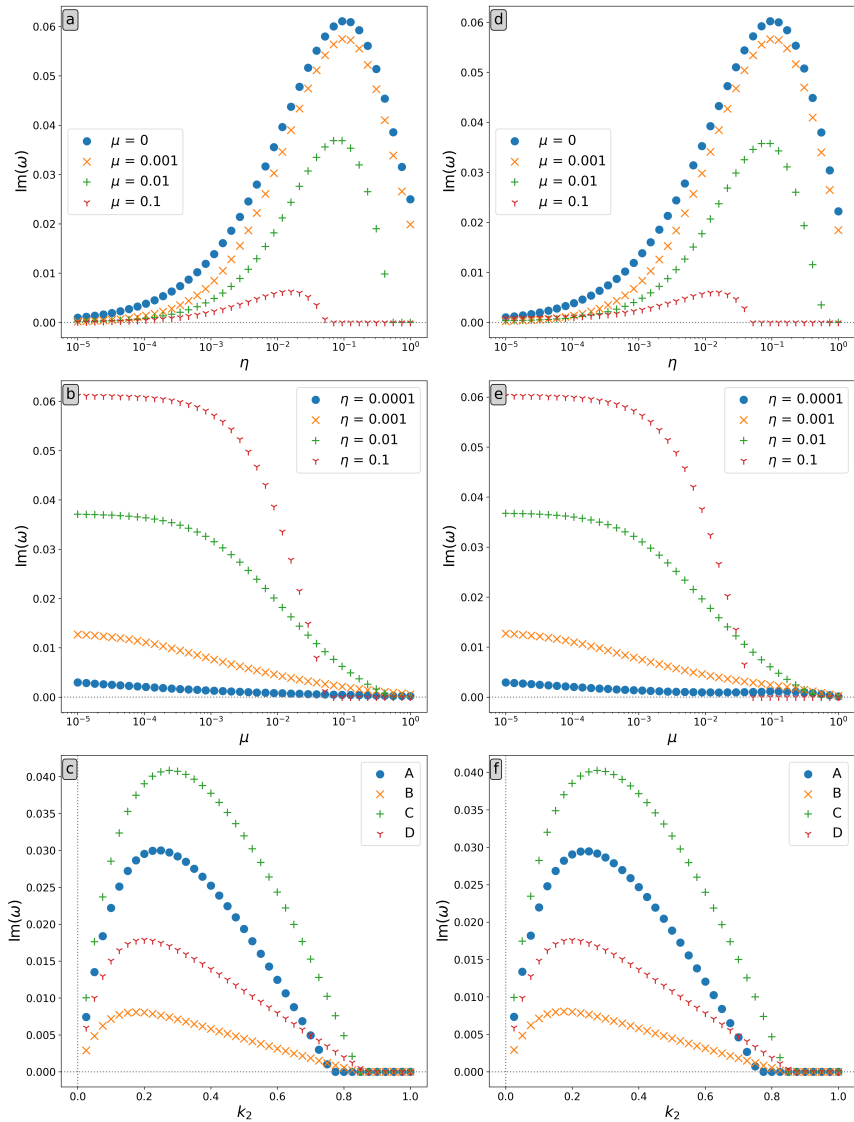


FIGURE 5.14: On the left (a-c), the tearing growth rate in the absence of flow. On the right (d-f), a background flow with $v_0 = 0.1$ and $a_v = 0.8$ is present. (a, d) Growth rate as a function of η for given values of μ and $\mathbf{k} = 0.5 \hat{\mathbf{e}}_2$. (b, e) Growth rate as a function of μ for given values of η and $\mathbf{k} = 0.5 \hat{\mathbf{e}}_2$. (c, f) Growth rate as a function of $\mathbf{k} = k_2 \hat{\mathbf{e}}_2$ for A) $\eta = 10^{-2}$ and $\mu = 10^{-2}$; B) $\eta = 10^{-3}$ and $\mu = 10^{-2}$; C) $\eta = 10^{-2}$ and $\mu = 10^{-3}$; D) $\eta = 2 \times 10^{-3}$ and $\mu = 2 \times 10^{-3}$.

Real stupidity beats artificial intelligence every time.

— Ridcully, in *Hogfather*
(Terry Pratchett)

6

Classification of *Legolas* data with neural networks

The results in this chapter were obtained in close collaboration with M.D. Kuczyński during a three-week research stay at the Max-Planck-Institut für Plasmaphysik in Greifswald, Germany, and further refined afterwards. Parts of this chapter have been included in a paper submitted to Computer Physics Communications.

As demonstrated in the last two chapters, the *Legolas* code is a great tool to investigate the linear eigenmodes and stability of a given system. In most of the applications discussed so far we were either interested in one particular instability or in separate wave categories (e.g. the translational and azimuthal modes in Taylor-Couette flow, Dahlburg et al., 1983, discussed in Sec. 5.2.1). Both instances present their own use case for neural network-aided classification. In a configuration featuring multiple discrete modes of interest (potentially instabilities) it may become hard to track a particular mode during the exploration of the parameter space. Alternatively, in a setup with various physical effects we may want to explain which physical effect is causing certain behaviour. Hence, we are interested in a method to separate modes of interest from the rest and to provide an initial guess for a mode's origin. Here, we explore the option of a supervised convolutional neural network, based on the results of Kuczyński et al. (2022), to aid in the analysis of MHD spectroscopic results by classifying modes into three classes. Whilst the particular network here is only applicable for one specific plasma configuration, in the future the same methodology can be applied to any desired application, for any amount of

classes.

The other use case would be to employ a neural network to cluster data into classes with similar features (such as the translational and azimuthal Taylor-Couette modes) without human intervention. Whilst we do not present any results of this unsupervised approach here, it also provides a promising research avenue.

6.1 Instabilities in jets

For this exploration of neural network classification of MHD eigenmodes, we consider a configuration in ideal MHD with flow from Baty and Keppens (2002), namely a jet with shear axial flow embedded in a helical magnetic field. The equilibrium assumes a constant density ρ_0 and velocity, magnetic field, and temperature profiles

$$\mathbf{v}_0(r) = \frac{V}{2} \tanh\left(\frac{R_j - r}{a}\right) \hat{\mathbf{e}}_3, \quad (6.1)$$

$$\mathbf{B}_0(r) = B_\theta \frac{r/r_c}{1 + (r/r_c)^2} \hat{\mathbf{e}}_2 + B_z \hat{\mathbf{e}}_3, \quad (6.2)$$

$$T_0(r) = T_a - \frac{B_\theta^2}{2\rho_0} \left(1 - \frac{1}{[1 + (r/r_c)^2]^2}\right), \quad (6.3)$$

where V is the asymptotic velocity, R_j the jet radius, a the radial width of the shear layer, r_c the characteristic length of the radial magnetic field variation, B_θ and B_z magnetic field strength parameters, and T_a the temperature at the jet axis.

Now, the associated spectrum contains (up to) two clearly distinct types of instabilities: one Kelvin-Helmholtz instability (KHI) and a parameter-dependent amount of current-driven instabilities (CDI). The spectra for two distinct parameter choices are shown in Fig. 6.1(a,b) at 151 grid points. In Fig. 6.1(a) the KHI and the series of CDI are indicated. Whilst they are easily identifiable in this first case by their position in the spectrum, this is harder for the case in Fig. 6.1(b), where some modes are not fully resolved at this resolution. In general, we identify the instabilities by their eigenfunction behaviour. The real part of the ρ -eigenfunction of the KHI, visualised in Fig. 6.1(c), is characterised by a strong perturbation at the jet boundary ($r = R_j$) whereas CDIs are characterised by oscillatory behaviour inside the jet ($r < R_j$), as illustrated in Fig. 6.1(d).

For this study, 240 *Legolas* runs of this configuration were performed in the interval $r \in [0, 2]$ for various values of V . These values and the remaining

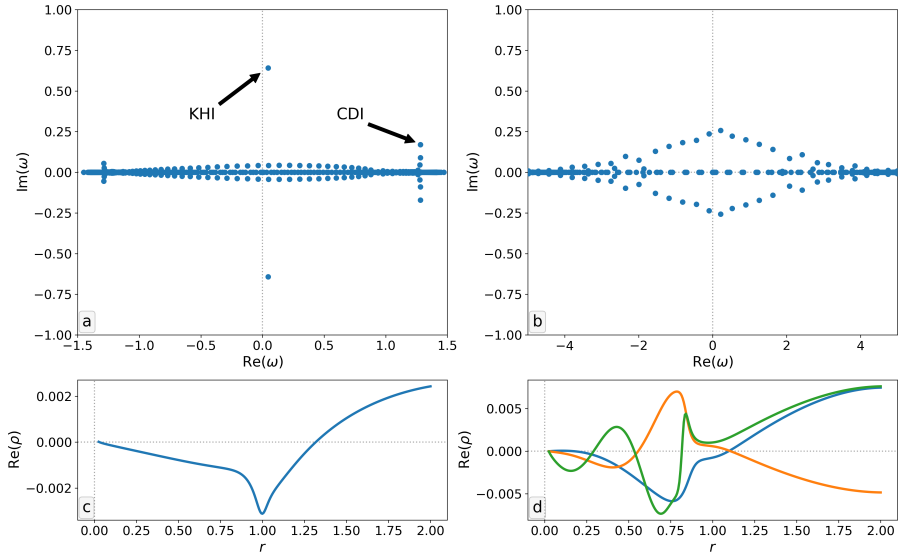


FIGURE 6.1: Spectra of configuration Eqs. (6.1-6.3) for parameters (a) $V = 1.72$ and $k_3 = 1.5$; (b) $V = 1.863$ and $k_3 = 6.5$. (c) $\text{Re}(\rho)$ -eigenfunction of the KHI in (a). (d) $\text{Re}(\rho)$ -eigenfunction of the three fastest growing CDIs in (a).

TABLE 6.1: Parameters of the data used in this study. The upper table shows the different values of V in the data set. The parameters in the lower table were identical in all cases.

V	1.29	1.43	1.5767	1.72	1.863	2.0067											
N	151	R_j	1	r_c	2	a	0.1	B_θ	1	B_z	0.25	T_a	1	ρ_0	1	k_2	-1

parameters' concrete values are given in Table 6.1. For each value of V , k_3 was varied from 0.5 to 7 in increments of $1/6$.

6.2 Mathematical framework

In this section we describe the applied classification algorithm to which the KHI and CDI classification problem belongs. Subsequently, a short primer on neural network architecture introduces the transformations employed in our network. Finally, we discuss maps under which the classification algorithm is invariant, and their importance in data generation and testing.

6.2.1 Statement of the problem

The goal of classification algorithms is to associate a label $l \in L$ with an input $x \in E$. Mathematically, this is a function from E to L ,

$$\text{Class} : E \rightarrow L. \quad (6.4)$$

Here, we aim to realise this mapping via a supervised machine learning algorithm and a subsequent, user-informed optimisation procedure.

6.2.2 Neural network construction

Our research question now becomes if this classification function can be satisfactorily approximated by a neural network. To address this question, we first need to understand how a neural network is generally structured. Subsequently, a brief overview of the precise hidden layers employed in our architecture is presented.

General maps

In general, a neural network is a function that takes some input, transforms the input with a series of operations, and returns a certain output. The operations occurring between the input and output are grouped in hidden layers. In each layer, at least two operations are combined: an affine transformation and a non-linear function.

Affine transformations are simple (matrix) operations of the form $\mathbf{W}\mathbf{x} + \mathbf{b}$, where \mathbf{x} represents the data (unaltered, or transformed by previous layers), \mathbf{W} the weights matrix and \mathbf{b} the so-called bias vector. The matrices \mathbf{W} and biases \mathbf{b} are the quantities that are optimised during the network training. However, the combination of such transformations is again affine and thus linear. To introduce non-linearity in a network, a non-linear function is applied pointwise after an affine transformation. These non-linear maps σ are termed activation functions (Erdmann et al., 2021). Taking both steps into account a layer L can thus be written as a transformation

$$L(\mathbf{x}) = \sigma(\mathbf{W}\mathbf{x} + \mathbf{b}). \quad (6.5)$$

Affine layers

In the affine transformations we differentiate between two operations in our network.

Dense. As the name implies, dense layers represent an affine transformation without any restrictions. This means that any computational unit, called a

node, in this layer is affected by all the nodes in the previous layer. Hence, they are referred to as a densely connected or fully connected layers (Chollet, 2018). Thinking in terms of matrix multiplication, it means that \mathbf{W} is a dense matrix, i.e. it contains few zero elements, if any. This is computationally expensive and is thus usually relegated to the final layers of a network, after some data reduction has already taken place.

Convolution. Whilst the fully connectedness of dense layers leads to the recognition of global features, convolution layers focus on local patterns. Each node in a convolution layer is only informed by a predefined number of nodes from the previous layer, which lie close to each other (Chollet, 2018). For an image (or equivalently, a matrix), a convolution layer applies an affine transformation to a rectangle of $p \times q$ pixels to assign a value to a pixel in the new layer. Pixel by pixel, the rectangle shifts across the entire image and computes a new pixel value with each step, thus constructing another image (Erdmann et al., 2021). In this way, a convolution layer takes into account the correlation of nearby pixels (Bishop, 2006). Note that the dimensions of the resulting “convoluted image” are smaller than those of the original image.

Activation functions

Contrary to affine transformations, which act on the data as a whole, activation functions are applied pointwise. Whilst various activation functions exist, our network employed only two: ReLU and sigmoid activations.

ReLU. In convolutional networks, the rectified linear unit (ReLU) function is the generally accepted default, partly due to its low computational cost. It simply leaves positive values unaffected and sets negative values to zero, i.e. $\text{ReLU}(z) = \max\{0, z\}$ (Goodfellow et al., 2016). When preceded by an affine transformation, the bias \mathbf{b} acts as a threshold for data to be passed on (Erdmann et al., 2021).

Sigmoid. In the context of activation functions the name sigmoid refers to the logistic sigmoid function

$$\sigma(x) = \frac{1}{1 + \exp(-x)}. \quad (6.6)$$

The main use case of this function is the confinement of data to the interval $(0, 1)$ to avoid divergences (Goodfellow et al., 2016).

Network improvements

Besides the actual transformations, both linear and non-linear, neural networks can also incorporate layers whose purpose mostly relates to the network's performance during training. The examples discussed here all featured in the final architecture.

Batch normalisation. In neural networks, the training process is executed in steps, with each step presenting a new batch of data. Normalisation of the data aims to accelerate the learning process by making data batches appear more similar. One particularly successful approach, named batch normalisation, calculates the data's mean μ and standard deviation σ and reparametrises it as $\bar{x} = (x - \mu)/\sigma$ inbetween an affine transformation and the following activation (Ioffe and Szegedy, 2015; Goodfellow et al., 2016; Chollet, 2018).

Dropout. To improve a network's stability, the dropout method is often adopted during training. When a dropout rate $p\%$ is administered to a layer, $p\%$ of the nodes of the previous layer that are used in the current calculation are arbitrarily set to zero during the calculation, thus effectively removing connections to the prior layer at random. As a consequence, subnetworks of the total network are trained separately, but inherit parameters from the parent network, thus creating overlap in their parameter space. After training concludes, the network uses all connections and the dropouts have no effect anymore (Goodfellow et al., 2016; Chollet, 2018; Erdmann et al., 2021).

Pooling. Similarly to a convolution layer, a pooling operation takes a volume of predetermined size (e.g. $p \times q$ pixels in an image) and reduces it to a single value in a fixed way. Unlike convolution, these volumes generally do not overlap (Erdmann et al., 2021). In our case, the average pooling returns the average value of each volume. This drastically scales down the data size and makes the representation mostly invariant to small changes in input (Goodfellow et al., 2016; Chollet, 2018).

6.2.3 Class preserving maps

Before concluding this section with hwo the input and output are handled, we present the idea of class preserving maps, which are a useful tool during the training and final filtering steps of the classification procedure.

Firstly, let $E_l \subset E$ be a subspace such that $\text{Class}(x) = l$ for all $x \in E_l$. An element of this space is denoted as x_l . Consider the set of maps U_l from that space E_l to itself, an element of which is denoted as $u_l : E_l \rightarrow E_l$. It is clear that $\text{Class}(u_l(x_l)) = l$. Now suppose that u_l does not have any fixed points, i.e. $\forall x_l : u_l(x_l) \neq x_l$. Then, for any training data point x_l , we can extend the

training data set by the element $u_l(x_l)$ provided that u_l is known. A map u_l may contain fixed points however, and thus care should be taken not to include repeated elements in the data set, which could introduce an imbalance in the training data.

Secondly, consider the set of maps U from E to itself that preserve the class label. Denoting such a map by u , we have

$$u : E \rightarrow E \text{ such that } \forall x \in E : \text{Class}(u(x)) = \text{Class}(x). \quad (6.7)$$

In addition to having the utility of extending the data set as described above for U_l , these maps have another application. Let x be an input whose class label is unknown. Rather than making a prediction on a single input x , one can also compare it with $u(x)$ which, in an ideal scenario, should result in the same label. The user is then able to choose a prediction dependent on their preferred filtering scheme. If the model is free from systematic errors this results in a higher likelihood of correct classification.

6.2.4 Handling of multiple inputs and decision making

In some applications, the input x is an ordered tuple. This could be, for example, a text-image pair or, as in our problem, an eigenvalue-eigenfunction pair $(\omega, \mathbf{f}_\omega)$. In such scenarios, it is common to implement separate branches for different constituents of the input (e.g. Boldeanu et al., 2021). In our model we first extract convolutional features of \mathbf{f}_ω in a separate branch, which results in a reduced representation $\bar{\mathbf{f}}_\omega$. Then, ω is simply concatenated with $\bar{\mathbf{f}}_\omega$. The combined result $(\omega, \bar{\mathbf{f}}_\omega)$ is then further fed into a regular neural network that in the end returns the probability of each class label l . Then, probability thresholds are optimised in order to maximise the chosen metric which judges the performance of the model. Finally, once the neural network is trained and the thresholds are chosen, a filtering scheme is incorporated based on the previously defined, class preserving maps $u^i \in U$. The complete scheme is shown in Fig. 6.2.

6.3 Application to *Legolas* jet data

Before diving into the network architecture, we return to the data structure, and how the data is expanded with the use of class preserving maps. Then, the network layers and architecture are presented in more detail. Finally, the approach to optimising the results with a filtering procedure is discussed.

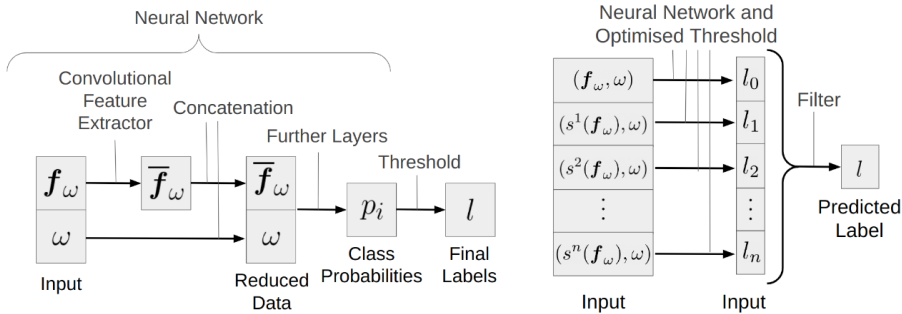


FIGURE 6.2: A schematic of the Eigenfunction Classification Algorithm (ECA).

6.3.1 Data generation

Since all 240 *Legolas* runs were performed on $N = 151$ grid points, each file contains $16N = 2416$ eigenmodes. Every eigenmode has 8 associated complex eigenfunctions discretised on a grid of $2N - 1 = 301$ grid points. Hence, the network accepts

1. an eigenfunction input as a complex matrix \mathbf{f}_ω of dimensions 301×8 , and
2. an eigenvalue input as a real 2-vector $(\text{Re}(\omega), \text{Im}(\omega))$.

We decided to use 80% (192) of these runs for training, 10% (24) for validation, and 10% for testing. The division of the files across the three categories was randomised.¹

The resulting data leaned heavily towards “uninteresting” modes (class 0), i.e. modes that are neither KHI (class 1) or CDI (class 2), with uninteresting modes ranging from 97% to 99.9% of all modes in each run. Therefore, we utilised the technique of class preserving maps, described in Sec. 6.2.3, in order to extend the data set. We defined the following maps:

1. multiplying the eigenfunctions by a complex phase factor,

$$u : E \rightarrow E : (\omega, \mathbf{f}_\omega) \mapsto (\omega, e^{i\theta} \mathbf{f}_\omega) \text{ with } \theta \in (0, 2\pi); \quad (6.8)$$

2. superposition.

The first map is class preserving because eigenfunctions are only determined up to a complex factor. The eigenfunctions are Fourier amplitudes $\hat{\mathbf{f}}_1(u_1)$ however, so the superposition of eigenfunctions is not a solution of the underlying physical problem. Nevertheless, a superposition of Fourier amplitudes is a proper

¹The exact distribution can be found at the end of this chapter.

superposition if $u_2 = u_3 = t = 0$ in the Fourier exponential in Eq. (4.6). Hence, it shares the characteristics of the modes it is constructed from and superposition should be a class preserving map.

In short, an artificial mode of a chosen class is constructed from pairs of modes $(\omega_1, \mathbf{f}_{\omega_1}), (\omega_2, \mathbf{f}_{\omega_2})$ of that class as

$$\mathbf{f}_{\omega_{\text{artificial}}} = e^{i\theta_1} \mathbf{f}_{\omega_1} + e^{i\theta_2} \mathbf{f}_{\omega_2}, \quad (6.9)$$

where θ_1, θ_2 are arbitrary phases. In addition, we use the average of the eigenvalues, i.e. $\omega_{\text{artificial}} = \frac{1}{2}(\omega_1 + \omega_2)$, as the eigenvalue associated with the artificial eigenfunction matrix. Note that the average of the eigenvalues has no physical bearing whatsoever, but its role in the network was assumed to be limited to informing the network of whether the mode was stable or unstable. During training, 25% of the modes in each batch belonged to class 0 and 37.5% to classes 1 and 2 each. 90% of the class 1 and 2 training data were artificial of the form Eq. (6.9) whereas the other 10% were of the form $e^{i\theta} \mathbf{f}_\omega$ for an arbitrary phase θ to avoid any bias effects from *Legolas*'s eigenfunction normalisation algorithms. In the validation step the three classes were represented equally and all modes were of the latter form (only including an arbitrary phase).

6.3.2 Network architecture

As visualised in Fig. 6.3, where the layers discussed here are marked with a symbol (*, †, ‡), the network architecture consists of two major blocks: one with only the eigenfunction information (\mathbf{f}_ω) and one with the addition of the eigenvalue (ω), which is added in the + layer. Before the concatenation with the eigenvalue, global average pooling (‡) reduces the representation $\bar{\mathbf{f}}_\omega$ (after convolution) to a vector. In the \mathbf{f}_ω branch (first block) weights layers (*) are convolution layers whilst in the $(\omega, \bar{\mathbf{f}}_\omega)$ branch (second block) they represent dense layers. Each dense layer includes a sigmoid activation. For dropout layers (†) a value of 0.1 was used.

6.3.3 Probability thresholds and performance metric

Ultimately, the goal is to extract the modes of interest from a large volume of data, which contains predominantly uninteresting modes. Hence, the final model should only dismiss a handful of interesting modes as uninteresting whilst eliminating the majority of truly uninteresting modes. To evaluate a model's performance we employ two metrics: precision and recall. Here, precision is the ratio of true positives (= modes marked as interesting that are indeed interesting) to all positives (= all modes marked as interesting) and recall is the ratio of true positives to the sum of true positives and false negatives (= modes marked as uninteresting that are actually interesting).

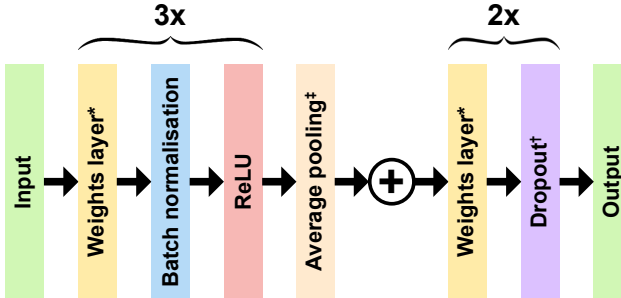


FIGURE 6.3: Diagram of the neural network.

After training the network, we denote the network's predicted probabilities for each class as (p_0, p_1, p_2) . For thresholds a and b , we first check if $p_1 \geq a$. If so, we predict class 1. If not, we compare p_2 to b . If $p_2 \geq b$, we predict class 2. If not, we predict class 0. To improve the classification algorithm, these thresholds a and b are optimised by imposing a desired recall value on the validation data and looking for the associated maximal precision as a function of a and b .

6.3.4 Filtering

Once the thresholds for a and b are established, the eigenfunctions of the testing data can again be subjected to the class preserving maps that multiply with a phase factor. The resulting data couples $(\omega, e^{i\theta} f_\omega)$ are evaluated by the network and classified according to the thresholds a and b . Doing this for m different phases θ_k ($k = 1, \dots, m$) gives us a total of $m + 1$ predictions for each mode's label (including the unmodified data). Subsequently, the final label is the label that was predicted the most often, with ties broken by interesting over uninteresting and if decidedly interesting, class 1 taking precedence over class 2.

6.4 Results

After training the network on 900 batches of 512 modes each, the a and b thresholds for class 1 and 2 categorisation were optimised demanding a minimal recall value of 0.9 on the validation data. The testing data was then subjected to four arbitrary phase shifts to obtain a total of 5 predictions for each mode. For each mode, the label that was predicted the most often was assigned, with ties broken first in favor of class 1, then class 2. The resulting confusion matrix

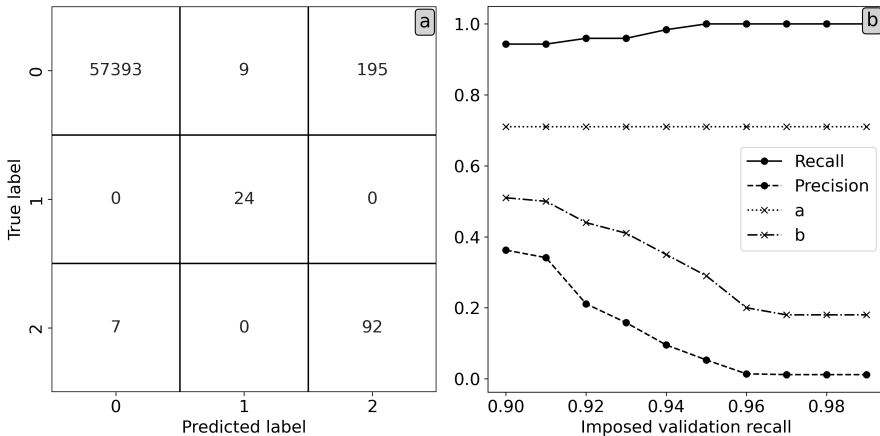


FIGURE 6.4: (a) Confusion matrix for a minimal recall of 0.9 on the validation data. (b) Recall, precision, and thresholds as functions of the imposed validation recall.

is shown in Fig. 6.4(a). The network thus achieves a recall of 0.943 and a precision of 0.3625, meaning that of the modes classified as 1 or 2 slightly more than 1/3 is truly interesting, whilst about 6% of all modes of interest were lost. By imposing different minimal validation recall values, we can control how many interesting modes can be lost. Of course, adapting the validation recall also changes the recall, precision, and threshold (a , b) values. For varying validation recall values, the recall, precision, and thresholds are visualised in Fig. 6.4. Unsurprisingly, higher validation recall values lead to higher recall and lower precision and threshold values. As the graph shows, the final recall is consistently higher than the imposed validation recall, with a validation recall of 0.95 sufficing to achieve a perfect recall (at the cost of lower precision though). It is remarkable however that the a threshold remains constant at a high value of 0.71 for varying recall values. This implies that the network assigns high probabilities to class 1 if the mode is truly a class 1 mode. It also means that if the minimal validation recall is increased to 0.95, there are no additional modes mislabelled as class 1, and the decrease in precision is solely due to the misclassification of class 0 modes as class 2 modes.

Returning to the confusion matrix, two more elements stand out. Firstly, the lower right 2×2 submatrix is diagonal. Hence, the network clearly distinguishes between class 1 and class 2 modes. This is in line with initial expectations, based on the eigenfunction shapes, like those shown in Fig. 6.1(c,d), which show strong behaviour at the jet boundary for KHI modes in contrast with the CDI behaviour in the jet's interior. Secondly, the number of class 0 modes that were misclassified as class 1 is much smaller than the number misclassified as class

2. In addition, all class 1 modes were correctly identified as such and the class 1 precision equals 0.75, highlighting that the network is better at identifying class 1 than class 2 modes.

6.5 Conclusion

Due to the large amount of eigenmodes of a single plasma configuration (one run of the MHD spectroscopic code *Legolas*), visual inspection of the modes to identify characteristics can be a monotonous and time-consuming task. In this chapter we have applied a convolutional neural network to a non-binary classification problem of ideal MHD eigenmodes in astrophysical jets, analysed with *Legolas*. For a recall of 94.3% the neural network left 0.55% of all modes for manual inspection. Furthermore, the neural network never confused class 1 and 2 modes in the test data. Since even this relatively simple network provided good results already, we conclude that neural networks offer a great opportunity for automated mode detection in *Legolas* data. To reach even better metrics, more intricate network architectures could be explored in the future, like residual neural networks (He et al., 2016), which allow for deeper networks (more layers) by simplifying the learning process (Chollet, 2018; Erdmann et al., 2021).

A significant drawback of the supervised approach however is of course the need for a large set of pre-classified data for training purposes. To sidestep this issue, future investigations could focus on unsupervised clustering algorithms to search for structures in *Legolas* data, like the translational-azimuthal distinction in Taylor-Couette flows (Dahlburg et al., 1983) or the surface-body wave dichotomy in flux tubes (Edwin and Roberts, 1983).

Finally, it remains an open question whether a generally-applicable neural network for *Legolas* data is possible. In particular, is it feasible to develop a neural network that can predict which physical effect, like shear flow or resistivity, is responsible for each instability in a spectrum? In this regard, another hurdle to overcome is that a generally-applicable network should work for various grid resolutions, unlike the network presented here. These questions are left for future research.

Data availability. The data set is publicly available on Kaggle as De Jonghe (2023). The files that were reserved for validation and testing are listed in Table 6.2.

TABLE 6.2: Files in the data set used for validation and testing. The remaining files were used for training.

Validation	Testing
0001-HEL1-V14333.dat	0003-HEL1-V17200.dat
0002-HEL1-V14333.dat	0007-HEL1-V12900.dat
0002-HEL1-V18633.dat	0007-HEL1-V14333.dat
0003-HEL1-V15767.dat	0009-HEL1-V17200.dat
0003-HEL1-V18633.dat	0009-HEL1-V20067.dat
0004-HEL1-V14333.dat	0013-HEL1-V15767.dat
0008-HEL1-V14333.dat	0016-HEL1-V14333.dat
0009-HEL1-V18633.dat	0017-HEL1-V20067.dat
0010-HEL1-V14333.dat	0018-HEL1-V20067.dat
0012-HEL1-V17200.dat	0026-HEL1-V12900.dat
0016-HEL1-V15767.dat	0026-HEL1-V14333.dat
0017-HEL1-V17200.dat	0026-HEL1-V15767.dat
0018-HEL1-V14333.dat	0028-HEL1-V20067.dat
0019-HEL1-V15767.dat	0029-HEL1-V14333.dat
0020-HEL1-V14333.dat	0030-HEL1-V12900.dat
0020-HEL1-V15767.dat	0031-HEL1-V20067.dat
0026-HEL1-V17200.dat	0032-HEL1-V20067.dat
0027-HEL1-V15767.dat	0034-HEL1-V12900.dat
0028-HEL1-V15767.dat	0035-HEL1-V17200.dat
0030-HEL1-V20067.dat	0037-HEL1-V15767.dat
0034-HEL1-V20067.dat	0037-HEL1-V18633.dat
0036-HEL1-V18633.dat	0039-HEL1-V14333.dat
0037-HEL1-V14333.dat	0039-HEL1-V17200.dat
0038-HEL1-V15767.dat	0040-HEL1-V15767.dat

*Now tell me what happened—in words. I want
your translation of the mathematics.*

— The First Speaker, in *Second Foundation*
(Isaac Asimov)

7

Conclusion & Outlook

If we consider the theoretical description of electron oscillations by Langmuir (1928); Tonks and Langmuir (1929) as the starting point of modern plasma physics theory, this research domain is less than a century old, but has booked remarkable progress in that time. Various models have since been developed to describe plasma behaviour on different scales, from the macroscopic MHD model to the microscopic kinetic description. The past century also saw the rise of computers and the accompanying computational methods, evolving alongside the emerging field of plasma physics. Nowadays, research in theoretical plasma physics is characterised by a strong emphasis on non-linear, time-evolving simulations, often requiring a lot of computational resources to achieve satisfactory resolutions.

In this thesis however, we took a step back and chose to focus on linear theory instead. With the realisation of the importance of two-fluid effects in reconnection layers such as the Harris sheet, whose thickness is on the order of the ion skin depth, simulations have started to move to HMHD and two-fluid models to capture these physics (Yamada et al., 2010). Though, as our analysis of the ion-electron model shows, many open questions persist even in linear theory. In addition, the application of numerical methods to linearised equations, such as the spectroscopic approach of the *Legolas* code, also remains a valuable technique to investigate how a system may evolve.

Prospects of the ion-electron analysis

Whilst most textbooks discussing two-fluid waves derive dispersion relations from a dielectric tensor formulation, concentrating on propagation parallel or perpendicular to the magnetic field, it was shown by Keppens and Goedbloed (2019b) that the polynomial formulation is equivalent. This dispersion

relation improves on the literature by offering an intuitive description across all propagation angles. Contrary to the convoluted naming conventions in the literature, which are based on properties at parallel and perpendicular propagation, the SAFMOX labelling scheme naturally arises from the polynomial relation due to the natural frequency ordering at oblique angles. Only at exactly parallel or perpendicular propagation are modes allowed to cross in the frequency-wave number diagram, highlighting the exclusive status of these angles.

At oblique angles all crossings are replaced by avoided crossings. From the group speed diagrams it is clear that avoided crossings are a type of critical point where transitions in a mode's behaviour occur, as evidenced by the reconnection of group speed curves when the wave number traverses an avoided crossing. Results by Huang and Lyu (2019) seem to imply that avoided crossings can also mark transformations of mode behaviour between electrostatic ($\omega \mathbf{B}_1 = \mathbf{k} \times \mathbf{E}_1 = 0$) and electromagnetic characteristics. A follow-up study regarding electrostatic and electromagnetic behaviour could extend the warm pair plasma results from Keppens et al. (2019) to the ion-electron plasma adopting the same methodology. Whilst analytic expressions may be obtainable for parallel and perpendicular propagation, we may have to resort to a numerical approach at intermediate propagation angles though. Similarly, how the polarisation changes along a mode curve, and especially past an avoided crossing, lends itself to investigation equally well. Additionally, our discussion on Faraday rotation in the Appleton-Hartree limit can likewise be extended to the full ion-electron model at any angle.

A meaningful extension of the ideal ion-electron treatment here is the inclusion of effective collision frequencies, both between species (ion-electron collisions) as within each species (ion-ion and electron-electron collisions), to handle the resistive damping of waves. The former type of interaction can be effectuated by introducing a collision term proportional to their velocity difference in both momentum equations (Goedbloed et al., 2019) whilst it suffices to perform the mass substitution $m_s \mapsto m_s(1 + i\nu_s/\omega)$ for intraspecies collisions of species s with a collision rate ν_s (Gurnett and Bhattacharjee, 2005; Kulsrud, 2005). Presumably, damping does not occur equally across all modes, and may depend on the wave number and frequency, again identifying avoided crossings as points of interest. Whilst a significant model extension on its own, application to whistler waves may prove relevant too. Historically, whistlers have been observed to propagate mostly parallel to the magnetic field. Hence, an investigation of whistlers in a damped ion-electron model may lead to a completer picture of whistler propagation across all directions of propagation.

Towards multifluid spectroscopy

With each addition of a non-ideal effect like collisional damping, the two-fluid equations become more intricate and harder to treat analytically. Likewise, the introduction of spatial variations in the equilibrium quantities, such as density stratification, complicates matters even more. Exploiting the established framework of the spectroscopic code *Legolas* however, the ion-electron equations could be solved numerically for any one-dimensionally varying equilibrium. Besides allowing us to explore the influence of inhomogeneities and non-ideal effects, it computes the eigenfunctions as well, in which case the mechanical, electrostatic, or electromagnetic nature of a wave can be ascertained by visual inspection too.

The development of such a spectroscopic two-fluid module is not without challenges though. Despite inheriting the structure and core routines from *Legolas*, a few complications can already be foreseen. First of all, *Legolas* adopts a mixture of quadratic and cubic finite elements for the various eigenfunctions in order to escape spectral pollution (Nijboer et al., 1997). Since the ion-electron formalism introduces additional variables, it is not known *a priori* what the optimal combination of finite elements is. This may again be a combination of quadratic and cubic elements, but it may also require elements of a higher order.

Secondly, after a choice of elements is made, the ion-electron solver has to be validated. Whilst an abundance of MHD spectra was available for comparison during the testing of the *Legolas* code, the spectroscopic exploration of the ion-electron model is unprecedented. Validation of this spectroscopic solver would be limited to analytic results, which are restricted to simple configurations. Alternatively, indirect validation may come from comparison to early stages of evolution in 2D or 3D simulations, for which we can rely on *Legolas*'s new visualisation tools.

Finally, since the spectroscopic approach relies on equilibrium perturbation, the initial input state has to satisfy the force-balance equations. With the addition of each new equation and perturbed variable, the force-balance conditions become more restrictive. Consequently, finding an appropriate equilibrium state for a two-fluid system may not be as straightforward as for MHD. Of course, if the force-balance equations cannot be solved analytically after imposing a chosen profile for one or more equilibrium quantities, the remaining equilibrium quantities may be determined with the use of numerical techniques at each grid point.

Aside from the potential force-balance issue, once the ion-electron equations are implemented in *Legolas*, the inclusion of additional particle species is relatively trivial since the form of the new equations is identical. Only the interaction terms require special attention. These supplementary species are also not limited to ions. The same set of mass, momentum, and energy equations

can be implemented for a neutral atom by simply omitting the coupling to the electric and magnetic field in the momentum equation, which vanishes because the charge of the atom is zero. Hence, the code could be utilised to probe partially ionised plasmas, with an ion species and its neutral atom counterpart. Of particular interest then is the coupling between charged and neutral particles, which governs the ion-neutral effects that were shown to be important in the solar corona (Martínez-Sykora et al., 2015) and may lead to confinement disruption in fusion devices (Mlodik et al., 2022).

Flow-driven and resistive instabilities

Many plasma configurations feature space-dependent magnetic fields and consequently, magnetic shear. For non-ideal plasmas, which are subject to a finite resistivity, this magnetic shear results in the resistive tearing instability. As a form of spontaneous magnetic reconnection, a complete understanding of its growth rate may be key in predicting the onset of reconnection-driven eruptive (or disruptive) events. Since background flow is often present in plasmas in some capacity, a study directed at the interaction of flow and resistivity acts as a fine starting point in charting the full complexity of the tearing growth rate. The parametric investigation of linear growth rates in Ch. 5 has proven that even in the absence of flow the growth rate already depends strongly on the combination of resistivity and plasma- β . Whilst the literature is peppered with analytic derivations of generally-applicable power laws describing the growth rate's dependence on the resistivity, the resistivity variation in *Legolas* revealed that the tearing growth rate does not scale monotonically with the resistivity, but reaches a β -dependent maximum and turning point for the test case of a direction-varying magnetic field in a slab. Furthermore, the addition of flow introduced a critical resistivity above which the tearing mode vanishes.

On top of that, with the inclusion of flow a whole new variety of parameters that affect the growth rate, enter the picture. Density, speed, and plasma- β all play a role. In particular, the interplay between the plasma- β and the flow speed demonstrates interesting nuance and specific parameters in the flow profile also play a role. Due to the dependence on the flow profile, *Legolas* could be employed as a computationally inexpensive diagnostic tool for concrete configurations, particularly for experiments and for comparison of linear theory to non-linear simulations.

In this regard, tokamak devices are a prime candidate for tearing mode research. A first generalisation of the results in Ch. 5 should then utilise *Legolas*'s cylindrical capabilities and focus on the influence of axial versus azimuthal flow. Incorporating toroidal effects present in tokamaks (see e.g. Chandra et al., 2005; Shao et al., 2021), however, would require an extension of the *Legolas* code to handle such geometries. Similar studies would also shed light on the influence of flow on coronal loop tearing (Hassam, 1990) and subsequent reconnection,

which may lead to a solar flare. Additionally, since *Legolas* is not limited to instabilities, but also captures fundamental waves and their overtones, such studies can connect to coronal loop seismology (see e.g. Andries et al., 2009) and tokamak wave observations (see e.g. Ochoukov et al., 2018; Spong et al., 2018).

Of course, if the background flow is characterised by velocity shear, it will give rise to the Kelvin-Helmholtz instability in certain regions of the parameter space, predominantly for super-Alfvénic speeds, but also for near-Alfvénic speeds. Since this instability grows faster than the tearing instability by an order of magnitude, the KHI takes over as the mechanism driving the system's evolution (Hofmann, 1975; Ofman et al., 1991). *Legolas* is well-suited to investigate the relation between the tearing instability and the KHI, and when exactly the KHI appears and starts to dominate.

Multifluid instabilities

Perhaps even more important than the influence of background flow, is the diversity of a plasma's constituent species. As demonstrated in Ch. 4, the electrons in HMHD play an important role in the growth rate of the tearing mode, especially if compressibility is taken into account. Furthermore, the presence of the Hall terms introduces new instabilities, like the Hall-shear instability (Kunz, 2008), that we can now explore systematically. Both options are ripe for further scrutiny and provide promising research avenues regarding plasma stability. Moreover, if *Legolas* is expanded to include the full ion-electron equations, all HMHD effects and instabilities can be evaluated in finer detail due to the description of electrons as a separate fluid.

The possibilities do not end with an ion-electron description either. The aforementioned plasma-neutral two-fluid (or multifluid) model for partially ionised plasmas hosts its own share of unique stability properties. Partial ionisation is known to affect prominent instabilities like the KHI (Soler and Ballester, 2022) and brings in even more instabilities, like the ambipolar-shear-instability described by Kunz (2008); Pandey and Wardle (2013), for which they determine dispersion relations in an MHD model extended with an ambipolar diffusion term.

Painting a realistic picture

Though the inclusion of Hall physics and viscosity in the *Legolas* code brings it closer to describing realistic one-dimensionally varying plasmas, an extension from HMHD to the multifluid model would kick it up another notch. In this sense, even linear theory still has a lot to offer. However, all plasma models are inherently non-linear. Therefore, linear theory should only be trusted up to a certain point after which non-linear effects take over.

Currently, 2D and 3D simulations of increasingly high resolutions are well-established as the premier way of exploring the non-linear regime. With each iteration simulations get closer to accurately reproducing observations. Even so, the complex nature of realistic simulations may prove a hindrance to the pursuit of physical insight without the proper tools to explain exactly which effect is responsible for its evolution. In this quest, linear theory and its modular implementation in *Legolas* may claim their place alongside non-linear simulations to aid in the justification of observed behaviour. Alternatively, the non-linear behaviour of a system may be inspected by allowing an equilibrium and an imposed perturbation defined by the superposition of linear eigenmodes to evolve non-linearly in time. This combination of linear techniques and non-linear, numerical simulations will definitely prove important for outstanding problems like magnetic reconnection, where the linear tearing instability provides the conditions for initiating evolutions dominated by non-linear topology reconfigurations.

Neural network feature detection

In this endeavour to connect linear and non-linear theory, neural networks are well-suited to detect perturbation features, as demonstrated in Ch. 6 with a classification problem. It is not yet clear though whether it is feasible to develop a network that is able to attribute certain wave properties to specific physical effects like resistivity. If this is possible however, this would be very promising to apply to observations (or simulations) too.

However, the network presented here was limited in scope and size, and already required a significant amount of classified data for training. Moving forward, a more general network, or networks working on 2D/3D simulation or observation data, should probably employ unsupervised learning, where the training data does not have to be classified beforehand, or semi-supervised learning, where only part of the training data is classified. The field of machine learning is rapidly evolving though, and with all these innovations come new, exciting possibilities.

With a modular implementation of physical effects in linear theory and feature-complete plasma simulations, with increasingly more options to analyse both with neural networks, the path forward offers fantastic prospects for impressive advancements in plasma physics.

A

Environment parameters

This appendix presents an overview of the parameters used for plasma environments throughout all chapters. These values do not represent exact environments, but rather serve as an indication of the orders of magnitude. They can be found in Table A.1. A few clarifications:

- Coronal loop values are based on hot loops in active regions.
- The values across HED experiments vary significantly. To obtain the values in the table, we compared three experiments: Fiksel et al. (2014); Fox et al. (2017); Hare et al. (2017).
- The ionosphere is divided into different layers. The parameters here reflect the general trend across all layers.
- The magnetotail parameters refer to the tail lobes, which are separated by the current sheet. At the plasmashell, the density is larger by two orders of magnitude (Mishin and Streltsov, 2021).
- Pulsar and magnetar magnetic field values are based on the pulsar J1734-3333 and magnetar Swift J1834, listed in Pétri (2019). The number densities were obtained with a Goldreich-Julian estimate (Goldreich and Julian, 1969).
- For the solar wind at 1 AU, rough averages were taken from the live data provided by the National Oceanic and Atmospheric Administration (2023) on 22 March 2023.
- Tokamak values were based on the JT-60U parameters in Hayashi (2010).
- All plasma- β were calculated from the specified number densities n , magnetic fields B , and temperatures T .

TABLE A.1: Overview of typical MHD parameter values for different plasma environments.

	n (m^{-3})	B (T)	T (K)	β	Sources
Coronal loop	10^{16}	0.01	3×10^6	0.01	Reale (2014); Goedbloed et al. (2019)
HED experiment	10^{25}	25	5×10^6	3	Fiksel et al. (2014); Fox et al. (2017); Hare et al. (2017)
Ionosphere	10^{11}	10^{-5}	10^3	3×10^{-5}	Baumjohann and Nakamura (2007)
Magnetar	3.4×10^{14}	$10^{6.08}$			Pétri (2019); Goldreich and Julian (1969)
Magnetosphere	10^{10}	3×10^{-5}	10^4	4×10^{-6}	Goedbloed et al. (2019); Mishin and Streltsov (2021)
Magnetotail	10^4	2×10^{-8}	10^7	0.009	Mishin and Streltsov (2021)
Plasmasphere	$> 10^8$	3×10^{-5}	10^4	4×10^{-8}	Mishin and Streltsov (2021)
Pulsar	2.5×10^{14}	$10^{5.62}$			Pétri (2019); Goldreich and Julian (1969)
Solar wind (1 AU)	10^7	7×10^{-9}	2×10^5	1.4	National Oceanic and Atmospheric Administration (2023)
Tokamak (JT-60U)	6×10^{19}	3.5	2.3×10^7	0.004	Hayashi (2010)

B

Ion-electron equations

The contents of this appendix were published in De Jonghe and Keppens (2020). The dispersion relation in App. B.1 was taken from Goedbloed et al. (2019) and is included here to offer a comprehensive overview of the ion-electron model. The computations and calculations of App. B.2 and B.3 were carried out by J. De Jonghe.

This appendix contains all details pertaining to the discussion of the ion-electron dispersion relation in Ch. 2. The exact form of the polynomial dispersion relation is offered in Sec. B.1, whilst the group speed expressions are available in Sec. B.2. Finally, Sec. B.3 discusses the accuracy of the crossing approximations in Sec. 2.2.1.

B.1 Polynomial dispersion relation

The ion-electron dispersion relation in a homogeneous medium at rest is a polynomial of the form

$$\sum_{\substack{m,n \\ 3 \leq m+n \leq 6}} \alpha_{mn} \omega^{2m} k^{2n} = 0. \quad (\text{B.1})$$

To offer a complete overview, all coefficients α_{mn} are listed here in the way they appear in Goedbloed et al. (2019).

$$\alpha_{60} = 1, \quad (\text{B.2})$$

$$\alpha_{50} = -(3 + E^2 + I^2), \quad (\text{B.3})$$

$$\alpha_{51} = -(2 + v^2 + w^2), \quad (\text{B.4})$$

$$\alpha_{40} = 3 + E^2 + I^2 + 2EI + E^2I^2, \quad (\text{B.5})$$

$$\alpha_{41} = 4 + 2E^2 + 2I^2 + (2 + \lambda^2E^2 + I^2)v^2 + (2 + E^2 + \lambda^2I^2)w^2 + c_s^2, \quad (\text{B.6})$$

$$\alpha_{42} = 1 + 2v^2 + 2w^2 + v^2w^2, \quad (\text{B.7})$$

$$\alpha_{30} = -(1 + EI)^2, \quad (\text{B.8})$$

$$\begin{aligned} \alpha_{31} = & -\left\{ 2(1 + EI)^2 + (1 + \lambda^2)(E^2 + I^2 - EI) + [1 + I^2 + \lambda^2(3 + EI)EI] v^2 \right. \\ & \left. + [1 + E^2 + \lambda^2(3 + EI)EI] w^2 + [2 + (1 - 3\lambda^2)EI] c_s^2 \right\}, \end{aligned} \quad (\text{B.9})$$

$$\begin{aligned} \alpha_{32} = & -\left\{ 1 + E^2 + I^2 + 2(1 + \lambda^2E^2 + I^2)v^2 + 2(1 + E^2 + \lambda^2I^2)w^2 + 2c_s^2 \right. \\ & \left. + [2 + \lambda^2(E^2 + I^2)] v^2w^2 \right\}, \end{aligned} \quad (\text{B.10})$$

$$\alpha_{33} = -(v^2 + w^2 + 2v^2w^2), \quad (\text{B.11})$$

$$\alpha_{21} = (1 + EI)(1 + \lambda^2)EI + (1 + EI)(1 + \lambda^2EI)c_s^2, \quad (\text{B.12})$$

$$\begin{aligned} \alpha_{22} = & (1 + EI)EI + \lambda^2(E^2 + I^2 - EI) + [(1 + \lambda^2)I^2 + 2\lambda^2EI(2 + EI)] v^2 \\ & + [(1 + \lambda^2)E^2 + 2\lambda^2EI(2 + EI)] w^2 + [2 + (1 - 5\lambda^2)EI] c_s^2 \\ & + (1 + \lambda^2EI)^2v^2w^2, \end{aligned} \quad (\text{B.13})$$

$$\alpha_{23} = (I^2 + \lambda^2E^2)v^2 + (E^2 + \lambda^2I^2)w^2 + c_s^2 + 2[1 + \lambda^2(E^2 + I^2)] v^2w^2, \quad (\text{B.14})$$

$$\alpha_{24} = v^2w^2, \quad (\text{B.15})$$

$$\alpha_{12} = -\lambda^2EI \{ EI + [2 + (1 + \lambda^2)EI] c_s^2 \}, \quad (\text{B.16})$$

$$\alpha_{13} = -\lambda^2 \{ E^2I^2(v^2 + w^2) + (E^2 + I^2)c_s^2 + 2EI(1 + \lambda^2EI)v^2w^2 \}, \quad (\text{B.17})$$

$$\alpha_{14} = -\lambda^2(E^2 + I^2)v^2w^2, \quad (\text{B.18})$$

$$\alpha_{03} = \lambda^4E^2I^2c_s^2, \quad (\text{B.19})$$

$$\alpha_{04} = \lambda^4E^2I^2v^2w^2. \quad (\text{B.20})$$

B.2 Group speed polynomials

As noted in Sec. 2.3.2, the group speed expressions are of the form

$$\frac{\partial \omega}{\partial k} = -(v_{ph} P_\omega)^{-1} \left[P_k \hat{e}_k + \frac{\lambda P_\lambda}{k^2} (\hat{e}_B - \lambda \hat{e}_k) \right] \quad (\text{B.21})$$

where the polynomials are given by the expressions

$$P_\omega = \sum_{\substack{1 \leq m \\ 0 \leq n \\ 3 \leq m+n \leq 6}} m \alpha_{mn} \omega^{2(m-1)} k^{2n}, \quad (\text{B.22})$$

$$P_k = \sum_{\substack{0 \leq m \\ 1 \leq n \\ 3 \leq m+n \leq 6}} n \alpha_{mn} \omega^{2m} k^{2(n-1)}, \quad (\text{B.23})$$

$$\text{and } P_\lambda = \sum_{\substack{0 \leq m,n \\ 3 \leq m+n \leq 6}} \frac{\partial \alpha_{mn}}{\partial \lambda^2} \omega^{2m} k^{2n}. \quad (\text{B.24})$$

TABLE B.1: In the upper left table, the terms contributing to P_ω are highlighted in blue. In the upper right table, those contributing to P_k are indicated in orange. In the bottom table, the terms with a contribution to P_λ are marked in red.

	1	k^2	k^4	k^6	k^8		1	k^2	k^4	k^6	k^8
ω^{12}	α_{60}					ω^{12}	α_{60}				
ω^{10}	α_{50}	α_{51}				ω^{10}	α_{50}	α_{51}			
ω^8	α_{40}	α_{41}	α_{42}			ω^8	α_{40}	α_{41}	α_{42}		
ω^6	α_{30}	α_{31}	α_{32}	α_{33}		ω^6	α_{30}	α_{31}	α_{32}	α_{33}	
ω^4		α_{21}	α_{22}	α_{23}	α_{24}	ω^4		α_{21}	α_{22}	α_{23}	α_{24}
ω^2			α_{12}	α_{13}	α_{14}	ω^2			α_{12}	α_{13}	α_{14}
1				α_{03}	α_{04}	1				α_{03}	α_{04}
	1	k^2	k^4	k^6	k^8		1	k^2	k^4	k^6	k^8
ω^{12}	α_{60}						α_{60}				
ω^{10}	α_{50}		α_{51}				α_{50}		α_{51}		
ω^8		α_{40}		α_{41}	α_{42}		α_{40}		α_{41}	α_{42}	
ω^6		α_{30}		α_{31}	α_{32}	α_{33}	α_{30}		α_{31}	α_{32}	α_{33}
ω^4			α_{21}	α_{22}	α_{23}	α_{24}		α_{21}	α_{22}	α_{23}	α_{24}
ω^2				α_{12}	α_{13}	α_{14}			α_{12}	α_{13}	α_{14}
1									α_{03}	α_{04}	

Which terms contribute to each polynomial is visualised in Table B.1. The factors α_{mn} that appear in the expressions for P_ω and P_k were already stated in App. B.1. However, the expression for P_λ contains factors of the form $\partial\alpha_{mn}/\partial\lambda^2$. For the sake of completeness, these derivatives are

$$\frac{\partial\alpha_{41}}{\partial\lambda^2} = E^2v^2 + I^2w^2 \quad (\text{B.25})$$

$$\frac{\partial\alpha_{31}}{\partial\lambda^2} = -\{E^2 + I^2 - EI + EI(3 + EI)(v^2 + w^2) - 3EIc_s^2\} \quad (\text{B.26})$$

$$\frac{\partial\alpha_{32}}{\partial\lambda^2} = -\{2(E^2v^2 + I^2w^2) + (E^2 + I^2)v^2w^2\} \quad (\text{B.27})$$

$$\frac{\partial\alpha_{21}}{\partial\lambda^2} = EI(1 + EI)(1 + c_s^2) \quad (\text{B.28})$$

$$\begin{aligned} \frac{\partial\alpha_{22}}{\partial\lambda^2} = & E^2 + I^2 - EI + I^2v^2 + E^2w^2 + 2EI(2 + EI)(v^2 + w^2) \\ & - 5EIc_s^2 + 2EI(1 + \lambda^2EI)v^2w^2 \end{aligned} \quad (\text{B.29})$$

$$\frac{\partial\alpha_{23}}{\partial\lambda^2} = E^2v^2 + I^2w^2 + 2(E^2 + I^2)v^2w^2 \quad (\text{B.30})$$

$$\frac{\partial\alpha_{12}}{\partial\lambda^2} = -EI\{EI + [2 + (1 + 2\lambda^2)EI]c_s^2\} \quad (\text{B.31})$$

$$\begin{aligned} \frac{\partial\alpha_{13}}{\partial\lambda^2} = & -\{E^2I^2(v^2 + w^2) + (E^2 + I^2)c_s^2 \\ & + 2EI(1 + 2\lambda^2EI)v^2w^2\} \end{aligned} \quad (\text{B.32})$$

$$\frac{\partial\alpha_{14}}{\partial\lambda^2} = -(E^2 + I^2)v^2w^2 \quad (\text{B.33})$$

$$\frac{\partial\alpha_{03}}{\partial\lambda^2} = 2\lambda^2E^2I^2c_s^2 \quad (\text{B.34})$$

$$\frac{\partial\alpha_{04}}{\partial\lambda^2} = 2\lambda^2E^2I^2v^2w^2 \quad (\text{B.35})$$

B.3 Test cases for parallel propagation

In Sec. 2.2.1 multiple analytical approximations were offered for various crossings in different regimes. These expressions were obtained by taking single term approximations of the quadratic branch for long and short wavelengths.

Naturally, it should be checked how accurate the final expressions are. In order to test this accuracy, the analytical results were compared with numerical solutions. Since the crossings and the accuracy vary based on the regime, test cases were used for each regime. For the $1 < E < E_{\text{cr}}$ regimes two test cases were used since some approximations were less accurate for values of E closer to 1. All test cases and their crossings are described in Table B.2.

TABLE B.2: Comparison of numerical crossings and analytical approximations. Each regime is represented by a test case (or two) specifying E , v , and w . All cases use $\mu = 1/1836$. Numerical solutions of crossings are given alongside their analytical approximations.

Regime	Parameters	Label	Numerical crossings	Analytic approximations
$E < 1$, $c_s < c_a$	$E = 0.5$	SA	(2.71827346e-04, 0.541448592)	(2.71827346e-04, 0.541448590)
	$v = 0.002$	SF	(0.499999496, 995.941087)	(0.499999496, 995.941087)
	$w = 0.0005$	MO	(1.00000067, 0.577194)	(1, 0.577193)
$E < 1$, $c_s > c_a$ (Fig. 2.2a)	$E = 0.5$	AF	(0.00479704 0.0958626)	(0.00479704, 0.0958626)
	$v = 0.1$	AF	(0.49493417 9.89402523)	(0.49493063, 9.89053971)
	$w = 0.05$	MO	(1.0016786 0.57977526)	(1, 0.57719297)
$1 < E < E_{\text{cr}}$, $c_s < c_a$	$E = 2$	SA	(0.00107681, 0.21518649)	(0.00107681, 0.21518649)
		SF	(1.99998749, 399.67127926)	(1.99998749, 399.67127926)
	$v = 0.01$	MO	(1.0000333, 0.81631022)	(1, 0.81627395)
		FM	(1.00009992, 1.41397011)	(1, 1.41382879)
		FM	(1.99995002, 199.9950021)	(1.99995002, 199.9950021)

$1 < E < E_{\text{cr}}$, $c_s < c_a$ (Fig. 2.2b)	$E = 10$ $v = 0.1$	SA	(0.00519572, 0.10382959)	(0.00519572, 0.10382958)
		SF	(9.99974909, 199.83187597)	(9.99974909, 199.83187597)
	$w = 0.05$	MO	(1.0045746, 0.95780243)	(1, 0.95320147)
		FM	(1.00559418, 1.05944303)	(1, 1.05380701)
$1 < E < E_{\text{cr}}$, $c_s > c_a$	$E = 2$ $v = 0.3$	FM	(9.99898056, 99.51358858)	(9.99899035, 99.98990347)
		AF	(0.03280859, 0.13121866)	(0.03280860, 0.13121867)
	$w = 0.25$	AF	(1.96610763, 7.86408174)	(1.96610208, 7.86346664)
		MO	(1.03208004, 0.85114203)	(1, 0.81627395)
		AM	(1.10491084, 1.56653326)	(1, 1.41382879)
	$E = 10$ $v = 0.3$	AM	(1.92716371, 5.49161664)	(1.94929139, 6.49763796)
		AF	(0.00122256, 0.00488966)	(0.00122256, 0.00488966)
$1 < E < E_{\text{cr}}$, $c_s > c_a$	$v = 0.3$ $w = 0.25$	AF	(9.99333248, 39.9732234)	(9.99333081, 39.9685369)
		MO	(1.04378574, 0.99723593)	(1, 0.95320147)
	$E = 10$ $w = 0.25$	AM	(1.05378906, 1.107997)	(1, 1.05380701)
		AM	(9.98999528, 33.132819)	(9.99010549, 33.300352)

$E_{\text{cr}} < E < 1/\mu,$ $c_s < c_a$	$E = 1835.5$ $v = 0.1$ $w = 0.05$	SA	(0.9997263, 19.99046107)	(0.9997263, 19.97821950)
		SF	(1835.49999863, 36680.06113394)	(1835.49999863, 36680.06113394)
		FM	(1.00503714, 1.00517377)	(1, 1.00013629)
		FM	(1835.4999945, 18354.99722243)	(1835.4999945, 18354.99994500)
$E_{\text{cr}} < E < 1/\mu,$ $c_s > c_a$	Unphysical			
$E > 1/\mu,$ $c_s < c_a$ (Fig. 2.2c)	$E = 2500$ $v = 0.1$ $w = 0.05$	SA	(1.36165477, 27.22974249)	(1.36165477, 27.21088544)
		SF	(2499.999999, 49959.22248234)	(2499.999999, 49959.22248234)
		AM	(1.00504145, 1.00560472)	(1, 1.00055264)
		FM	(1.00503662, 1.00512158)	(1, 1.00008472)
		FM	(2499.99999596, 24999.99995962)	(2499.99999596, 24999.99995962)
		AM	(1.36165165, 13.47752584)	(1.36165173, 13.61651735)
$E > 1/\mu,$ $c_s > c_a$	Unphysical			

C

Specifics of the *Legolas* code

The contents of Sec. C.1 appeared for the first time in this form in De Jonghe et al. (2022). The initial calculations were performed by N. Claes and J. De Jonghe independently, and subsequently compared and finalised. The Hall and viscosity terms were added by J. De Jonghe. The code extensions described in Sec. C.3 and C.4 were implemented by J. De Jonghe and also appeared in De Jonghe et al. (2022). N. Claes suggested the algorithm in Sec. C.5, which was implemented by J. De Jonghe.

As established in Sec. 4.1, the *Legolas* code is a spectroscopic HMHD code to quantify all eigenmodes of a 1D force-balanced state in Cartesian or cylindrical geometry. In this appendix the underlying equations and some further code extensions are outlined. Sec. C.1 states the linearised HMHD equations, incorporating flow, viscosity (and viscous heating), resistivity (and resistive heating), radiative cooling, thermal conduction, external gravity, and the Hall and electron effects. In Sec. C.3 we discuss the specifics of the incompressible approximation and Sec. C.4 gives an overview of the calculated eigenfunctions. Finally, Sec. C.5 explains how an accumulated grid was obtained for the Harris sheet study in Ch. 5.

C.1 Linearised MHD equations

As explained originally in Claes et al. (2020) and Sec. 4.1, after assuming Fourier forms for each perturbed variable f_1 ,

$$f_1(\mathbf{r}, t) = \hat{f}_1(u_1) \exp[i(k_2 u_2 + k_3 u_3 - \omega t)], \quad (\text{C.1})$$

the Fourier coefficients are transformed as

$$\begin{aligned} \varepsilon \hat{\rho}_1 &\rightarrow \tilde{\rho}_1, & i\varepsilon \hat{v}_1 &\rightarrow \tilde{v}_1, & \hat{v}_2 &\rightarrow \tilde{v}_2, & \varepsilon \hat{v}_3 &\rightarrow \tilde{v}_3, \\ \varepsilon \hat{T}_1 &\rightarrow \tilde{T}_1, & i\hat{A}_1 &\rightarrow \tilde{a}_1, & \varepsilon \hat{A}_2 &\rightarrow \tilde{a}_2, & \hat{A}_3 &\rightarrow \tilde{a}_3, \end{aligned} \quad (\text{C.2})$$

where ε is a scale parameter equal to 1 in Cartesian geometry and equal to r in cylindrical coordinates. Dropping tildes for notational convenience, denoting derivation with respect to u_1 with a prime $'$, and introducing the notation

$$\mathcal{F} = \left(\frac{k_2}{\varepsilon} B_{02} + k_3 B_{03} \right), \quad (\text{C.3})$$

the linearised MHD equations implemented in *Legolas*, including the viscosity and Hall terms, become

$$\omega \rho_1 = -\rho'_0 v_1 - \rho_0 \left(v'_1 - k_2 v_2 - k_3 v_3 \right) + \rho_1 \left(\frac{k_2}{\varepsilon} v_{02} + k_3 v_{03} \right), \quad (\text{C.4})$$

$$\begin{aligned} \omega \rho_0 v_1 = & \varepsilon \left(\frac{\rho_1 T_0 + \rho_0 T_1}{\varepsilon} \right)' + g \rho_1 + B_{02} \left\{ -\frac{k_2 k_3}{\varepsilon} a_2 + \frac{k_2^2}{\varepsilon} a_3 + [\varepsilon (k_3 a_1 - a'_3)]' \right\} \\ & + B_{03} \left\{ -k_3^2 a_2 + k_2 k_3 a_3 + \varepsilon \left[\frac{1}{\varepsilon} (a'_2 - k_2 a_1) \right]' \right\} + B'_{03} (a'_2 - k_2 a_1) \\ & + (\varepsilon B_{02})' (k_3 a_1 - a'_3) - \frac{\varepsilon'}{\varepsilon} v_{02}^2 \rho_1 + \rho_0 \left(\frac{k_2}{\varepsilon} v_{02} + k_3 v_{03} \right) v_1 \\ & - 2\varepsilon' \rho_0 v_{02} v_2 - i\mu \left(\frac{\varepsilon'}{\varepsilon^2} + \frac{k_2^2}{\varepsilon^2} + k_3^2 \right) v_1 \\ & + \frac{i\mu}{3} \varepsilon \left(\frac{1}{\varepsilon} v'_1 - \frac{k_2}{\varepsilon} v_2 - \frac{k_3}{\varepsilon} v_3 \right)' + 2 \frac{i\mu \varepsilon'}{\varepsilon} k_2 v_2 + i\mu \left[\varepsilon \left(\frac{v_1}{\varepsilon} \right)' \right]', \end{aligned} \quad (\text{C.5})$$

$$\begin{aligned}
\omega \rho_0 \varepsilon v_2 = & \frac{k_2}{\varepsilon} (\rho_1 T_0 + \rho_0 T_1) + B_{03} \left[- \left(\frac{k_2^2}{\varepsilon} + \varepsilon k_3^2 \right) a_1 + \frac{k_2}{\varepsilon} a'_2 + \varepsilon k_3 a'_3 \right] \\
& + \frac{(\varepsilon B_{02})'}{\varepsilon} (k_3 a_2 - k_2 a_3) - \frac{(\varepsilon v_{02})'}{\varepsilon} \rho_0 v_1 + \rho_0 (k_2 v_{02} + \varepsilon k_3 v_{03}) v_2 \\
& + \frac{i\mu}{\varepsilon} \left(2 \frac{\varepsilon'}{\varepsilon} k_2 v_1 + \frac{1}{3} k_2 v'_1 - \frac{1}{3} k_2 k_3 v_3 \right) \\
& - i\mu \left(\frac{\varepsilon'}{\varepsilon} + \frac{4}{3} \frac{k_2^2}{\varepsilon} + \varepsilon k_3^2 \right) v_2 + i\mu (\varepsilon v'_2)',
\end{aligned} \tag{C.6}$$

$$\begin{aligned}
\omega \rho_0 v_3 = & k_3 (\rho_1 T_0 + \rho_0 T_1) + B_{02} \left[\left(\frac{k_2^2}{\varepsilon} + \varepsilon k_3^2 \right) a_1 - \frac{k_2}{\varepsilon} a'_2 - \varepsilon k_3 a'_3 \right] \\
& + B'_{03} (k_3 a_2 - k_2 a_3) - \rho_0 v'_{03} v_1 + \rho_0 \left(\frac{k_2}{\varepsilon} v_{02} + k_3 v_{03} \right) v_3 \\
& + \frac{i\mu}{3} k_3 (v'_1 - k_2 v_2) - i\mu \left(\frac{k_2^2}{\varepsilon^2} + \frac{4}{3} k_3^2 \right) v_3 + i\mu \left[\varepsilon \left(\frac{v_3}{\varepsilon} \right)' \right]',
\end{aligned} \tag{C.7}$$

$$\begin{aligned}
\omega \rho_0 T_1 = & -\rho_0 T'_0 v_1 + \rho_0 \left(\frac{k_2}{\varepsilon} v_{02} + k_3 v_{03} \right) T_1 - (\gamma - 1) \rho_0 T_0 \left(v'_1 - k_2 v_2 - k_3 v_3 \right) \\
& - i(\gamma - 1) \mathcal{L}_T \rho_0 T_1 - i(\gamma - 1) \left(\mathcal{L}_0 + \mathcal{L}_\rho \rho_0 \right) \rho_1 \\
& - i(\gamma - 1) \frac{\kappa_{\parallel,0} - \kappa_{\perp,0}}{B_0^2} \mathbf{F}^2 T_1 - i(\gamma - 1) \kappa_{\perp,0} \left(\frac{k_2^2}{\varepsilon^2} + k_3^2 \right) T_1 \\
& + i(\gamma - 1) \frac{\kappa_{\parallel,0} - \kappa_{\perp,0}}{B_0^2} T'_0 \mathbf{F} \left(k_3 a_2 - k_2 a_3 \right) + i(\gamma - 1) \left(\varepsilon T'_0 \kappa_{\perp,1} \right)' \\
& + i(\gamma - 1) \left[\varepsilon \kappa_{\perp,0} \left(\frac{T_1}{\varepsilon} \right)' \right]' + i(\gamma - 1) T_1 \frac{d\eta}{dT} \left[B_{03}'^2 + \left(\frac{(\varepsilon B_{02})'}{\varepsilon} \right)^2 \right] \\
& + 2i(\gamma - 1) \eta_0 \left\{ B_{03}' \left[k_3 (k_2 a_3 - k_3 a_2) + \varepsilon \left(\frac{1}{\varepsilon} a'_2 - \frac{k_2}{\varepsilon} a_1 \right)' \right] \right. \\
& \quad \left. + \frac{(\varepsilon B_{02})'}{\varepsilon} \left[\frac{k_2}{\varepsilon} (k_2 a_3 - k_3 a_2) + (\varepsilon k_3 a_1 - \varepsilon a'_3)' \right] \right\} \\
& + 2i\mu \left[\frac{(\varepsilon')^2}{\varepsilon} v_{02} v_2 + \varepsilon v'_{02} v'_2 + \varepsilon v'_{03} \left(\frac{v_3}{\varepsilon} \right)' - \frac{\varepsilon'}{\varepsilon^2} k_2 v_{02} v_1 \right], \tag{C.8}
\end{aligned}$$

$$\begin{aligned}
\omega \left\{ \varepsilon a_1 + \eta_H v_1 + \frac{\eta_e}{\rho_0} \left[\left(\frac{k_2^2}{\varepsilon} + \varepsilon k_3^2 \right) a_1 - \frac{k_2}{\varepsilon} a'_2 - \varepsilon k_3 a'_3 \right] \right\} \\
= & B_{02} v_3 - \varepsilon B_{03} v_2 + (k_2 v_{02} + \varepsilon k_3 v_{03}) a_1 - v_{02} a'_2 - \varepsilon v_{03} a'_3 \\
& - i\eta_0 \left(\frac{k_2^2}{\varepsilon} + \varepsilon k_3^2 \right) a_1 + i\eta_0 \frac{k_2}{\varepsilon} a'_2 + i\eta_0 \varepsilon k_3 a'_3 \\
& + \eta_H \left[\left(\frac{k_2}{\varepsilon} v_{02} + k_3 v_{03} \right) v_1 - 2\varepsilon' v_{02} v_2 + \frac{1-f_e}{\rho_0} (\rho'_0 T_1 - T'_0 \rho_1) \right] \tag{C.9} \\
& + i\mu \frac{\eta_H}{\rho_0} \left\{ \left[\varepsilon \left(\frac{v_1}{\varepsilon} \right)' \right]' - \left(\frac{k_2^2}{\varepsilon^2} + k_3^2 \right) v_1 + 2 \frac{\varepsilon'}{\varepsilon} k_2 v_2 \right. \\
& \quad \left. - \frac{\varepsilon'}{\varepsilon^2} v_1 + \frac{\varepsilon}{3} \left[\frac{1}{\varepsilon} (v'_1 - k_2 v_2 - k_3 v_3) \right]' \right\},
\end{aligned}$$

$$\begin{aligned}
& \omega \left\{ a_2 + \eta_H \varepsilon v_2 + \frac{\eta_e}{\rho_0} \left[\varepsilon \left(\frac{1}{\varepsilon} (k_2 a_1 - a'_2) \right)' + k_3 (k_3 a_2 - k_2 a_3) \right] \right\} \\
& = -B_{03} v_1 + v_{03} (k_3 a_2 - k_2 a_3) + i B'_{03} \frac{d\eta}{dT} T_1 - i \eta_0 k_3 (k_3 a_2 - k_2 a_3) \\
& \quad + i \eta_0 \varepsilon \left(\frac{1}{\varepsilon} a'_2 - \frac{k_2}{\varepsilon} a_1 \right)' + \eta_H \left[(k_2 v_{02} + \varepsilon k_3 v_{03}) v_2 - \left(v'_{02} - \frac{\varepsilon'}{\varepsilon} v_{02} \right) v_1 \right] \\
& \quad + i \mu \frac{\eta_H}{\rho_0} \left\{ (\varepsilon v'_2)' - \left(\frac{k_2^2}{\varepsilon} + \varepsilon k_3^2 \right) v_2 + 2 \frac{\varepsilon'}{\varepsilon^2} k_2 v_1 - \frac{\varepsilon'}{\varepsilon} v_2 \right. \\
& \quad \left. + \frac{1}{3} \frac{k_2}{\varepsilon} (v'_1 - k_2 v_2 - k_3 v_3) - \frac{\rho_1}{\rho_0} \left(v''_{02} + \frac{\varepsilon'}{\varepsilon} v'_{02} - \frac{\varepsilon'}{\varepsilon^2} v_{02} \right) \right\}, \tag{C.10}
\end{aligned}$$

$$\begin{aligned}
& \omega \left\{ \varepsilon a_3 + \eta_H v_3 + \frac{\eta_e}{\rho_0} \left[(\varepsilon (k_3 a_1 - a'_3))' - \frac{k_2}{\varepsilon} (k_3 a_2 - k_2 a_3) \right] \right\} \\
& = B_{02} v_1 - v_{02} (k_3 a_2 - k_2 a_3) - i \frac{(\varepsilon B_{02})'}{\varepsilon} \frac{d\eta}{dT} T_1 + i \eta_0 \frac{k_2}{\varepsilon} (k_3 a_2 - k_2 a_3) \\
& \quad - i \eta_0 \left(\varepsilon k_3 a_1 - \varepsilon a'_3 \right)' + \eta_H \left[\left(\frac{k_2}{\varepsilon} v_{02} + k_3 v_{03} \right) v_3 - v'_{03} v_1 \right] \\
& \quad + i \mu \frac{\eta_H}{\rho_0} \left\{ \left[\varepsilon \left(\frac{v_3}{\varepsilon} \right)' \right]' - \left(\frac{k_2^2}{\varepsilon^2} + k_3^2 \right) v_3 + \frac{k_3}{3} (v'_1 - k_2 v_2 - k_3 v_3) \right. \\
& \quad \left. - \frac{\rho_1}{\rho_0} \left(v''_{03} + \frac{\varepsilon'}{\varepsilon} v'_{03} \right) \right\}. \tag{C.11}
\end{aligned}$$

C.2 Solvers

Legolas supports a host of algorithms for solving the eigenvalue problem by linking to the *LAPACK* (Anderson et al., 1999) and *ARPACK* libraries (Lehoucq et al., 1998). Here, we only discuss the **QR-invert** and **inverse-iteration** options, though more algorithms are available. A complete overview can be found at <https://legolas.science/general/solvers/>.

C.2.1 QR-invert

If this solver option is selected, the generalised eigenvalue problem $\mathbf{A}\mathbf{x} = \omega\mathbf{B}\mathbf{x}$ is first transformed to a regular eigenvalue problem of the form

$$\mathbf{B}^{-1}\mathbf{A}\mathbf{x} = \omega\mathbf{x}, \quad (\text{C.12})$$

not by directly inverting \mathbf{B} , but by solving the linear system

$$\mathbf{B}\mathbf{X} = \mathbf{A} \quad (\text{C.13})$$

for \mathbf{X} using an LU factorisation of \mathbf{B} . This is handled with a call to *LAPACK*'s `zgbsv` subroutine. This solution for \mathbf{X} is then passed to *LAPACK*'s `zgeev` subroutine, which solves a regular eigenvalue problem through QR iteration (see e.g. Demmel, 1997). This method calculates the entire spectrum, including eigenfunctions.

C.2.2 inverse-iteration

Contrary to the QR iteration, inverse iteration calculates only one eigenvalue and requires an initial guess σ , called the shift. One iteration calculates

$$\begin{aligned}\tilde{\omega}_{i+1} &\leftarrow (\bar{x}_i^\top \mathbf{A} x_i) / (\bar{x}_i^\top \mathbf{B} x_i) \\ y_{i+1} &\leftarrow (\mathbf{A} - \sigma\mathbf{B})^{-1} \mathbf{B} x_i \\ x_{i+1} &\leftarrow y_{i+1} / \|y_{i+1}\|_2\end{aligned}$$

where x is the approximated eigenvector and $\tilde{\omega}$ the eigenvalue approximation. Here, y_{i+1} is determined by solving the linear system $(\mathbf{A} - \sigma\mathbf{B})y_{i+1} = \mathbf{B}x_i$ for y_{i+1} with an LU decomposition of $(\mathbf{A} - \sigma\mathbf{B})$. With this iterative procedure x converges to the eigenvector corresponding to the dominant eigenvalue of $(\mathbf{A} - \sigma\mathbf{B})^{-1}\mathbf{B}$, which is the eigenvalue of $\mathbf{B}^{-1}\mathbf{A}$ closest to the shift σ . The iteration stops when either the convergence criterion

$$\|\mathbf{A}\mathbf{x}_i - \tilde{\omega}_{i+1}\mathbf{B}\mathbf{x}_i\| < |\tilde{\omega}_{i+1}| \epsilon \quad (\text{C.14})$$

is met for a user-specified tolerance ϵ , or a preset maximal amount of iterations is exceeded. For the case in this thesis, these values were set to $\epsilon = 10^{-7}$ and 1000 iterations. For more details about this procedure, see e.g. Demmel (1997); Trefethen and Bau III (1997).

C.3 Incompressible approximation

In Ch. 4 and 5 results from the literature were used to validate the implementation of the Hall and viscous terms, respectively. However, many of these earlier calculations were performed with the equations for an incompressible plasma, i.e. satisfying $\nabla \cdot \mathbf{v} = 0$. Since the *Legolas* code

employs the full set of compressible MHD equations, we need an approximation of the incompressible regime to compare to these former conclusions.

In theory, the incompressible limit corresponds to an infinite heat capacity ratio, i.e. $\gamma \rightarrow \infty$. In practice, we discard all terms in the linearised energy equation's right hand side except for the term $-(\gamma - 1)p_0 \nabla \cdot \mathbf{v}_1$, which relates to the finite pressure perturbation. Then, the perturbed divergence becomes $\nabla \cdot \mathbf{v}_1 = \omega T_1 / T_0(\gamma - 1)$, whose real and imaginary parts clearly go to zero for $\gamma \rightarrow \infty$. Implementation-wise, γ is set to a value of 10^{12} such that $|\nabla \cdot \mathbf{v}_1|$ remains very small on the whole domain, usually yielding values smaller than 10^{-12} in the region of the spectrum near the origin. The value of $|\nabla \cdot \mathbf{v}_1|$ is indeed observed to increase for increasingly large eigenvalues.

C.4 Derived quantities

The code extension presented here allows for the computation of physically relevant, derived quantities such as the perturbed magnetic field (as opposed to the auxiliary vector potential \mathbf{A}_1) or the entropy perturbation (as opposed to the density or temperature eigenfunction). Whilst these derived eigenfunctions hold no new physical information compared to the eight original eigenfunction, they may highlight different properties in a better way and thus act as a diagnostic toolkit, e.g. to evaluate specific eigenmode changes due to viscosity and Hall extensions.

There are various physical quantities of interest that can be derived from the eight eigenfunctions $(\rho_1, v_1, v_2, v_3, T_1, A_1, A_2, A_3)$ that *Legolas* computes (every eigenfunction here is now using the changed notation $f_1 \equiv \hat{f}_1(u_1)$ and belonging to a specific set (k_2, k_3, ω)). The most evident is the perturbed magnetic field \mathbf{B}_1 , which is a combination of the A_j -eigenfunctions ($j = 1, 2, 3$), through

$$\mathbf{B}_1 = \nabla \times \mathbf{A}_1 = i \left(\frac{k_2}{\varepsilon} A_3 - k_3 A_2 \right) \hat{\mathbf{e}}_1 + (ik_3 A_1 - A'_3) \hat{\mathbf{e}}_2 + \frac{1}{\varepsilon} [(\varepsilon A_2)' - ik_2 A_1] \hat{\mathbf{e}}_3, \quad (\text{C.15})$$

where a prime denotes the derivative with respect to u_1 from now on. We can similarly compute its divergence $\nabla \cdot \mathbf{B}_1$ to validate that it is numerically zero, and its curl, $\nabla \times \mathbf{B}_1$, yielding the perturbed current. Besides these magnetic-field-derived quantities, we can also determine the divergence of the velocity perturbation $\nabla \cdot \mathbf{v}_1$, which serves as a diagnostic tool when exploiting the incompressible approximation, and the perturbed vorticity $\nabla \times \mathbf{v}_1$. Further worth mentioning is the entropy perturbation

$$S_1 = (p\rho^{-\gamma})_1 = \rho_0^{1-\gamma} T_1 + (1-\gamma)\rho_0^{-\gamma} T_0 \rho_1, \quad (\text{C.16})$$

where we used the ideal gas law $p = \rho T$ to write the entropy in terms of density and temperature.

In addition, in the presence of an equilibrium magnetic field \mathbf{B}_0 , all perturbed vector quantities $(\mathbf{B}_1, \nabla \times \mathbf{B}_1, \mathbf{v}_1, \nabla \times \mathbf{v}_1)$ can be expressed in a reference frame consisting of a component along the equilibrium magnetic field and two perpendicular components. This is of interest to verify or determine the (theoretically expected) polarisations of specific eigenmodes. Note that the unit vector $\hat{\mathbf{e}}_1$ is always perpendicular to the equilibrium magnetic field due to the chosen equilibrium form (4.1).

C.5 Grid accumulation

Due to the heavily localised transitions in the equilibrium profiles in the study of the Harris current sheet (Sec. 5.1.2), an equidistant grid would require many more grid points than a centrally-accumulated grid to properly resolve the region of steepest change in the middle. Therefore, an accumulated grid was constructed using the algorithm below for an interval $x \in [a, b]$ and function f (Quarteroni, 2009).

```

Declare array auxGrid
Declare array finalGrid
auxGrid(1) ← a
i ← 1
while auxGrid(i) < b do
    auxGrid(i + 1) ← auxGrid(i) + f(x)
    i ← i + 1
end while
κ ← (b - auxGrid(i - 1))/(auxGrid(i) - auxGrid(i - 1))
finalGrid(1) ← a
for j from 2 to i - 1 do
    finalGrid(j) ← auxGrid(j - 1) + κf(auxGrid(j - 1))
end for
finalGrid(i) ← b

```

In our specific case, we used the Gaussian function

$$f(x) = p_1 - (p_1 - p_3) \exp\left(\frac{-(x - p_2)^2}{2p_4}\right). \quad (\text{C.17})$$

However, whilst this method creates an accumulated grid centered around p_2 , the resulting grid is not symmetrical around p_2 . A symmetrical grid is desired because it ensures that the spectrum's symmetry, in the case of an odd flow profile, is not broken by numerical errors. Therefore, after generating the grid following the procedure above, we only keep the points that are smaller than p_2 , mirror them around p_2 , and add p_2 itself in the middle to create the final symmetrical grid.

Bibliography

- E. Ahedo and J. J. Ramos. Parametric analysis of the two-fluid tearing instability. *Plasma Phys. Control. Fusion*, 51(5):055018, 2009. ISSN 0741-3335.
- H. Alfvén. Existence of electromagnetic-hydrodynamic waves. *Nature*, 150(3805):405–406, 1942. doi:10.1038/150405d0.
- E. Anderson, Z. Bai, C. Bischof, S. Blackford, J. Demmel, J. Dongarra, J. Du Croz, A. Greenbaum, S. Hammarling, A. McKenney, and D. Sorensen. *LAPACK Users' Guide*. Society for Industrial and Applied Mathematics, Philadelphia, PA, third edition, 1999. ISBN 0-89871-447-8 (paperback).
- J. Andries, T. Van Doorsselaere, B. Roberts, G. Verth, E. Verwichte, and R. Erdélyi. Coronal seismology by means of kink oscillation overtones. *Space Sci. Rev.*, 149(1-4):3–29, 2009. ISSN 00386308. doi:10.1007/s11214-009-9561-2.
- E. V. Appleton. Wireless studies of the ionosphere. *J. Inst. Elec. Engrs.*, 71:641, 1932.
- A. Artemyev, O. Agapitov, D. Mourenas, V. Krasnoselskikh, V. Shastun, and F. Mozer. Oblique whistler-mode waves in the Earth's inner magnetosphere: Energy distribution, origins, and role in radiation belt dynamics. *Space Sci. Rev.*, 200(1-4):261–355, 2016.
- J. F. Bamber, W. Gekelman, and J. E. Maggs. Whistler wave mode conversion to lower hybrid waves at a density striation. *Phys. Rev. Lett.*, 73:2990–2993, 1994. doi:10.1103/PhysRevLett.73.2990.
- H. Barkhausen. Zwei mit Hilfe der neuen Verstärker entdeckte Erscheinungen. *Physikalische Zeitschrift*, 20:401–403, 1919.
- H. Baty and R. Keppens. Interplay between Kelvin-Helmholtz and Current-driven Instabilities in Jets. *Astrophys. J.*, 580(2):800–814, 2002. ISSN 0004-637X. doi:10.1086/343893.
- W. Baumjohann and R. Nakamura. Magnetospheric contributions to the terrestrial magnetic field. In G. Schubert, editor, *Treatise on geophysics*, volume 5, chapter 5.03, pages 77–92. Elsevier Science, 2007.
- W. Baumjohann and R. A. Treumann. *Basic Space Plasma Physics*. Imperial College Press, 1997. ISBN 9781860940798.

- M. Bawa'aneh, A. Al-Khateeb, and A. Sawalha. Microwave propagation in warm, collisional magnetion media. *IEEE Trans. Plasma Sci. IEEE Nucl. Plasma Sci. Soc.*, 41(9):2496–2500, 2013. ISSN 0093-3813.
- T. F. Bell, U. S. Inan, J. Bortnik, and J. D. Scudder. The Landau damping of magnetospherically reflected whistlers within the plasmasphere. *Geophys. Res. Lett.*, 29(15):23–1–23–4, 2002. doi:10.1029/2002GL014752.
- P. M. Bellan. *Fundamentals of Plasma Physics*. Cambridge University Press, 2006. doi:10.1017/CBO9780511807183.
- P. M. Bellan. Improved basis set for low frequency plasma waves. *J. Geophys. Res. Space Phys.*, 117(A12), 2012. doi:10.1029/2012JA017856.
- L. Berčič, D. Verscharen, C. Owen, L. Colombar, M. Kretzschmar, T. Chust, M. Maksimovic, D. Kataria, C. Anekallu, E. Behar, M. Berthomier, R. Bruno, V. Fortunato, C. Kelly, Y. Khotyaintsev, G. Lewis, S. Livi, P. Louarn, G. Mele, G. Nicolaou, G. Watson, and R. Wicks. Whistler instability driven by the sunward electron deficit in the solar wind: High-cadence solar orbiter observations. *Astronomy and astrophysics (Berlin)*, 656:A31–, 2021. ISSN 0004-6361.
- V. S. Beskin, A. V. Gurevich, and Y. N. Istomin. *Physics of the Pulsar Magnetosphere*. Cambridge University Press, 2006. ISBN 9780521032537; 0521032539; 9780511564673; 0511564678; 0521417465; 9780521417464.
- C. M. Bishop. *Pattern Recognition and Machine Learning (Information Science and Statistics)*. Springer-Verlag, Berlin, Heidelberg, 2006. ISBN 0387310738.
- D. Biskamp. *Nonlinear Magnetohydrodynamics*. Cambridge Monographs on Plasma Physics. Cambridge University Press, 1993. doi:10.1017/CBO9780511599965.
- D. Biskamp. *Magnetic Reconnection in Plasmas*. Cambridge Monographs on Plasma Physics. Cambridge University Press, 2000. doi:10.1017/CBO9780511599958.
- J. A. Bittencourt. *Fundamentals of Plasma Physics*. Springer New York, 2004. ISBN 9780387209753.
- M. Boldeanu, H. Cucu, C. Burileanu, and L. Mărmureanu. Multi-input convolutional neural networks for automatic pollen classification. *Appl. Sci.*, 11(24), 2021. ISSN 2076-3417. doi:10.3390/app112411707.
- T. J. M. Boyd and J. J. Sanderson. *Physics of Plasmas*. Cambridge University Press, 2003. ISBN 9780521452908,0521452902.

- S. I. Braginskii. Transport processes in a plasma. In M. A. Leontovich, editor, *Reviews of Plasma Physics*, volume 1. Consultants Bureau, New York, 1965.
- V. A. Buts, A. N. Lebedev, and V. Kurliko. *The Theory of Coherent Radiation by Intense Electron Beams*. Particle Acceleration and Detection. Springer-Verlag, 2006.
- C. Cattell, J. R. Wygant, K. Goetz, K. Kersten, P. J. Kellogg, T. von Rosenvinge, S. D. Bale, I. Roth, M. Temerin, M. K. Hudson, R. A. Mewaldt, M. Wiedenbeck, M. Maksimovic, R. Ergun, M. Acuna, and C. T. Russell. Discovery of very large amplitude whistler-mode waves in earth's radiation belts. *Geophys. Res. Lett.*, 35(1), 2008. doi:10.1029/2007GL032009.
- D. Chandra, A. Sen, P. Kaw, M. Bora, and S. Kruger. Effect of sheared flows on classical and neoclassical tearing modes. *Nucl. Fusion*, 45(6):524, 2005. doi:10.1088/0029-5515/45/6/015.
- X. L. Chen and P. J. Morrison. Resistive tearing instability with equilibrium shear flow. *Phys. Fluids B*, 2(3):495–507, 1990. doi:10.1063/1.859339.
- F. Chollet. *Deep Learning with Python*. Manning Publications Co., USA, 2018. ISBN 1617294438.
- N. Claes, J. De Jonghe, and R. Keppens. Legolas: A Modern Tool for Magnetohydrodynamic Spectroscopy. *Astrophys. J., Suppl. Ser.*, 251(2):25, 2020. ISSN 0067-0049. doi:10.3847/1538-4365/abc5c4.
- N. Claes, J. De Jonghe, and R. Keppens. Erratum: “Legolas: A Modern Tool for Magnetohydrodynamic Spectroscopy” (2020, ApJS, 251, 25). *Astrophys. J., Suppl. Ser.*, 254(2):45, 2021. ISSN 0067-0049. doi:10.3847/1538-4365/ac02c1.
- B. Coppi, J. M. Greene, and J. L. Johnson. Resistive instabilities in a diffuse linear pinch. *Nucl. Fusion*, 6(2):101–117, 1966. ISSN 0029-5515.
- C. Crabtree, L. Rudakov, G. Ganguli, and M. Mithaiwala. Collisionless and collisional dissipation of magnetospherically reflecting whistler waves. *Geophys. Res. Lett.*, 39(16), 2012. doi:10.1029/2012GL052921.
- R. B. Dahlburg, T. A. Zang, D. Montgomery, and M. Y. Hussaini. Viscous, resistive magnetohydrodynamic stability computed by spectral techniques. *Proc. Natl. Acad. Sci. U.S.A.*, 80(18):5798–5802, 1983. ISSN 0027-8424.
- P. A. Damiano, A. N. Wright, and J. F. McKenzie. Properties of Hall magnetohydrodynamic waves modified by electron inertia and finite Larmor radius effects. *Phys. Plasmas*, 16(6):062901, 2009. ISSN 1089-7674.

- J. De Jonghe. Legolas: MHD instabilities in an astrophysical jet. 2023. doi:10.34740/KAGGLE/DS/2750846.
- J. De Jonghe and R. Keppens. A two-fluid analysis of waves in a warm ion-electron plasma. *Phys. Plasmas*, 27(12), 2020. ISSN 10897674. doi:10.1063/5.0029534.
- J. De Jonghe and R. Keppens. Two-Fluid Treatment of Whistling Behavior and the Warm Appleton-Hartree Extension. *J. Geophys. Res. Space Phys.*, 126(5):1–24, 2021a. ISSN 21699402. doi:10.1029/2020JA028953.
- J. De Jonghe and R. Keppens. Laser-induced Cherenkov radiation in a warm two-fluid model. In *47th EPS Conference on Plasma Physics, EPS 2021*, pages 1235–1238, 2021b. ISBN 9781713837046.
- J. De Jonghe, N. Claes, and R. Keppens. Legolas : magnetohydrodynamic spectroscopy with viscosity and Hall current. *J. Plasma Phys.*, 88:905880321, 2022. doi:10.1017/S0022377822000617.
- J. W. Demmel. *Applied numerical linear algebra*. Society for Industrial and Applied Mathematics, 1 edition, 1997. ISBN 9780898713893; 0898713897.
- J. F. Denisse and J. L. Delcroix. *Théorie des ondes dans les plasmas*. Dunod, 1961. Transl.: Plasma Waves, 1963, John Wiley.
- D. Dobrott, S. C. Prager, and J. B. Taylor. Influence of diffusion on the resistive tearing mode. *Phys. Fluids*, 20(11):1850–1854, 1977. doi:10.1063/1.861803.
- D. Q. Eckhardt and I. H. Herron. Suppression of magnetorotational instability in viscous resistive magnetized Taylor–Couette flow. *Z. Angew. Math. Phys.*, 69(2):1–11, 2018. ISSN 0044-2275.
- P. M. Edwin and B. Roberts. Wave Propagation in a Magnetic Cylinder. *Sol. Phys.*, 88(1-2):179–191, 1983. doi:10.1007/BF00196186.
- R. Erdélyi and M. Goossens. Resonant absorption of Alfvén waves in coronal loops in visco-resistive MHD. *Astron. Astrophys.*, 294:575–586, 1995.
- M. Erdmann, J. Glombitza, G. Kasieczka, and U. Klemradt. *Deep Learning for Physics Research*. World Scientific, 2021. doi:10.1142/12294.
- G. Fiksel, W. Fox, A. Bhattacharjee, D. H. Barnak, P.-Y. Chang, K. Germaschewski, S. X. Hu, and P. M. Nilson. Magnetic reconnection between colliding magnetized laser-produced plasma plumes. *Phys. Rev. Lett.*, 113:105003, 2014. doi:10.1103/PhysRevLett.113.105003.

- W. Fox, J. Park, W. Deng, G. Fiksel, A. Spitkovsky, and A. Bhattacharjee. Astrophysical particle acceleration mechanisms in colliding magnetized laser-produced plasmas. *Phys. Plasmas*, 24(9):092901, 2017. doi:10.1063/1.4993204.
- H. P. Furth, J. Killeen, and M. N. Rosenbluth. Finite-resistivity instabilities of a sheet pinch. *Phys. Fluids*, 6(4):459–484, 1963. doi:10.1063/1.1706761.
- S. P. Gary and H. Li. Whistler heat flux instability at high beta. *Astrophys. J.*, 529(2):1131, feb 2000. doi:10.1086/308294.
- S. P. Gary and C. W. Smith. Short-wavelength turbulence in the solar wind: Linear theory of whistler and kinetic Alfvén fluctuations. *J. Geophys. Res. Space Phys.*, 114(A12):n/a, 2009. ISSN 0148-0227.
- S. P. Gary, R. M. Skoug, and W. Daughton. Electron heat flux constraints in the solar wind. *Phys. Plasmas*, 6(6):2607–2612, 1999. ISSN 1070-664X.
- T. Gebhardt and S. Grossmann. The Taylor-Couette eigenvalue problem with independently rotating cylinders. *Z. Phys., B Condens. matter*, 90(4):475–490, 1993. ISSN 0722-3277.
- H. Goedbloed and R. Keppens. The super-Alfvénic rotational instability in accretion disks about black holes. *Astrophys. J., Suppl. Ser.*, 259(2):65, 2022. doi:10.3847/1538-4365/ac573c.
- H. Goedbloed, R. Keppens, and S. Poedts. *Magnetohydrodynamics of Laboratory and Astrophysical Plasmas*. Cambridge University Press, 2019. doi:10.1017/9781316403679.
- P. Goldreich and W. H. Julian. Pulsar Electrodynamics. *Astrophys. J.*, 157:869, 1969. doi:10.1086/150119.
- I. Goodfellow, Y. Bengio, and A. Courville. *Deep Learning*. MIT Press, 2016.
- D. A. Gurnett and A. Bhattacharjee. *Introduction to Plasma Physics: With Space and Laboratory Applications*. Cambridge University Press, 2005. doi:10.1017/CBO9780511809125.
- D. A. Gurnett, S. D. Shawhan, N. M. Brice, and R. L. Smith. Ion cyclotron whistlers. *J. Geophys. Res.*, 70:1665–1688, 1965.
- E. Hameiri, A. Ishizawa, and A. Ishida. Waves in the Hall-magnetohydrodynamics model. *Phys. Plasmas*, 12:072109, 2005. doi:10.1063/1.1952887.

- J. D. Hare, L. Suttle, S. V. Lebedev, N. F. Loureiro, A. Ciardi, G. C. Burdiak, J. P. Chittenden, T. Clayson, C. Garcia, N. Niasse, T. Robinson, R. A. Smith, N. Stuart, F. Suzuki-Vidal, G. F. Swadling, J. Ma, J. Wu, and Q. Yang. Anomalous heating and plasmoid formation in a driven magnetic reconnection experiment. *Phys. Rev. Lett.*, 118:085001, 2017. doi:10.1103/PhysRevLett.118.085001. URL <https://link.aps.org/doi/10.1103/PhysRevLett.118.085001>.
- A. B. Hassam. Tearing Modes in Solar Coronal Loops. *Astrophys. J.*, 348:778, 1990. doi:10.1086/168286.
- N. Hayashi. Advanced tokamak research with integrated modeling in JT-60 upgrade. *Phys. Plasmas*, 17(5):056112–056112–13, 2010. ISSN 1070-664X.
- K. He, X. Zhang, S. Ren, and J. Sun. Deep residual learning for image recognition. In *2016 IEEE Conference on Computer Vision and Pattern Recognition (CVPR)*, pages 770–778, Los Alamitos, CA, USA, 2016. IEEE Computer Society. doi:10.1109/CVPR.2016.90.
- D. P. Hinson, F. M. Flasar, A. J. Kliore, P. J. Schinder, J. D. Twicken, and R. G. Herrera. Jupiter’s ionosphere: Results from the first galileo radio occultation experiment. *Geophys. Res. Lett.*, 24(17):2107–2110, 1997. ISSN 0094-8276.
- I. Hofmann. Resistive tearing modes in a sheet pinch with shear flow. *Plasma Physics*, 17(2):143–157, 1975. doi:10.1088/0032-1028/17/2/005.
- M. Hosseinpour, Y. Chen, and S. Zenitani. On the effect of parallel shear flow on the plasmoid instability. *Phys. Plasmas*, 25(10):102117, 2018. doi:10.1063/1.5061818.
- Y.-K. Hsieh and Y. Omura. Nonlinear damping of oblique whistler mode waves via Landau resonance. *J. Geophys. Res. Space Phys.*, 123(9):7462–7472, 2018. doi:10.1029/2018JA025848.
- Y. C. Huang and L. H. Lyu. Atlas of the medium frequency waves in the ion-electron two-fluid plasma. *Phys. Plasmas*, 26(9):092102, 2019. ISSN 1089-7674.
- J. D. Huba. *Hall Magnetohydrodynamics - A Tutorial*, pages 166–192. Springer Berlin Heidelberg, Berlin, Heidelberg, 2003. ISBN 978-3-540-36530-3. doi:10.1007/3-540-36530-3_9.
- M. Imai, O. Santolík, S. T. Brown, I. Kolmašová, W. S. Kurth, M. A. Janssen, G. B. Hospodarsky, D. A. Gurnett, S. J. Bolton, and S. M. Levin. Jupiter lightning-induced whistler and sferic events with waves and MWR during Juno perijoves. *Geophys. Res. Lett.*, 45(15):7268–7276, 2018. ISSN 0094-8276.

- S. Ioffe and C. Szegedy. Batch normalization: Accelerating deep network training by reducing internal covariate shift. In F. Bach and D. Blei, editors, *Proceedings of the 32nd International Conference on Machine Learning*, volume 37 of *Proceedings of Machine Learning Research*, pages 448–456, Lille, France, 2015. PMLR.
- A. Ishida, C. Z. Cheng, and Y.-K. M. Peng. Properties of low and medium frequency modes in two-fluid plasma. *Phys. Plasmas*, 12(5):052113–052113–9, 2005. ISSN 1089-7674.
- N. Iwamoto. Collective modes in nonrelativistic electron-positron plasmas. *Phys. Rev. E*, 47:604–611, 1993. doi:10.1103/PhysRevE.47.604.
- R. Keppens and H. Goedbloed. Wave modes in a cold pair plasma: the complete phase and group diagram point of view. *J. Plasma Phys.*, 85(1):175850101, 2019a. doi:10.1017/S0022377819000102.
- R. Keppens and H. Goedbloed. A fresh look at waves in ion-electron plasmas. *Frontiers in Astronomy and Space Sciences*, 6:11, 2019b. ISSN 2296-987X. doi:10.3389/fspas.2019.00011.
- R. Keppens, H. Goedbloed, and J.-B. Durrive. Waves in a warm pair plasma: a relativistically complete two-fluid analysis. *J. Plasma Phys.*, 85(4):905850408, 2019. doi:10.1017/S0022377819000552.
- R. Keppens, B. Popescu Braileanu, Y. Zhou, W. Ruan, C. Xia, Y. Guo, N. Claes, and F. Bacchini. MPI-AMRVAC 3.0: updates to an open-source simulation framework, 2023.
- M. G. Kivelson and C. T. Russell. *Introduction to Space Physics*. Cambridge University Press, 1995. doi:10.1017/9781139878296.
- M. D. Kuczyński, M. Borchardt, R. Kleiber, A. Könies, and C. Nührenberg. Magnetohydrodynamic eigenfunction classification with a Neural Network. *J. Comput. Appl. Math.*, 406:113889, 2022. ISSN 03770427. doi:10.1016/j.cam.2021.113889.
- R. M. Kulsrud. *Plasma Physics for Astrophysics*. Princeton University Press, 2005. ISBN 9780691120737.
- M. W. Kunz. On the linear stability of weakly ionized, magnetized planar shear flows. *Mon. Notices Royal Astron. Soc.*, 385(3):1494–1510, 2008. ISSN 0035-8711. doi:10.1111/j.1365-2966.2008.12928.x.
- I. Langmuir. Oscillations in ionized gases. *Proc. Natl. Acad. Sci.*, 14(8):627–637, 1928. ISSN 0027-8424.

- R. Lehoucq, D. Sorensen, and C. Yang. *ARPACK Users' Guide: Solution of Large-scale Eigenvalue Problems with Implicitly Restarted Arnoldi Methods*. Software, Environments, Tools. Society for Industrial and Applied Mathematics, 1998. ISBN 9780898714074.
- G. R. J. Lesur. Magnetohydrodynamics of protoplanetary discs. *J. Plasma Phys.*, 87(1):205870101, 2021. doi:10.1017/S0022377820001002.
- J. H. Li and Z. W. Ma. Nonlinear evolution of resistive tearing mode with sub-Alfvénic shear flow. *J. Geophys. Res. Space Phys.*, 115(9):6–11, 2010. ISSN 21699402. doi:10.1029/2010JA015315.
- J. H. Li and Z. W. Ma. Roles of super-Alfvénic shear flows on Kelvin–Helmholtz and tearing instability in compressible plasma. *Phys. Scr.*, 86(4):045503, 2012. doi:10.1088/0031-8949/86/04/045503.
- R. A. López, S. M. Shaaban, M. Lazar, S. Poedts, P. H. Yoon, A. Micera, and G. Lapenta. Particle-in-cell simulations of the whistler heat-flux instability in solar wind conditions. *Astrophys. J. Lett.*, 882(1):L8–, 2019. ISSN 2041-8205.
- N. F. Loureiro, A. A. Schekochihin, and D. A. Uzdensky. Plasmoid and Kelvin–Helmholtz instabilities in Sweet–Parker current sheets. *Phys. Rev. E*, 87: 013102, 2013. doi:10.1103/PhysRevE.87.013102.
- M. Lyutikov. Beam instabilities in a magnetized pair plasma. *J. Plasma Phys.*, 62(1):65–86, 1999. doi:10.1017/S0022377899007837.
- Q. Ma, A. V. Artemyev, D. Mourenas, W. Li, R. M. Thorne, C. A. Kletzing, W. S. Kurth, G. B. Hospodarsky, G. D. Reeves, H. E. Spence, and J. Wygant. Very oblique whistler mode propagation in the radiation belts: Effects of hot plasma and Landau damping. *Geophys. Res. Lett.*, 44(24):12–12,066, 2017. ISSN 0094-8276.
- D. H. Mackay and A. R. Yeates. The Sun's global photospheric and coronal magnetic fields: Observations and models. *Living Rev. Sol. Phys.*, 9(1):6, 2012. ISSN 1614-4961. doi:10.12942/lrsp-2012-6.
- J. Martínez-Sykora, B. De Pontieu, V. Hansteen, and M. Carlsson. The role of partial ionization effects in the chromosphere. *Philos. Trans. Royal Soc. A*, 373(2042):20140268, 2015. doi:10.1098/rsta.2014.0268.
- E. F. Milone and W. J. F. Wilson. *Solar System Astrophysics: Planetary Atmospheres and the Outer Solar System*. Astronomy and Astrophysics Library. Springer New York, New York, NY, 2nd ed. 2014 edition, 2014. ISBN 1461490898.

- E. Mishin and A. Streltsov. *Nonlinear Wave and Plasma Structures in the Auroral and Subauroral Geospace*. Elsevier, 2021. ISBN 0128207604; 9780128207604.
- M. E. Mlodik, E. J. Kolmes, I. E. Ochs, T. Rubin, and N. J. Fisch. Partial-ionization deconfinement effect in magnetized plasma. *Phys. Plasmas*, 29(11):112111, 2022. doi:10.1063/5.0114967.
- P. Muggli, J. Yoshii, T. Katsouleas, C. Clayton, and C. Joshi. Cerenkov radiation from a magnetized plasma: a diagnostic for PBWA experiments. In *Proceedings of the 1999 Particle Accelerator Conference (Cat. No.99CH36366)*, volume 5, pages 3654–3656. IEEE, 1999.
- D. Nakamura, A. Ikeda, H. Sawabe, Y. H. Matsuda, and S. Takeyama. Record indoor magnetic field of 1200 T generated by electromagnetic flux-compression. *Rev. Sci. Instrum.*, 89(9):095106, 2018. doi:10.1063/1.5044557.
- Y. Narita, R. Nakamura, W. Baumjohann, K.-H. Glassmeier, U. Motschmann, B. Giles, W. Magnes, D. Fischer, R. B. Torbert, C. T. Russell, R. J. Strangeway, J. L. Burch, Y. Nariyuki, S. Saito, and S. P. Gary. On electron-scale whistler turbulence in the solar wind. *Astrophys. J. Lett.*, 827(1):L8, 2016. ISSN 2041-8213.
- National Oceanic and Atmospheric Administration. Real time solar wind, 2023. URL <https://www.swpc.noaa.gov/products/real-time-solar-wind>.
- R. Nijboer, B. Holst, S. Poedts, and J. Goedbloed. Calculating magnetohydrodynamic flow spectra. *Comput. Phys. Commun.*, 106(1):39–52, 1997. ISSN 0010-4655. doi:10.1016/S0010-4655(97)00082-9.
- R. Ochoukov, V. Bobkov, B. Chapman, R. Dendy, M. Dunne, H. Faugel, M. García-Muñoz, B. Geiger, P. Hennequin, K. G. McClements, D. Moseev, S. Nielsen, J. Rasmussen, P. Schneider, M. Weiland, and J.-M. Noterdaeme. Observations of core ion cyclotron emission on ASDEX Upgrade tokamak. *Rev. Sci. Instrum.*, 89(10):10J101, 2018. doi:10.1063/1.5035180.
- L. Ofman, X. L. Chen, P. J. Morrison, and R. S. Steinolfson. Resistive tearing mode instability with shear flow and viscosity. *Phys. Fluids B*, 3(6):1364–1373, 1991. ISSN 0899-8221.
- L. Ofman, P. J. Morrison, and R. S. Steinolfson. Nonlinear evolution of resistive tearing mode instability with shear flow and viscosity. *Phys. Fluids B*, 5(2):376–387, 1993. ISSN 08998221. doi:10.1063/1.860523.
- B. P. Pandey and M. Wardle. Magnetic-diffusion-driven shear instability of solar flux tubes. *Mon. Notices Royal Astron. Soc.*, 431(1):570–581, 2013. ISSN 0035-8711. doi:10.1093/mnras/stt184.

- S. Parenti. Solar prominences: Observations. *Living Rev. Sol. Phys.*, 11(1):1, 2014. ISSN 1614-4961. doi:10.12942/lrsp-2014-1.
- R. B. Paris and W. N. Sy. Influence of equilibrium shear flow along the magnetic field on the resistive tearing instability. *Phys. Fluids*, 26(10):2966–2975, 1983. doi:10.1063/1.864061.
- F. J. Pérez-Invernón, N. G. Lehtinen, F. J. Gordillo-Vázquez, and A. Luque. Whistler wave propagation through the ionosphere of Venus: Whistler wave propagation on Venus. *J. Geophys. Res. Space Phys.*, 122(11):11–11,644, 2017. ISSN 2169-9380.
- J. Pétri. The illusion of neutron star magnetic field estimates. *Mon. Notices Royal Astron. Soc.*, 485:4573–4587, 2019. doi:10.1093/mnras/stz711.
- R. K. Pollard and J. B. Taylor. Influence of equilibrium flows on tearing modes. *Phys. Fluids*, 22(1):126–131, 1979. doi:10.1063/1.862451.
- E. Priest. *Magnetohydrodynamics of the Sun*. Cambridge University Press, 2014. doi:10.1017/CBO9781139020732.
- F. Pucci, M. Velli, and A. Tenerani. Fast magnetic reconnection: “ideal” tearing and the Hall effect. *Astrophys. J.*, 845(1):25, 2017. doi:10.3847/1538-4357/aa7b82.
- J. Pétri. Theory of pulsar magnetosphere and wind. *J. Plasma Phys.*, 82(5), 2016. ISSN 0022-3778.
- A. Quarteroni. *Numerical Models for Differential Problems*, volume 2. Springer-Verlag, 2009. ISBN 978-88-470-1070-3.
- F. Reale. Coronal loops: Observations and modeling of confined plasma. *Living Rev. Sol. Phys.*, 11(1):4, 2014. ISSN 1614-4961. doi:10.12942/lrsp-2014-4.
- M. Rheinhardt and U. Geppert. Hall-drift induced magnetic field instability in neutron stars. *Phys. Rev. Lett.*, 88(10):1011031–1011034, 2002. ISSN 0031-9007.
- B. Roberts. *MHD Waves in the Solar Atmosphere*. Cambridge University Press, 2019. doi:10.1017/9781108613774.
- S. Rosenberg and W. Gekelman. Electric field measurements of directly converted lower hybrid waves at a density striation. *Geophys. Res. Lett.*, 25(6):865–868, 1998. ISSN 0094-8276.

- G. Rüdiger, R. Hollerbach, M. Schultz, and D. Elstner. Destabilization of hydrodynamically stable rotation laws by azimuthal magnetic fields. *Mon. Notices Royal Astron. Soc.*, 377(4):1481–1487, 2007. ISSN 0035-8711. doi:10.1111/j.1365-2966.2007.11682.x.
- J. Shao, H. Liu, Y. Xu, Z. Chen, T. Wang, J. Cheng, X. Wang, J. Huang, H. Liu, X. Zhang, K. Xu, C. Tang, and T. J.-T. Team. Effect of the toroidal flow and flow shear on the $m/n = 2/1$ tearing mode in J-TEXT tokamak. *Plasma Phys. Control. Fusion*, 63(6):065017, 2021. doi:10.1088/1361-6587/abf85e.
- X. Shao, B. Eliasson, A. S. Sharma, G. Milikh, and K. Papadopoulos. Attenuation of whistler waves through conversion to lower hybrid waves in the low-altitude ionosphere. *J. Geophys. Res. Space Phys.*, 117(A4), 2012. ISSN 0148-0227.
- C. Shi, M. Velli, F. Pucci, A. Tenerani, and M. E. Innocenti. Oblique tearing mode instability: Guide field and Hall effect. *Astrophys. J.*, 902(2):142, 2020. doi:10.3847/1538-4357/abb6fa.
- T. Shimizu, K. Kondoh, and S. Zenitani. Numerical MHD study for plasmoid instability in uniform resistivity. *Phys. Plasmas*, 24(11):112117, 2017. doi:10.1063/1.4996249.
- R. Soler and J. L. Ballester. Theory of fluid instabilities in partially ionized plasmas: An overview. *Frontiers in Astronomy and Space Sciences*, 9, 2022. ISSN 2296-987X. doi:10.3389/fspas.2022.789083.
- D. A. Spong, W. W. Heidbrink, C. Paz-Soldan, X. D. Du, K. E. Thome, M. A. Van Zeeland, C. Collins, A. Lvovskiy, R. A. Moyer, M. E. Austin, D. P. Brennan, C. Liu, E. F. Jaeger, and C. Lau. First direct observation of runaway-electron-driven whistler waves in tokamaks. *Phys. Rev. Lett.*, 120:155002, 2018. doi:10.1103/PhysRevLett.120.155002.
- G. A. Stewart and E. W. Laing. Wave propagation in equal-mass plasmas. *J. Plasma Phys.*, 47(2):295–319, 1992.
- T. H. Stix. *Waves in Plasmas*. American Inst. of Physics, 1992. ISBN 9780883188590.
- L. Storey. An investigation of whistling atmospherics. *Philos. Trans. Royal Soc. A*, 246:113–141, 1953. doi:10.1098/rsta.1953.0011.
- T. E. Stringer. Low-frequency waves in an unbounded plasma. *Journal of Nuclear Energy, Part C: Plasma Physics, Accelerators, Thermonuclear Research*, 5(2):89–107, 1963. ISSN 0368-3281.

- A. Tenerani, A. F. Rappazzo, M. Velli, and F. Pucci. The tearing mode instability of thin current sheets: The transition to fast reconnection in the presence of viscosity. *Astrophys. J.*, 801(2):145, 2015. doi:10.1088/0004-637x/801/2/145.
- T. Terasawa. Hall current effect on tearing mode instability. *Geophys. Res. Lett.*, 10(6):475–478, 1983. doi:<https://doi.org/10.1029/GL010i006p00475>.
- K. S. Thorne and R. D. Blandford. *Modern Classical Physics: Optics, Fluids, Plasmas, Elasticity, Relativity, and Statistical Physics*. Princeton University Press, 2017. ISBN 9781400848898.
- L. Tonks and I. Langmuir. Oscillations in ionized gases. *Phys. Rev.*, 33:195–210, 1929. doi:10.1103/PhysRev.33.195.
- L. N. Trefethen and D. Bau III. *Numerical linear algebra*. Society for Industrial and Applied Mathematics, 1997. ISBN 9780898713619; 0898713617.
- R. Treumann and W. Baumjohann. *Advanced Space Plasma Physics*. Imperial College Press, 1st edition, 1997. ISBN 1860940269,9781860940262,9781860943072.
- R. Treumann and W. Baumjohann. Collisionless magnetic reconnection in space plasmas. *Frontiers in Physics*, 1, 2013. ISSN 2296-424X. doi:10.3389/fphy.2013.00031.
- N. M. Viiall and J. E. Borovsky. Nine outstanding questions of solar wind physics. *J. Geophys. Res. Space Phys.*, 125(7):e2018JA026005–n/a, 2020. ISSN 2169-9380.
- J. Wesson. *Tokamaks*. International series of monographs on physics. Oxford University Press, Oxford, 4 edition, 2011.
- A. P. Willis and C. F. Barenghi. A Taylor-Couette dynamo. *Astron. Astrophys.*, 393(1):339–343, 2002. doi:10.1051/0004-6361:20021007.
- L. N. Wu and Z. W. Ma. Linear growth rates of resistive tearing modes with sub-Alfvénic streaming flow. *Phys. Plasmas*, 21(7):072105, 2014. doi:10.1063/1.4886360.
- M. Yamada, R. Kulsrud, and H. Ji. Magnetic reconnection. *Rev. Mod. Phys.*, 82:603–664, 2010. doi:10.1103/RevModPhys.82.603.
- P. H. Yoon, V. S. Pandey, and D.-H. Lee. Oblique nonlinear whistler wave. *J. Geophys. Res. Space Phys.*, 119(3):1851–1862, 2014. doi:10.1002/2013JA018993.

- J. Yoshii, C. Lai, T. Katsouleas, C. Joshi, and W. Mori. Radiation from Cerenkov wakes in a magnetized plasma. *Phys. Rev. Lett.*, 79(21):4194–4197, 1997.
- N. Yugami, T. Higashiguchi, H. Gao, S. Sakai, K. Takahashi, H. Ito, Y. Nishida, and T. Katsouleas. Experimental observation of radiation from Cherenkov wakes in a magnetized plasma. *Phys. Rev. Lett.*, 89(6):065003/4–065003/4, 2002.
- X. Zhang, L. J. Li, L. C. Wang, J. H. Li, and Z. W. Ma. Influences of sub-Alfvénic shear flows on nonlinear evolution of magnetic reconnection in compressible plasmas. *Phys. Plasmas*, 18(9):092112, 2011. doi:10.1063/1.3643792.
- J. Zhao. Dispersion relations and polarizations of low-frequency waves in two-fluid plasmas. *Phys. Plasmas*, 22(4):042115, 2015. ISSN 1089-7674.
- J. Zhao. Properties of whistler waves in warm electron plasmas. *Astrophys. J.*, 850(1):13, 2017. ISSN 1538-4357.
- J. S. Zhao, Y. Voitenko, M. Y. Yu, J. Y. Lu, and D. J. Wu. Properties of short-wavelength oblique Alfvén and slow waves. *Astrophys. J.*, 793(2):107, 2014. ISSN 1538-4357.

Curriculum

Jordi De Jonghe

Date of birth 18 August 1996
Nationality Belgian
GitHub jordidj
ORCiD 0000-0003-2443-3903 

Education

- **Doctoral Programme in Science (PhD): Mathematics (2019-2023)**
Centre for mathematical Plasma-Astrophysics, KU Leuven, Leuven, Belgium
Thesis title: Linear theory of plasma waves and instabilities: From ion-electron to MHD descriptions
Supervisor: Prof. Dr. Rony Keppens
- **Master of Science (MSc): Physics (Theoretical physics) (2017-2019)**
KU Leuven, Leuven, Belgium
Thesis title: Instantons and holography
Supervisor: Prof. Dr. Thomas Van Riet
Cum Laude
- **Bachelor of Science (BSc): Physics (2014-2017)**
KU Leuven, Leuven, Belgium
Thesis title: The EmDrive
Supervisor: Prof. Dr. Thomas Van Riet & Dr. Thibaut Demaerel
Cum Laude
- **Bachelor of Science (BSc): Mathematics (2014-2017)**
KU Leuven, Leuven, Belgium
Thesis title: Normal modes of magnetohydrodynamics
Supervisor: Dr. Francesco Pucci
Cum Laude

Additional training

- HPC introduction (8 October 2019, KU Leuven)
- Fortran for programmers (14 October 2019, KU Leuven)
- Central lecture Scientific Integrity (18 November 2019, KU Leuven)
- Teaching assistant training (2019, KU Leuven)
- Waves and Instabilities (2020, KU Leuven B-KUL-G0B26A)
- Science Communication and Outreach (2020, KU Leuven B-KUL-G0R44A)

Publications

- **Journal article:** N. Claes, J. De Jonghe, and R. Keppens. Legolas: A Modern Tool for Magnetohydrodynamic Spectroscopy. *Astrophys. J., Suppl. Ser.*, 251(2):25, 2020. ISSN 0067-0049. doi:10.3847/1538-4365/abc5c4.
- **Journal article:** J. De Jonghe and R. Keppens. A two-fluid analysis of waves in a warm ion-electron plasma. *Phys. Plasmas*, 27(12), 2020. ISSN 10897674. doi:10.1063/5.0029534.
- **Journal article:** J. De Jonghe and R. Keppens. Two-Fluid Treatment of Whistling Behavior and the Warm Appleton-Hartree Extension. *J. Geophys. Res. Space Phys.*, 126(5):1–24, 2021a. ISSN 21699402. doi:10.1029/2020JA028953.
- **Erratum:** N. Claes, J. De Jonghe, and R. Keppens. Erratum: “Legolas: A Modern Tool for Magnetohydrodynamic Spectroscopy” (2020, ApJS, 251, 25). *Astrophys. J., Suppl. Ser.*, 254(2):45, 2021. ISSN 0067-0049. doi:10.3847/1538-4365/ac02c1.
- **Conference proceedings:** J. De Jonghe and R. Keppens. Laser-induced Cherenkov radiation in a warm two-fluid model. In *47th EPS Conference on Plasma Physics, EPS 2021*, pages 1235–1238, 2021b. ISBN 9781713837046.
- **Journal article:** J. De Jonghe, N. Claes, and R. Keppens. Legolas : magnetohydrodynamic spectroscopy with viscosity and Hall current. *J. Plasma Phys.*, 88:905880321, 2022. doi:10.1017/S0022377822000617.

Talks & seminars

- **A two-fluid analysis of waves in a warm ion-electron plasma.** Oral presentation at AAPPS-DPP 2020, virtual, 28 October 2020.
- **Waves in a warm ion-electron plasma: A two-fluid analysis and model applications.** Seminar at Centre for mathematical Plasma-Astrophysics, KU Leuven, Leuven, Belgium, 11 February 2021.
- **Waves in a warm, ideal two-fluid plasma and model applications.** Poster presentation at EPS 2021, virtual, 25 June 2021.
- **The *Legolas* code: A new tool for MHD wave spectroscopy.** Oral presentation at Magnetohydrodynamics: Physics for the 21st Century, Lorentz center, Leiden, the Netherlands, 11 October 2021.
- **Influence of equilibrium flow on the resistive tearing mode.** Oral presentation at EFTC 2021, virtual, 13 October 2021.
- **Resistive tearing growth rate modification by equilibrium flow.** Poster presentation at COSPAR 2022, Athens, Greece, 19-20 July 2022.
- ***Legolas*: MHD spectroscopic analysis of the tearing mode.** Oral presentation at CmPA Retrospective in honor of prof. Stefaan Poedts, Centre for mathematical Plasma-Astrophysics (KU Leuven), Leuven, Belgium, 9 September 2022.
- **Modification of resistive tearing growth rate by equilibrium flow.** Oral presentation at AAPPS-DPP 2022, virtual, 13 October 2022.
- **Neural network eigenmode classification in the MHD spectroscopy code *Legolas*.** Seminar at Centre for mathematical Plasma-Astrophysics, KU Leuven, Leuven, Belgium, 17 November 2022.

Research stays & collaborations

- **Neural network eigenmode classification in the MHD spectroscopy code *Legolas*,** at the Max-Planck-Institut für Plasmaphysik, Greifswald, Germany (3-22 October 2022).

Teaching experience

- **Calculus I.** 2019-2022 (first year of bachelor in physics / mathematics), KU Leuven (B-KUL-G0Y37A), teaching assistant.
- **Calculus II.** 2020-2023 (first year of bachelor in physics / mathematics), KU Leuven (B-KUL-G0Y40A), teaching assistant.
- **Calculus & Analyse.** 2019, 2021-2022 (first year of bachelor in bio-engineering), KU Leuven (B-KUL-I0O64A), teaching assistant.
- **Wiskunde II, deel 1.** 2020 (first year of bachelor in biology), KU Leuven (B-KUL-G0O17E), teaching assistant.
- **Master thesis guidance.** 2021-2023, assistant.

FACULTY OF SCIENCE
DEPARTMENT OF MATHEMATICS
CENTRE FOR MATHEMATICAL PLASMA-ASTROPHYSICS
Celestijnenlaan 200B box 2400
B-3001 Leuven

